The Optical Calibration of the Sudbury Neutrino Observatory

Bryce Anton Moffat

A thesis submitted to the Department of Physics
in conformity with the requirements for the degree of
Doctor of Philosophy

Queen's University
Kingston, Ontario, Canada
July, 2001

Für Antje,
die so laaaange warten mußte...

Abstract

SNO is designed to detect Cherenkov light emitted in low-energy interactions over the range 0-20 MeV. The primary signals being studied by the Observatory are interactions of ^{8}B solar neutrinos with D_2O. The optical calibration of the Sudbury Neutrino Observatory (SNO) is a vital pre-requisite to the precision of the analysis of solar neutrino data from the detector.

The optical calibration uses a light diffusing sphere and a pulsed nitrogen/dye laser with five selectable dyes to sample the detector optical properties as a function of wavelength and position. The principal detector optical parameters determined are the D_2O and H_2O attenuations, and the angular response of the photomultipliers.

The attenuation of light in the ultra-pure D_2O is measured at six wavelengths between 337 nm and 620 nm to be between $(4.44 \pm 1.33) \times 10^{-5}\,\mathrm{cm}^{-1}$ at 620 nm and $(10.17 \pm 1.45) \times 10^{-5}\,\mathrm{cm}^{-1}$ at 372 nm. These results are a factor of $\sim 1/3$ lower than previous measurements of Boivin et al. [1]. At this low level, the attenuation plays a greatly reduced role in determining the energy response of SNO to neutrino interactions.

The *in situ* measurement of the photomultiplier (PMT) angular response is well determined over the range 0–40°by the optical data. The PMT response is 5 to 10% higher than the calculations and *ex situ* measurements of Lay [2] and Lyon [3] over the range of incident angles ($25 \sim 40°$) most relevant to the neutrino measurement in the D_2O fiducial volume. The uncertainty in the PMT angular response increases with incident angle up to approximately 1% at the largest angles sampled.

Monte Carlo simulations and analytic calculations of the detector response to electrons and gamma-rays rely on the measured optical parameters. Both methods provide a way to interpolate between and to extrapolate beyond the radioactive source

measurements taken at specific locations in the detector. Gamma rays from ^{16}N are used to verify the energy response calculations and agreement is to $\lesssim 1\%$ at the sampled positions within the 550 cm heavy water fiducial volume. The effects of systematic variations in the inputs to the detector optics measurement have only a small effect ($\lesssim 0.13\%$) on the overall detector response to Cherenkov interactions. However, uncertainties in the extrapolation of the photomultipier angular response beyond the measured range increase this uncertainty to $\sim 1.25\%$.

Contents

Acknowledgements

I would like to thank everyone who contributed to the success of my thesis, and in particular:

- My advisor, Aksel Hallin, has been an inexhaustible source of ideas and has often encouraged me to follow a more pragmatic approach to solving problems. I have benefitted greatly from his experience and from his availability to help with all aspects of my work.
- Art McDonald, the director of the SNO project, has provided a truly unique opportunity to work at the forefront of solar neutrino research. He often gave me some much-needed perspective on the big picture.
- Peter Skensved, who often shared his insight into many physical and engineering problems, was also instrumental in both allowing and preventing computer use and abuse, and vice-versa.
- Fraser Duncan had many helpful suggestions and organized much of the data taking, including the crucial September 2000 optical scans.
- Chuck Hearns's practical expertise and incredible work habits contributed enormously to the physical tools at the heart of this thesis: the laserball, the um-

bilicals, and the SNO detector itself. Thanks also for all the important small breaks, without which I surely would've gone crazy.

- Mark Boulay for his herculean efforts at analyzing SNO data, including the many computer techniques he developed along the way, and for being a good lab mate.
- Richard Ford for building the laser and for his previous work on the optical calibration.
- Barry Robertson for helping me focus on the essentials and for carefully reading my thesis.
- Mark Chen for bringing a fresh scientific perspective and for giving me the opportunity to continue work with him – in Germany!
- Hugh Evans for his stories and some rather delicious sailing trips.
- George Ewan, the founder of the Sudbury Neutrino Observatory, for teaching me about nuclear astrophysics.
- The other members of the Queen's SNO group: Hamish Leslie and Hay-Boon Mak for discussions of physics, Alvin Bell for help with electronics, Phil Harvey for his awesome programming.
- The other SNO graduate students who put so much effort into getting SNO working and running: Chris Jillings, Ed Korpach, Andre Hamer, Matt Dayon; and the newer students, Mark Kos and Bryan Fulsom, for getting their hands dirty with data analysis from the get-go. Also thanks to the summer students, especially Martin Pickel for his help investigating Rayleigh scattering.
- The SNO Collaboration for contributing to the operation of the experiment and to the numerous analysis discussions which helped bring this work into focus.

- All the Sudbury SNO staff for organizing things in Sudbury, and INCO for the safe and efficient use of their mine.
- The Natural Sciences and Research Engineering Research Council of Canada, the Fonds pour la Formation de Chercheurs et l'Aide à la Recherche, and Queen's University for providing funding throughout my studies.
- The Queen's physics department for a good working climate, and all the other physics grad students for discussions and fun diversions.
- Margaret Morris for her caring advice and friendliness in all matters to do with the physics department, and Alison Cunninghame for her help organizing trips to Sudbury.
- Annie Hsu for reading my thesis and for taking in my last big plants.
- Gary Contant for machining parts in a hurry, and for trying to fish out the lake.
- My parents, Ann and Tony Moffat, for their encouragment and support throughout my studies, and my "little" sister Lesley who made it to Germany before me.
- Antje Moffat for her patience, love and support – whether near or far, you were always on my side.
- Nanna and Grandad for their encouragement, and the Kershaws for looking after me in Sudbury.
- Murray, Nancy, Jeff, Louise, Sarah, Ben and Oscar Overington for having me to stay in their home and making my life pleasant, especially during the final stages of this thesis.

- My friends for accompanying me through the vagaries of my life as a graduate student and making it fun and enjoyable. Whether playing Skat, squash, or ultimate frisbee, going for pints and food, or maybe getting married, you helped to keep my body, mind and spirit together.

Statement of Originality

The work presented in this thesis is the author's own and is original except where noted here. All use of other's work is appropriately cited in the text.

The results presented in this thesis are the result of many years of collaborative research within SNO. In the scope of neutrino physics, the Sudbury Neutrino Observatory (SNO) is made unique by the use of heavy water (D_2O). While the microscopic properties of neutrino interactions with the deuteron have been studied theoretically for many years, there are many experimental difficulties in building a detector based on deuteron-rich heavy water.

The author's contribution to the SNO experiment is the optical characterization of the detector. Measurements of the optical attenuation of high purity heavy water and the *in situ* optical properties of the photomultiplier light sensor assemblies are the primary contributions of the author, and represent the bulk of the material in this thesis. The impact of the uncertainties in the optical model parameters on the detector energy response is the author's main contribution to the goals of the SNO experiment.

The analysis of optical data is developed by the author through the use of an independent set of computer programs. The optical programs rely on the ROOT libraries [4] and the QSNO libraries by Boulay [5] for supporting routines. These programs take as input the calibrated timing spectra produced by the SNOMAN package [6, 7], which is the foundation of all SNO analyses and was developed by many people. The optical computer programs are extensible and robust, and have already been used by another student to analyze new optical data [8].

The light source used for the optical measurements was designed and built by R.J. Ford over the course of his studies at Queen's University ([9, 10, 11]). The light diffusing ball was conceptually designed and tested as a part of his work. The ball and mounting hardware used for calibrations during production data taking was built by the author. The feedback from the analysis of optical data proved crucial in improving the design and in achieving a better approximation to a point source.

The calibration program for SNO relies on underwater umbilical cables to supply moveable sources with light, power and radioactive gases. The large variety of different types of cables made commercial production prohibitively expensive (∼\$60k setup fee per cable type). For the short cable lengths required (of order 100 feet), a 14 month development effort was pursued by the author at Queen's which resulted in an inexpensive method (∼\$500 per cable) for making all of the cables needed for SNO. The method for making these cables was developed by the author, with technical and logistical help from other members of the SNO group at Queen's.

The analysis of the uncertainty in the energy response of SNO due to the uncertainties in the optical parameters was performed by the author (Chapter 9). This work was done with the "RSP" response processor and other computer codes written and extensively tested by M. Boulay (Queen's University). M. Boulay also processed the ^{16}N source data which is used to confirm that the optical parameters used in RSP reproduce the actual detector response.

List of Figures

List of Tables

List of Acronyms

ADC	Analog to Digital Converter.
AV	Acrylic Vessel.
CC	Charged-current.
CERN	European Organization for Nuclear Research.
	Originally: Conseil Européen pour la Recherche Nucléaire.
CERNLIB	Library routines for FORTRAN from CERN.
DAQ	Data Acquisition System.
ECA	Electronics Calibration (low-level channel ADC slopes and offsets).
ES	Elastic scattering.
FCAR	Fonds pour les chercheurs et l'aide à la recherche
	(Québec Government science funding agency).
FORTRAN	FORmula TRANslator (computer programming language).
HEPA filter	High Efficiency Particulate Arrestance air filter.
ID	Inner diameter.
LED	Light Emitting Diode.
LSND	Liquid Scintillator Neutrino Detector, at Los Alamos.
NC	Neutral-current.

NSERC	Natural Sciences and Engineering Research Council of Canada (Canadian Government science funding agency).
MPE	Multiple photo-electron correction for PMT's hit by ≥ 2 photons.
MSW	Mikheev-Smirnov-Wolfenstein effect (matter-enhanced neutrino oscillations).
OCA	Optical Calibration (bulk attenuations, PMT angular response).
OD	Outer diameter.
PCA	Phototube Calibration (timing only).
PDF	Probability Distribution Function.
PGT	Pulsed Global Trigger.
PMT	Photomultiplier tube (also phototube).
PSUP	PMT support structure (stainless steel geodesic).
QSNO	Queen's SNO analysis package integrated with ROOT.
RCH	Root Calibration Histogram (10000 channels $\times$ 400 ns).
RDT	Root Delta Time histograms (10000 channels).
RMS	Root mean square.
ROOT	Object-oriented data analysis package in C++. (See `http://root.cern.ch`).
SK	Super-Kamiokande.
SNO	Sudbury Neutrino Observatory.
SNOMAN	SNO Monte Carlo and Analysis program.
SNP	Solar Neutrino Problem.
SNU	Solar Neutrino Unit (10^{-36} captures/target nucleus/s).
SSM	Standard Solar Model.
UV	Ultraviolet.
XSNOED	X-Windows SNO Event Display.

ZDAB	ZEBRA Data Acquisition/Analysis Bank.
ZEBRA	Data management library for CERNLIB in FORTRAN.

1 Introduction

SNO is an enormous optical instrument designed to detect low levels of light and, in particular, the short bursts of Cherenkov light associated with solar neutrino interactions. The detector distinguishes itself from other large-volume water detectors in several important ways. Heavy water at the centre is used to detect solar neutrinos through three separate interaction channels: charged current, neutral current and elastic scattering. An acrylic vessel contains the heavy water and separates it from a layer of ordinary water, which acts as a radiation shield. Light in the detector is captured by photomultiplier tubes which have been augmented with reflecting light collectors. Accurate measurement of the solar neutrino interaction rates depends on the knowledge of the detector operating conditions, of which the optical properties are the dominant physical effect. The main focus of the thesis is on calibration of SNO as an optical instrument.

1.1 Neutrinos

The basic constituents of ordinary matter in the universe are electrons, neutrinos, neutrons and protons. Of these, neutrinos are the least well understood. Both electrons and neutrinos are elementary particles and are known collectively as leptons (light particles). Protons and neutrons are the most stable baryons (heavy particles), and are formed by two different combinations of three elementary quarks.

Neutrinos are electrically neutral, spin-1/2 leptons which only interact with other particles via the weak interaction and gravity. Each charged lepton is associated with a neutrino: electron and electron neutrino (e, ν_e), muon and muon neutrino (μ, ν_μ), and tau and tau neutrino (τ, ν_τ). The three generations are arranged in increasing mass, and are referred to as flavours in the Standard Model of particle physics.

Neutrinos are very abundant particles in the universe. Their very low interaction probability makes them very difficult to detect, but also allows them to escape from inaccessible regions where they are produced in copious amounts, like the centre of the sun. The interaction probability increases with neutrino energy, which makes the higher energy neutrinos significantly easier to observe than the low energy neutrinos.

Of the neutrinos in the universe, relic neutrinos from the big bang are the most abundant and permeate all space, though their very low energy renders them undetectable. Neutrinos from the nuclear fusion reactions at the core of every star and from supernovae are second in abundance and have energies in the MeV range. High energy atmospheric neutrinos with energies near 1 GeV are produced in the cascades of decaying unstable particles produced by cosmic rays impinging on the earth's atmosphere. Finally, neutrinos with very high energies are observed in terrestrial detectors, and are theorized to come from highly accelerated cosmic rays in cosmic beam dumps or may be produced in such exotic sources as gamma-ray bursters [12].

The interaction of neutrinos with matter is mediated by the neutral Z^0 and charged $W^\pm$ bosons of the weak force. The large masses of these bosons ensures that the weak force is only experienced over very short distances. By comparison, the electromagnetic force is mediated by photons, which have zero rest mass and infinite range.

In the Standard Model, the neutrino masses are set to zero. Very small neutrino masses would have a negligible impact on the success of the model for calculations of experimentally observed particle interactions. The upper limit on the electron neutrino mass is $m_{\nu_e} < 3\,\mathrm{eV}$ [13]. Neutrinos travel at nearly the speed of light, depending on how close their mass is to zero.

All of the neutrinos have been observed in interactions with ordinary matter. The ν_τ is the latest neutrino flavour to be directly observed, and was announced recently by the DONUT experiment at Fermilab [14].

The low probability for neutrino interactions with matter forces neutrino experiments to be very sensitive and very large. The experiments must be very well shielded from spurious reactions which emulate the signature left by neutrino interactions. Detector materials must be carefully selected to minimize the amount of radioactive substances they contain. In order to reduce the rate of cosmic ray interactions, neutrino detectors are built as deep as possible underground. The overburden of rock prevents all but cosmic ray muons of the highest energies from penetrating to the detector.

1.2 Solar Neutrinos

The sun is a main-sequence star which maintains its gravity-energy balance through hydrogen burning in its core. For stars near the mass of our sun, hydrogen is fused into helium by the proton-proton (pp) chain reaction. This reaction doesn't proceed in one step, but is accomplished through a sequence of interactions with four main branches. The main products of this chain are helium nuclei (^{4}He), positrons (e^+), electron neutrinos (ν_e) and energy (E):

$$4\mathrm{p} \to {}^4\mathrm{He} + 2\mathrm{e}^+ + 2\nu_\mathrm{e} + E \tag{1.1}$$

where $E = 26.73\,\mathrm{MeV} - E_{\nu_e}$ is the energy released to the star and E_{ν_e} is the energy carried away by the two neutrinos. The average energy of the two neutrinos is $\langle E_{\nu_e}\rangle \sim$

0.6 MeV [15]. Each of the four reaction paths resulting in a ^{4}He nucleus is called a termination. Further details are given in Chapter 2.

Despite the small fraction (0.02%) of pp-chain terminations which include ^{8}B decay, the neutrinos from this part are the only ones which have been observed in real-time detectors. These neutrinos have a higher energy spectrum (0-14 MeV) than almost all the other neutrinos emitted in the main branches of the fusion chain. This makes solar neutrinos from this branch easier to observe because their cross-section for interaction is much higher and because the electrons they produce upon interaction in the detectors are above detector radioactive backgrounds.

The chain of nuclear reactions occuring deep in the sun produces an enormous flux of neutrinos. The small interaction cross-sections of these neutrinos allows them to leave the sun and reach earth, but also hinders our efforts at detecting them. The cross-section for interactions with deuterium is approximately $\sigma \sim 2.5 \times 10^{-42}\,\mathrm{cm}^2$ for $E_{\nu_e} = 10\,\mathrm{MeV}$ [16]. For comparison, the electromagnetic interaction cross-section for gamma-rays (γ) of the same energy in water is $\sigma \sim 0.5 \times 10^{-28}\,\mathrm{cm}^2$, mostly from Compton scattering off an atomic electron, with a small contribution from pair production in the nuclear field [13].

All the radiant energy which reaches us from the surface of the sun was first produced in its core. Radiative transfer inside the sun involves photons on a random walk with a mean free path of order 1 cm. The radius of the sun is $R_\odot = 6.961 \times 10^8$ m, which is 109 times larger than the radius of the earth ($R_\oplus = 6.378 \times 10^6$ m). It takes photons approximately 10000 years to percolate up to the surface from the centre (Shu [17, pp. 89-90], Bahcall [15, p. 45]). Neutrinos, in contrast, emerge from the solar core in about 2 seconds because they are unimpeded by the solar plasma. Travelling at the speed of light, both photons and neutrinos cover the distance to the earth (1 astronomical unit $= 1.496 \times 10^{11}$ m) in 8.3 minutes[1]. Observing neutrinos from the

[1] The astrophysical constants in this section come from Particle Data Group [13].

sun allows us to see what is going on in the solar core in real time.

In experiments designed to detect solar neutrinos, the rate of background signals must be reduced as far as possible below the expected rate of neutrino reactions. This is essential because the neutrino interaction cross-section is extremely small compared to the cross-section for neutron or gamma-ray induced reactions, which produce similar signatures in the detector. Background reduction is accomplished by a combination of judicious materials selection, clean construction and continuous cleaning during operation.

1.2.1 Solar Neutrino Experiments

Five experiments have reported on observations of solar neutrinos over the last 30 years. These experiments are outlined briefly below. Solar neutrinos have been observed in only five experiments prior to SNO. The Homestake ^{37}Cl detector ([18]) in the Homestake Gold Mine at Lead, South Dakota, USA has a threshold of 814 keV and is able to observe the integrated interaction rate of ^{7}Be, ^{8}B and CNO neutrinos (see Section 2.1). The Kamiokande ([19]) and Super-Kamiokande ([20, 21]) detectors, both located in the Kamioka metal mine of the Mitsui Mining and Smelting Co. in Japan, observed neutrinos from ^{8}B only, initially above a 7.5 MeV threshold and most recently above a 5.5 MeV threshold. Two experiments based on ^{71}Ga are ongoing: SAGE ("Soviet-American Gallium Experiment") in the Caucasus Mountains of Russia [22, 23], and Gallex ("Gallium Experiment", [24]) which has become GNO ("Gallium Neutrino Observatory", [25]) in the Gran Sasso Laboratory in Italy. The gallium experiments observe neutrino captures from all pp-chain neutrinos because the threshold is only 233 keV.

The Sudbury Neutrino Observatory (SNO) is the most recent experiment to contribute to the field of solar neutrinos. In this experiment, the unique properties of real-time neutrino detection on deuterium provide an unprecedented ability to measure the neutrino spectrum reaching the earth from the sun. Like the light water Cherenkov detectors (Kamiokande and Super-Kamiokande), only solar neutrinos from the ^{8}B and branch of the pp-chain are of sufficiently high energy to be measured above radioactive background signals.

Chlorine Experiment (Homestake)

The first experiment to observe solar neutrinos is a counting detector, looking for several Argon atoms per week from neutrino absorption on ^{37}Cl:

$$^{37}\mathrm{Cl} + \nu_e \rightarrow {}^{37}\mathrm{Ar} + \mathrm{e}^- \qquad (1.2)$$

The threshold for this reaction is low enough ($E_\nu \geq 0.814\,\mathrm{MeV}$) to observe a combination of neutrinos from all branches in the solar proton fusion chain except the initial proton-proton fusion step.

Water Cherenkov Experiments (Kamiokande and Super-Kamiokande)

In the 1980's a very large water-filled detector called Kamiokande was built in Japan to attempt to observe proton decay. The protons of the hydrogen atoms in the water were observed for signs of spontaneous decay. A large fraction of the proton rest mass $m_\mathrm{p}\mathrm{c}^2 = 938\,\mathrm{MeV}$ would be deposited in the detector as a result of such a decay. However, no proton decay events were observed, and as a result the limits on the proton lifetime were extended past 10^{32} years for the observable decay modes.

Because water is abundant and transparent, it is used as an effective bulk detecting medium for Cherenkov light from the energetic electrons produced by neutrino interactions. Cherenkov light is produced by charged particles travelling faster than the phase velocity of light in a dielectric medium. Each centimeter of the particle's track generates an electromagnetic shock wave containing several hundred ultra-violet and visible photons. Detector radioactive backgrounds from long-lived isotopes are a problem if they produce signals comparable to the neutrinos.

By lowering the threshold light level for recording events, the Kamiokande collaboration was able in 1986 to observe solar neutrino elastic scattering interactions with the electrons in the water in real time. These observations were conclusively demonstrated to be coming from solar neutrinos by the angular correlation of recoil electrons with the sun's position in the sky. This experiment was able to count neutrinos from only the higher energy fusion branches in the solar fusion chain, from ^{8}B disintegration and ^{3}He+p fusion because the detector threshold was above 7 MeV. Since 1996 a much larger new version of this detector called Super-Kamiokande has been in operation. This new detector has more than 25 times the sensitive volume of Kamiokande, and Super-Kamiokande has made good use of its enormous size to measure the elastic scattering interactions of solar neutrinos with electrons. The observed flux of solar neutrinos is a little less than half the expected value.

Both Kamiokande and Super-Kamiokande are also used to investigate atmospheric neutrinos, and Super-Kamiokande is being used to measure neutrino beam properties. The atmospheric neutrinos have much higher energies than the solar neutrinos, come almost uniformly from all directions and produce either muons or electrons on interaction with the water. These distinguishing features clearly separate the atmospheric from the solar neutrino events.

In Super-Kamiokande, the angular dependence of atmospheric neutrino interactions is precisely measured. Although the atmospheric ν_e interactions follow the expected behaviour, the atmospheric ν_μ interactions fall well below the expected rates for long path lengths through the earth. This provides strong evidence for neutrino oscillations of type $\nu_\mu \leftrightarrow \nu_\tau$.

Gallium Experiments (Gallex/GNO and SAGE)

Towards the end of the 1980's, two new radiochemical experiments using ^{71}Ga were constructed, one in the Soviet Union using metallic Gallium and one in Italy using $GaCl_3$ solution. The neutrino absorption reaction

$$^{71}\mathrm{Ga} + \nu_e \rightarrow {}^{71}\mathrm{Ge} + \mathrm{e}^- \tag{1.3}$$

has a threshold of $E_\nu = 0.233\,\mathrm{MeV}$, low enough to permit observation of neutrinos from all branches of the solar proton fusion chain. Both of the gallium experiments obtain a result which is low by several standard deviations with respect to standard solar model and particle physics predictions. Both the ^{37}Cl and the ^{71}Ga radiochemical transmutation detectors provide a lower threshold than real-time scattering detectors, but require integration over several weeks to obtain a measurable signal of about 0.5 atoms/day.

1.2.2 Results of the Solar Neutrino Experiments

The results of the solar neutrino experiments to date can be combined to provide more than simply a count of the total number of neutrinos. The different energy thresholds of the three interaction targets (Ga, Cl and electrons in water) used in the five experiments should provide a consistent picture of the spectrum of solar neutrinos reaching the earth. However, combining the results from the five operating neutrino detectors leads to an impossible combination of neutrino fluxes from the various interdependent branches in the solar proton fusion chain. This lack of agreement between the calculated and observed neutrino interaction rates is known as the solar neutrino problem.

The solar neutrino problem has been repeatedly confirmed and constrained over the last 30 years [26]. The ratio between experimental results and theoretical predictions is constant. After intensive theoretical and experimental research, it has been concluded that electron neutrinos must be disappearing at an energy-dependent rate from the spectrum on their way to earth (see Hata and Langacker [27], for example). Several models exist which predict this effect on the neutrino spectrum, the most popular of which predict neutrino mass and flavour mixing during propagation. The Super-Kamiokande and SNO experiments are capable of measuring the flavour changes in the atmospheric and solar neutrino spectra, respectively. With the completion of these two second-generation water Cherenkov detectors we may finally be beyond the solar neutrino problem and into the realm of new measured neutrino properties.

1.2.3 The SNO Detector

In the early 1980's two scientists formed a plan to make use of the Canadian surplus supply of heavy water (D_2O) in a laboratory deep underground to observe neutrinos from the sun using capture on deuterium. George Ewan (Queen's University) and Herbert Chen (University of California at Irvine) are the founding scientists of the Sudbury Neutrino Observatory project. They formed a collaboration to see if the stockpile of Canadian heavy water could be put to use counting solar neutrinos in real-time, using electron-scattering, flavour-insensitive and flavour-sensitive absorption on the deuteron. The SNO detector was proposed in 1987 as a new laboratory to be operated in Canada as a National Facility. The project proposal [28] describes many aspects of the detector design in detail. Further design considerations are given in a follow-up document [29]. These documents describe the motivation and the science behind the experiment.

In contrast to light water, where solar neutrino events arise only from neutrino-electron scattering, the heavy water in SNO permits three correlated observations to be made in the same detector. Using the same detector is advantageous from the point of view of understanding common detector-related systematic uncertainties. SNO is unique among all solar neutrino detectors in being able to measure both the energy spectrum of solar ν_e and the total number of neutrinos of any flavour (ν_e, ν_μ,

ν_τ) which reach the detector.

When a ν_e interacts with the deuteron via the weak charged current (exchange of a W-boson), the result is a final state where an electron shares momentum and energy with the much heavier pair of protons. Referred to as the charged current (CC) mode in SNO, this reaction is:

$$\nu_{\mathrm{e}}\mathrm{d} \rightarrow \mathrm{e}^{-}\mathrm{pp}. \tag{1.4}$$

This reaction is flavour sensitive, as it only proceeds for electron neutrinos and not for the other two flavours. The protons take very little energy from the collision, leaving the electron energy very well correlated with the incident neutrino energy. By measuring the spectrum of electrons produced in these charged-current interactions, the solar electron neutrino energy spectrum can be reconstructed.

Neutrinos of all flavours can dissociate the deuteron by a weak neutral current interaction involving the exchange of a Z-boson. This neutral current (NC) reaction is:

$$\nu_\alpha\mathrm{d} \rightarrow \nu_\alpha\mathrm{pn} \tag{1.5}$$

where ν_α indicates a neutrino of any flavour (ν_e, ν_μ, or ν_τ). This interaction is independent of the neutrino flavour, and the broken deuteron releases a neutron into the heavy water. The total flux of neutrinos is obtained by counting the total number of neutrons and subtracting the number of background neutrons not produced by neutrinos. SNO is extremely clean, and the number of background neutrons is expected to be less than 5% of the solar neutrino induced neutron signal.

Neutrino elastic scattering interactions with electrons in the heavy water occur with approximately six times higher probability for ν_e than for ν_μ or ν_τ [30]. The elastic scattering (ES) interaction is:

$$\nu_\alpha e^- \to \nu_\alpha e^-. \tag{1.6}$$

The electrons produced are well correlated in direction with the incident neutrinos, and hence with the direction to the sun from the earth. This correlation with the sun demonstrates unequivocally that the electrons arise from solar neutrino interactions and allows these signals to be separated from other signals in the detector.

Electron scattering occurs at the same rate in both H_2O and D_2O because there are ten electrons per molecule in each substance. By contrast, the neutrino interaction cross-section on the deuteron is much larger than that of electron elastic scattering, averaged over the ^{8}B neutrino spectrum. Thus, SNO will observe a similar number of neutrino events per year from the CC and ES interactions as the much larger light water Super-Kamiokande detector will with only the ES interaction.

It has been over a 13 years since SNO was first given funding. The first decade was spent in design and construction of the various detector parts and the infrastructure necessary to support operations. Now, SNO is finally online and detecting solar neutrino interactions in its large transparent sphere of heavy water.

1.3 Synopsis of this Thesis

The correct calibration of electron events occurring within SNO is vital to the understanding of the detector. This thesis is about the optical calibration of SNO. Knowledge of the optical properties of the detector elements is essential to removing the spatial and directional dependences in the data, and is an essential part of the measurement of the solar neutrino spectrum.

As an optical instrument, SNO has several unique features:

- A large D_2O sample, maintained at very high purity;
- A volume of H_2O which acts to shield the D_2O from external radioactivity;
- A thin spherical shell of acrylic (the acrylic vessel or AV) which contains the D_2O and separates it from the H_2O.
- Light sensors (photomultiplier tubes or PMT's) with precise timing (1.5 ns) arrayed to cover nearly the full solid angle about the central water volume.

The optical calibration measures the attenuation coefficients of the heavy and light water, and the angular response of the light sensors as a function of wavelength. The measured optical properties for the detector are fundamental to the ability to reconstruct the energy of events to high precision throughout the detector volume.

To correctly calibrate the energy of neutrino events in the detector, the Cherenkov light signal must be corrected for attenuation and for the efficiency of the PMT's. Although the water used in the detector is exceptionally clean and clear, a small amount of absorption and scattering affect the light on its way to the PMT's. This has an impact on the distribution of event energies throughout the D_2O volume, and is a function of event position and direction. For example, for events occurring near the edge of the detector, the Cherenkov light either goes straight out through very little water, or traverses the entire detector volume. The sensitivity of the PMT's to light signals varies with the incident angle of the light: their response is approximately uniform to light coming from the D_2O volume but falls off rapidly for light in the H_2O. The small variation in PMT efficiency with incident angle, even for the D_2O volume, affects the visible energy of events as a function of the radial position of the event in the AV. Events of the same intrinsic energy register different levels of light. Knowledge of the optical properties of the detector are essential to removing their position- and direction-dependent effects on the event data.

A program of extensive calibrations using multiple sources is pursued in SNO which allows the precise *in situ* measurement of the detector response. These sources include a quasi-isotropic laser light source (known as the laserball) and Cherenkov light from selected radioactive decays. In this thesis, light signals from a laser light source are analyzed to construct a self-consistent model of the detector's optical properties. The author contributed to the development of this source, and he designed and built special umbilical cables to provide services to this and all other SNO calibration sources. The principal services provided are laser pulses through optical fibres, electrical power and signal return lines, and radioactive gas transport.

This thesis is organized around the optical calibration. Chapter 2 presents a discussion of solar neutrinos and the experiments used to observe them. SNO is described in Chapter 3, with emphasis on the aspects relevant to the optical properties. Chapter 4 gives an overview of the optical model used to parameterize the optical properties of the detector. Chapter 5 gives details concerning the cables used in the calibration program and describes the artificial light source used in the optical measurements. The optical data sets are presented first in Chapter 6. In Chapter 7 the results of the optical fit procedure are laid out. A discussion of the optical calibration results appears in Chapter 8, and includes a comparison to literature values for the attenuation lengths and the distillation of best-fit parameters to be used in the Monte Carlo detector simulations and in analytic calculations of the detector response. Chapter 9 contains an evaluation of the uncertainty in the energy calibration due to uncertainties in the optical parameters. Finally, conclusions and suggestions for further work are outlined in Chapter 10.

2 Solar Neutrino Physics

The stellar environment which supports the fusion cycle producing energy at the centre of the sun is a hot plasma. Consisting of electrons, hydrogen, helium and traces of other elements, the fully ionized plasma behaves reasonably like an ideal gas. The plasma is only hot enough in the central 3% of the sun (by volume) to support fusion, though this volume also contains about half of the sun's mass [15]. Neutrinos emitted by several reactions in the fusion cycle can be studied to get an understanding of the inner workings of the sun.

In this chapter, a brief discussion of stellar fusion and solar neutrinos is presented. The experiments which measure solar neutrinos are described. The solar neutrino problem is the result of the low measured ν_e fluxes compared to the theoretical predictions. A brief description of neutrino oscillations as the favoured explanation for the low experimental results is followed by an introduction to the physics of neutrino measurements using heavy water in SNO.

2.1 Stellar Fusion

In stars the size of the sun, the source of nuclear energy is the fusion of protons into helium nuclei. This can be accomplished via two distinct channels: the proton-

proton (pp) chain, operating at lower central temperatures, and the CNO cycle, which is effective at higher temperatures. The choice of the pp-chain over the CNO cycle was a matter of some debate until the advent of precision solar models, which were computed for the first time in sufficient detail during the 1960's [15]. These models enabled the solar core temperature to be placed at $T_c \simeq 16 \times 10^6$K and permit the conclusion that the sun produces about 98.5% of its energy via the pp-chain, and only 1.5% by the CNO cycle [31].

The pp-chain accomplishes hydrogen burning to helium in solar mass stars $M \lesssim 1.2 M_\odot$, where $M_\odot$ is the mass of the sun [32]. Over the lifetime of the star, the stellar interior undergoes significant changes in size, luminosity and core temperature, although the mass remains essentially constant. Models of the sun typically fix the initial elemental abundances (as observed in solar-system meteorites and at the unmixed surface of the sun) and allow the model to progress until the current mass, size and luminosity are obtained. When the model converges on the current measured solar parameters, the model provides the age of the sun, the distribution of mass and temperature throughout its volume, and the present day neutrino fluxes from its central region.

The CNO cycle is a catalytic process which processes protons into helium nuclei. This cycle is the dominant source of energy in stars only slightly more massive than the sun ($M \gtrsim 1.2 M_\odot$) which have a core temperature $T_c \gtrsim 18 \times 10^6$K. About 1% by mass of the elements C, N or O must be available in the star to act as catalysts. With time, the amount of N increases at the expense of C and O because of the bottleneck reaction rate ^{14}N(p,γ)^{15}O [32].

In much more massive stars (10–100$M_\odot$), the CNO cycle dominates the energy production for hydrogen burning. As these stars evolve, ever hotter temperatures and shorter burning phases allow fusion of elements up to iron, which has the highest binding energy per nucleon of all the elements.

The CNO cycle is omitted from further discussion because it contributes only a small fraction (1.5%) to the energy generation in the sun [31]. As well, CNO cycle neutrinos make only a small contribution to the neutrino interaction rates in current radiochemical detectors.

2.1.1 Proton-Proton Fusion

Nuclear fusion of protons into ^{4}He by the pp chain is the slowly burning source of energy behind the long ($\sim 10^{10}$ years) burning cycle of solar mass stars. The site of this activity is the centre of the sun and is delimited by the inner 30% of the radius or 2.7% of the volume containing about half the mass of the star.

Figure 2.1 shows the reactions in the solar pp-chain, with the four terminations as labelled in Table 2.1. Table 2.1 also gives the energy liberated by the reaction (Q-values), the average energy released to neutrinos $\langle q_\nu \rangle$, and the fraction of pp-chain terminations expected for each branch. A termination occurs when the outcome of a reaction is one or more ^{4}He nuclei. For each termination, Table 2.1 also gives the effective energy transferred to the star (Q_{eff}). The fraction of terminations column is calculated for the present-day sun with core temperature $T_c = 15.6 \times 10^6$K [15]. The PPIII termination is the most important for solar neutrino observations to date because of the large neutrino energies emitted by ^{8}B decay, which make them easiest to detect despite their relatively low production rate. On average, 1.85 ($= 2 \times 0.85 + 1 \times 0.15$) pp neutrinos are produced per termination, while the other neutrinos are all produced in keeping with the termination fractions.

The spectrum of neutrinos from the pp-chain is shown in Figure 2.2. SNO is only sensitive to ^{8}B neutrinos because of the detector's intrinsic energy resolution and threshold. Neutrino absorption (CC-reaction, Equation 1.4) on deuterium proceeds only for $E_\nu > 1.44\,\text{MeV}$, while neutral current (NC-reaction, Equation 1.5) breakup of the deuteron has a threshold of $E_\nu > 2.22\,\text{MeV}$.

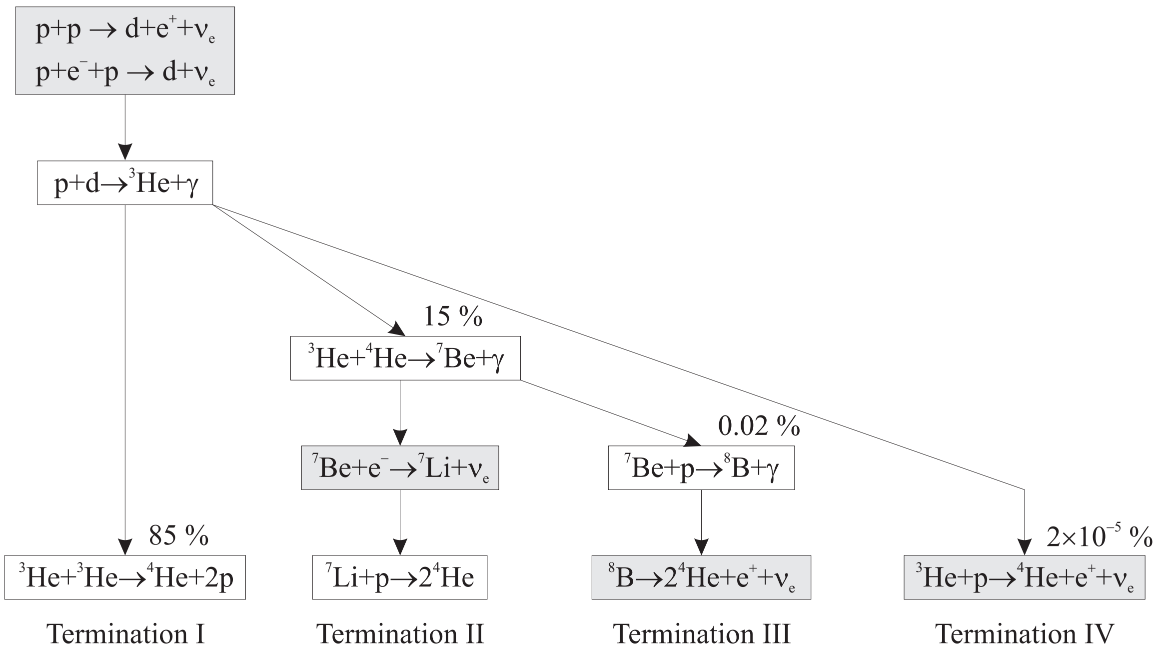

Figure 2.1: *Fusion reaction chain in the proton-proton burning sequence. This chain reaction provides 98.5% of the energy at the core of the sun. The relative probability of each branch is indicated in percent [15], and a summary of the reactions is given in Table 2.1.*

Reaction	Q (MeV)	$\langle q_{\nu_e} \rangle$ (MeV)	Fraction of Terminations	Remarks
$pp \to d\ e^+ \nu_e$	1.442	0.265	100%	
$pe^- p \to d\ \nu_e$	1.442	1.442	0.4%	
$dp \to {}^3He\ \gamma$	5.494	–	100%	
${}^3He\ {}^3He \to {}^4He\ pp$	12.860	–	85%	Termination I: 2.0% loss to ν_e $Q_{\text{eff}} = 26.20$MeV
${}^3He\ {}^4He \to {}^7Be\ \gamma$	1.586	–	15%	
${}^7Be\ e^- \to {}^7Li\ \nu_e$	0.862	(90%) 0.862	13.5%	
	0.384	(10%) 0.384	1.5%	
${}^7Li \to {}^4He\ \alpha$	17.347	–	15%	Termination II: 4.0% loss to ν_e $Q_{\text{eff}} = 25.66$MeV
${}^7Be\ p \to {}^8B\ \gamma$	0.137	–	0.02%	
${}^8B \to {}^8Be^*\ e^+ \nu_e$	17.980	6.710	0.02%	
${}^8Be^* \to \alpha\alpha$	–	–	0.02%	Termination III: 28.3% loss to ν_e $Q_{\text{eff}} = 19.17$MeV
${}^3He\ p \to {}^4He\ e^+ \nu_e$	19.795	9.625	0.00002%	Termination IV: 36.0% loss to ν_e $Q_{\text{eff}} = 17.11$MeV

Table 2.1: *Summary of the proton-proton chain reactions illustrated in Figure 2.1. The net reaction is* $4p \to {}^4He\ 2e^+\ 2\nu_e$, $Q = 26.73\,MeV$ *[15], and the amount of energy transferred to the star is* Q_{eff}.

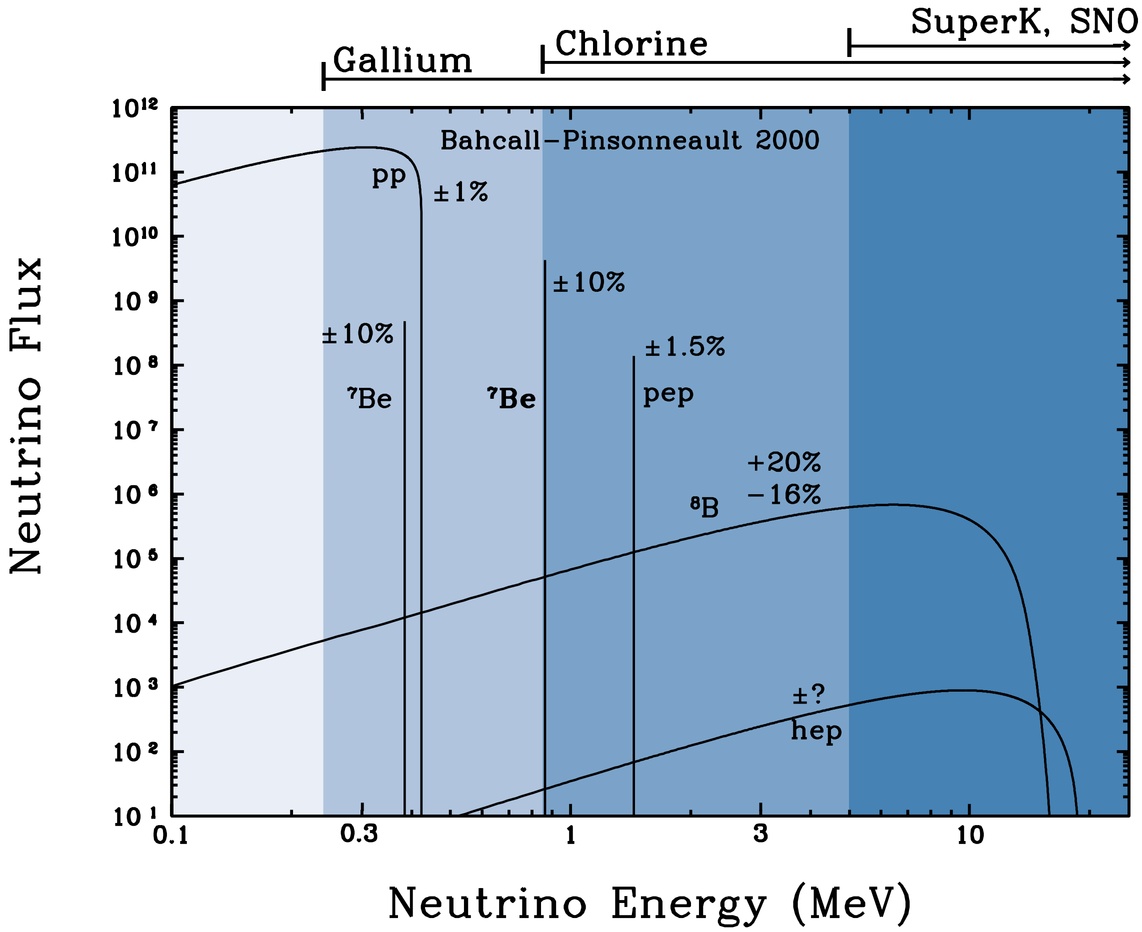

Figure 2.2: *Predicted solar neutrino spectrum in the SSM (Bahcall-Pinsonneault 2000 from [31]).*

2.2 Solar Neutrinos

The standard solar model (SSM) makes predictions based on standard physics, with input parameters coming from various sources. For example, the age of the solar system comes from measured ages of the oldest meteorites which are discovered on earth. Predictions of the SSM range from the solar oscillation modes (pressure waves) to the neutrino flux from the nuclear reaction chain in the core which sustains its luminosity. The SSM has been tested in many ways for accuracy. The outstanding problem with the model continues to be that the absolute number and energy distribution of the observed neutrinos is in strong disagreement with the theoretical predictions. This is known as the solar neutrino problem (SNP).

Potential astrophysical solutions to the SNP cannot be reconciled with the growing number of neutrino experiments. Solutions which change the solar models in a substantial way have been ruled out on physical grounds or because of additional observational constraints. For example, helioseismological results for the speed of pressure waves in the sun are used to confirm the temperature and density profiles of solar models. Solar models must be able to reproduce the age, size and total luminosity of the sun [31]. The most favoured solution lies in particle physics, as neutrino flavour oscillations arising from small mass-differences between neutrino mass eigenstates.

2.2.1 Experimental Results

Current results from the five experiments (see Section 1.2.1 are summarized in Table 2.2. Kamiokande refers to the 2079 days of observation by the Kamiokande II and III experiments, while SuperKam refers to the 1117 days of observation by the Super-Kamiokande experiment. The increase in fiducial volume by a factor of 33.1 of the Super-Kamiokande detector (22500 tons) over the Kamiokande detector (680 tons)

Experiment	Result	SSM	Units	Ratio
Homestake	$2.56 \pm 0.16 \pm 0.16$	$7.6^{+1.3}_{-1.1}$	SNU	0.34 ± 0.06
Kamiokande	$2.80 \pm 0.19 \pm 0.33$	$5.05^{+20\%}_{-16\%}$	$10^6\,\mathrm{cm}^{-2}\mathrm{s}^{-1}$	0.55 ± 0.13
SuperKam.	$2.40 \pm 0.03^{+0.08}_{-0.07}$	$5.05^{+20\%}_{-16\%}$	$10^6\,\mathrm{cm}^{-2}\mathrm{s}^{-1}$	0.48 ± 0.09
Gallex/GNO	$74.1^{+6.7}_{-6.8}$	128^{+9}_{-7}	SNU	0.58 ± 0.07
SAGE	$75.4^{+7.0+3.5}_{-6.8-3.0}$	128^{+9}_{-7}	SNU	0.59 ± 0.07
Gallium	74.7 ± 5.0	128^{+9}_{-7}	SNU	0.55 ± 0.05

Table 2.2: *Summary of experimental results for solar neutrino observations. The units for the radiochemical experiments are SNU, where 1 SNU=* 10^{-36} *interactions per target atom per second.*

means the Super-Kamiokande data sample consists of 18 times more events, with corresponding decreases in statistical errors. Gallex refers to the original Gallex I, II, III and IV runs, while GNO refers to additional runs with the same detector since 1997. The Gallium result is a weighted average of the Gallex/GNO and SAGE results. The SSM of Bahcall et al. [31] is used for the comparison ratio of experiment to theoretical prediction.

Figure 2.3 compares the results of a global fit to all solar neutrino experimental results as of 1997 with a series of standard and non-standard solar models [27]. Although the experimental precision has improved during the intervening years, the conclusions drawn from this analysis have remained the same: changes to solar models are not able to account for the observed fluxes of neutrinos from both the ^{7}Be and the ^{8}B branches of the pp-chain. The rate of fusion is a sensitive function of the stellar temperature [Bahcall and Ulmer [33]; see also Pagel [34]]. Neutrino fluxes from all variants of solar evolution models can be parametrized by the present core temperature T_c of the sun. The models lie in a band well beyond the 99% confidence level of the combined fit to the solar neutrino observations from Homestake, Kamiokande, Super-Kamiokande, SAGE and GALLEX.

The neutrinos from the minuscule ^{8}B branch of the solar fusion chain provide all

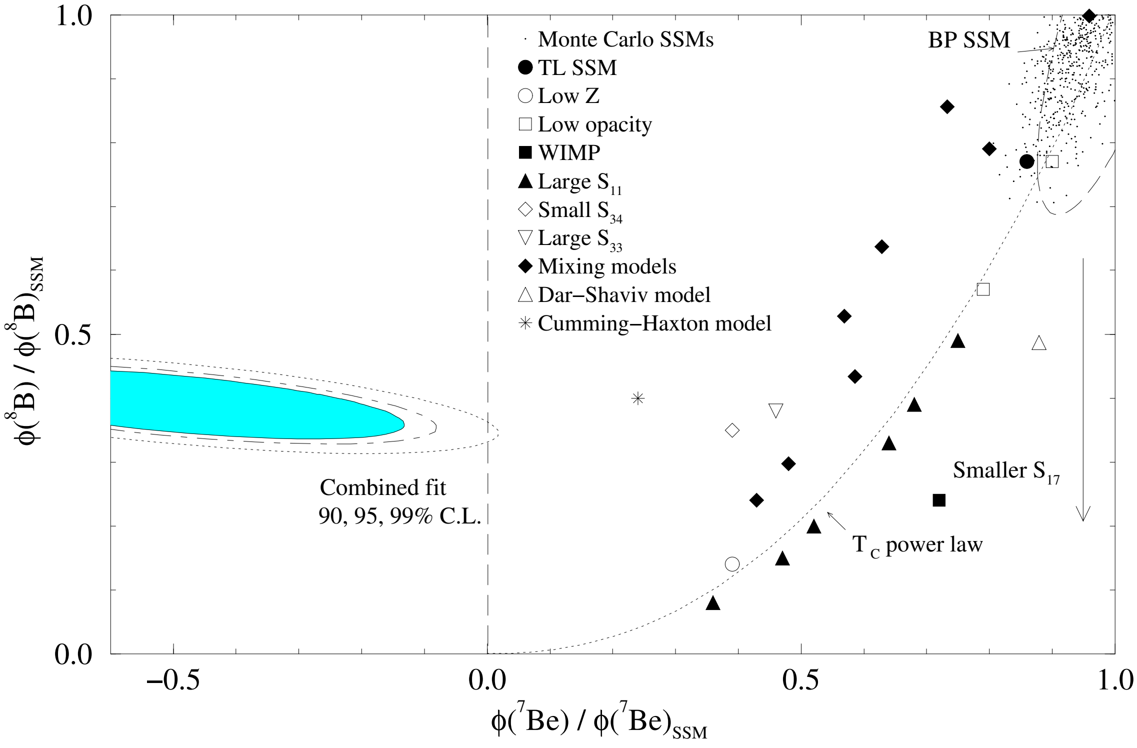

Figure 2.3: *Comparison of a combined fit of the Kamiokande, Homestake and Gallium (SAGE, Gallex) results at 90, 95 and 99% confidence level (C.L.) for the ratio ϕ/ϕ_{SSM} of ^7Be and ^8B fluxes to the standard solar model (SSM) predictions (Bahcall and Pinsonneault [35] then; now updated in Bahcall et al. [31]). The ratio of the neutrino fluxes predicted by modified solar models to the SSM fluxes is indicated by $\bigcirc$ through $*$ symbols. Even radical changes to the solar models cannot account for the combined experimental results. Figure from Hata and Langacker [27].*

the signal in large water-filled Cherenkov detectors. These neutrinos come from the β-decay of ^{8}B nuclei in the sun:

$$^{8}\mathrm{B} \rightarrow {}^{8}\mathrm{Be}^{*}\nu_{e}\mathrm{e}^{+}. \tag{2.1}$$

The shape of the neutrino spectum can be calculated to very high precision (1 part in 10^5, see Bahcall et al. [36]) based on terrestrial measurements of the positron spectrum and of the subsequent breakup of the excited broad resonance ^{8}Be*. The excited state ^{8}Be* decays rapidly by emitting two alpha-particles:

$$^{8}\mathrm{Be}^{*} \rightarrow 2\alpha. \tag{2.2}$$

The standard literature source for measurements of the 2α energy spectrum is Warburton [37], though recent measurements by Ortiz et al. [38] claim better control of systematic errors and therefore much smaller uncertainties in the deduced neutrino spectrum than in Bahcall et al. [36]. The Ortiz et al. [38] calculation of the neutrino spectrum from ^{8}B indicates a slightly harder neutrino spectrum than previously (*i.e.* more neutrinos at higher energy). The integrated cross-section for solar neutrinos detected by SNO is not calculated in [38], though the change with respect to [36] is expected to be small based on the +2.1% change calculated for Super-Kamiokande.

2.3 Neutrino Physics

The solar neutrino problem is unlikely to have an astrophysical solution. Solar models have been shown to make robust predictions for neutrino rates, and reasonable changes in the model input parameters have been unable to reproduce the pattern of experimental evidence [27]. Comparisons with helioseimological data have shown that these models reproduce the sound speeds in the outer 90% of the sun to very high accuracy [31]. The same models must also accurately predict the environment of the solar core, where the neutrinos are produced. The environment of the core affects the total numbers of neutrinos emitted, but not the neutrino energy spectrum. An energy-dependent distortion of the ν_e flux is required to explain all the solar neutrino experimental results.

The remainder of this section concentrates on neutrino physics relevant to solar neutrinos, with particular emphasis on SNO:

Neutrino emission: β-decay spectra for pp and ^{8}B neutrinos, and line spectra for ^{7}Be and pep neutrinos.

Neutrino propagation: Energy and path-length dependent effects, such as neutrino oscillations, might be modifying the observed spectrum. This type of phenomenon has the potential to resolve the solar neutrino problem.

Neutrino detection cross-sections: Absorption on deuterium and electron elastic scattering used in real-time Cherenkov detectors. Absorption for the radiochemical experiments based on ^{37}Cl and ^{71}Ga.

Neutrino signals: Overview of the detection using Cherenkov light in the water experiments.

2.3.1 Neutrino Emission from the Sun

The centre of the sun is made up of a hot, dense, electrically neutral plasma and is essentially an ideal gas composed of mostly hydrogen, helium and electrons. Temperature is the primary variable controlling the rate of fusion reactions in the core, and thereby the total rate of production of neutrinos from those reactions. The energy spectrum of pp-chain neutrinos can be calculated to high accuracy based on the well understood theory of nuclear β-decay.

Despite the differences between the solar environment and terrestrial laboratory conditions, corrections to the β-decay spectrum are less than about 1%. On earth, the nuclei are part of atoms and the orbital electrons can screen the nuclear charge and affect the emitted β spectrum. At the centre of the sun the nuclei are part of a hot electrically neutral plasma, and corrections for plasma screening (Debye-Hückel) and for thermal motion are made to the β spectrum. The spectral shape of the ^{8}B neutrinos is calculable to an accuracy of better than 1 part in 10^5 [36].

The total rates of the initial pp and pep reactions (top grey box in Figure 2.1) in the pp-chain have to be calculated theoretically since there are no experimental measurements. However, the simplicity of the initial and final states makes this calculation very robust [15]. All of the other rates require extrapolation of reaction cross-sections from higher energies accessible in terrestrial laboratories to the solar regime. A discrepancy here affects the total rate of these reactions, but has almost no effect on the energies of the final states. For the ^{8}B neutrinos, the uncertainty on the rate is $+20\%/-16\%$ [31]. A large part of this uncertainty comes from the high temperature dependence ($\sim T_c^{24\pm5}$ in [33]) for this branch of the pp-chain.

2.3.2 Neutrino Propagation

The present Standard Model defines neutrino properties to be consistent with β-decay lifetimes and β-spectra, and the number of light neutrino species is inferred from the invisible Z^0 decay width ($N_\nu = 2.988 \pm 0.023$; Particle Data Group [13]). The possibility of non-zero neutrino masses and mixing between neutrino flavours are not part of the model – and are therefore open to input from new experimental observations.

Neutrino Oscillations

The mechanism for particle mass generation in the Standard Model has not yet been theoretically or experimentally determined. Particle eigenstates for the mass generation interaction are likely to be different from the electroweak particle flavour eigenstates. The flavour states (ν_e, ν_μ, ν_τ) are created and observed through weak interactions, and propagate as a mixture of mass eigenstates (ν_1, ν_2, ν_3). The three neutrino flavours are related to the mass eigenstates by a mixing matrix $U_{\alpha i}$:

$$\begin{pmatrix} \nu_e \\ \nu_\mu \\ \nu_\tau \end{pmatrix} = \begin{pmatrix} U_{e1} & U_{e2} & U_{e2} \\ U_{\mu 1} & U_{\mu 2} & U_{\mu 3} \\ U_{\tau 1} & U_{\tau 2} & U_{\tau 3} \end{pmatrix} \begin{pmatrix} \nu_1 \\ \nu_2 \\ \nu_3 \end{pmatrix} \tag{2.3}$$

where α denotes the flavour state and i labels the mass state. The matrix $U_{\alpha i}$ is taken to be unitary, in analogy to the Cabibbo-Kobayashi-Maskawa matrix for mixing of weak and mass eigenstates in the quark sector. The probability for oscillation from one flavour to another is obtained for propagation using the Hamiltonian, which for free space is simply the particle energy. For neutrinos emitted as ν_α propagating through a vacuum the probability of being detected as ν_β is:

$$P(\nu_\alpha \to \nu_\beta) = \delta_{\alpha\beta} - 4 \sum_{j>i} U_{\alpha i} U_{\beta i} U^*_{\alpha j} U^*_{\beta j} \sin^2 \left(\frac{1.27 \Delta m^2_{ij} L}{E_\nu} \right) \tag{2.4}$$

where $\delta_{\alpha\beta}$ is the Kronecker delta function, $U^*_{\alpha i}$ is the complex conjugate of $U_{\alpha i}$, $\Delta m^2_{ij} = |m^2_i - m^2_j|$ (eV^2) is the difference in the squared masses of mass eigenstates i and j, $L\,$(m) is the distance between the source and the detector, and $E_\nu\,$(MeV) is the neutrino energy. In this model, lepton number is not conserved as the neutrino oscillates. There are two independent Δm^2_{ij} and three mixing angles, which are hidden in the $U_{\alpha i}$ matrix elements.

Mixing among three neutrino states is the general case for the three flavours of neutrinos of the Standard Model. For simplicity, a two-generation framework is usually assumed when analyzing solar neutrino experimental results. The simplification is valid when at least one of the the neutrino masses is quite different: $m_3 \gg m_2 \sim m_1$, such that $\Delta m^2_{21} \ll \Delta m^2_{32} \simeq \Delta m^2_{31}$ (see Gonzalez-Garcia et al. [39]). Under this assumption the neutrino oscillation probabilities are only significant between pairs of neutrino flavours, with the third possibility almost completely decoupled from the oscillations. The neutrino mixing matrix then contains only a single mixing angle θ between the two flavour and the two mass states:

$$\begin{pmatrix} \nu_e \\ \nu_\alpha \end{pmatrix} = \begin{pmatrix} \cos\theta & \sin\theta \\ -\sin\theta & \cos\theta \end{pmatrix} \begin{pmatrix} \nu_1 \\ \nu_2 \end{pmatrix} \tag{2.5}$$

where $\nu_\alpha = \nu_\mu$ or ν_τ. The probability of observing an electron neutrino after traveling a distance L from its source is:

$$P(\nu_e \to \nu_e) = 1 - \sin^2 2\theta \sin^2\left(\frac{1.27\Delta m^2_{12} L}{E_\nu}\right) \tag{2.6}$$

The fraction of ν_e which are observed as ν_e depends on the mixing angle θ, and on the difference between the squared masses of the mass eigenstates, the neutrino energy and the distance from the source.

Neutrino oscillations alter both the energy spectrum and the flavour distribution of neutrinos emitted in weak decays. For detectors which are only sensitive to solar ν_e, the total event rate will be reduced. If the detector has the ability to measure the energy distribution of the neutrinos, the spectrum will appear distorted. So far, all solar neutrino experiments have observed a deficit of ν_e interactions, and none has had sufficient energy resolution to be able to measure small distortions in the neutrino energy spectrum. A flavour-independent measurement of the total flux of neutrinos provides confirmation that the SSM predicts the correct total flux of neutrinos. The ratio of the number of detected ν_e to the total number of neutrinos provides another indication whether neutrino flavour oscillations are taking place, provided this ratio is different from unity.

Neutrino Oscillations in Matter

The resonant amplification of the oscillation probability as neutrinos pass through matter was first described by Wolfenstein [40]. The idea was pursued by Mikheev and Smirnov [41], who demonstrated that the resonant condition could be met for neutrinos leaving the dense solar core as they passed through less dense regions further out in radius. A sign error in the conversion formula is corrected in Bethe [42].

The MSW effect arises from the additional scattering interaction available to ν_e in matter. All neutrino flavours ν_ℓ ($\ell = \mathrm{e}, \mu, \tau$) interact with the electrons in matter by neutral Z^0 exchange:

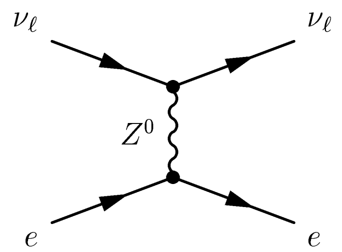

(2.7)

For solar neutrino energies, only the electron neutrino is energetic enough to produce electrons via charged-current interactions involving W-boson exchange:

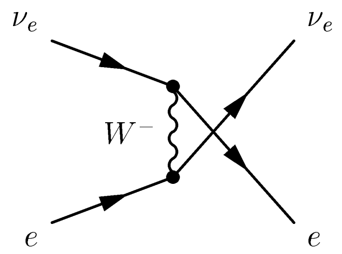

(2.8)

The extra interaction mechanism for ν_e changes the propagation properties of the ν_e component relative to the $\nu_{\mu,\tau}$ components of the neutrino state. The matter propagation Hamiltonian for two generations of neutrinos is [43]:

$$H = \begin{pmatrix} -\frac{\Delta m^2_{12}}{4E_\nu}\cos 2\theta + \sqrt{2}G_F N_e & \frac{\Delta m^2_{12}}{4E_\nu}\sin 2\theta \\ \frac{\Delta m^2_{12}}{4E_\nu}\sin 2\theta & \frac{\Delta m^2_{12}}{4E_\nu}\cos 2\theta \end{pmatrix} \tag{2.9}$$

where G_F is the Fermi weak coupling constant and N_e is the electron density. In general, this matrix has two eigenvalues. However, neutrinos with specific energies passing through regions with a critical electron density undergo resonant conversion when the eigenvalues of the Hamiltonian becomes nearly degenerate; this occurs when:

$$\frac{\Delta m^2_{12}}{4E_\nu}\cos 2\theta = \sqrt{2}G_F N_e. \tag{2.10}$$

Resonant conversion means that the oscillation probability $P(\nu_e \to \nu_e)$ reaches its maximum possible amplitude, and does not depend on the vacuum mixing angle θ. For neutrino oscillations in matter, Equation 2.6 becomes:

$$P(\nu_e \to \nu_e; N_e) = 1 - \sin^2 2\theta_m \sin^2\left(\pi\frac{L}{\ell_m}\right) \tag{2.11}$$

where θ_m is the matter mixing angle given by:

$$\tan 2\theta_m = \frac{\frac{\Delta m^2_{12}}{2E_\nu}\sin 2\theta}{\frac{\Delta m^2_{12}}{2E_\nu}\cos 2\theta - \sqrt{2}G_F N_e}. \tag{2.12}$$

and ℓ_m is the matter oscillation length:

$$\ell_m = \frac{2\pi}{\sqrt{\left(\frac{\Delta m^2_{12}}{2E_\nu}\cos 2\theta - \sqrt{2}G_F N_e\right)^2 + \left(\frac{\Delta m^2_{12}}{2E_\nu}\right)^2 \sin^2 2\theta}}. \tag{2.13}$$

The oscillation amplitude $\sin^2 2\theta_m$ has a typical resonance form:

$$\sin^2 2\theta_m = \frac{\left(\frac{\Delta m^2_{12}}{2E_\nu}\right)^2 \sin^2 2\theta}{\left(\frac{\Delta m^2_{12}}{2E_\nu}\cos 2\theta - \sqrt{2}G_F N_e\right)^2 + \left(\frac{\Delta m^2_{12}}{2E_\nu}\right)^2 \sin^2 2\theta}. \tag{2.14}$$

Under the MSW resonance condition (Equation 2.10), $\sin^2 2\theta_m = 1$ and mixing between the neutrino states is maximal ($\theta_m = 45°$) and independent of the vacuum mixing angle θ. Therefore, the probability of neutrino flavour transition in matter can be large even for very small values of the vacuum mixing angle.

Figure 2.4 shows the 99% confidence limits on the allowed MSW solutions to the solar neutrino problem described in Bahcall et al. [44]. In this figure, the matter mixing angle is denoted θ rather than θ_m. The solutions for active neutrino species are:

- LMA (Large mixing angle): $\tan^2 2\theta = 0.26$, $\Delta m^2 = 4.2 \times 10^{-5}\,\mathrm{eV}^2$,
- SMA (Small mixing angle): $\tan^2 2\theta = 5.5 \times 10^{-4}$, $\Delta m^2 = 5.2 \times 10^{-6}\,\mathrm{eV}^2$,
- LOW (Low mass squared difference): $\tan^2 2\theta = 0.72$, $\Delta m^2 = 7.6 \times 10^{-8}\,\mathrm{eV}^2$,
- Just So^2: $\tan^2 2\theta = 1.0$, $\Delta m^2 = 5.5 \times 10^{-12}\,\mathrm{eV}^2$,
- VAC (Vacuum oscillations): $\tan^2 2\theta = 0.38$, $\Delta m^2 = 1.4 \times 10^{-10}\,\mathrm{eV}^2$.

These solutions have different energy-dependent effects on the solar neutrino spectrum, as shown in Figure 2.5. A distorted energy spectrum is the main signature of the SMA solution. All the solutions reproduce the observed experimental interaction rates. Also shown are the effects of MSW resonant conversion in the earth during the night, where the neutrinos must travel through the earth to reach the detector. However, above the SNO or Super-Kamiokande analysis threshold of $\sim 5\,\mathrm{MeV}$ the day/night differences are very slight.

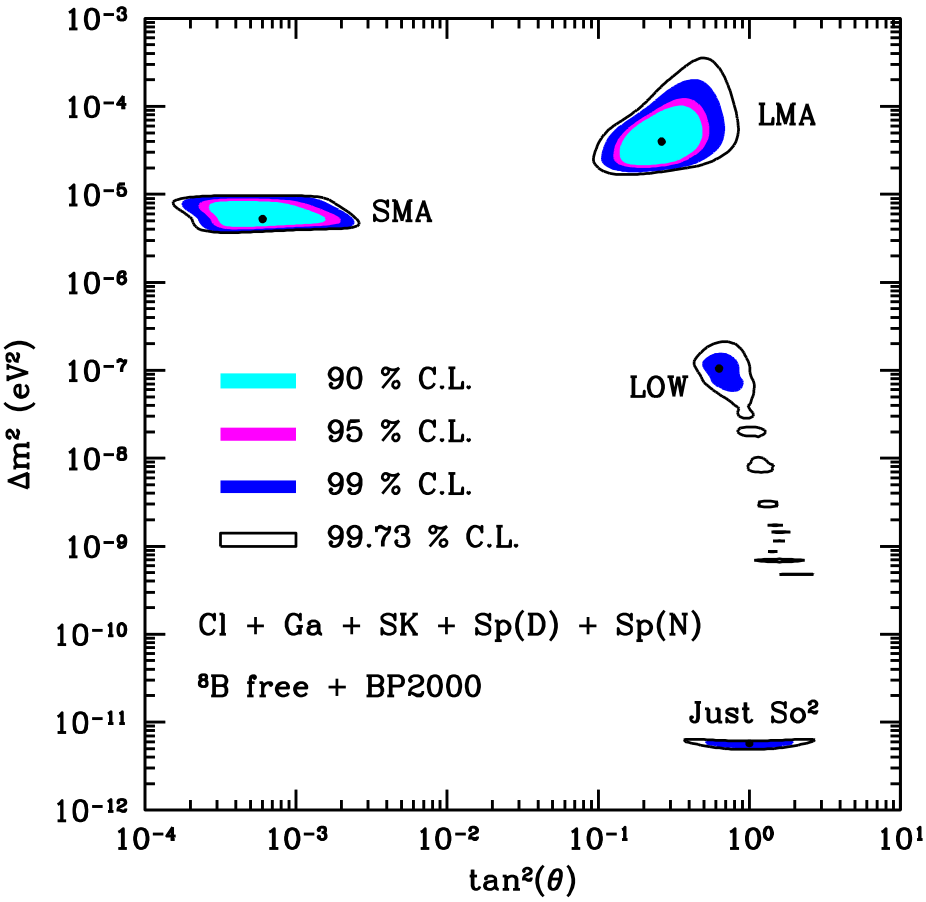

Figure 2.4: *MSW solutions to the solar neutrino problem: allowed regions at 90%, 95%, 99% and 99.73% confidence limits (C.L.) found from the experimental rates in the Chlorine (Cl) and Gallium (Ga) experiments, and from and day/night spectrum data from Super-Kamiokande (Sp(D) and Sp(N)). The solar ^8B flux is a free parameter, while the other neutrino fluxes are constrained by the SSM [31]. The best fit parameters are indicated by dots. Figure from [44].*

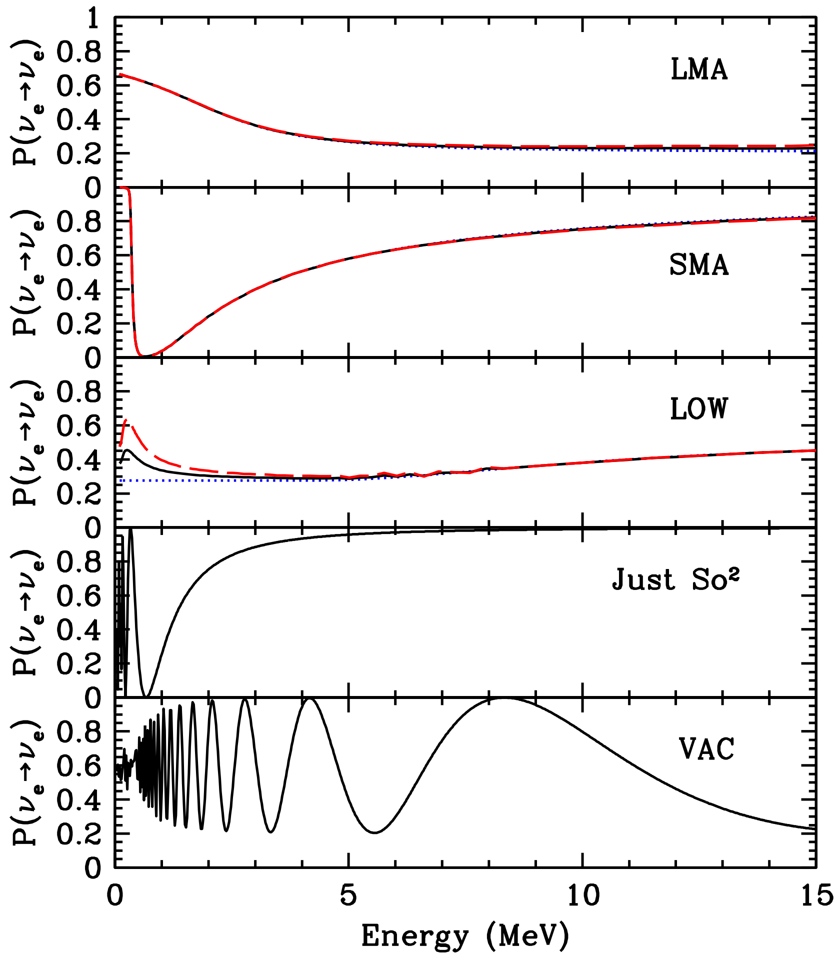

Figure 2.5: *MSW solution survival probabilities for ν_e created in the sun to be detected as ν_e at the earth, averaged over one year. The dashed lines include regeneration at night, the dotted lines are for calculations for the daytime and do not include regeneration, and the solid lines correspond to the average survival probability. Figure from [44].*

The MSW effect can leave three distinct signatures on the observed neutrino spectrum. First, the total number of detected neutrinos of all flavours is measured by the rate of NC reactions in SNO. When compared to the observed number of electron neutrinos deduced from the CC reaction rate, the ratio NC/CC provides nearly unequivocal evidence for neutrino oscillations. Second, the energy dependence of the MSW effect can cause distortions in the observed spectrum, provided the changes to the neutrino spectrum are large enough to show up when the experimental energy resolution is taken into account. And third, daily variations in the neutrino rate can arise from ν_e regeneration on passage through the earth for combinations of MSW parameters which allow resonant mixing at terrestrial electron densities.

The literature on MSW solutions to the solar neutrino problem is very rich. Bahcall et al. [44] gives a clear overview of the MSW effect in the context of solar neutrinos and the implications of SNO measurements of the CC and NC interaction rates. Spectral information from the CC reaction measured in SNO can further constrain the allowed MSW solutions, as shown in Bahcall et al. [45], provided the uncertainty on the calibrated energy scale is $\lesssim 1\%$.

2.3.3 Neutrino Detection in D_2O

Solar neutrinos interact with D_2O in one of three possible ways: CC, NC and ES reactions (see Equations 1.4, 1.5 and 1.6). Absorption on deuterium produces a measurement of the spectrum of solar ν_e by the CC interactions, and a measurement of the total flux of solar neutrinos, independent of flavour, via the NC interactions. The ES interactions allow a cross-check with the Super-Kamiokande results using H_2O to be made.

Neutrino Absorption on Deuterium

Neutrino absorption on deuterium was originally calculated for solar neutrinos by Kelly and Überall [46], with the important addition of the Fermi function for recoil of the protons and the electron in the final state by Ellis and Bahcall [47]. These calculations considered only s-wave and some p-wave functions for the deuteron, with only the most basic exchange Feynman diagrams. A resurgence of interest in the precise calculation of this cross-section manifested itself with the coming of SNO. The most recent full calculations of the neutrino cross-sections on deuterium is by Nakamura et al. [48, NSGK]. These authors use a phenomenological Lagrangian approach which has been shown to agree well with experimental results for two-nucleon systems. In NSGK the cross-section is presented in tabular form as a function of neutrino energy. To aid in interpolating between the tabled points, the analytic function for the differential cross-section given in Butler et al. [16, BCK] is used, with forced agreement for the integrated cross-section at the tabulated values of NSGK for $E_\nu < 20\,\mathrm{MeV}$. The BCK calculation is based on effective field theory (EFT); in comparing their results with earlier calculations using nuclear potential models, the unknown axial two-body counterterm $L_{1,A}$ in the EFT calculation is the main source of theoretical uncertainty. The current experimental data is insufficient to constrain the value of this term.

The uncertainty in the total νd cross-sections for CC and NC interactions is estimated to be approximately 2.5%. When one takes the ratio $R = \sigma_{\mathrm{CC}}/\sigma_{\mathrm{NC}}$, however, many common factors in the model cancel and the resulting uncertainty in R is reduced to the 1% level [48].

Neutrino-Electron Scattering

Both SNO and Kamiokande/Super-Kamiokande make use of the electrons in water for measurements of the solar flux of ^{8}B neutrinos. The cross-section for $\nu - e$ elastic scattering is calculated including radiative corrections and an updated value for the weak mixing angle $\sin^2 \hat{\theta}_W$ in Bahcall et al. [30]. The radiative corrections amount to a change of less than 4% in the electron recoil spectrum for solar ^{8}B neutrinos.

2.3.4 Neutrino Signals from the Cherenkov Effect

The Nobel Prize for the Cherenkov effect was awarded in 1958, 24 years after P.A. Cherenkov first studied the emission light by liquids as a graduate student at the Lebedev Institute in Moscow. That the Cherenkov effect is due to particles exceeding the phase velocity of light in a given medium was first explained by I.M. Frank and I.V. Tamm in a paper in 1937. The Cherenkov effect is well described in Jackson [49] and Jelley [50], and a concise summary can be found in Particle Data Group [13]. Chapter 4 contains more information about the Cherenkov light observed in SNO.

The amount of Cherenkov light emitted by a charged particle is proportional to the total track length of the particle. In a dense medium, particles lose a uniform amount of energy per unit distance travelled. The total amount of Cherenkov light emitted is therefore directly proportional to the energy of the particle. The total intensity of light from a typical electron ($E_e \sim 10\,MeV$) in water is only of order several hundred photons, however, which requires very sensitive light sensors and a minimum of extinction.

The directionality of Cherenkov light provides an opportunity to observe neutrino-electron scattering events pointing away from the neutrino source. In the case of solar neutrinos, this has been accomplished in real time by the Kamiokande and Super-Kamiokande experiments, as well as by SNO. In addition to detector granularity, multiple-scattering of the electron degrades the direction resolution obtainable by reconstruction to 28° in SNO [51]. Many events are required to provide adequate pointing accuracy back to the source, which is a factor in looking for supernova-induced bursts of events.

3 Elements of the Sudbury Neutrino Observatory

SNO is a large and exceptionally clean detector containing both heavy and light water. Separate water purity systems are used to maintain the two water volumes at low levels of radioactivity, with the side effect that the waters are also kept optically very transparent. A spherical acrylic vessel (AV) segregates the two water volumes, with the D_2O at the centre of the photomultiplier array used to detect Cherenkov light from neutrino interactions. The detector is a sensitive, fine-grained optical instrument which is well suited for making optical measurements of its properties. The focus of this chapter is on the aspects of the detector most relevant to understanding its optical properties such as the water purification systems, the photomultiplier tubes and the heavy water acrylic containment vessel.

For a complete technical description of SNO, see Boger et al. [52]. Several aspects of the detector operations have changed since this article was written. In particular, the D_2O was not recirculated at all because the radioactivity levels were low enough from the start. All of the optical calibration results and the neutrino spectrum presented in this thesis are based on production data.

3.1 Physical Construction

An overview of the SNO laboratory and detector is given in Figure 3.1(a). The detector consists of a transparent acrylic sphere 12 m in diameter, supported from a deck structure by ten rope loops made of synthetic fibre (Vectran), as shown in Figure 3.1(b). The sphere holds one gigagram of heavy water. Surrounding the AV is a geodesic structure 17.8 m in diameter made of stainless-steel struts and carrying 9438 inward-looking photomultiplier tubes (PMT's). The barrel-shaped cavity, 22 m in diameter and 34 m in height, is filled with purified light water to provide support and shielding. The inner detector contains 9×10^5 ℓ of D_2O and is surrounded by PMT's mounted in nearly water- and light-tight panels in a support structure and bathing in 1.7×10^6 ℓ of H_2O. The outer detector beyond the PSUP contains a further 5.7×10^6 ℓ of H_2O which shields the inner detector from radioactivity in the rock walls of the cavity.

The SNO detector is located in the INCO, Ltd., Creighton mine near Sudbury, Ontario, Canada. The center of the detector vessel is 2039 m below the surface in a cavity excavated from the "6800-foot" level of the mine. The granitic rock overburden (mainly norite) corresponds to approximately 6000 m water equivalent shielding from cosmic ray muons. At this depth, only about 70 muons from atmospheric cosmic ray showers pass through the detector inside the photomultiplier array per day [53].

3.2 Water Systems

The water systems have been optimized to provide and maintain radioactively clean H_2O and D_2O. Ultra-pure water has the additional benefit of being very clear optically. Such a large volume of pristine D_2O has never before been available for optical measurements.

In this description of the water systems, the elements relevant to the optical

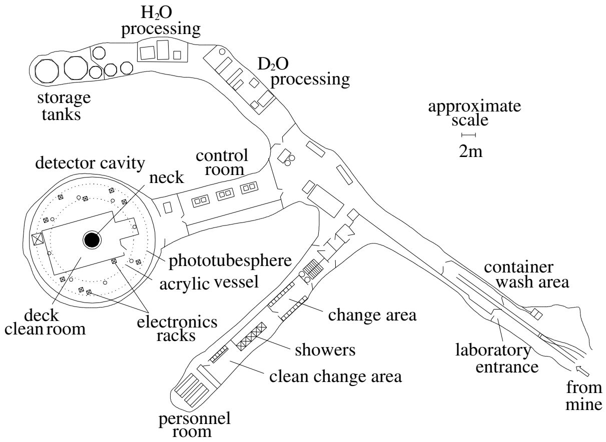

(a) View from above.

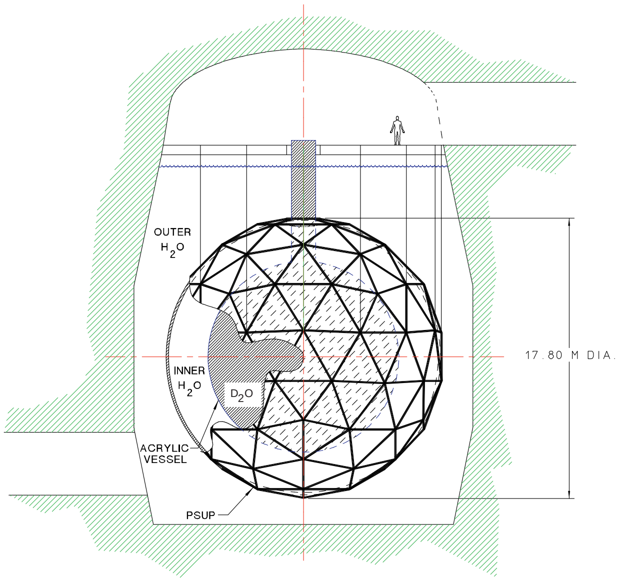

(b) Side view of the detector.

Figure 3.1: *General layout of the SNO laboratory and detector [52].*

properties are highlighted. Impurities in the water, even in minute amounts, can affect both the absorption and scattering of light. For information about the system relating to the radioactive cleanliness and assays, refer to Boger et al. [52].

The SNO water system is comprised of two separate systems: one for the light water (H_2O) and one for the heavy water (D_2O), both of which are located underground near the detector. The source of light water for the H_2O system is a surface purification plant that produces potable water for the mine. Underground, the water is pretreated, purified and degassed to levels acceptable for the SNO detector, regassed with pure N_2, and finally cooled before it is put into the detector. Ultrapure water will leach out soluble components from its environment, and can also support biological activity on solid surfaces or on suspended particles. The H_2O is therefore deoxygenated and continuously circulated to remove ions, organics and suspended solids. The regassing step for the H_2O is essential to the operation of the underwater connectors to the PMT's. Under degassed H_2O conditions, the gas in the connectors diffuses out through the rubber water seals. The low residual gas pressure in the connectors leads to high-voltage breakdown by Paschen's Law. This effect is avoided in SNO by saturating the H_2O with pure N_2.

The source of D_2O was the Ontario Hydro Bruce heavy water plant beside Lake Huron. The heavy water has an isotopic abundance of deuterium of $99.917 \pm 0.005\%$ [52], and is essentially pure D_2O with trace amounts of HDO and H_2O. The D_2O was trucked to the SNO site and transported underground, where it was cleaned and stored temporarily before it was put into the AV. The D_2O in the detector can be recirculated to maintain its purity, though this was not done until February 2001. The reasons for this decision are twofold:

- Water flow in the acrylic pipes inside the AV generates light which makes the detector ineffective for observing solar neutrinos.

- Radon in the water will decay away with time, while with recirculation there is a risk that gas leaks in the purification system will introduce more radon than is removed.

During recirculation, the D_2O passes through a reverse osmosis system, a degassing unit, and an ultra-filtration system. Unlike the H_2O the D_2O is not regassed before returning to the detector.

3.3 The Acrylic Vessel

The D_2O containment vessel must meet diverse requirements, some of which present opposing design constraints. The primary design criteria for the containment vessel are:

- Isolate 1000 tonnes of D_2O from surrounding H_2O;
- Minimize the total mass of radioactive impurities;
- Maximize optical transparency;
- Design for assembly in the mine.

The design criteria listed above resulted in the containment vessel shown in Figure 3.2. The rope grooves, belly plates, acrylic tiles and D_2O recirculation pipes all affect the optical calibration measurement. The principal features of the D_2O containment vessel are listed in Table 3.1.

The 12 meter diameter acrylic sphere is suspended from ten loops of rope, which are attached to the vessel by means of rope grooves located around the equator of the sphere. The choice of rope suspension was driven by radioactivity and optical considerations: a rope under tension offers excellent load bearing capacity for a minimum mass, and it presents the minimum obstruction of the Cherenkov light that neutrino interactions produce.

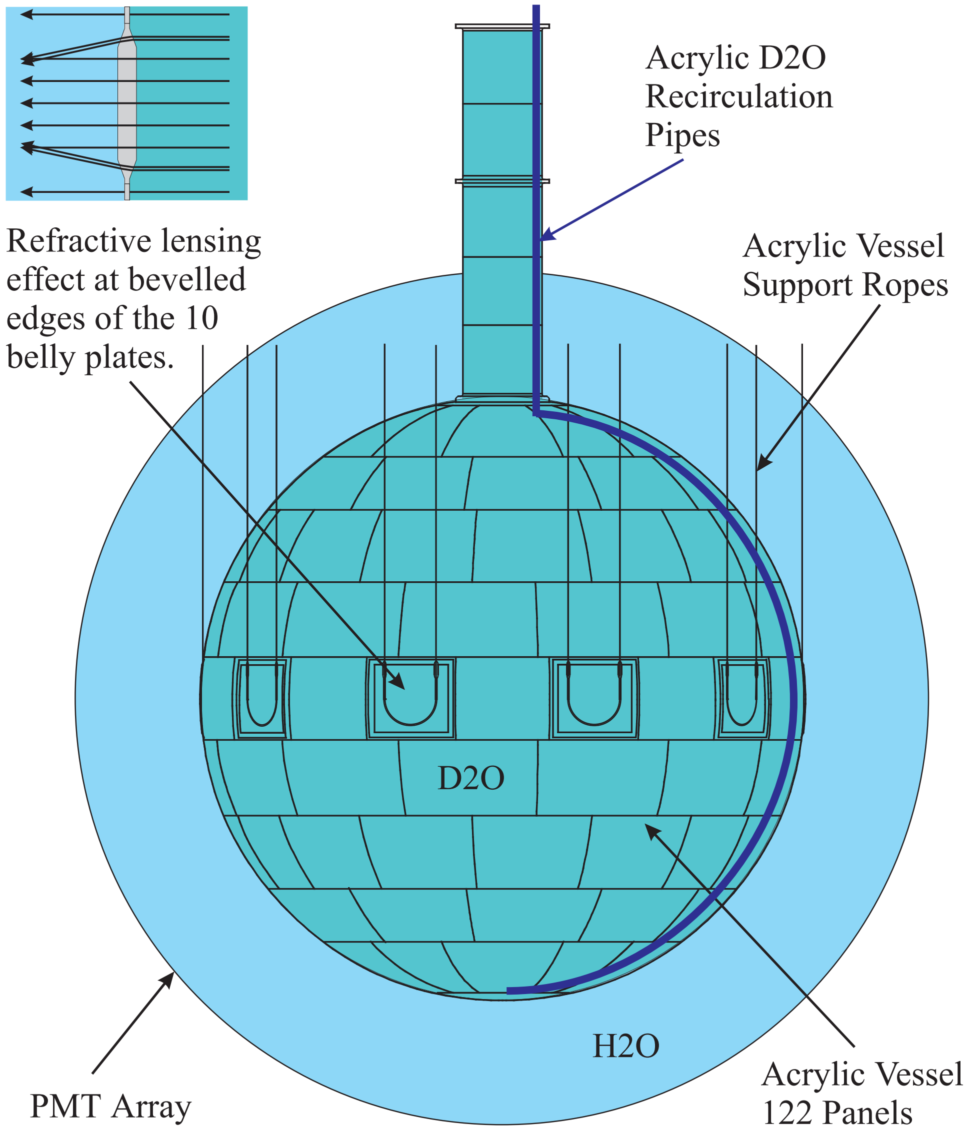

Figure 3.2: *The acrylic vessel and other optical elements of the SNO detector.*

Sphere:	Capacity	997.91 tonnes of D_2O
	Internal diameter	1201 cm
	Wall thickness (nominal)	5.5 cm
	Mass of acrylic	30.0 tonnes
	Light absorption coefficient	0.009 cm^{-1} at 400 nm
		0.026 cm^{-1} at 360 nm
		0.100 cm^{-1} at 320 nm
Chimney:	Capacity (normal operation)	8.61 tonnes of D_2O
	Internal diameter	146 cm
	Height	680 cm
	Mass of acrylic	2.53 tonnes

Table 3.1: *Principal features of the acrylic vessel at 20° C.*

To allow the insertion of calibration devices, the sphere is provided with a 1.46 m diameter by 6.8 m tall chimney. Piping for D_2O recirculation and sampling also enters and exits the vessel through this chimney. For filling and purification recirculation requirements 7.6 cm diameter acrylic pipes introduce D_2O at the bottom of the vessel and remove it from the top of the chimney. D_2O may be extracted via 3.8 cm diameter pipes from four different levels in the vessel and one in the chimney for measurements of both chemical and radioactive water quality.

A total of 122 ultraviolet transmitting (UVT) acrylic panels were used in the construction of the spherical part of the containment vessel. These panels are nominally 5.5 cm thick, with the exception of the ten equatorial panels containing grooves for the suspension ropes. These rope groove panels are nominaly 11 cm thick and the ropes are 3.4 cm in diameter.

Acrylic sheet was chosen as the construction material for a number of reasons. A simple hydrocarbon, UVT acrylic can be manufactured with very low intrinsic radioactivity. Cast acrylic sheet is commercially available in sizes acceptable for mine transportation. It is readily thermoformed into spherical segments and is easily machined: during construction the curvature was typically maintained to ±6 mm.

The light transmission of UVT acrylic matches reasonably the spectral response of the PMT's. To ensure accurate knowledge of light absorption in the AV, optical absorption coefficients were measured for each production batch of acrylic sheets.

3.4 Photomultiplier Tubes

The optical and electronic properties of the photomultiplier tubes determine how well the detector is able to capture and characterize the low-level light signals arising from the Cherenkov effect in the water. The main design features of the PMT's are:

- High photon detection efficiency (peak of about 21.5% at 440 nm);
- Fast anode pulse rise time and fall time and low photoelectron (pe) transit time spread, for a single-photoelectron timing resolution width $\sigma_t \sim 1.5$ ns;
- Low prepulse, late-pulse and after-pulse fractions;
- Minimal amount of radioactivities in all components.

Schott Glaswerke produced a new borosilicate glass (Schott 8246) for SNO. Schott refitted a furnace with a special low-radioactivity liner to produce 16000 mouthblown bulbs for SNO and the LSND Project [54]. The Th and U impurities in this glass are less than 40 ppb. In addition, the glass has outstanding optical transmission properties at short wavelengths, with a bulk light absorption coefficient lower than 0.5 cm^{-1} at 320 nm wavelength.

3.5 PMT Support Structure

The photomultiplier tubes, their light concentrators and associated hardware are collectively referred to as the PMT Support Structure (PSUP). The PSUP also functions as a highly impermeable barrier to waterborne contamination, ensuring that the highly purified water in the sensitive region between the PMT's and the AV is effectively isolated from the dirtier water in the outer regions.

The PSUP is a geodesic sphere that supports the panel arrays that house the PMT's and concentrators. The geodesic sphere has a radius of approximately 890 cm and is suspended by 15 stainless steel wire rope cables from the cavity deck, as shown in Figure 3.1(b). The position of the array is adjustable in the z-direction (up-down) by ± 10 cm. When submerged, the array becomes buoyant, and is therefore secured to the cavity floor at a set of anchor points, each with a pulley and cable that attaches to the main PSUP suspension brackets.

3.5.1 PMT Housing and Light Concentrators

The PMT's are secured in hexagonal ABS (Acrylonitrile-Butadiene-Styrene) black plastic housings that also support light concentrators (reflectors) [55] for each inward-looking PMT as shown in Figure 3.3.

The concentrators increase the effective area of the photocathode to maximize the number of photons detected, and limit the angular acceptance of the photomultipliers so that only the central part of the detector (where backgrounds are lowest) is in view. They are designed with a three-dimensional critical angle of 56.4°, which means the detector is viewed by each PMT out to a radius of 7 m. By themselves, the 9438 inward facing PMT's provide a light sensitive photocathode coverage of 34%. The 27 cm diameter concentrators increase the effective photocathode coverage to about 59%, but the reflectivity of the concentrator reduces this figure to 54%.

A concentrator is made of 18 pieces of thin dielectric-coated aluminum sheet curved and placed around the holder of ABS plastic. The optical coating consists of a layer of specular aluminum covered by a low refractive index layer of magnesium fluoride, which is in turn covered by a high refractive index layer of mixed titanium (TiO_2) and praeseodymium (Pr_2O_3) oxides. The coating thicknesses are optimized

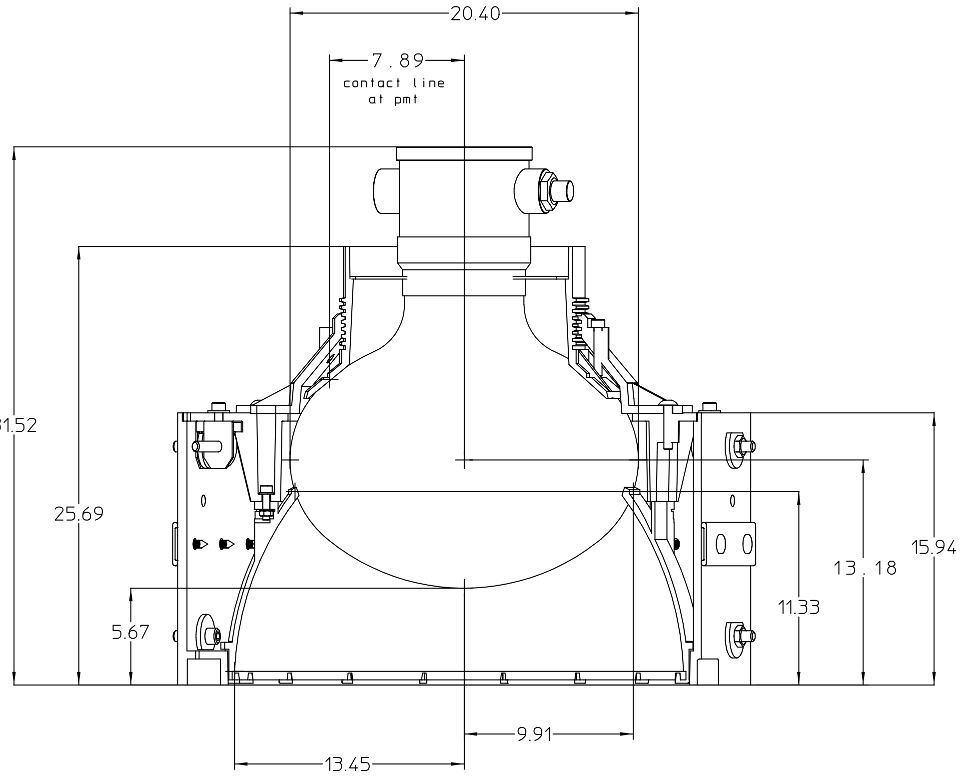

Figure 3.3: *Photomultiplier mounted in a hexagonal ABS cell, which also forms the light-concentrator housing [52]. Dimensions are in cm.*

to maximize reflectance in water over the visible and near-UV range of wavelengths, and over a wide range of incident angles. The mean effective reflectance in water is 82±3%.

The top dielectric layer also forms a protective barrier against corrosion in water and was applied to the back exposed surface of the aluminum pieces as well. A protective layer of titanium oxide was applied to the edges. The material was subjected to extensive aging tests prior to construction. It was found to have a useful life of many years under deoxygenated deionized water with a pH around 7, the normal environment in SNO.

The hexagonal PMT assemblies are collected together into flat arrays of between 7 and 21 PMT's to form a set of repeating arrays used to tessellate the spherical surface of the geodesic structure. Each panel array is secured to the geodesic structure with three adjustable mounts. These mounts permit the delicate panel arrays to accommodate the geodesic structure struts flexing under changing load conditions (most notably, when going from a fully instrumented dry array to a fully submerged array). This alignment is critical to ensure that each PMT views the full D_2O volume. During construction, a laser pointing normally to the plane of each panel was used to align the arrays to withing 0.5° of the nominal centre of the PSUP.

3.6 Electronics

Light signals inside SNO are first captured by the PMT's, then combined into 400 ns long events by the electronics system on the deck above the water volume. The system is typically triggered by at least 18 channels firing within a window of 100 ns, but can also be triggered by external signals or by large pulses on individual channels. The electronics system is designed to have a very wide dynamic range so that signals from single photons to several 1000 photons can be measured. With a timing resolution of ~ 0.2 ns the electronics is well-suited to precise measurements of the PMT signals which have an intrinsic transit time spread of 1.5 ns.

While the solar neutrino event rate is very low (a few per day), the electronics must be able to handle calibration source rates ($\lesssim 300$ Hz), noise rates ($\lesssim$few kHz), and burst rates from potential supernovae ($\lesssim$few MHz). All PMT channels function independently, and the integrated charge and relative timing of the channels are processed and stored whenever the global detector trigger conditions are met. Digitized forms of these signals are stored pending readout by the data acquisition system (described in Section 3.7).

The electronics system can also be fired asynchronously relative to its internal clocks. This trigger is the external asynchronous (EXTA) trigger, and is used extensively when running the laserball for the optical calibrations (see Section 3.8.3) to ensure essentially 100% trigger efficiency. The time offset between the laser light pulse and the EXTA trigger remains constant from pulse to pulse, unlike the other triggers where the timing is latched to the electronics 50 MHz clock and can vary by up to 20 ns from pulse to pulse.

3.7 Data Acquisition

In this section the design and functioning of the SNO Data Acquistion System (DAQ) is outlined. The data from the SNO electronics are built into events by correlating the time stamps of PMT hits with global triggers stored in a central master trigger card (MTC). The DAQ system provides a user interface for controlling the settings of the detector electronics: channel thresholds, high voltage settings (including ramping the voltage up or down), online status of the PMT channels, and trigger threshold settings. The DAQ system also provides information for monitoring the detector status, such as the event rate, and includes a dispatcher which sends events to other SNO computer systems as they are acquired.

The readout of the electronics is both controlled and monitored via a user interface Program, the "SNO Hardware Acquisition and Readout Control (SHARC)." SHARC controls SNO's calibration sources through a manipulator computer that moves the sources around inside the detector. The source position and status are slowly varying quantities, and are stored by SHARC as a calibration block which is associated with groups of events (runs) during which the detector operating conditions remain constant. Source information that changes more quickly (additional trigger information, more precise timing) is integrated into the event data stream by routing the relevant signals from the sources to spare electronics channels. Interpretation of the data is left to the offline analysis.

Individual channels (bad PMT's or electronics channels) are taken offline through software. If channels become permanently disabled, they are physically eliminated from the data chain by removing the resistor which supplies high voltage to the PMT.

3.8 Calibration

Accurate measurement of the physics processes in the SNO detector requires a chain of calibrations and calculations to connect the raw measured quantities of PMT charge and time to a full description of the interaction in terms of energy, direction, and particle type. This set of calibrations includes built-in electronic calibrations, a dedicated optical light source, various types of tagged and untagged radioactive sources and detailed radioassays of the detector materials. The major calibration tools are listed in Table 3.2 and briefly described in the following sections. Taken together with a comprehensive Monte Carlo simulation of the detector, this set of calibrations is the basis for an overdetermined model of the detector that can be used to interpolate the energy scale and for particle identification across the full response

Electronic Pulsers	Time slope (ns per count) and pedestal. Charge slope (pC per count) and pedestal.
Laserball	Common time reference (t_0). Walk (time vs. pulse amplitude). Attenuation in D_2O, Acrylic, and H_2O. Scattering in D_2O, Acrylic, and H_2O. Reflection and scattering from structures. Single photoelectron (pe) response. Relative single pe efficiency. Multiple photoelectron response.
Radioactive Sources: Gas: ^{16}N, ^{8}Li Encapsulated: ^{252}Cf, Th, U	Gamma and electron energy response. Neutron capture efficiency. Angular resolution for Cherenkov events.
Accelerator Source: ^{3}H(p,γ)^{3}He	Gamma energy response.
Tagged Sources: ^{252}Cf, ^{24}Na, ^{228}Th	Gamma energy response. Neutron capture efficiency.
Radioassay	Backgrounds from construction materials. Backgrounds from water contaminants.

Table 3.2: *Calibration devices for the SNO detector and their principal uses.*

range of the detector.

After correcting for relative response due to position and direction, an event is assigned an energy according to a calibrated N_{hit} scale. The ^{16}N source sets the absolute scale and provides a measurement of the energy resolution for a 6.13-MeV gamma ray. The energy response to electrons will be inferred from this measurement since the difference in response between gamma rays and electrons is well modeled with the EGS4 code. For each event there is a small probability for recording unrelated noise hits. The rate of background hits is directly measured by regularly sampling the detector by pulsing the global detector trigger. The high-energy end of the scale is checked with the pt 20 MeV gamma ray accelerator source.

The detector angular resolution is primarily determined from theoretical treatment of electron scattering and production of Cherenkov light, together with the geometry of the PMT array. The treatment can be verified through the Monte Carlo against data from the ^{16}N gamma source.

3.8.1 Source Manipulator

The detector response is position dependent, so a general-purpose manipulator has been developed to provide calibration source deployment at accurately known positions in two orthogonal planes in the D_2O. In addition, six calibration access tubes run from the deck to positions in the light water. The source manipulator is located in a plane by two Vectran ropes that run down the vessel neck, through pulleys on the manipulator and terminate at fixed locations on the acrylic vessel as shown in Figure 3.4. A third, central rope connects directly to the source. The source can be introduced at the neck and visit 65% of the plane with a position accuracy of better than 5 cm.

At the deck interface the source is pulled up into a glove box where a person can work on a source while keeping the detector isolated from light and airborne radioactivity. The source can then be pulled through a gate valve into an interlock box where it can be removed or serviced.

Many of the calibration sources require power cable, signal cable and/or gas capillary connections to equipment on deck. To provide uniform and reliable manipulator operation, these auxiliaries are cabled into a standard sized umbilical cable. The umbilical cable runs through the center of the source carriage to a compression fitting at the top of the source. The cable connections are then internal to the source. The umbilical cables are stored and paid out from a pulley array mechanism held under tension, thereby avoiding twisting of the umbilical cable. The umbilical cables are further described in Chapter 5 and in Appendix A.

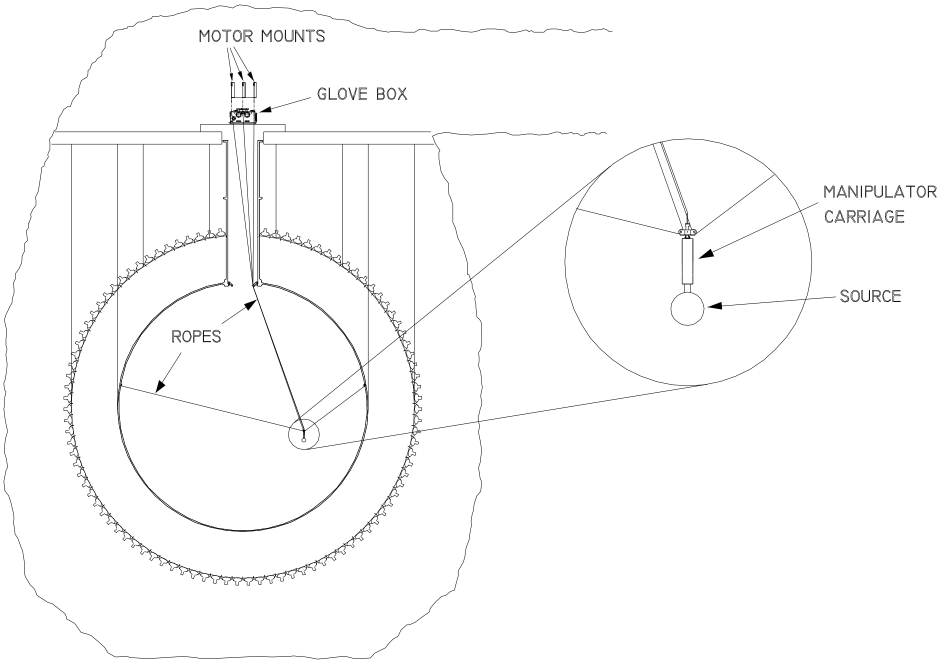

Figure 3.4: *SNO calibration source manipulator system.*

3.8.2 Time and Charge Calibration

The conversion of the digitized values for PMT charge and time to photoelectrons (pe) and nanoseconds (ns) is a two-step process involving electronic pulses and light flashes from the centre of the detector. The electronic pulser calibration yields the transfer functions and offsets (pedestals) for converting the digitized values stored by the electronics into physical units. A common time reference for all channels (t_0) is established using the the laserball at 500 nm (to guarantee low attenuation in all media) positioned at the centre of the detector.

3.8.3 Optical Calibration

The goal of the optical calibration is the determination of attenuation and scattering coefficients for the heavy water, light water, and acrylic. As well, the variations in PMT efficiency with average incident angle of the light are to be measured *in situ* under the operating conditions of the detector. With regular data at multiple wavelengths, the time-evolution of these detector parameters can be followed.

By using the various measured optical coefficients, it is possible to calculate the response of the detector to Cherenkov light produced by a neutrino or background particle interaction. This calculation can be carried out semi-analytically, or it may rely on a Monte Carlo to simulate the optical transport of Cherenkov photons. The results of the response calculation can then be used to interpolate (in space and amplitude) between the various energy calibration sources (discussed below).

An optical source known as the laserball is used in both the optical calibration and the electronics calibration. This source is a quasi-isotropic light diffusing sphere illuminated by output from a wavelength-selectable dye laser. The laser emission time ($\lesssim$ 0.6 ns) is well suited to making precision timing calibrations.

The laserball system was initially developed at Queen's by Ford [9, 10]. The laser

(Laser Photonics Inc. LN203C) provides pulsed radiation at 337.1 nm with a 600 ps pulse width and peak power of 150 kW. The laser pulses at up to 45 Hz and can be used directly or as a pump for one of several dye cells that provide wavelengths in the range of 360–700 nm. The laser pulse rate, selected dye cell and attenuation filters can be adjusted remotely by computer control. The output from the dye lasers is focused into quartz fibre with length 1 m and diameter 1 mm (Fiberguide Industries SFS-1000N) to enhance the uniformity of the output light intensity distribution.

The laser pulses are transmitted to the detector by a bundle of 22 high-OH 100 μm silica core step-index fibres. These fibres were selected for their good UV transmission, low dispersion and low cost. The fibre-optics end at the centre of a 10 cm diameter diffuser ball which distributes the light quasi-isotropically through the detector. A plug at the neck of the ball contains a fibre optic positioning guide tube, allowing the umbilical cable to be detached from the laserball and reconnected with no effect on the light output pattern. A miniature monitoring PMT (Hamamatsu R5600) was installed to monitor the light intensity at the source, but the small solid angle intercepted by this PMT means that it is only useful at light levels much greater than those used to calibrate the detector. The diffuser ball light pulse width is $\sigma_t \sim 1$ ns, which is well suited to measuring the timing characteristics of the PMT's.

3.8.4 Radioactive Gas Transport Sources

There are three gas transport sources: a ^{16}N gamma ray source, a ^{8}Li beta source, and a ^{17}N neutron source. The ^{16}N source is deployed regularly, and the ^{8}Li source has been deployed in December 2000.

The gas transport sources consist of a D-T generator neutron source, a neutron target chamber, gas capillaries, and decay chambers that can be deployed within the detector. The D-T generator, producing 14 MeV neutrons, is enclosed in concrete 30 m from the detector. Various target chambers can be moved into the neutron flux. Gases from the target chamber are routed via capillaries to the deck area and down into the source through umbilical cables. The decay chambers are attached to the manipulator carriage and can be positioned accurately when lowered into the detector.

The ^{16}N is produced via (n,p) interactions on the oxygen in CO_2 gas and decays by a beta delayed 6.13 MeV (66%) or 7.12 MeV (4.8%) gamma ray with a 7.13 s half-life. The cylindrical decay chamber is 10.3 cm long and 5.7 cm in radius, and is made from 5 mm thick stainless steel so that the electrons (which have a 10 MeV endpoint energy) are absorbed. A beta tag is provided by a 3 mm thick scintillator sleeve on the inside of the chamber with a 5 cm PMT. The source has been tested in the SNO detector and can produce up to 300 ^{16}N decays per second [56].

3.9 Off-Line Analysis and Simulation Code

The off-line software is required to perform two major functions: the reduction of SNO data into a form suitable for analysis by low-level calibration and event reconstruction, and a detailed and complete simulation by Monte Carlo techniques of all significant signals and backgrounds using as accurate a model of the detector and its response as possible. These functions are combined in the SNO Monte Carlo and Analysis code, or SNOMAN. Written in FORTRAN, the SNOMAN program is described in two internal reference manuals [6, 7].

The data from the SNO detector are written to tape in the form of packed ZEBRA banks [57]. SNOMAN processors unpack the data and calibrate it by applying pedestal, slope and offsets to the raw ADC data from the DAQ to produce PMT hits with corrected times and charges. SNOMAN relies on a database of detector parameters called SNODB to provide the detector status, configuration and performance information necessary to interpret the data from SNO. After the calibration processor, the data handling is identical for Monte Carlo and detector data.

3.9.1 Monte Carlo Simulation

The SNOMAN simulations of particles is based on three well-tested software packages: the propagation of electrons, positrons and gamma rays is handled by EGS4 [58, modified to produce tracks and vertices], the propagation of neutrons is handled by routines from MCNP [59], and the muon physics is taken from GEANT [60].

The Monte Carlo code for which reliable, well-tested software like EGS4 was not available was written by the SNO collaboration. Photon propagation includes the effects of attenuation, refraction, reflection, and Rayleigh scattering as a function of wavelength and polarization. Other types of scattering, such as Mie scattering, are expected to be negligible for the levels of cleanliness expected in SNO and are not included in the simulations. The light concentrator/PMT response has been the focus of substantial software development and experimental effort. A detailed stand-alone simulation of a concentrator and PMT was written [2] and tested against experiment [3], then installed as a SNOMAN processor. However, *in situ* measurements of the PMT-concentrator optics show a significant difference for the tubes installed in the detector. The reasons for this discrepancy are still being investigated by the collaboration. In the meantime, a phenomenological model of the PMT response is being used. This model treats the concentrator aperture as a flat disk with sensitivity dependent on incident angle as determined from the optical calibration. The lack of a full three dimensional PMT structure means that this model cannot correctly account for reflections from the PMT and its reflector. For this reason, the model is applicable only to prompt light from all sources.

3.9.2 Analysis Tools

Several important analysis tools have been developed by the Queen's University SNO research group, in particular by Boulay [5]. These tools are written in C++ and use the ROOT libraries [4]. These tools are designed for a full analysis of SNO data of all types, and are collectively known as QSNO.

Low-level calibrations are performed by SNOMAN on the detector data obtained from ZEBRA data analysis banks (ZDAB's). The output QSNO/ROOT data structure is a ROOT event tree which stores the complete information available in the ZDAB structure, including event identifiers and lists of hit PMT's with their calibrated hit times and charges. However, the QSNO data structure takes full advantage of the C++ object-oriented paradigm of encapsulating data and code into a common object: procedures and functions needed to compute derived quantities from the data are defined alongside the data storage structures.

Programs written to analyze SNO data can be compiled against the ROOT and QSNO libraries, or they can be run interactively. The interactive nature of QSNO and the availability of the full data structure for the events makes this a very effective tool. The SNOMAN analysis code is more cumbersome because it does not allow direct interactive access to the complete data structure contained in the ZDAB banks.

The optical calibration routines are integrated with the QSNO package as a library known as QOCA. This library includes classes to store the optical intensity and light path information derived from laserball runs at various positions. The main purpose of the routines in the QOCA library is to fit the parameters of the detector optical model to the data taken with the laserball. A complete description of the optical calibration classes is presented in Section 6.2.

For visualization of SNO data, the XSNOED graphical display tool written by P. Harvey of Queen's University is indispensable. This program can be used to view live SNO events from the dispatcher or stored events from ZDAB or ROOT files. A version has been integrated with the QSNO library which allows the user to view synthetic events from the optical calibration where each PMT's charge actually corresponds to the occupancy or the distance from the source, for example. XSNOED is also able to display the time and charge distributions for each channel from the ROOT summary histogram RCH files (see Section 6.2.2).

4 Optical Calibration: Overview

An *in situ* measurement of the optical properties of the SNO detector is essential to the construction of a realistic model for the propagation and detection of light from all sources. The main detector elements to be characterized are the heavy and light water, the acrylic vessel, and the phototube array.

The SNO detector is essentially a large transparent volume surrounded by photomultiplier tubes. All physics interactions of interest occur inside the PSUP and produce bursts of Cherenkov light. The locations of the interactions can be determined by reconstruction using the precise relative timing of the detected photons.

Directional information contained in the Cherenkov light is highly correlated with the type of interaction. In the case of single electrons or gamma rays, the light is emitted preferentially in the same direction as that of the original particle. The directional correlation between a neutrino and the electron produced through interaction provides key information used to extract the relative rates of CC and ES interactions in SNO. Backgrounds from the uranium and thorium decay chains include multiple electrons and gamma rays with very little directional correlation between them, and result in a relatively diffuse light distribution. These background events don't have a direction but can be statistically separated based on the degree of diffuseness of the measured light.

The conditions for light propagation in the detector must be carefully controlled and monitored in order to make a precise measurement of the energy and direction of interactions occuring throughout the detector volume. This is accomplished by ensuring the detector media are clean and transparent, and by measuring the optical properties of the photomultipliers, the acrylic and the water.

4.1 Why is the Optical Calibration Necessary?

There are three principal reasons why it is essential to minimize the energy uncertainty to perform a successful analysis of solar neutrino data in SNO:

1. SNO is making a measurement of CC, NC and ES solar neutrino interactions above a threshold of approximately 6 MeV. The neutrino events will be summed over the entire fiducial volume, so the detector response at all positions must be known. For a $\pm 1\%$ uncertainty in the absolute energy scale, the uncertainty on the derived flux of neutrinos undergoing CC interactions is $\pm 3.8\%$, ES is $\pm 2.8\%$, and NC is $^{+1.2\%}_{-2.1\%}$ [5]. The energy scale is the largest systematic uncertainty in the derived fluxes, followed by the fiducial volume uncertainty from position reconstruction ($\pm 2.9\%$ for CC and ES fluxes, $\pm 1.5\%$ for the NC flux).

2. MSW distortions in the energy spectrum are very small above the SNO analysis threshold for most of the oscillation scenarios. The precision of the energy scale must be of order $\pm 1\%$ to be able to rule out certain of the currently allowed oscillation parameter solutions (Bahcall et al. [45]).

3. The energy threshold is determined by the contributions of radioactive backgrounds to the observed spectra of events at low energy. Isolation of the background relies on a good energy calibration throughout the detector volume.

The major contributions to the energy uncertainty are:

- The extrapolation of radioactive source data with respect to position. The uncertainty is dominated by the uncertainty in the optics.
- The extrapolation of ^{16}N source data to higher and lower energies. This is independent of optics, and is expected to be a small effect. It is tested with a variety of other sources at different energies.
- The interpolation of the energy scale in time. This requires detailed understanding of the properties and state of the electronics and PMT's, and has proven to be the most difficult systematic. There could be a contribution due to changing optics as well.

The visible event energies are determined by the spatial and temporal distribution of PMT hits, as well as by the total number of hits. The goal of the optical calibration is to obtain the basic detector parameters necessary to understand the position-, direction- and energy-dependent corrections to the visible event energies.

The absolute energy scale is most reliably determined by monoenergetic sources at the centre of the detector, where the response is uniform and detector properties are most symmetric. The goal of $\lesssim 1\%$ uncertainty due to optical effects is to ensure that the optical corrections do not dominate the total uncertainty on the neutrino spectral shape determination.

The desired precision for the response correction implies an optical measurement with commensurate optical parameter uncertainties. The required precision on individual optical parameters is dependent on the values of the parameters. For example, the uncertainty on water attenuation coefficients can be high if the attenuation is very low.

The uncertainty in the detector response is a combination of stochastic fluctuations in Cherenkov light production by electromagnetic cascades in the water, and of the systematic effects of detector elements on the registered signals. The major effects to be considered are:

- attenuation in the light and heavy water (homogenous and isotropic media) and in the AV (segmented sphere made from tiles with similar average properties),
- bulk scattering in the light and heavy water and in the AV,
- reflections from detector elements such as the AV, PSUP and PMT's,
- PMT efficiencies as a function of:
  - orientation with respect to the incident light (PMT angular response beyond the effect of solid angle),
  - channel threshold and gain,
  - wavelength (intrinsic quantum efficiency of the photocathode material), and
  - location in the detector (residual magnetic effects and aging effects with submersion history).

The dominant optical effects on the detector response will be shown to be the PMT angular response, the acrylic attenuation and the light water attenuation.

The Cherenkov spectrum is modified by differential extinction in the various media. The media extinctions, PMT quantum efficiency[1] (QE) and the emitted and observed Cherenkov spectra are shown for a source at the centre of SNO in Figure 4.1. Extinction in the acrylic determines the detectable Cherenkov spectrum below 350 nm. The PMT QE is a function of wavelength extending from 240 nm to

[1]Strictly speaking, the quantum efficiency refers to the wavelength-dependent probability of the photocathode producing photo-electrons by the photo-electric effect. Other efficiencies, which depend on the purely electronic effects (*e.g.* the anode electron collection efficiency), are normalized out of the overall PMT efficiency. The term "quantum efficiency" is often used in the context of SNO to refer to the wavelength-dependent probability of registering a hit in a PMT.

700 nm with a maximum value of approximately 21.5% near 420 nm. The drop in QE for long wavelengths is the dominant effect determining the shape of the detected spectrum beyond 500 nm. The media transmission curves are derived from the data presented in Chapter 8. The PMT QE curve is taken from SNOMAN for the PMT and reflector combination, and is originally from work by Lay [2].

Figure 4.2 illustrates the light trajectories in the uniquely simple case of the light source at the centre of the detector. Prompt light reaches the PMT's directly from the source, while reflections cause delayed PMT signals. Prominent reflections are from the AV, the PSUP, and the 35° PMT reflection, which is enhanced by the geometry at the joint of the PMT glass bulbs and the light collecting reflectors (see Appendix B). The timing spectrum for light emitted by the source at the centre is shown in Figure 4.3. Approximately 80% of the light is detected in the prompt peak, with much smaller fractions in the reflected peaks or in the peaks due to pre- and late-pulsing in the PMT's (described in Section 5.1). An enormous simplification of the analysis comes from consideration of prompt light only. In this case, reflections from detector elements can be excluded by applying timing windows to the observed signals.

4.2 Cherenkov Light in SNO

In a dielectric medium, relativistic charged particles emit Cherenkov light of wavelength λ provided the particle's velocity v exceeds the phase velocity of light:

$$v > \frac{c}{\sqrt{\epsilon(\lambda)}} = \frac{c}{n(\lambda)} \tag{4.1}$$

where $\epsilon(\lambda)$ is the dielectric constant and $n(\lambda)$ is the index of refraction of the medium [49]. The Cherenkov light is emitted along a cone with an opening half-angle θ_C given

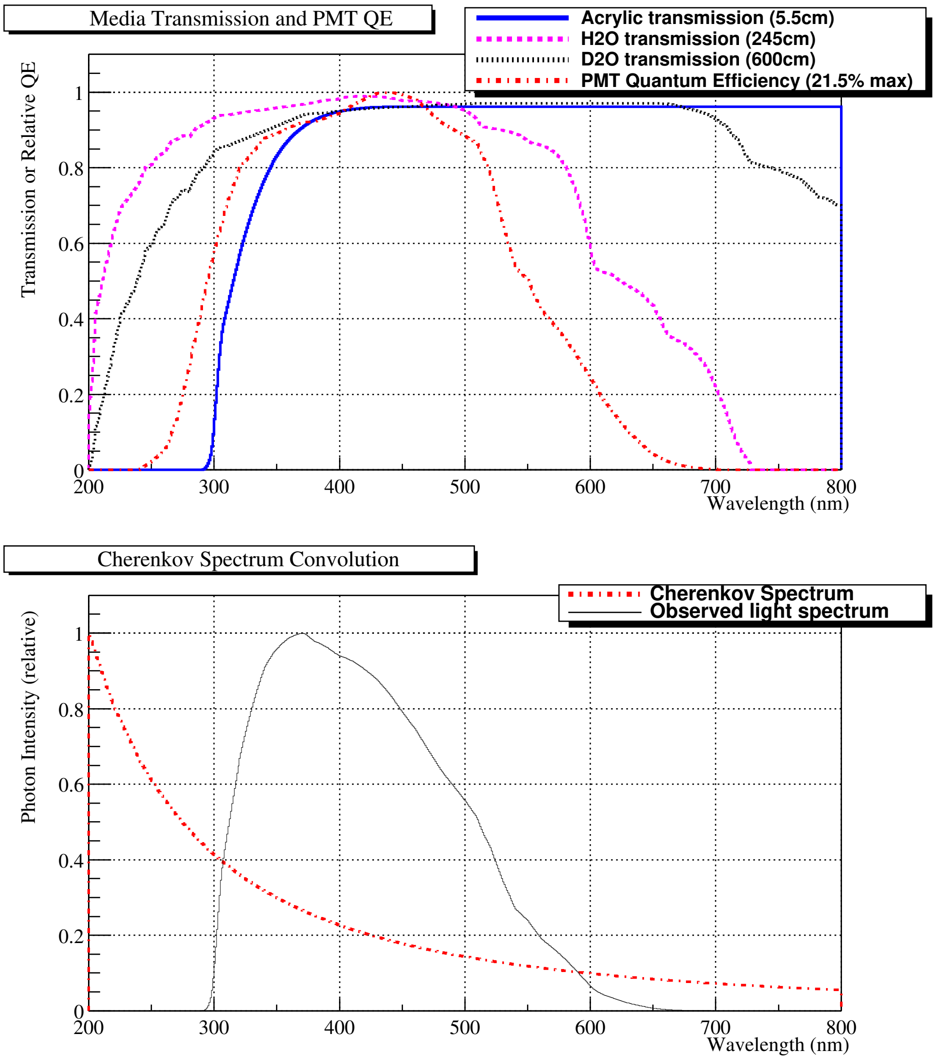

Figure 4.1: *Cherenkov spectrum convolved with PMT quantum efficiency and media extinctions.*

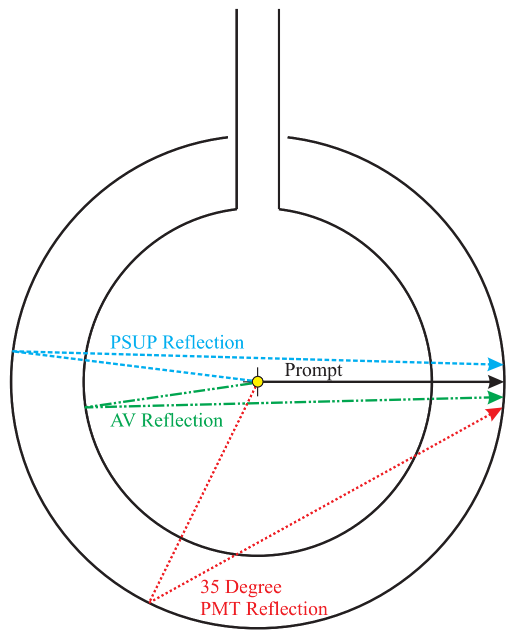

Figure 4.2: *Light paths from the centre of the detector.*

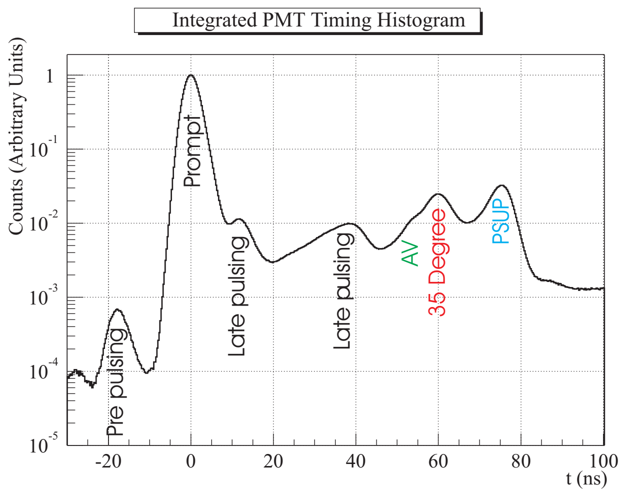

Figure 4.3: *Time spectrum for light emitted from the centre of the detector. Data from a central laserball run at 500 nm taken in February 2000. The pre- and late-pulsing are described in Section 5.1.*

by:

$$\cos\theta_C = \frac{1}{n(\lambda)\beta} \tag{4.2}$$

where $\beta = v/c$ is the relativistic velocity of the emitting particle. The Cherenkov light is linearly polarized perpendicular to the surface of the cone or, equivalently, in the plane formed by the direction of propagation of the particle and of the Cherenkov photon. The trajectory of energetic particles is sufficiently straight at the scale of the wavelength of the emitted Cherenkov light that interference effects in the wavefront are negligible [50].

The number of Cherenkov photons emitted is a function of the track length of the charged particle, its velocity and charge, and the index of refraction of the medium. The differential Cherenkov spectrum is given by:

$$\frac{\mathrm{d}^2 N_C}{\mathrm{d}x\,\mathrm{d}\lambda} = \frac{2\pi\alpha z^2}{\lambda^2}\left(1 - \frac{1}{n^2(\lambda)\beta^2}\right) \tag{4.3}$$

where $\mathrm{d}^2 N_C$ is the number of photons emitted per unit track length $\mathrm{d}x$ over the spectral range $\mathrm{d}\lambda$, z is the charge of the moving particle (in units of the electron charge e), and $\alpha = 1/137$ is the fine structure constant. For Cherenkov light emitted inside the AV, the spectrum will be altered most in the short wavelength region (300 nm to 400 nm) where acrylic attenuation is greatest. Outside the AV, the amount of Cherenkov light detected will depend on whether it had to traverse the acrylic vessel on its way to the phototube (inward-going events) or went directly through light water only (outward-going events).

The indices of refraction for both H_2O and D_2O are shown in Figure 4.4. The data points at individual wavelengths come from steam tables in Schiebener et al. [61] for H_2O, and from a table of values in Hellwege [62] for D_2O. The functions used for the index of refraction are taken from Boardman [63] (as entered into the SNOMAN Monte Carlo program described in Section 3.9), and from Buiteveld et al. [64] for

H_2O. The SNOMAN functions are:

$$n_{\mathrm{H_2O}} = 1.302 + 0.01562\,\mathrm{e}^{0.32hc/\lambda} \tag{4.4}$$

$$n_{\mathrm{D_2O}} = 1.302 + 0.01333\,\mathrm{e}^{0.32hc/\lambda} \tag{4.5}$$

$$n_{\mathrm{Acrylic}} = 1.452 + 0.02\,\mathrm{e}^{0.32hc/\lambda} \tag{4.6}$$

The difference between the SNOMAN functions and the data points for the two waters is less than 0.1%.

The SNOMAN function for the index of refraction of acrylic is difficult to verify against literature values for n_{Acrylic}. The optical properties of acrylic depend on many factors inherent in its manufacture, such as curing temperature and trace elements used in the monomer or curing agent. However, typical light signals in SNO spend very little time in the 5.5 cm thick acrylic vessel so reconstruction based on timing is negligibly affected by changes to n_{Acrylic}. The acrylic vessel is a thin shell, and light rays refracting through it will experience primarily a displacement rather than an angular direction change. The uncertainty in the path length through acrylic depends on n_{Acrylic}, which was determined along with the light absorption coefficients when the AV panels were individually measured [65, 66].

The group velocity of light, which affects the speeds at which the photons travel through the various detector media on their way to the PMT's, is related to the index of refraction and its first derivative by the dispersion relation:

$$v_g = \frac{c}{n + \omega\frac{\mathrm{d}n}{\mathrm{d}\omega}} = \frac{c}{n - \lambda\frac{\mathrm{d}n}{\mathrm{d}\lambda}} \tag{4.7}$$

where v_g is the group velocity, $c = 3 \times 10^8$ m/s is the speed of light, n is the index of refraction, $\omega = 2\pi c/\lambda$ is the angular frequency and λ is the wavelength. Over the wavelength range 300 nm to 800 nm, the group velocity changes by nearly 7%, which

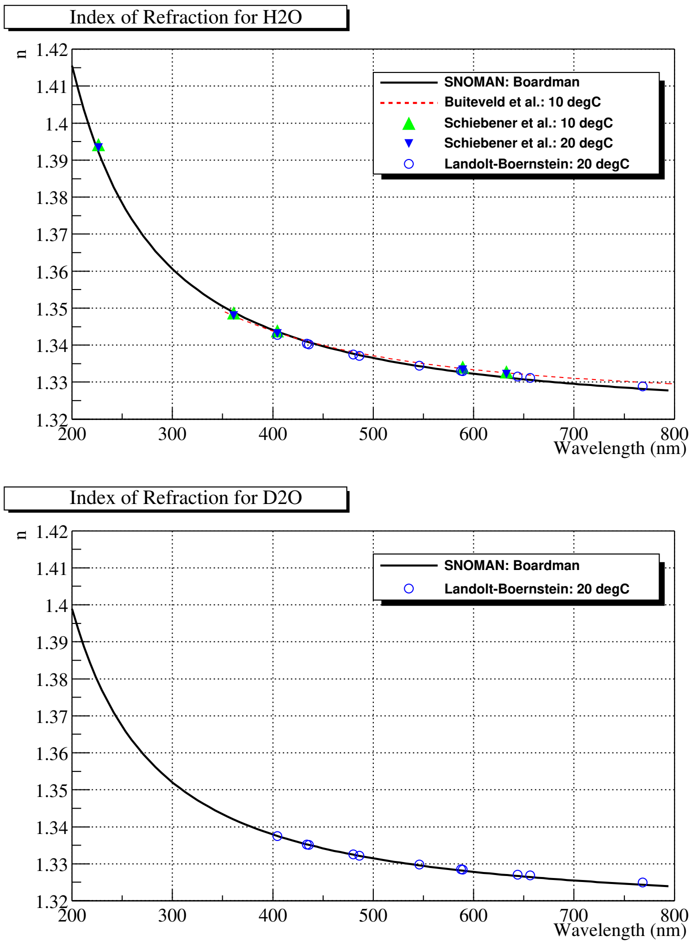

Figure 4.4: *The indices of refraction for H_2O and D_2O as a function of wavelength.*

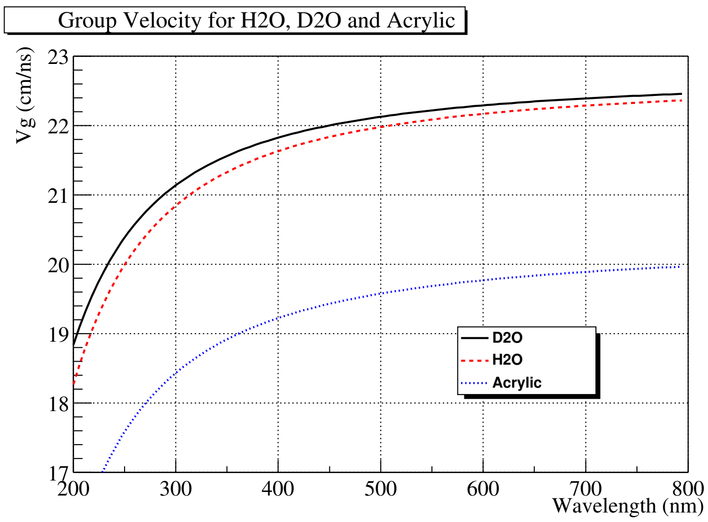

Figure 4.5: *The group velocity of light in H_2O, D_2O and Acrylic as a function of wavelength.*

may impose a fundamental limit on the attainable reconstruction accuracy. As seen in Figure 4.5, half this variation is between 300–400 nm where the Cherenkov emission and acrylic attenuation are greatest. Studying this wavelength region in detail is important to the optical model and to understanding the detector's response.

4.3 Optical Model of the SNO Detector

The SNO detector consists of a number of optical elements which allow light to propagate and to be detected by the spherical shell of PMT's on the PSUP. The optical model of the detector is fully developed in the Monte Carlo simulation contained in SNOMAN. A simplified model based on geometric optics is essential to the measurement of the physical properties of the detector. The parameters of this model are the attenuations of the transparent media and the PMT response as a function of incident angle. The model also includes parameters to quantify the light intensity distribution from the laserball used to make the measurements *in situ*. The simplified model contains all the components needed to characterize the detector properties as a function of wavelength, position and direction. As well, the resulting measurements can be used directly in the Monte Carlo.

The optical model relies on the assumption that the detector can be well characterized by average properties. This implies that the water is homogeneous and isotropic, and that the phototube response depends only on the incident angle of the light. Although each of the acrylic vessel panels has a somewhat different attenuation coefficient, a single acrylic attenuation coefficient is assumed with a value equal to the average absorption. This is reasonable because the acrylic panel positions are uncorrelated with the externally measured attenuation coefficients [67]. The RMS width of the distribution of acrylic absorption coefficients for the detector panels is 9-21% (see Table 7.1, from data provided by Earle [65]), and is due to variations in the acrylic batch material formulation and in the processing by the manufacturer [66]. The conditions in the detector are unlikely to significantly alter the absorption coefficients of the acrylic over time [66].

4.3.1 Optical Model

The optical model used to describe the detector and the laserball includes:

1. Detector properties:

    a) Attenuation in the various media: D_2O, Acrylic, and H_2O.

    b) Reflection and transmission at the water/acrylic boundaries.

    c) PMT channel efficiency.

    d) Angular response of the phototube and reflector assembly.

    e) Multiple-photoelectron corrections.

2. Laserball properties:
   a) Intensity distribution as a function of angle.
   b) Total intensity over a run.
   c) Position.
   d) Orientation.

The prompt intensity N_{ij} observed in a phototube j for a run i is parametrized in the form:

$$N_{ij} = N_i \Omega_{ij} R_{ij} T_{ij} L_{ij} \epsilon_j \mathrm{e}^{-(d_d \alpha_d + d_a \alpha_a + d_h \alpha_h)}, \tag{4.8}$$

where the terms are defined as follows:

$\boldsymbol{N_i}$ The number of photons emitted by the laserball in run i, and detected within a prompt timing window at each PMT. This term is the intensity normalization for the run.

$\boldsymbol{\Omega_{ij}}$ The solid angle of PMT j for run i.

$\boldsymbol{R_{ij}}$ Phototube and reflector assembly angular response beyond solid angle.

$\boldsymbol{T_{ij}}$ Fresnel transmission coefficient for the heavy water/acrylic/light water interfaces.

$\boldsymbol{L_{ij}}$ Laserball light distribution. This is more naturally expressed as a function of the angles relative to the laserball: $L(\cos\theta_{\mathrm{LB}}, \phi_{\mathrm{LB}})$.

$\boldsymbol{\epsilon_j}$ Efficiency of channel j: combination of overall PMT efficiency and electronic threshold. Often referred to as the "quantum efficiency" (QE), which is used to refer to the wavelength-dependent probability of registering a hit.

$\boldsymbol{d_d}$, $\boldsymbol{d_a}$ and $\boldsymbol{d_h}$ Distances for light paths through heavy water, acrylic and light water, respectively.

$\boldsymbol{\alpha_d}$, $\boldsymbol{\alpha_a}$, $\boldsymbol{\alpha_h}$ The attenuation coefficients of the heavy water, acrylic and light water.

The optical model accounts for light coming directly from the source. This light was identified by imposing a narrow time window on the data to identify the prompt light in each PMT (see Sections 6.2.1 and 6.2.3).

By building a data set which includes many different source positions, it is possible to break covariances between the model parameters, such as between α_h and R_{ij}. However, the distances through the light water and the acrylic are linearly related for positions inside the AV, as shown in Figure 4.6. For data taken only inside the AV, the covariance between α_h and α_a is impossible to break, so previous measurements for acrylic attenuation are used as fixed inputs to the optical model and only α_h is fit. The covariance matrix obtained for the fit is further described in Section 7.2.

Intensity data from source positions outside the AV are desirable from the point of view of breaking the correlation between d_h and d_a, and for probing higher angles of incidence at the PMT's for R_{ij}. However, these data are strongly affected by nearly prompt reflections from the AV, making it much more complicated to extract the prompt intensity for the PMT's. The model analyzed in this thesis is developed for data taken exclusively inside the AV to ensure that the prompt intensity can be determined accurately.

The attenuation length of the heavy and light water is of order 50–100 m over the wavelength range 350–500 nm (see Chapter 8). For shorter wavelengths, the attenuation length is expected to decrease for both types of water [68]. For longer wavelengths (500–700 nm), the light water absorption length decreases rapidly due to the excitation of OH resonances [69, 70], reaching 3.6 m at 620 nm [71]. For the heavy water the correponding DO resonances do not contribute significantly to the

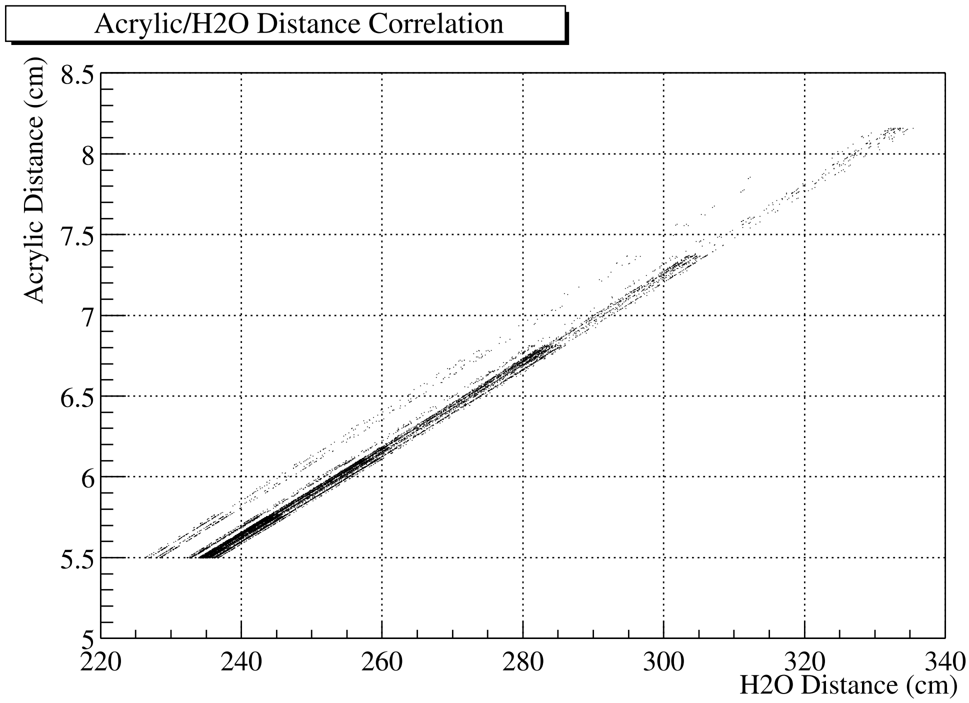

Figure 4.6: *Linear relationship between the path lengths through acrylic (d_a) and light water (d_h). For data taken with the laserball inside the AV, the acrylic and light water attenuation coefficients are highly covariant because of the correlation of d_a with d_h. Each point corresponds to a PMT in the optical data set, which includes laserball runs up to 500 cm away from the centre of the detector (see Chapter 6). The arrangement of the PMT's in flat panels, which are themselves not all arrayed at precisely the same radius on the PSUP, produces the banding seen in the plot.*

absorption in this wavelength range [70], and the attenuation length remains long ($\gtrsim 100$ m; see Chapter 8).

4.4 Implementation of the Optical Model

There are several terms in the optical model which can be calculated precisely. The solid angle (Ω_{ij}), the Fresnel transmission coefficient (T_{ij}), and the MPE correction (M_{ij}) are calculated by the model along with the direct optical path from the laserball to each PMT. The fit procedure minimizes the χ^2 for the occupancy ratio between an off-centre and a central run (see Section 4.4.1). This eliminates the individual PMT efficiencies from the fit. The remaining parameters are left variable.

The variable parameters of the optical model described in Section 4.3 are implemented as far as possible using histograms or arrays of numbers rather than functions. This allows the parameters to be completely independent from external constraints, such as an imposed functional form. For example, the PMT angular response could be modeled as a scaling function multiplied by the SNOMAN simulated angular response. However, this would constrain the fit to a questionable form and, although such fits have been done, an unconstrained fit has been used throughout this work.

Any of the parameters can be individually fixed or left variable in the fit. The three attenuation coefficients (α_d, α_a and α_h) are stored as real numbers, and the run normalizations (N_i) are stored in an array with one entry for each off-centre run.

In the fit, the PMT response $R_{ij} = R(\theta_{\mathrm{PMT}})$ was a 1-dimensional histogram with 90 bins of width 1° and centred on the integer bin values. This parametrization of R_{ij} was chosen because it doesn't impose a functional form on the PMT response, and the small bin width allows a good representation of the function at all angles. The PMT incident angle θ_{PMT} is the angle between the direct light path from the laserball position in run i to PMT j and the normal vector at the front face of the

PMT (see Figure 4.9). The first bin, from -0.5°to 0.5°, is initialized to 1 at the start of fitting and remains fixed to avoid a meaningless global normalization. The response is zero after 75° and the data inside the vessel only extend to 45°(when runs up to $R = 550\,\text{cm}$ are included). Typically, only about 40 variable model parameters are needed to characterize the PMT angular response.

The water (α_d and α_h) and acrylic (α_a) attenuations, and the PMT angular response are the detector parameters of the optical model. The remaining parameters are concerned with the laserball light intensity distribution and normalization, and will be referred to as the laserball parameters.

The laserball distribution $L_{ij} = L(\cos\theta_{LB}, \phi_{LB})$ is a combination of a polynomial mask function $P_m(\cos\theta_{LB})$ and a 2-dimensional histogram $H(\cos\theta_{LB}, \phi_{LB})$ with 12×36 bins. The azimuthal angle ϕ_{LB} and polar angle θ_{LB} of the ray from the laserball position in run i to PMT j are used in the binned lookup in $H(\cos\theta_{LB}, \phi_{LB})$ and in the evaluations of $P_m(\cos\theta_{LB})$. Figure 4.9 shows the position of θ_{LB}, while ϕ_{LB} depends on both the position and orientation of the laserball. All elements of the histogram H are initialized to 1 for a flat starting distribution. The shadow of the cylindrical manipulator support for the laserball imposes a rather rapidly changing feature in the polar light distribution, as illustrated in Figure 4.7. The polynomial allows the model to incorporate this shadowing as a common function, without requiring a large number of $\cos\theta_{LB}$ bins in the laserball distribution histogram. The mask function is implemented as a sixth-order polynomial in $(1 + \cos\theta_{LB})$:

$$P_6(\cos\theta_{LB}) = 1 + \sum_{n=1}^{6} a_n (1 + \cos\theta_{LB})^n \tag{4.9}$$

where the polynomial coefficients $a_n = 0$ at initialization to obtain a flat distribution. The functional dependence on $(1 + \cos\theta_{LB})$ was chosen to guarantee a mask function value of $P_6(-1) = 1$ below the laserball ($\theta_{LB} = \pi$). A sixth order polynomial was chosen visually because it smoothly matches the polar intensity variation of the laserball. The P_6 function is intended to smoothly follow the gross features of the laserball intensity distribution, while the histogram H provides flexibility in adjusting the details.

4.4.1 Prompt Occupancy Ratio Method

To eliminate the unknown PMT efficiencies ϵ_j in Equation 4.8, the ratio between the intensities in two runs was used. To ensure reasonably uniform illumination, a run taken at the centre of the detector was used for the denominator in the intensity ratio. The intensity ratio is estimated by the PMT prompt occupancy ratio, which is calculated from the detector data by applying a number of corrections to the raw number of prompt counts in each PMT channel for each laserball run. These calculations are described in sequence below. The PMT number j and run index i are used as in Equation 4.8.

The number of prompt hits (N_{prompt}) is measured for each PMT by summing the hits in a narrow time window centered on the arrival time for light from the source. This ensures that only direct light from the source is included in the analysis. The raw prompt occupancy is then calculated as

$$\mathrm{OCC}_{\mathrm{raw}} = \frac{N_{\mathrm{prompt}}}{N_{\mathrm{pulses}}} \tag{4.10}$$

where N_{pulses} is the total number of laser pulses in the run.

The light intensity reaching the PMT's is underestimated by $\mathrm{OCC}_{\mathrm{raw}}$ because the PMT's register only single hits even when multiple photoelectrons (MPE) are produced in the PMT from a single laser pulse. The MPE-corrected occupancy is derived from the raw occupancy by inverting the Poisson counting statistical probability

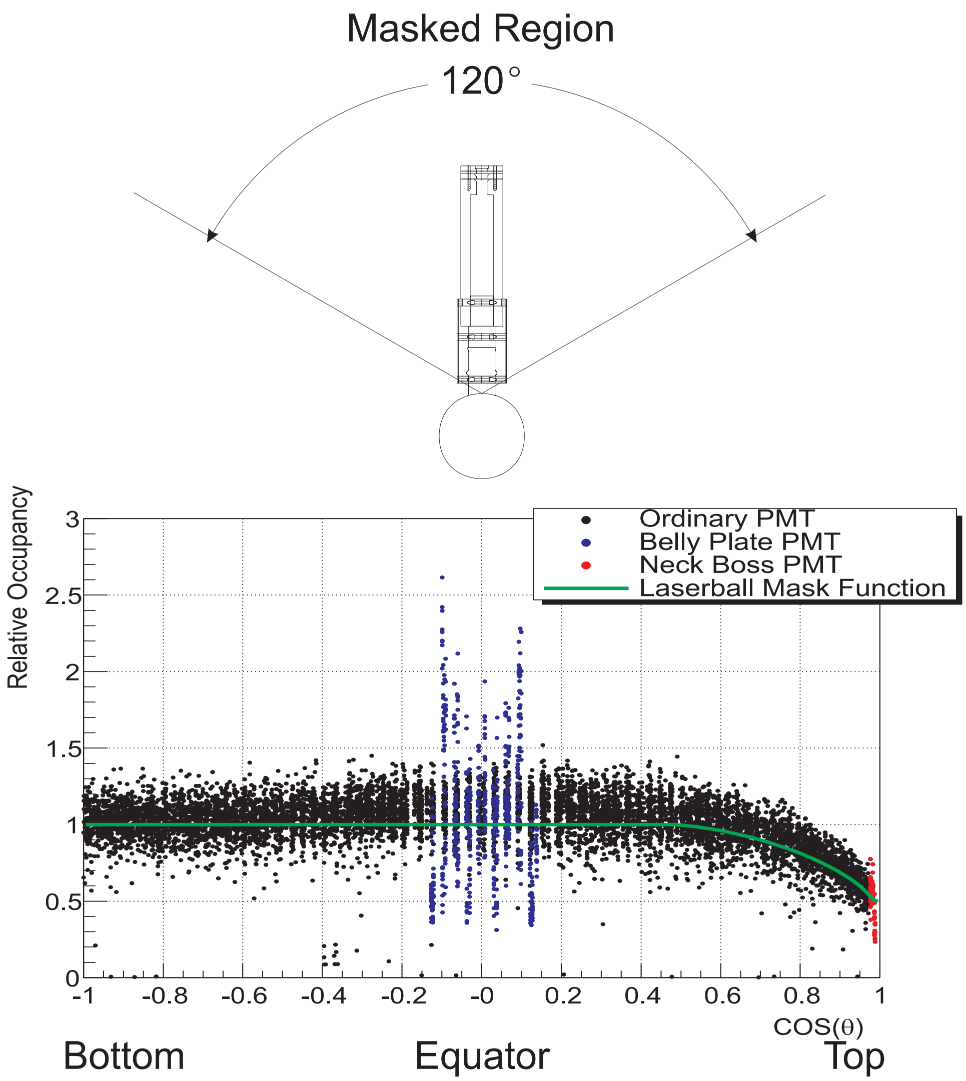

Figure 4.7: *Laserball masked region and function. The laserball is masked by its supporting hardware (top) which affects the light distribution as a function of polar angle. The relative occupancy of PMT channels in a laserball run at the centre of the detector for the 500 nm laser dye (bottom) displays the smooth reduction in intensity for* $\cos\theta_{LB} \gtrsim 0.5$ *to about 50% over the top of the laserball. Also shown are the occupancy variations due to refraction through the bevelled edges of the belly plates and the smaller changes to PMT occupancies due to the joint between the AV and the chimney ("Neck Boss", for* $\cos\theta_{LB} \gtrsim 0.98$ *at this laserball position).*

distribution for small numbers of incident photons:

$$\mathrm{Prob}(\geq 1\ \mathrm{hit}) = 1 - \mathrm{Prob}(0\ \mathrm{hits}) = 1 - \mathrm{e}^{-\mu} \tag{4.11}$$

where $\mathrm{Prob}(\geq 1\ \mathrm{hit}) = \mathrm{OCC}_{\mathrm{raw}}$, and μ is the mean of the Poisson distribution for the true photon occupancy in photons/PMT/pulse. The MPE-corrected prompt occupancy is:

$$\mathrm{OCC}_{\mathrm{prompt}} = \mu = -\ln(1 - \mathrm{OCC}_{\mathrm{raw}}). \tag{4.12}$$

The MPE-corrected number of prompt photons ($N^{\mathrm{MPE}}_{\mathrm{prompt}}$) is then calculated as an estimator of the prompt intensity (N_{ij}) of the optical model (see Equation 4.8):

$$N^{\mathrm{MPE}}_{\mathrm{prompt}} = N_{\mathrm{pulses}}\mathrm{OCC}_{\mathrm{prompt}} = -N_{\mathrm{pulses}} \ln(1 - \frac{N_{\mathrm{prompt}}}{N_{\mathrm{pulses}}}). \tag{4.13}$$

The uncertainty in $N^{\mathrm{MPE}}_{\mathrm{prompt}}$ is due to counting statistics in N_{prompt}:

$$\Delta N^{\mathrm{MPE}}_{\mathrm{prompt}} = \frac{\sqrt{N_{\mathrm{prompt}}}}{1 - N_{\mathrm{prompt}}/N_{\mathrm{pulses}}}. \tag{4.14}$$

The uncertainty in N_{pulses} has been assumed to be negligible. To reduce notational complexity in what follows, the measured MPE-corrected number of prompt photons is used as the estimator of the prompt intensity in the optical model. Therefore, from this point on, $N_{ij} = N^{\mathrm{MPE}}_{\mathrm{prompt},ij}$ with an uncertainty $\Delta N_{ij} = \Delta N^{\mathrm{MPE}}_{\mathrm{prompt},ij}$.

The terms in the optical model which can be precisely calculated from the source-PMT geometry are the solid angle Ω_{ij} and the Fresnel transmission coefficient T_{ij}. These two terms are used to correct for these effects in forming the occupancy ratio for the data:

$$\mathrm{OR}^{\mathrm{data}}_{ij} = \frac{N_{ij}}{N_{0j}} \left(\frac{\Omega_{0j} T_{0j}}{\Omega_{ij} T_{ij}} \right). \tag{4.15}$$

The optical model value for the occupancy ratio follows immediately as:

$$\mathrm{OR}_{ij}^{\mathrm{model}} = \left(\frac{N_i}{N_0}\right)\frac{R_{ij}L_{ij}}{R_{0j}L_{0j}}\mathrm{e}^{-(\delta d_d\alpha_d + \delta d_a\alpha_a + \delta d_h\alpha_h)}. \tag{4.16}$$

where δd_d, δd_h and δd_a are the differences in the distance of propagation of light through the heavy water, light water and a specific acrylic panel referenced by the run index j and PMT index i. The other quantities remain as defined in Equation 4.8. The runs are now indexed with respect to run $i = 0$ for the normalizing central run and $i = 1, 2, \ldots, N_{\mathrm{runs}}$ for the off-centre runs.

The occupancy ratio is used to determine the optical model parameters by minimizing a χ^2 goodness-of-fit estimator:

$$\chi^2 = \sum_{i}^{N_{\mathrm{runs}}}\sum_{j}^{N_{\mathrm{PMT}}} \frac{\left(\mathrm{OR}_{ij}^{\mathrm{data}} - \mathrm{OR}_{ij}^{\mathrm{model}}\right)^2}{\sigma_{ij}^2 + \sigma_{\mathrm{PMT}}^2(\theta_{ij,\mathrm{PMT}})} \tag{4.17}$$

where $\sigma_{ij} = \Delta\mathrm{OR}_{ij}$ is the statistical uncertainty in OR_{ij} and is due to counting statistics in the measurement of N_{ij}:

$$\Delta\mathrm{OR}_{ij}^{\mathrm{data}} = \mathrm{OR}_{ij}^{\mathrm{data}}\sqrt{\left(\frac{\Delta N_{ij}}{N_{ij}}\right)^2 + \left(\frac{\Delta N_{0j}}{N_{0j}}\right)^2}. \tag{4.18}$$

The additional uncertainty, $\sigma_{\mathrm{PMT}}(\theta_{ij,\mathrm{PMT}})$, in the χ^2 is included to account for the increasing variability in PMT response with incident angle θ_{PMT}. This variability arises from non-uniform photocathode coverage inside the PMT's, and is affected by the light pattern produced by the reflectors on the PMT glass envelope (see Section 4.5). A measurement of the variability in the PMT response with incident angle is presented in Section 7.1.2.

The number of variable model parameters in the χ^2 is approximately 500:

- 3 attenuations: α_d, α_a and α_h,

- ~ 40 PMT response bins for $R(\theta_{\mathrm{PMT}})$ up to $40°$,
- ~ 22 run normalizations (N_i), one for each off-centre run,
- 6 laserball mask coefficients for $P_6(\cos\theta_{LB})$, and
- 432 laserball distribution bins for $H(\cos\theta_{LB}, \phi_{LB})$.

The number of data points contributing to the χ^2 is $\sim 140,000$, as discussed below in Section 4.4.2. Given the large number of degrees of freedom in the χ^2, the model is overconstrained, and the χ^2 surface is very smooth. The χ^2 surface is discussed in Section 7.3.

4.4.2 Data Selection in the Fit

Before the occupancy ratio data are fit, many data points are discarded. The dominant cuts are due to light ray geometry (discussed below), which removes about 27% of the PMT's. An additional 3% are cut based on anomalous occupancy ratio (high or low), or are considered outliers because of a high contribution to the χ^2(discussed below).

By looking at the channel occupancies in XSNOED, five geometric cuts have been identified:

Belly plate: Refraction through the bevelled edges of the belly plates roughly doubles the occupancies of a projected square of PMT's sitting behind the plate. The light reaching neighbouring tubes behind the rim of the belly plate are correspondingly much lower than average.

The ten belly plates are uniformly spaced around the equator of the AV. The belly plates are square panels with bevelled edges, and extend over $\pm 7.79°$ as seen from the centre of the vessel. The belly plate cut is somewhat larger: rays passing inside a square of $\pm 9^\circ$ about the belly plate centres have the corresponding PMT's cut from the analysis. By itself, this cut removes 8.3% of the data points

AV rope: There are ten rope loops supporting the AV at the ten belly plates, which leads to 20 rope cuts. PMT's with a light ray having a distance of closest approach to any rope $d_{\min} < 15\,\text{cm}$ are cut. By itself, this cut affects 4.8% of the PMT's.

D_2O pipes: The D_2O recirculation pipes were installed with attachment blocks down the side of the AV corresponding to "Construction North", which is the direction of the positive y-axis in detector cartesian coordinates. The attachment blocks are bonded to the AV tiles away from any bonds and repairs. Although the drawings show the pipes on great circles from the top to the bottom of the AV, the reality is somewhat uncertain. To avoid effects due to refraction or simply due to absorption, the pipe cut is made purposely wide.

PMT's illuminated by rays which pass through the AV near a pipe are discarded from the fit. There are multiple pipes running down the side of the AV to three different levels in the detector. Consequently, there are three regions affected by the pipe cuts: near the top ($\theta < 30^\circ$, cut $75 < \phi \leq 105^\circ$), below the equator ($\theta = 120^\circ$, cut $80 < \phi \leq 100^\circ$), and at the bottom ($\theta = 180^\circ$, cut $85 < \phi \leq 95^\circ$). 5.3% of the data points are removed by this cut alone.

Neck ring or chimney: The neck ring and chimney tend to obscure the PMT's located behind them, as do the AV support ropes (3.43 cm diameter).

Rays which pass within 30 cm of the neck ring or go through the AV chimney are flagged and the corresponding PMT's are not included in the fit. 1.2% of the data points are affected by this cut alone.

Prompt AV reflection: When the laserball is close to the acrylic vessel, certain PMT's on the opposite side of the detector are contaminated by a significant level of near-prompt light reflected from the AV. This effect only becomes prominent with the laserball at $R \gtrsim 450$ cm. For example, with the laserball at $(0, 0, -500)$ cm the reflection from the AV increases the prompt occupancy of a narrow band of PMT's near the equator. Figure 4.8 illustrates the geometry of the direct ray and of the prompt AV reflection. The intensity of the prompt light reflected from the AV is enhanced beyond the normally small amount of light reflected from the AV: the glancing rays which have nearly the same timing as the direct rays also have large Fresnel reflection coefficients from the water/acrylic interfaces.

For source radii in the range [450:580] cm, the QOCAFit algorithm rejects PMT's on the far side of the detector by requiring $\hat{p} \cdot \hat{s} \geq 0.1$, where $\hat{p}$ is the PMT position unit vector and $\hat{s}$ is the source position unit vector.

The amount of data affected by this cut depends on the run positions. For the 386 nm data, which includes three runs at $R > 450$ cm, 3.3% of the data points were removed from the fit by this cut alone. However, for these three runs the cut removes more than half the PMT's on the opposite side of the detector. The PMT's on the near side are not cut, and include the highest PMT incidence angles and largest acrylic and H_2O path lengths sampled by the optical data.

The cut percentages cited in the list are exclusive to each cut; another 3.9% of the data points are cut due to some combination of the geometric cuts.

Before fitting begins, the data are indexed in a lookup table which cross-references the run and PMT number with the occupancy ratio. Channels are pruned from this list following a sequential series of cuts:

1. No dubious rays from geometrical cuts, and a reasonable value and statistical

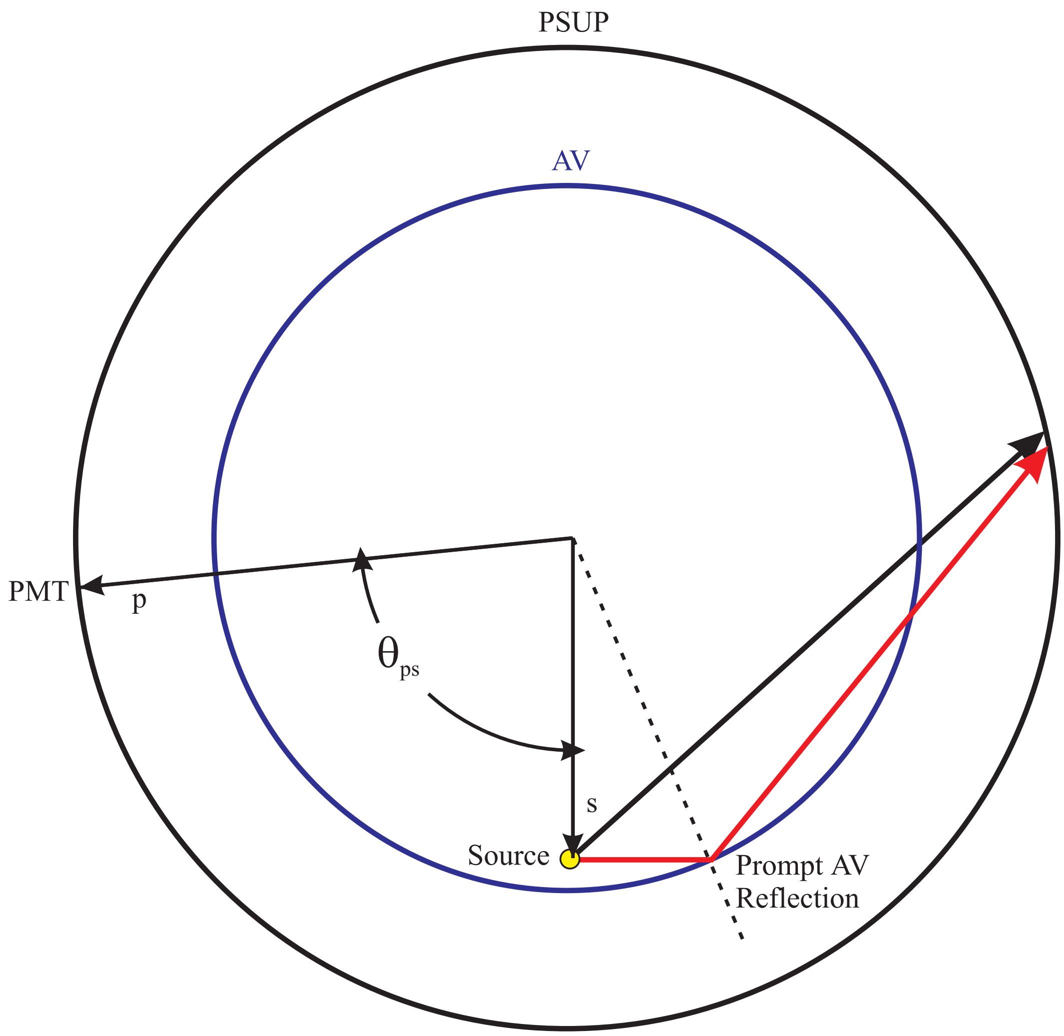

Figure 4.8: *Illustration of prompt AV reflections for source positions with $R \gtrsim 450\,cm$. For certain PMT's, the time difference between the direct light from the source and light reflected from the AV is less than the prompt window width used to derive the prompt occupancy. The vectors from the centre of the detector to the source ($\vec{s}$) and to a PMT ($\vec{p}$) were used to remove PMT's from consideration in the optical fit by requiring $\cos\theta_{sp} = \hat{s}\cdot\hat{p} \geq 0.1$.*

error on the occupancy ratio ($0.5 \leq \mathrm{OR}_{ij}^{\mathrm{data}} < 1.8$ and $\Delta\mathrm{OR}_{ij}^{\mathrm{data}}/OR_{ij}^{\mathrm{data}} \leq 0.25$). Approximately 30% of the data are removed by these cuts, of which 27% are removed by the geometric cuts.

2. High contributions to $\chi^2(\chi_{ij}^2 > \chi_{\mathrm{lim}}^2)$ are removed. This cut affects 0.5% of the data points.

3. Remove channels in crates and cards with bad calibrations or anomalous channel occupancies or trigger rates. Although $\sim 0.7\%$ of the channels would be removed by this cut, it is applied sequentially after the above cuts, and no additional channels are identified only by this method.

4. Only those PMT angular response bins with at least 25 PMT's were left variable in the fit. The few PMT's which are in a response bin of $R(\theta_{\mathrm{PMT}})$ with less than 25 others are removed from the list of data points in the fit. This cut only ever removes the channels in the highest angular bin, corresponding to 0.01% of the data.

A typical data set consists of approximately 200,000 data points for 22 runs, of which 140,000 remain in the fit after all cuts.

4.4.3 Optical Fit Procedure

To calculate the occupancy ratio for any given PMT, the optical model only uses 15 parameters of the optical model. As part of the Levenberg-Marquardt minimization in `mrqmin`, the standard Numerical Recipes routine `mrqcof` [72] executes a double loop over all ~ 500 model parameters to build the covariance matrix from the parameter derivatives at each point. This results in about $500 \times 500 = 250\,000$ iterations per data point. An important optimization of the routine involves keeping track of the

15 parameters that have non-zero derivatives, and only adding those parameter contributions to the covariance matrix elements. When this is done, only $15 \times 15 = 225$ matrix elements are affected.

Without any changes to `mrqcof`, the optical fit routine took about 6 h to complete for the 386 nm data set from September 2000. With the modified `mrqcof`, which keeps track of the 15 parameters affecting each data point, the gain in execution time is impressive: about a factor of 100. This is lower than the factor of ~ 1000 expected solely on the basis of the total number of loop iterations because of the time spent doing the bookkeeping needed to determine array indices for the non-zero parameter derivatives. The gain in speed means the optical fit only takes a few minutes. The fit process can be repeated many times, and even performing all the fits for each of the systematic model variations takes only a fraction of the time previously required for a single fit!

To ensure convergence of the fit, each model or data set variant was fit four times before a final nominal fit. In each fit, the rejection of outlier points based on the individual contributions χ^2_{ij} was recomputed for the initial model parameters. The procedure for obtaining a "nominal" fit for a given data set was as follows:

1. Initialize parameters to default values: uniform laserball distribution, α_a fixed to *ex situ* measurements, and long water attenuations ($\alpha_h = 10^{-4}\,\mathrm{cm}^{-1}$, $\alpha_d = 5 \times 10^{-5}\,\mathrm{cm}^{-1}$).

2. First fit with data point selection $\chi^2_{ij} < \chi^2_{\mathrm{lim}} = 100$.

3. Refit ($\chi^2_{ij} < \chi^2_{\mathrm{lim}} = 100$).

4. Refit ($\chi^2_{ij} < \chi^2_{\mathrm{lim}} = 25$).

5. Refit ($\chi^2_{ij} < \chi^2_{\mathrm{lim}} = 25$).

6. Save the parameter values for re-use.

7. Nominal fit with χ^2_{lim}=25.

For each fit after the first, the parameters from the previous fit were left in place to seed the next fit and for outlier rejection.

The data points in each fit can vary because data point selection was done based on the deviation of the data from the initial model values. Just before the nominal fit, the parameter values were saved. These values were used to seed the fit in subsequent systematics studies, such as fits with different prompt time window widths. This ensured that the data selection and starting point was identical to those of the nominal fit.

4.4.4 Solid Angle

The solid angle calculation is the largest correction to the intensity of the PMT's in the optical model. For laserball positions in the vessel, the solid angle can vary by an order of magnitude. By way of contrast, the other effects in the optical model (*e.g.* attenuations, PMT angular response, Fresnel transmission, laserball light distribution) altered the observed occupancies by only of order $1-10\%$. Therefore, it is absolutely essential to calculate the solid angle correctly.

The method used to calculate the solid angle in the optical model fits was to calculate the ray paths to the edges of the front face of the PMT collectors. The PMT coordinate system consists of a plane containing the light source, the PMT and the PMT normal vector $\boldsymbol{n}_{\mathrm{PMT}}$. The two points P1 and P2 are at the edge of the PMT in this plane, while points P3 and P4 are on the plane normal vector. Figure 4.9 displays the geometry used in the calculation. The four rays to points P1...4 define an elliptical solid angle as seen from the laserball:

$$\Omega_{\mathrm{Ray}} \sim \sin(\alpha/2)\sin(\beta/2) \tag{4.19}$$

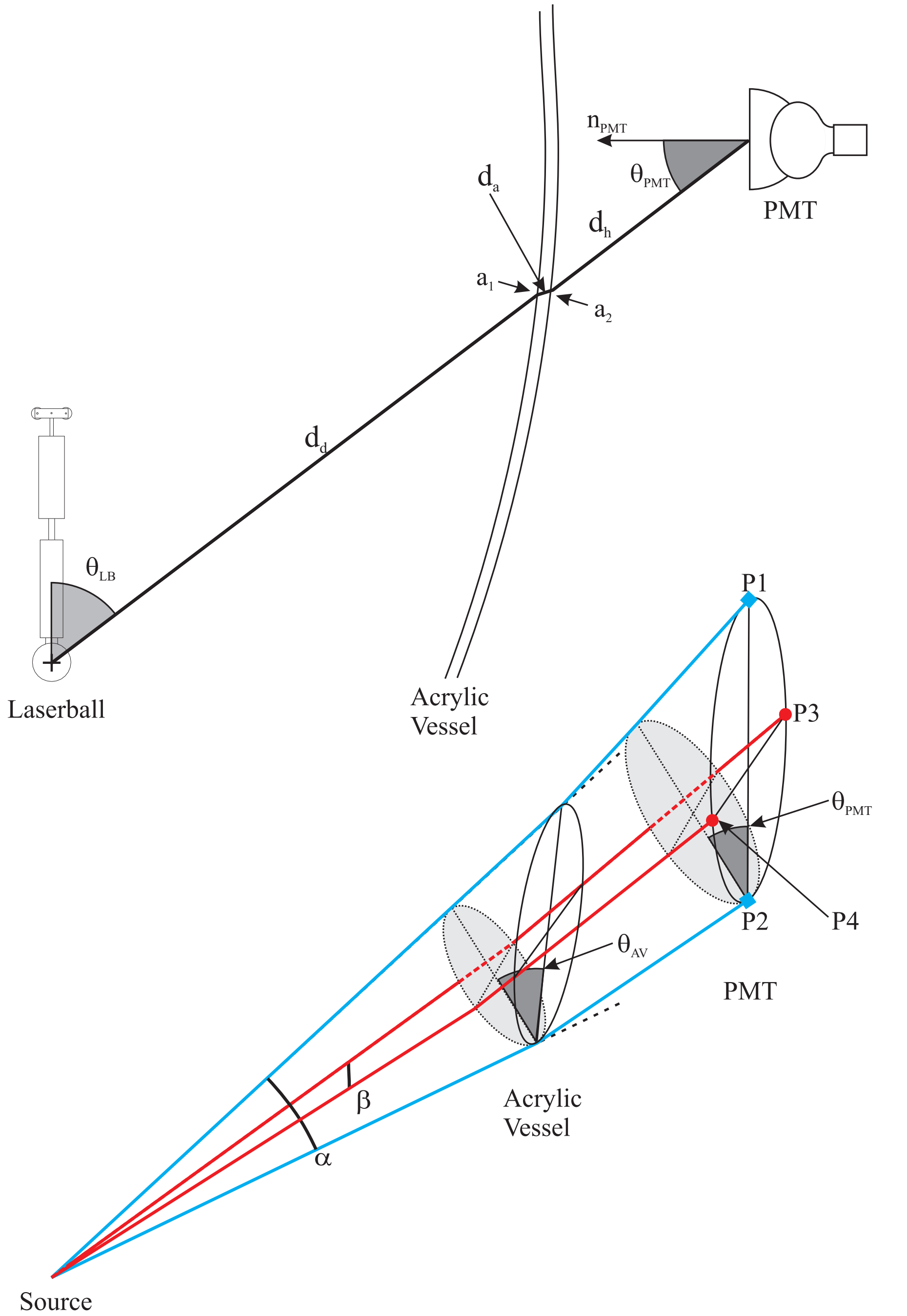

Figure 4.9: *Elements of the solid angle calculation. See text for details.*

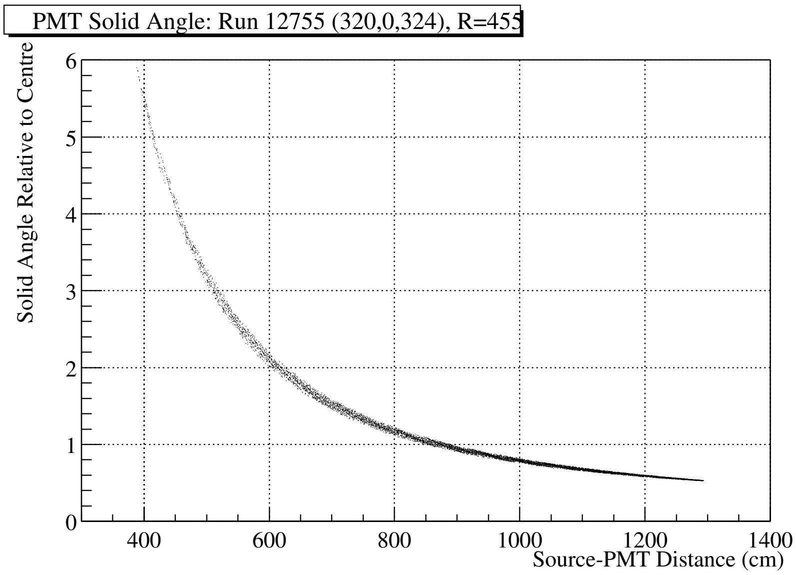

Figure 4.10: *PMT solid angle for run 12755 at $R = 455\,cm$ relative to detector centre. Calculation performed in QOptics (see Section 6.2.4).*

Figure 4.10 shows the solid angle correction relative to the centre of the detector for a run with the laserball at $R = 455\,\mathrm{cm}$.

A straightforward, approximate way to calculate the solid angle is the projected area of the PMT on a sphere at the same distance from the source:

$$\Omega_{\text{Distance}} \sim \frac{\cos\theta_{\text{PMT}}}{R^2} = \frac{\cos\psi}{(d_d + d_a + d_h)^2} \tag{4.20}$$

where ψ is the incident angle of light with respect to the front face of the PMT reflector, and constant factors have been left out of the equation. This is the method proposed by [11] for the optical analysis. The difference between this approximate calculation and the ray method of Equation 4.19 is less than 1% inside the acrylic vessel. In Figure 4.11 the ratio $\Omega_{\text{Ray}}/\Omega_{\text{Distance}}$ is shown for Run 12755 at a radius of 455 cm. Despite this small difference, the solid angle calculation in the present fit

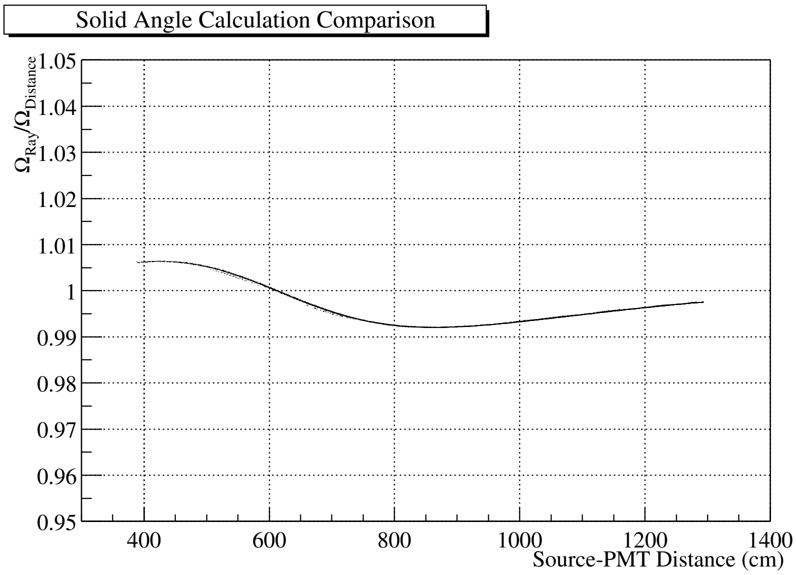

Figure 4.11: *Solid angle comparison between distance and ray-tracing calculations.*

results is based on the ray path method. This is done to avoid potential systematic effects on the optical model parameters due to artificial intensity variations which are generated by the approximate solid angle calculation.

4.4.5 Prompt Attenuation from Absorption and Scattering

Rayleigh scattering from microscopic density fluctuations is an intrinsic phenomenon in bulk liquids. Scattered light affects the observed light distribution intensity and the timing of the observed photon signals. The Rayleigh scattering coefficient can be calculated and subtracted from the attenuation measurements to obtain separate estimates of the absorption and scattering in the water volumes. This separation is important for the Monte Carlo simulation of the detector, where absorption and scattering are simulated separately.

The timing cut imposed on the observed light signals affects the contributions of absorption and scattering to the net observed prompt attenuation. Scattering does not completely remove light from the prompt peak because of the significant probability of forward scattering. The net attenuation can be expressed as:

$$\alpha_{\mathrm{net}} = \alpha_{\mathrm{abs}} + k\alpha_{\mathrm{scat}} \tag{4.21}$$

where k is the fractional contribution of scattering to the net absorption. If all the scattered light were completely removed from the prompt time window, one would obtain $k = 1$. The light which remains in the prompt time window results in a lower net attenuation coefficient with $0 < k \leq 1$.

Equation 4.21 can be used to estimate the absorption separately from the attenuation, given a reliable calculation for α_{scat} and k. Further discussion of scattering and its contribution to the prompt attenuation is found in Section 8.4, where the contributions of Rayleigh scattering to the net attenuation in both H_2O ($k_h \sim 1.0$) and D_2O ($k_d \sim 0.82$) have been evaluated using simulations at 386 nm in SNOMAN. A simulation at a single wavelength is sufficient to obtain k for all wavelengths because k is determined primarily by the timing of the Rayleigh scattered light, which depends on geometry, rather than the total intensity of the scattered light, which depends on wavelength.

In Figure 4.12 the effects of attenuation in the three media are shown for 386 nm data (Run 12755 at a radius of 455 cm). The intensity lost to attenuation is less than 10% for all media. This effect is much smaller than the factor of ~ 12 variation in intensity that arises from the change in PMT solid angle shown in Figure 4.10. The PMT's in panels at the nodes of the PSUP structure (where groups of steel struts meet) are up to 8 cm closer to the centre of the vessel than the mean for other panels of PMT's. This displacement is included in the light path calculations, and changes the relationship between the total source-PMT distance and the distance through each medium most conspicuously for the H_2O distance (d_h).

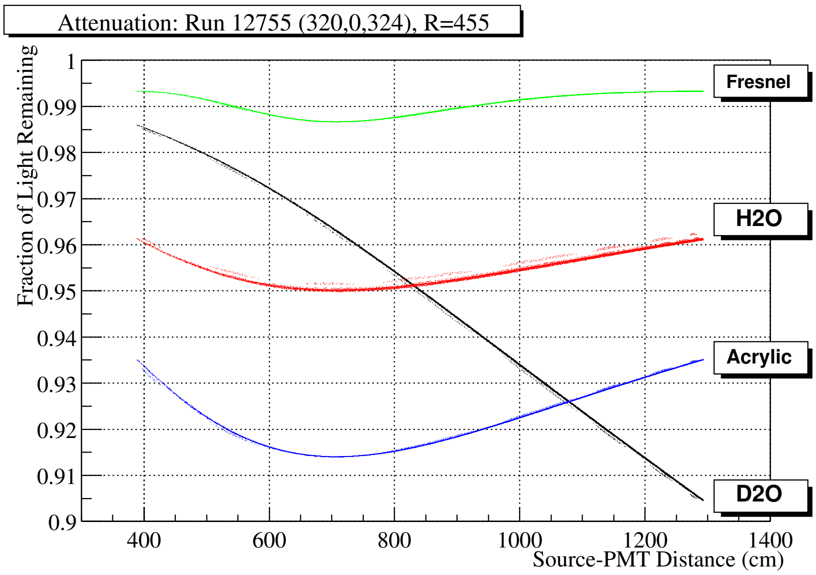

Figure 4.12: *Attenuation and Fresnel transmission losses as a function of distance for Run 12755 at 386 nm. The partial lines slightly offset from the main series of points are due to the flat PMT panels at the nodes of the PSUP structure, which are slightly inside the mean PMT panel radius.*

4.4.6 PMT Angular Response

The three-dimensional structure of the PMT-reflector assembly is modeled by a flat disk at the front opening of the reflector support structure. This is referred to as the "Grey Disk" PMT model. The efficiency as a function of incident angle is a parameter of the model. Although all the internal details of the structure are not included in this simplified model, the average behaviour is well described, as will be shown in detail in Chapter 7.

For a light source at a particular radius, the distribution of incidence angles is dominated by a group of PMT's within about 10°. Figure 4.13 shows the relative abundance of PMT incident angles as a function of source radius. The angular response of the PMT's can be measured most effectively by positioning the source at a series of points uniformly distributed in radius.

4.5 The PMT and its Reflector

The SNO PMT's are designed to accept light primarily from the heavy water volume. The light concentrating reflectors have three main purposes:

1. Increase the effective light collecting area of the detector,

2. Prevent instrumental light from affecting neighbouring channels, and

3. Prevent incident light from scattering between neighbouring PMT's.

Instrumental light includes Cherenkov signals from $\beta\gamma$ decays in the PMT glass and light from high-voltage breakdown. The reflector geometry increases the PMT response for the forward 120°, while blocking light from other angles (see Figure 7.6). The entire volume of the detector out to a radius of approximately 730 cm is visible to each PMT, and the photon detection efficiency is a weak function of incident angle

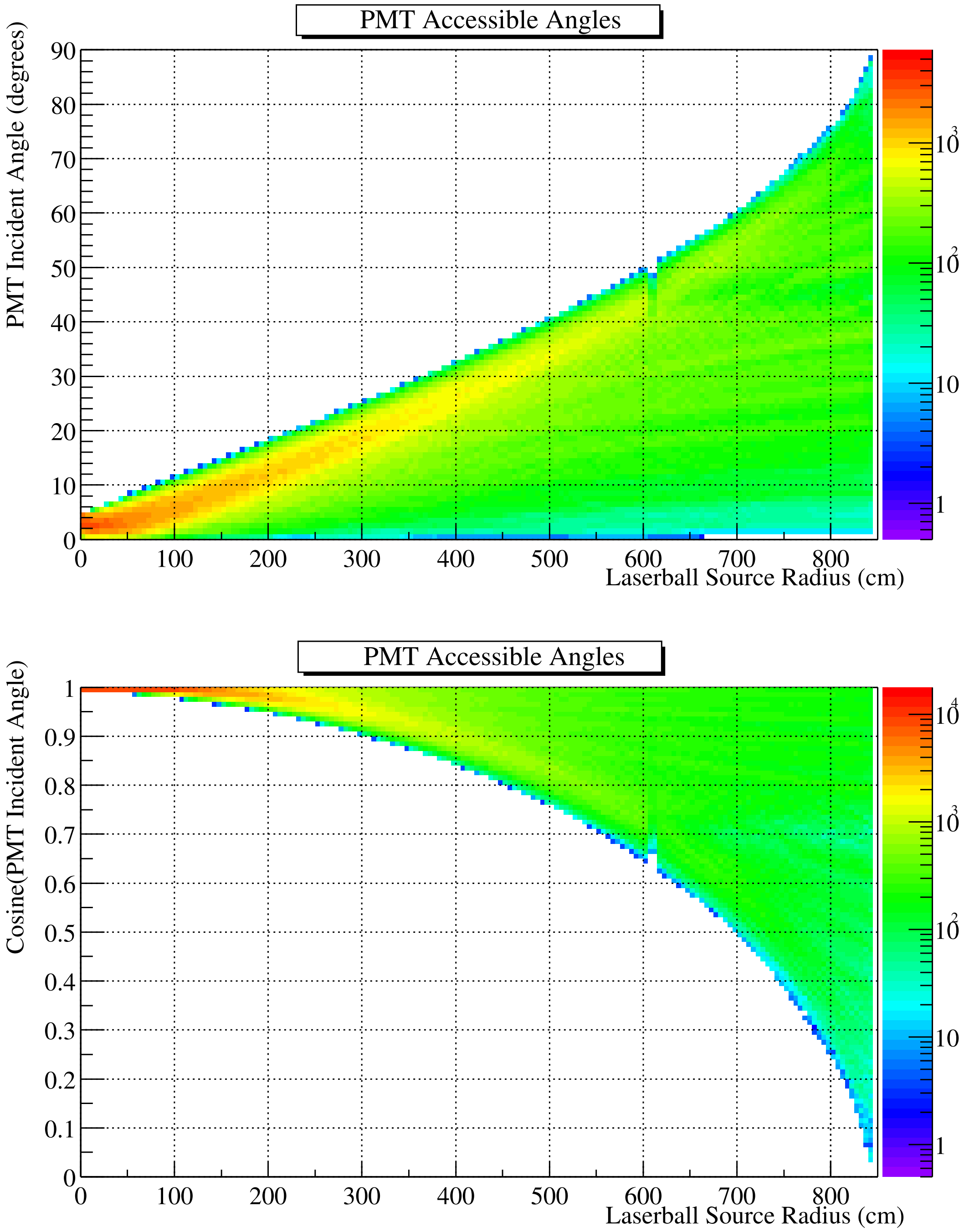

Figure 4.13: *Light incident angles as a function of source radius. The vertical colour gradient indicates the number of PMT's illuminated at a given angle of incidence and source radius. Calculated with QOptics class in ROOT.*

over this volume. Without the reflectors, light from events in the detector would scatter from the glass envelope of one PMT and reach other neighbouring PMT's. These reflections would degrade the effective timing resolution, and the intensity contributions from these light paths would be difficult to deal with in the optical model.

The increase in light collection can be estimated based on the dimensions of the PMT (diameter $d_{\rm PMT} = 20.4\,{\rm cm}$) and the reflector front face opening (diameter $d_{\rm refl} = 26.9\,{\rm cm}$). The coverage $C_{\rm bare}$ for 9400 bare PMT's in the SNO detector (radius $R = 845\,{\rm cm}$) is

$$C_{\rm bare} = 9400\frac{\pi(d_{\rm PMT}/2)^2}{4\pi R^2} = 34.2\% \tag{4.22}$$

while the effective coverage $C_{\rm eff}$ for 9400 PMT's with reflectors is

$$C_{\rm eff} = 9400\frac{\pi(d_{\rm refl}/2)^2}{4\pi R^2} = 59.5\% \tag{4.23}$$

This is reduced somewhat in practice because the increased area is not uniformly efficient. The reflector is not perfectly reflecting, and its geometry coupled with the spherical PMT is unable to gather all the light incident on the reflector and distribute it onto the PMT photocathode.

The increase in coverage by a factor of 1.74 is significant for observing the low light levels associated with Cherenkov events. For example, 6 MeV gamma-rays produce approximately 45 hits in the detector which has a statistical width of 15%. For bare PMT's, the same gamma-rays would produce only 23 hits with a statistical width of 21%. The light collection efficiency of the PMT's is enhanced for events occurring in the heavy water at the expense of events in the light water region.

The PMT and reflector assembly is shown face-on in Figure 4.14. The pattern of illumination is concentrated, and can be expected to enhance differences between PMT's due to uneven photocathode thickness, particularly at larger angles of incidence. The photos are taken with the camera directly in front of the assembly. In

(a) Bare PMT. *(b) White sheet over PMT.*

Figure 4.14: *Photographs of a SNO PMT and its reflector with illumination at normal incidence.*

Figure 4.15(a), a flash was used to highlight the reflections from the reflector petals. In Figure 4.15(b), a white cloth covers the round face of the PMT to act as a screen. Light reflected from the petals is concentrated in a narrow ring approximately 0.5 cm wide at the joint between the PMT and the reflector petals.

Figure 4.15 shows the light distribution on the glass surface of the PMT under different angles of illumination. Above each photo is a cross-section schematic of the PMT/reflector assembly, rotated to 15°, 30°, 45°, and 60° as indicated in the figure. The photos are taken with the camera directly in front of the assembly and the PMT was rotated with respect to the beam of incident light to obtain the different incident angles.

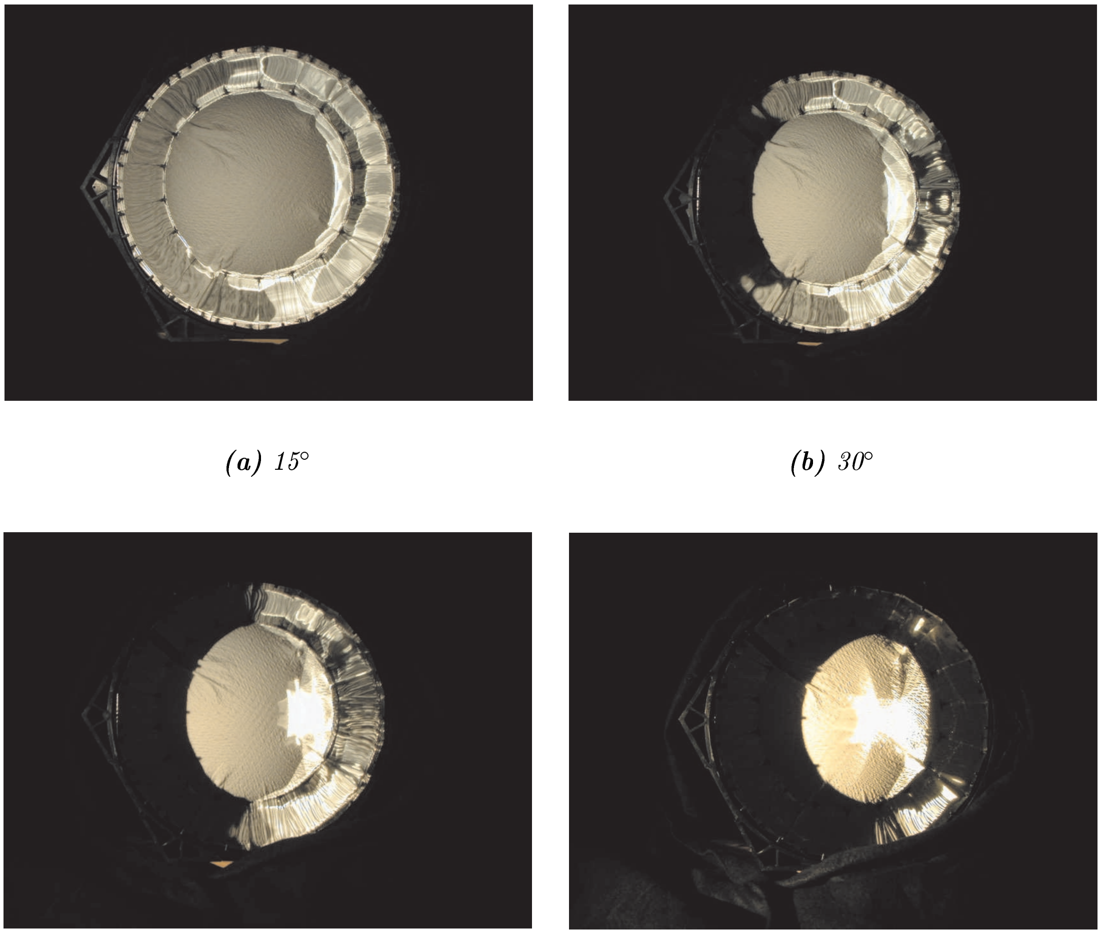

(a) *15°* ***(b)*** *30°*

(c) *45°* ***(d)*** *60°*

Figure 4.15: *The SNO PMT and its reflector with illumination at several incident angles.*

5 Optical Calibration: Hardware

The hardware associated with the optical calibration measurements includes the laser and laserball light source, and the fibre-optic umbilical cable which connects them. The manipulator system described in Section 3.8.1 is an important ancillary system as it allows the laserball to be deployed throughout the detector.

5.1 PMT Signals

The PMT's occasionally generate extraneous signals which occur at well-defined time offsets relative to the prompt light signals. These signals are referred to as pre-, late- and after-pulsing, depending on the time they occur relative to the prompt signal, and are illustrated in Figure 4.3.

Pre-pulsing occurs when the incident photon passes through the PMT envelope and photocathode and strikes the first dynode directly, and no photoelectron is produced at the cathode. The photoelectron transit time from cathode to first dynode is skipped, resulting in a signal about 15 ns earlier than the prompt light. The rate for such signals is less than 10^{-3} of the prompt rate at low light intensity levels such as the $\sim 5\%$ detector occupancy of the optical data runs. In this context, detector occupancy refers to the fraction of PMT channels registering a hit for a given event.

The channel occupancy is slightly different: it is the probability of a particular PMT channel firing during an event, and is an average over many events. For the nearly uniform PMT efficiencies and thresholds across the detector, the mean of the individual channel occupancies is approximately equivalent to the overall detector occupancy.

Photons escaping from the dynode stack are a likely cause of the late-pulsing. At a rate of about 1.5% of the prompt rate, these photons go back to the photocathode and start another photoelectron down the dynode chain. The peak about 15 ns after the prompt light arises from photons emitted back from the first dynode. The later peak, increasing in rate up to about 40 ns after the prompt light, comes from photons flying up from positions further down the dynode stack. These late-pulses are visible only because the original (prompt) pulse doesn't have enough gain to fire the discriminator. A lack of amplification down the dynode chain or mis-firing on the anode at the bottom can be the cause of the low gain.

After-pulsing of the PMT is thought to come from collisions of (photo-)electrons on residual gas molecules in the PMT's. The ionized gas molecules proceed to drift slowly up to the cathode and produce a delayed PMT signal. The timing distribution for this type of interaction is much more diffuse because of the uncertainty in the drift velocity of gas molecules of unknown type. Figure 4.3 does not show an identifiable after-pulse peak because the drift time scale for ionized gas molecules is of order μs, far longer than the 130 ns extent of the histogram in the figure.

The effects of these extraneous PMT signals on the optical data is rendered negligible because a prompt time window cut is imposed on the data. The prompt time window width used in the optical analysis is below 20 ns, with a nominal width of 8 ns (see Section 6.2.3). The small amount of light lost to pre- and late-pulsing is therefore included in the overall efficiency of the PMT channel for detecting prompt light from the laserball. By using occupancy ratios and eliminating the PMT channel efficiencies from the optical model (see Section 4.4.1), even the effect of the extraneous pulses on the efficiency is eliminated from the analysis of optical data. However, a correct and realistic Monte Carlo simulation of the SNO detector requires that the contributions of these extraneous signals to events be evaluated for the PMT's in the detector. At present (summer 2001), an average time distribution is used in the SNOMAN Monte Carlo. The distribution is from 200 PMT's tested at Queen's and is shown as Figure 6.13 in Ford [11].

5.2 Laser System

The laser system consists of a short pulse-length nitrogen laser (λ = 337.1 nm) which can be made to pump a series of laser dyes at longer wavelengths [10]. Figure 5.1 shows the layout of the laser with its four selectable dye cells. The light is attenuated and injected into a low-absorption, low-dispersion fibre-optic umbilical (see Section 5.5) which is terminated by a small diffusing sphere known as the laserball. The position of the fibre end in the laserball is adjusted to emit light as isotropically as possible into the SNO detector.

The available wavelengths are included with other key parameters of the laser system in Table 5.1, while the spectra of the dyes are shown in Figure 5.2. The dyes are selected to provide good coverage of the Cherenkov spectrum. The dye spectra come from the manufacturer's information sheets for a somewhat more powerful laser [73]. The wavelength spectrum for Kiton Red was not available from the manufacturer, although they do give a central value of 628 nm and a range of 603–647 nm.

The laser system will be used for two essential calibrations of SNO: the phototube calibration (PCA) and the optical calibration (OCA). The PCA is used to measure the timing offsets of all channels, and to correct for the timing slew of the threshold discriminators as a function of collected charge (discriminator "walk"). The timing offsets are measured corrections for small differences in PMT cable lengths and in the

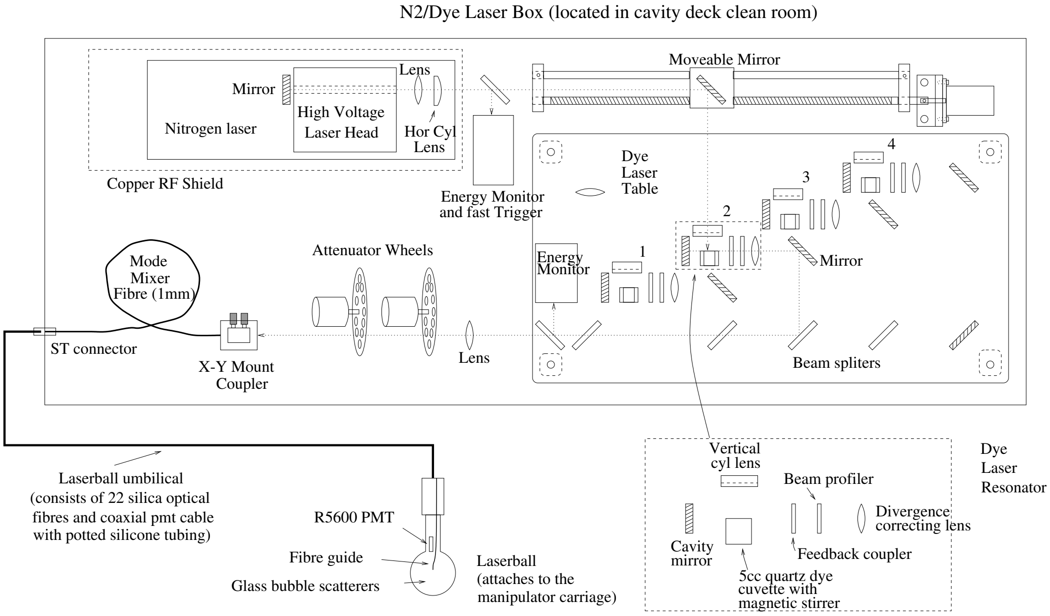

Figure 5.1: *N_2/dye laser system overview [11].*

Pulse width	$t_{\mathrm{N_2}} \sim 0.6$ ns $t_{\mathrm{dyes}} \sim 0.3$ to 0.5 ns
Pulse Energy	$\mathrm{E_{N_2}} \sim 100\ \mu$J/pulse or 1.7×10^{14} photons $\mathrm{E_{dyes}} \sim 10$ to $30\ \mu$J/pulse
Pulse Rate	1 to 45 Hz
337.1 nm	$\mathrm{N_2}$ laser fundamental, $\sigma_\lambda \sim 0.1$ nm
365 nm	PBD, $\sigma_\lambda \sim 8$ nm, second peak at 377 nm
386 nm	BBQ, $\sigma_\lambda \sim 8$ nm
406 nm	DPS, $\sigma_\lambda \sim 7$ nm
421 nm	Bis-MSB, $\sigma_\lambda \sim 6$ nm
500 nm	Coumarin 500, $\sigma_\lambda \sim 23$ nm
620 nm	Kiton Red, $\sigma_\lambda \sim 15$ nm

Table 5.1: *Nitrogen/dye laser characteristics for the Laser Photonics LN-203C with dyes procured from Exciton.*

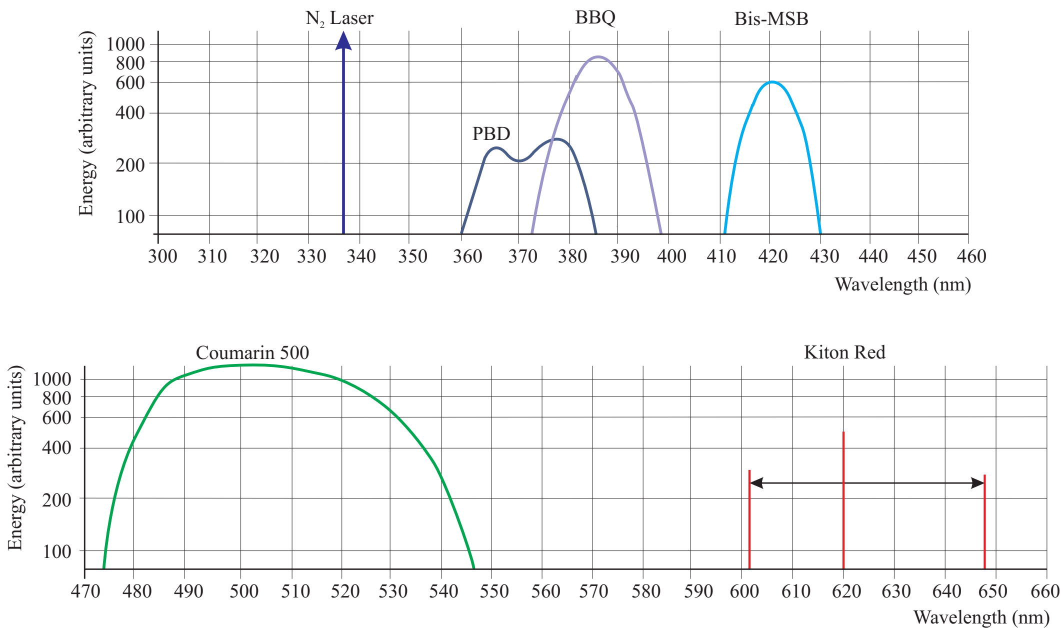

Figure 5.2: *Laser wavelengths for the N_2/dye laser.*

electronics channel layout and chip timing.

The PCA requires short pulse lengths and precise triggering of the laser system. The intrinisic PMT time spread is approximately 1.5 ns [52], so the combination of laser pulse width, dispersion in the fibre optic and in the laserball diffusing sphere must be kept close to this value. Table 5.2 shows the relevant contributions to timing dispersion in the laser system. The fibre optic dispersion numbers come from Ford [11, Table 4.3, p. 88] for the original SFS-100/110/240/310N fibres from Fiberguide Industries and the dispersion measurements were carried out by Sean White at Queen's University in 1995. The fibres have since been replaced and the new fibre optic umbilical was made with 45 m lengths of fibre rather than 35 m to accommodate the longer cable length needed to run the source at off-centre positions (guide tube runs; see Figures 6.1 and 6.2) in the underground laboratory.

The PCA is accomplished by varying the laser intensity with the laserball at the

Wavelength	Laser width	Fibre optic dispersion	Laserball dispersion	Net width
337.1 nm	0.6 ns	0.48 ± 0.05 ns	0.3 ns	0.77 ns
365 nm	0.3 – 0.5 ns	0.49 ± 0.08 ns	0.3 ns	0.57 – 0.70 ns

Table 5.2: *Laser system timing characteristics for 45 m of optic fibre.*

centre of the detector, while the OCA is done at low intensity with the laserball at many different positions. The PCA could be done at any wavelength, but was invariably done at 500 nm to avoid intensity losses in the acrylic vessel. An important requirement for the OCA is the availability of a variety of wavelengths over the range of the detectable Cherenkov light spectrum. The number of Cherenkov photons emitted increases dramatically at lower wavelengths – but this effect must be convolved with the transmission of the acrylic vessel, with a UV cutoff at about 300 nm, and the quantum efficieny of the phototubes, which has a broad distribution from 240 nm to 700 nm. The net convolved detected Cherenkov spectrum is peaked near 380 nm, with a mean and RMS width of 420 ± 70 nm, as shown in Figure 4.1.

Optical calibrations are done at very low intensity so that each hit phototube has seen essentially only a single photon. Counting single photons ensures that one is only sensitive to the quantum efficiency of the photocathode and the relative threshold for each tube for detecting single photoelectrons. An integrated charge measurement of the light intensity would suffer contamination from late light (from reflections off other detector elements), as well as being subject to the subtleties of the phototube gain calibration. Higher intensities are mainly used for detector diagnostics, such as to probe the PMT and electronics charge response. At high enough intensities, the threshold no longer has any effect on the data and the tube gain plays the dominant role in determining the signal level.

5.3 Laserball

The laserball was originally designed by R. Ford during his M.Sc. [9] and further developed during his Ph.D. [11]. The idea is to produce an essentially isotropically emitting source. The behaviour of such a source was then studied using an isotropic point source in the Monte Carlo.

The ball as constructed has several operational shortcomings which were not previously identified, particularly relating to the effects on the optics of the manipulator supporting hardware. Although the ball is intrinsically almost isotropic in emission, the mounting hardware located directly above it causes a significant region to be shadowed. As well, a significant fraction of the upward-going light was refracting through the acrylic parts of the mounting hardware. Acrylic was originally chosen for ease of machining and to allow full view of all connections during assembly. Modeling the effects of refraction proved intractable because of the high precision required on all dimensions of the mounting hardware. In consequence, a stainless steel light shield was built to prevent refracted light from reaching the PMT's. The laserball is shown in Figure 5.3, with and without its mask.

The redesigned laserball is expected to improve upon several points:

- all-metal construction of mounting hardware (eliminates light leakage and distortions in the light intensity distribution due to refraction in the acrylic mounting hardware of the original laserball);
- ease of assembly (elimination of the 2.5 cm sliding travel between the hollow acrylic cylinder and the acrylic laserball neck piece);
- larger canister reduces the bending required for the optical fibres and allows more room for other connections to be made.

The current laserball and the new, redesigned laserball are shown in Figures 5.4 and

5.5, respectively. The parts for the redesigned source were built in November 2000 and are awaiting final assembly. The new ball may include a pH-meter, or temperature or conductivity probes for sampling the heavy water as a function of position in the detector.

Laserballs are filled with silicone gel containing small hollow glass bubbles in suspension. Nearly 0.5 kg of RTV6196 silicone gel from GE Silicones is needed to fill the laserball, while the glass bubbles from 3M have an average diamter of 50 μm and are suspended in the gel by physical agitation of the laserball during the 15 min cure time. The scattering length of light inside the laserball is of order 1 cm. This length is a compromise between guaranteeing good isotropy in the far field, which requires a short scattering length, and reducing dispersion and absorptive losses, which demands a long scattering length. The far-field anisotropy of the laserball is adjusted by the positioning of the fibre tip at the centre of the ball; the required repeatability is ~ 1 mm, as shown in Ford [9].

A scattering length near 1 cm means that the surface of last scattering is not a thin shell near the edge of the ball, but rather a diffuse region in the centre of the ball. Simulations of the ball scattering have indicated that the effective ball diameter is closer to 2 cm, and that the angular distribution of light from a point on the surface strongly favours directly outward going light.

5.4 Calibration Source Manipulator

The manipulator provides reasonable positioning accuracy throughout 65% of two planes in the detector. The two planes are known as East-West and North-South by reference to the location of the two side ropes. When the laserball is attached to a given pair of side ropes, its orientation is fixed. The four possible orientations of the source are noted in the log when the optical data is taken, and is integral to the

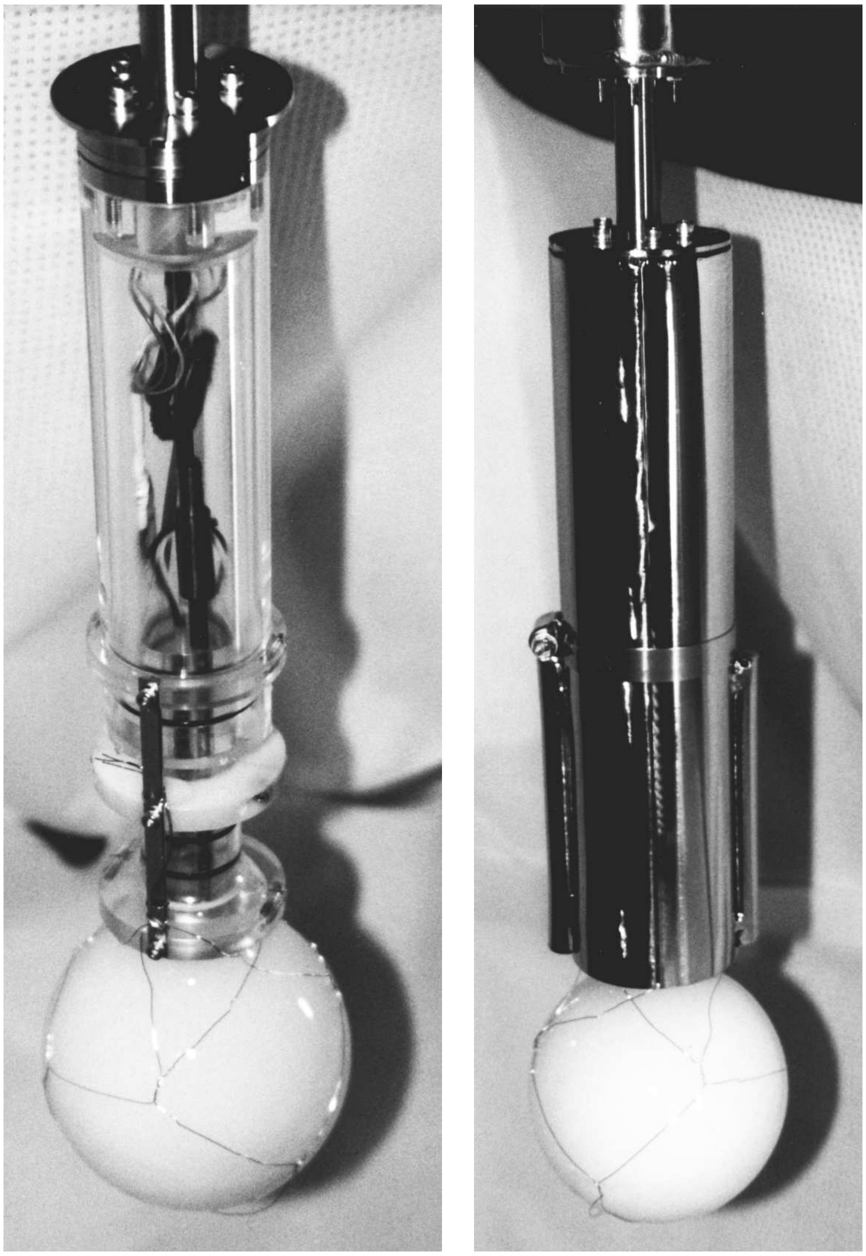

(a) *Without mask.* ***(b)*** *With mask.*

Figure 5.3: *Laserball with and without its stainless steel mask (February, 2000). The mask serves to contain light emitted from the ball and deviated by refraction or reflection from the acrylic mounting hardware.*

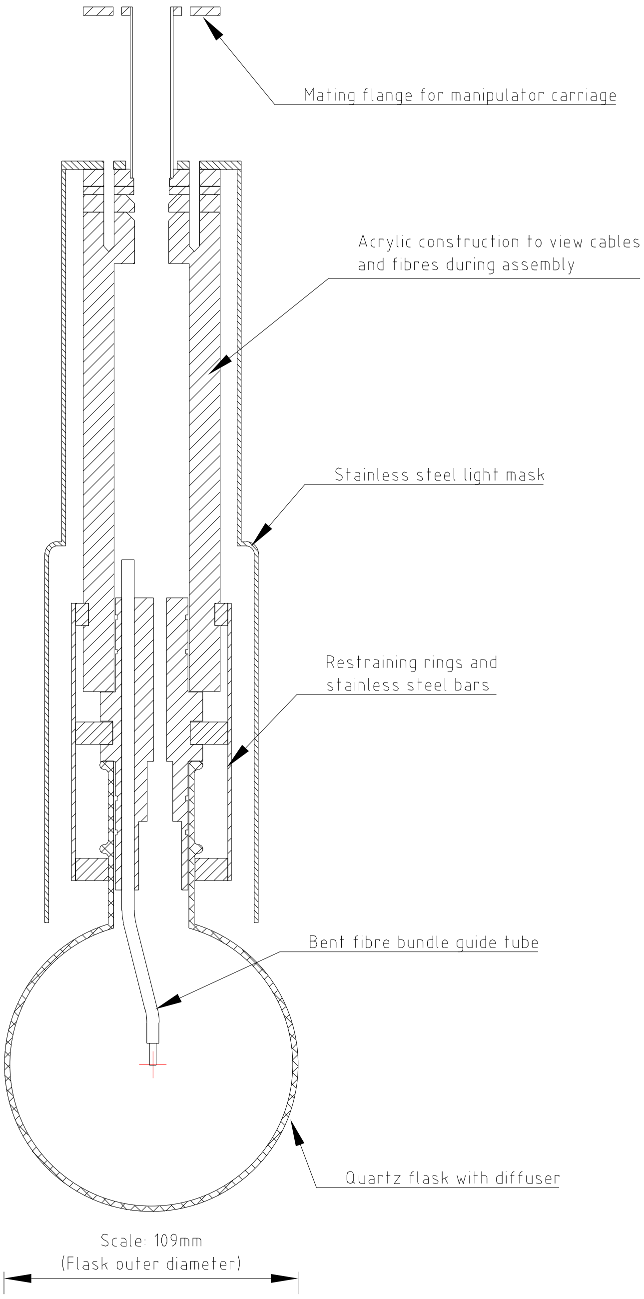

Figure 5.4: *Current laserball in cross-section.*

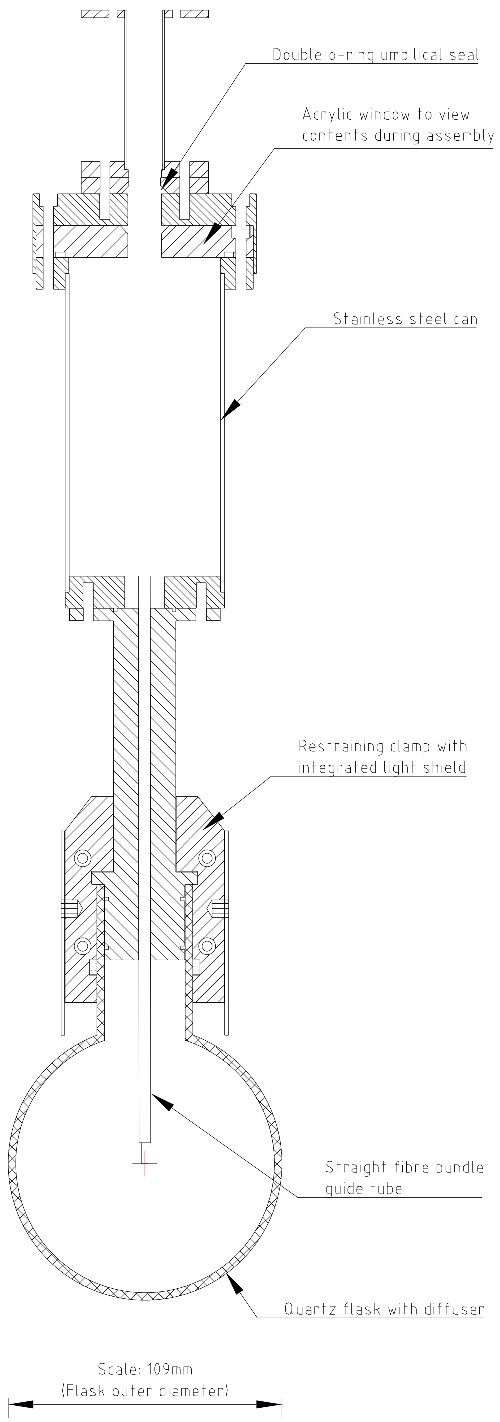

Figure 5.5: *Redesigned laserball in cross-section.*

determination of the laserball light distribution, as will be discussed in Section 7.1.3.

When the manipulator positions the source somewhere in the detector, the central rope is used to support most of the weight of the source, the tension on the two side ropes determine the source position, and the umbilical supplies the source with light and acts as a safety line in case the central rope should fail. The positioning accuracy is typically better than 2 cm, while the maximum error is less than 5 cm and occurs in high-tension regions [74]. The calibration of the side rope lengths determines the positioning uncertainty and reproducibility from run to run. To reduce the effect of hysteresis in the rope length under varying loads, the rope lengths are calibrated after subjecting the ropes to large tensions when no sources are attached.

To cross-check the position calculation from the rope lengths, the tensions in the ropes can be used in reference to a pre-calculated tension map of the manipulator plane. Gross differences ($\gtrsim$ 10 cm) are used to signal a problem to the operator.

Along with the ropes which control the location of the source, the manipulator system deploys an umbilical cable which connects the source to its supplies on the detector deck. A block-and-tackle mechanism is used to avoid twisting the umbilical connections. An 8" drive wheel lets out or takes in the umbilical through a pair of 4" pinch rollers. Redundant umbilical length information is obtained from a stepper motor and an optical encoder. Behind the drive wheel, the umbilical is taken up passively onto a set of twelve 8" pulleys by a pressure cylinder which maintains a constant force separating two groups of 6 pulleys. The size of the pulleys determines the total length of umbilical required to deploy sources to the bottom of the AV. To go over the pinch rollers repeatedly, the minimum bending radius for the umbilical cable must be small.

5.5 Umbilicals

In order to deploy calibration sources throughout the detector, radioactively clean, multi-purpose underwater cables are essential. The cables permit light, radioactive gases, power and trigger signals to be transferred to and from the source. The cables have to be flexible and small in diameter for ease of manipulation. Only 30 m of each source cable type is needed to reach all points of interest inside SNO. Such cables are not available for purchase, and could not be commissioned from external suppliers at reasonable cost. Cost estimates were up to \$60,000 (CDN) per cable type, the bulk of which is for the set-up costs for production of kilometer lengths of cable. The author conducted a 1.5 year research program which resulted in a method to produce flexible, clean and manipulable cables for all sources at a cost of approximately \$500 (CDN) per cable.

Design requirements for the calibration source umbilicals include:

- Radioactively clean: suitable for deployment in SNO for periods of up to several weeks at a time without introducing significant contamination,
- Water seal to protect cable components,
- Highly flexible with a small bending radius,
- Low specific gravity in D_2O and consistent linear density over its length makes the cable easier to manipulate.

Many types of umbilicals were designed and constructed. Principal among them are the fibre-optic umbilical for the laserball and the gas transport umbilical for the ^{16}N decay chamber. Table 5.3 provides a synopsis of the other sources for which umbilicals were made.

All the umbilicals follow the same basic pattern: a round central tube or wire with smaller wires wrapped around it in a helix. The helically-wrapped wires tend to

Laserball	Fibre bundle: 22 low-dispersion fibres (to ∼ 300 nm). Small coaxial cable for small PMT intensity measurement. Power and ground wires for small PMT.
^{16}N	Coaxial gas lines (teflon capillary in 6.35 mm OD polyflow tube). Small coaxial cable for PMT/Scintillator trigger. Power and ground wires for PMT.
PC-source Activated NaI	Fast coaxial cable (3 kV high voltage bias; signal return). Power and ground wires for in-source power supply.
pt-source	High-voltage cable (40 kV) for accelerator. Medium-voltage wire (3 kV) for focusing grid. Power and ground for heater coil in source.
^{8}Li	Special 5/8" OD (15.875 mm) umbilical. Coaxial gas lines (teflon capillary in 10 mm OD polyflow tube). Small coaxial cable for trigger. Power and ground wires.

Table 5.3: *Umbilicals for specific sources.*

centre the central member inside the silicone jacket. This is an important advantage for obtaining umbilical cables with a low allowable bending radius. Initial trials with straight wires in the umbilicals produced impressive looking failure patterns in the wires as they went over the 6" and 8" pulleys of the manipulator system. Helical wrapping of the smaller wires allows some local freedom of motion in the wires which is sufficient to relieve tensile and compressive forces experienced as the umbilical is driven over the pulleys.

A photo of a typical umbilical section is shown in Figure 5.6. This photo shows the small conductors helically wrapped around a central core and encased in the silicone tube. The two umbilicals shown have four stranded conductors and a small coaxial cable. The lower one also has a reinforcing steel cable, which is included as a safety line should the umbilical accidentally be required to support the full weight of a source. The breaking strength of the umbilicals is about 300 N, while with the steel cable the breaking strength rises to over 1000 N.

Figure 5.6: *Typical 1/2" OD (12.70 mm) umbilicals.*

The helically wrapped central member is drawn into a silicone tube 0.5" OD×100' long (=12.7 mm OD×30.5 m). The space between the silicone tube and the wires is then filled ("potted") by injecting a liquid silicone compound from one end of the cable. The liquid silicone cures over several days and forms a robust, impermeable bond between the silicone tubing jacket and the inner wires. Figure 5.7 shows a cross section of the laserball umbilical.

The silicone compound is injected to fill the volume between the wires around the central member and the outer silicone jacket. Although the compound bonds chemically to the silicone tube, it only encases the other components. During manipulation, small voids form between the solidified silicone compound and the wires, which leads to a build-up of static electricity through friction. This static charge is slow to dissipate, and generates large amounts of light (by SNO standards) during motion. Typically, hundreds of events per second with thousands of PMT hits are produced. When motion stops, the "umbilical light" disappears within a few seconds. This light is not an issue for triggered sources (such as the laserball), and untriggered source data is taken starting at least one minute after the source has reached its position.

Details of the umbilical fabrication can be found in Appendix A. Materials and

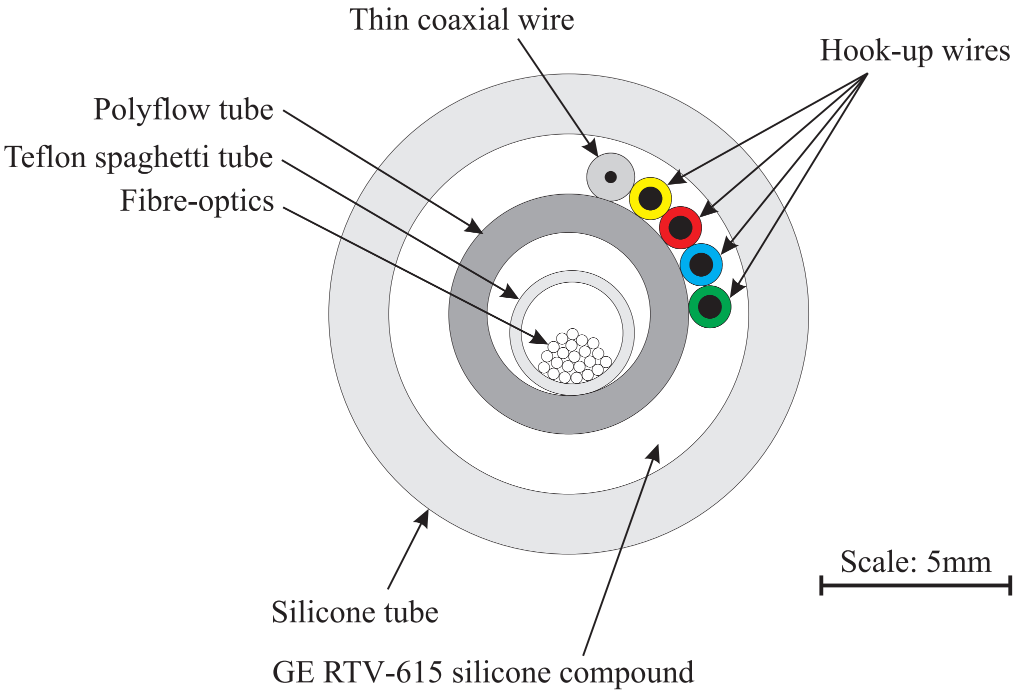

Figure 5.7: *Cross section of the laserball umbilical.*

component selection, and the wire winding and potting procedures are given for all umbilicals made for SNO calibration devices.

6 Optical Calibration: Data and Simulated Data

6.1 Data Sets

Four data sets of optical data have been taken after SNO was filled with water. The first two data sets were engineering runs taken prior to production data taking in SNO, and are not included in any further analysis. During production running, two data sets were taken and form the core input to the optical analysis and detector response calculations presented in this thesis.

The first two data sets were taken 28 June – 2 July, 1999 and 26–29 October, 1999 at a variety of positions and wavelengths. These data were taken without regard for masking the laserball support structures and include many systematics which are difficult to take into account. Figure 5.3 shows the unmasked laserball, as described in Ford [11]. Light from the ball can refract through the acrylic support structure causing the source to appear more as an extended source than as a point source. Although this effect is small in absolute terms, it is difficult to model because of the high accuracy with which all the dimensions would have to be known. The analytic solid angle calculation is based on the approximation of a point source of light centred on the laserball itself. The effect on the intensity is comparable to the effects of the media attenuations and PMT response which are to be measured. For all these reasons, these data will not be considered further.

The third data set was an extensive position scan in both the XZ- and YZ-planes taken from 7–11 February, 2000 at 365 nm and 500 nm. The February positions are shown in Figure 6.1. The small circles are the scaled size of the laserball (10.4 cm diameter), and the hatched areas are inaccessible to the manipulator. The laserball is shown with its connections to the manipulator hardware and suspended from the central and side ropes. The umbilical is not shown, but can be expected to closely mimic the positions of the ropes.

The February 2000 data set included rotated central runs where the laserball was lowered into the detector in each of the four orientations allowed by the two pairs of manipulator ropes (north/south and east/west). The orientation of the source was defined by the direction of a slot which allowed the manipulator side ropes to be connected and disconnected from the source. The slot pointed out of the plane of the side ropes. Half of the off-centre runs were taken with the slot pointing south, the other half with the slot pointing east. Two central runs were taken at 337 nm and 386 nm with the slot facing east.

As of February 2000, all laserball runs included the stainless steel mask shown in Figure 5.3. The laserball mask prevented light refracted by the acrylic mounting hardware from influencing the light distribution.

The last data set, taken over the period 5–19 September, 2000, made use of additional laser dyes to obtain data in the XZ-plane at 337 nm, 365 nm, 386 nm, 420 nm, 500 nm and 620 nm. The September positions are shown in Figure 6.2. Central runs with the laserball in each of the four orthogonal orientations were also taken at all wavelengths to ensure that the anisotropy of the ball would be sampled independently of detector properties. All of the off-centre data were taken with the

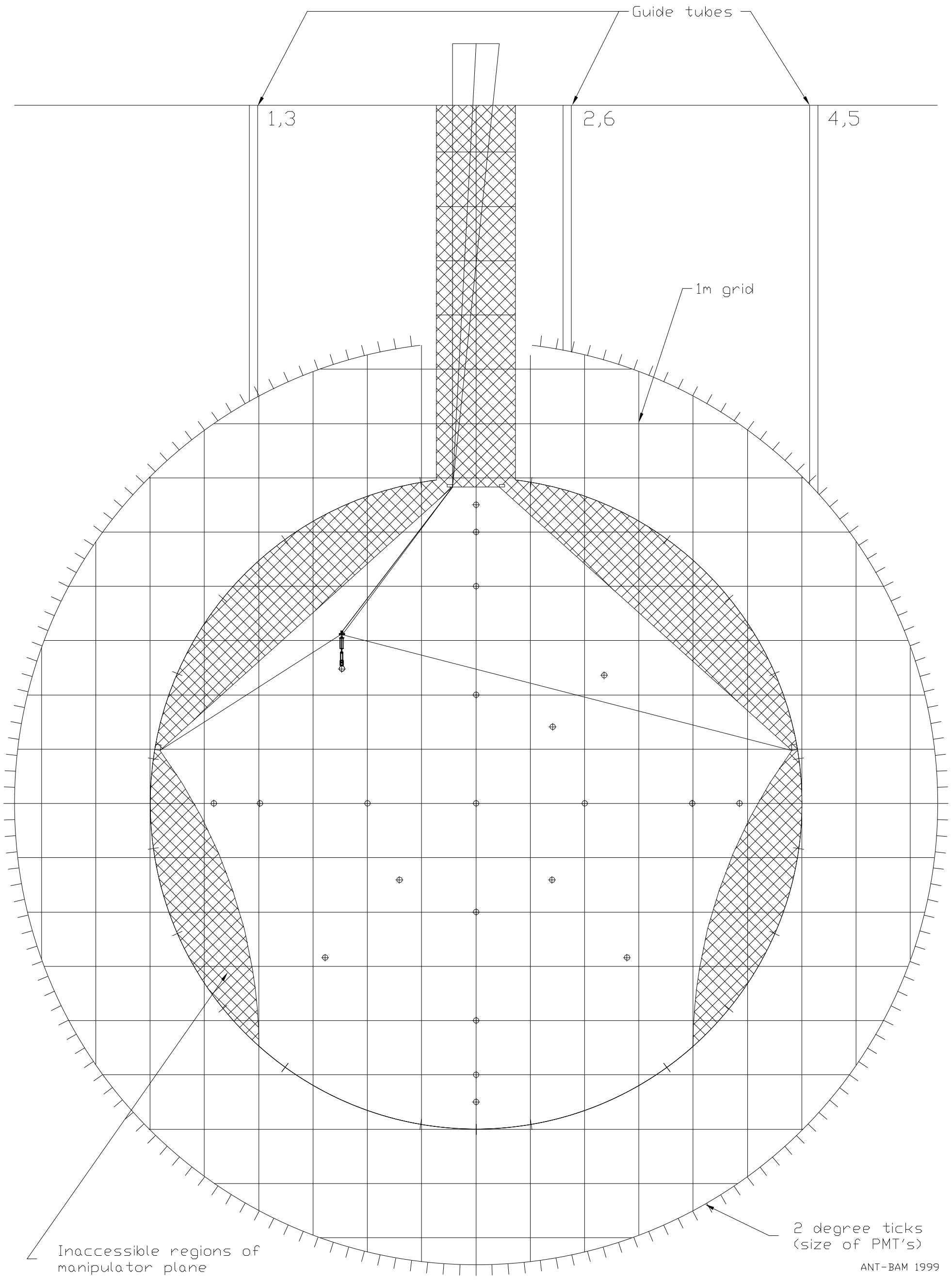

Figure 6.1: *February, 2000 optical data in either the XZ- or YZ-planes.*

rope slot at the top of the source pointing south.

The February data includes about 40 runs for each wavelength, 20 runs in each of the manipulator rope planes. The September data set only has about 20 runs per wavelength in a single plane. The total volume of data is similar for the two data sets, and accounts for a significant fraction ($\sim 1/3$) of the total SNO data stored on tape. Each of the data sets took slightly longer than two calendar weeks to acquire.

6.2 Optical Data Processing

The optical data taken in SNO passes through a series of steps before it can be processed and analyzed to extract optical constants:

1. Raw data in ZEBRA Data Acquisition/Analysis Bank (ZDAB) format ($\sim$ 1 Gb per run).
2. Root Calibration Histograms (RCH) format ($\sim$ 10 Mb per run).
3. Root Delta Time (RDT) format ($\sim$ 1 Mb per run).
4. Queen's Optical Calibration Tree (QOCATree) format ($\sim$ 160 Mb per data set).
5. Queen's Optical Fit (QOCAFit) format ($\sim$ 14 Mb per data set)

The data processing chain for the optical fit is shown as a flow chart in Figure 6.3, and is described in detail in this section.

6.2.1 Raw Laserball Data

The raw data are detector events for single laser pulses, and are typically taken with an external trigger which coincides with the laser firing. The laser can fire reliably in the range 2–45 Hz. Because the laser system has neutral density filters on

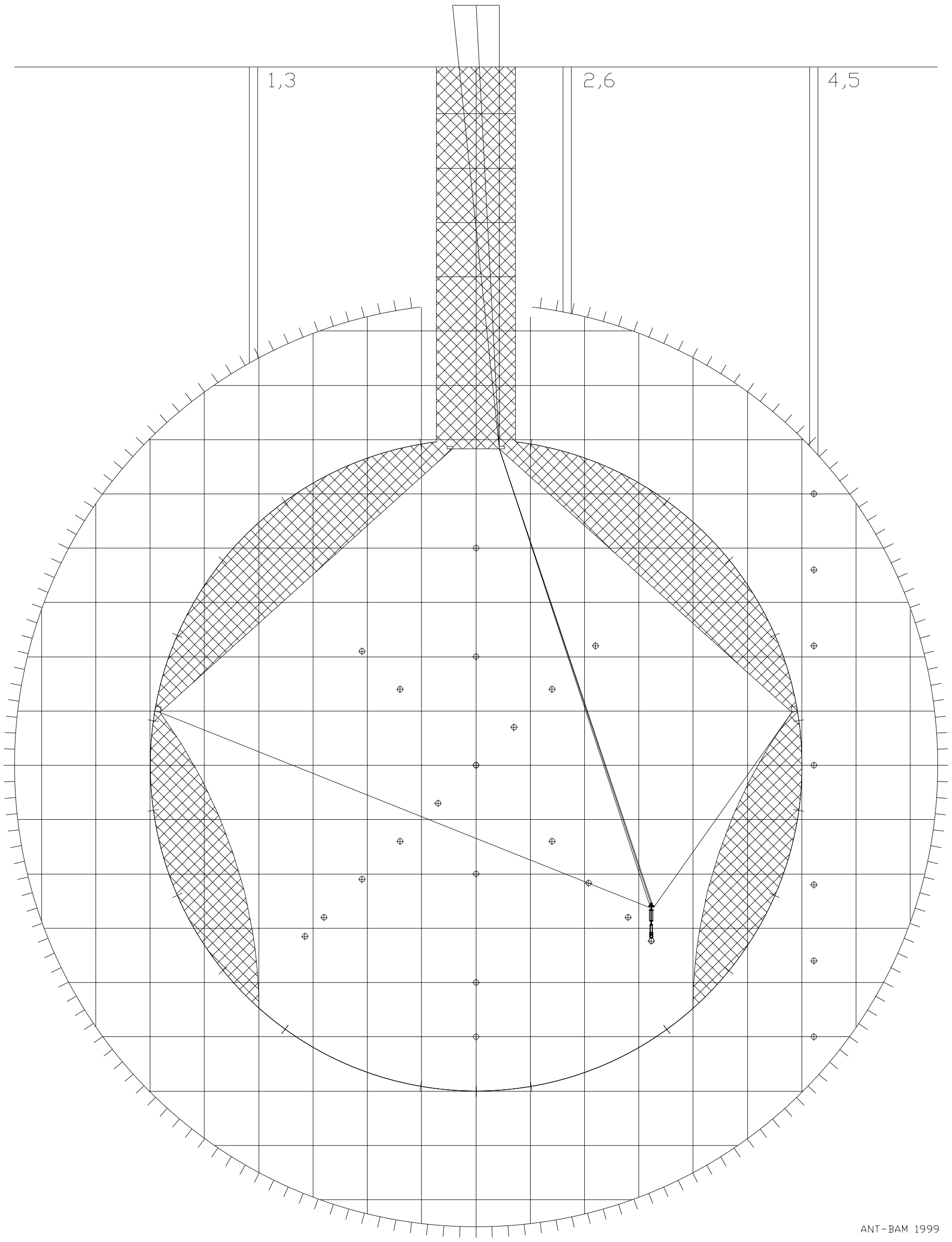

Figure 6.2: *September, 2000 optical data in the XZ-plane.*

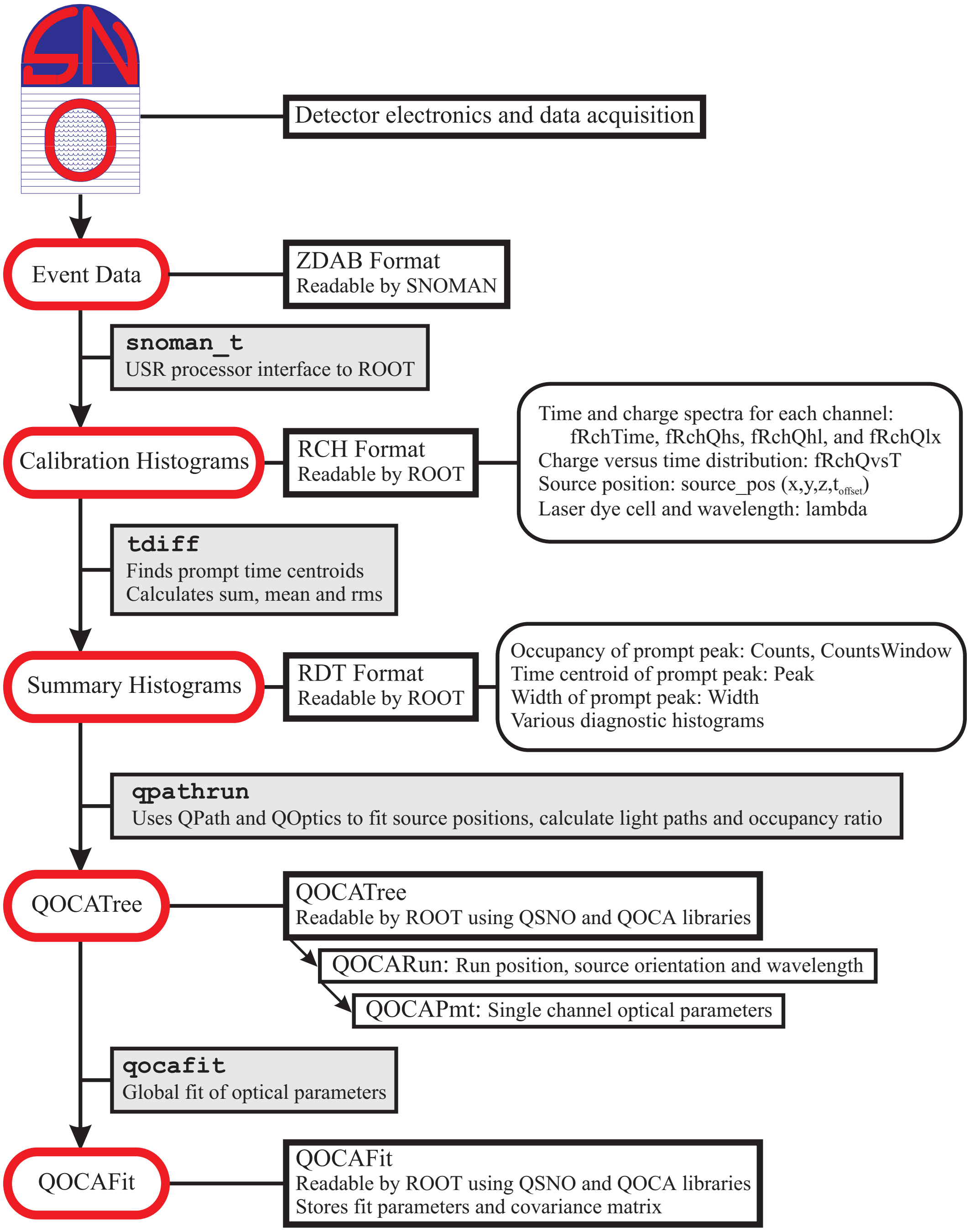

Figure 6.3: *Data processing and analysis chain for the optical fit procedure.*

discrete steps, the intensity seen by the detector must be carefully tuned to optimize the data throughput. Due to limitations in detector data throughput, the laser hit rate must be limited to less than approximately 30000 hits/second, or 670 N_{hit} events[1] at 45 Hz.

The raw occupancy is defined as the number of times a given PMT detects one or more photons over a series of events, and is a measure of the average intensity at the phototube. The prompt occupancy is the number of hits observed in a narrow time window which selects only those photons which came directly from the source (*i.e.* no reflections and little chance of scattering). To obtain a prompt phototube occupancy with an error of $1/\sqrt{N_{\mathrm{prompt}}} \sim 2\%$ one needs to obtain $N_{\mathrm{prompt}} \sim 2500$. For events inside the acrylic vessel, the prompt light accounts for about 80% of the total light, which forces the total number of counts per channel up to 3125. For a typical detector configuration with 9400 active channels, 500 hit channels/event, and 45 events/second, the run duration can be estimated by:

$$t_{\mathrm{run}} \sim \frac{3125}{\frac{500}{9400}45} \sim 22 \text{ minutes} \tag{6.1}$$

To reduce the magnitude of the MPE correction on the intensity, it is desirable to keep the raw PMT occupancy near 5%. Multiple photoelectrons affect the raw occupancy because a single PMT hit is registered regardless of the number of incident photons. The MPE-corrected occupancy is only slightly higher than the raw occupancy, and is a better estimate of the average light intensity at the PMT. At 5% occupancy, the probability of multiple hits in the same tube is only about 2.5% per pulse, resulting in an MPE-corrected occupancy of $-\ln(1-0.05) = 5.13\%$. The MPE correction is small for low occupancies, but is necessary because its effect on the observed light levels is comparable in magnitude to the other optical effects to be

[1] The quantity N_{hit} is defined as the number of hit PMT's per event. In the case of the laserball, each event is triggered by a pulse of light from the laser.

measured.

The fixed level discriminators used in the SNO electronics introduce another effect which, in principle, must be taken into account to obtain the intensity at each PMT. However, the ratio of MPE-corrected occupancies in a single PMT is insensitive to the discriminator setting (Jillings [75]). The optical calibration based on occupancy ratios can confidently proceed using the usual MPE correction without further consideration of discriminator threshold effects.

To gather data with a 2% statistical uncertainty on the number of counts in each channel, the minimum occupancy per pulse can be calculated from the maximum laser pulse rate and a reasonable run length of 30 minutes: 360 N_{hit}/pulse (or about 3.8% raw occupancy for 9400 channels). At the other extreme, the maximum N_{hit} is determined by the throughput of the DAQ. Experience has shown that an average of 600 N_{hit}/pulse at 45 Hz is stable. This allows a run with similar counting statistics per channel to be taken in only 18 minutes.

6.2.2 Root Calibration Histograms

The `rootify` script developed by M.G. Boulay was used to convert raw detector data in ZDAB format to standard ROOT files containing PMT channel data in the form of summary histograms. This script ran a version of SNOMAN with a modified user ("USR") processor to put the data in a suitable format and export it as a ROOT file.

Raw data were read in from disk or tape and the standard phototube timing calibrations (PCA) were applied. The main output of this step was a two-dimensional histogram of PMT channel number versus PMT time (10000 channels $\times$ 400 ns). This histogram was constructed by subtracting a constant time offset and an estimate of the time of flight between the source and the PMT:

$$t_{i,\mathrm{RCH}} = t_i - t_{0,\mathrm{RCH}} - t_{\mathrm{flight}} \tag{6.2}$$

$$= t_i - t_{0,\mathrm{RCH}} - d/v_{\mathrm{RCH}} \tag{6.3}$$

where $t_{i,\mathrm{RCH}}$ is the RCH-corrected time, t_i is the PCA-corrected time the i'th PMT fired the detector, $t_{0,\mathrm{RCH}}$ is the mean time offset required to place the prompt peak time centroid near 0 ns for all channels, d is the source-PMT distance and v_{RCH} is the group velocity of light used to construct the RCH histogram. In this way, all the channels have their prompt light peak within about 1 ns of $t = 0$ in the RCH histogram.

The PCA puts all the times at about 100 ns instead of 0 ns for prompt light from the centre. The PCA offset from 0 ns is variable with time: it is a function of the delay between the laser trigger pulse and the light detected from the laserball, and is subject to the whims of the maintainers of the PCA code. For these reasons, it was found desirable to include a method for subtracting all residual offsets to generate RCH histograms with the prompt peak centred near 0 ns.

6.2.3 Root Delta Time

The `tdiff` program analyzes the prompt time window for each channel stored in the RCH file. The output is a set of histograms which store the integrated counts, peak time and peak width for each channel.

The prompt peak finding algorithm is based on a simple windowed mean of the time spectrum for each channel. An 8 ns window centred at $t = 0$ ns is moved forward or backward in time until the window centre is within 0.05 ns of the mean of the time spectrum bins in the window. The channel time is taken to be the centre of the window, with time width equal to the RMS of the time spectrum within the window.

The number of counts is the integral over the time spectrum bins included in the window. Integrated counts for longer or shorter time windows are obtained using the same central time value as for the 8 ns window, changing only the extents of the sum over histogram bins. The prompt time window width ranges from 2 ns (comparable to the intrinsic timing spread of the PMT's) to 20 ns (to avoid contamination from late-pulsing and near-prompt reflections from detector elements such as the AV).

The integration window for a typical channel is shown in Figure 6.4. The prompt light peak is approximately gaussian in shape, and can be well characterized by the mean and width over a fixed interval. The prompt peak dominates the time spectrum for all source positions, although near the AV or in the H_2O the effects of nearly-prompt reflections distort the timing spectrum significantly. For this reason, only source positions in the central 500 cm radius of the detector are used for the optical analysis. In principle, the reflections could be taken into account and the optical analysis extended to all regions of the detector.

6.2.4 Queen's Optical Calibration Tree

For a given wavelength, multiple laserball positions can be used simultaneously in a fit for the optical model parameters.

To organize all the data from multiple laserball positions at a given wavelength, the data are stored in a hierarchical data tree called a QOCATree (for Queen's Optical Calibration Tree). A QOCATree is made up of QOCARun's, which contains run information such as position, wavelength and run number, as well as a list of QOCAPmt's. The QOCAPmt structure contains all the detailed output of the optical path calculations such as distances and flags indicating paths with suspect optics.

The QPath class is used to fill a QOCATree from RCH and RDT histograms. QPath has methods for reading the occupancy data from the RDT file, fitting the run positions, calculating the optical paths between the laserball and every PMT,

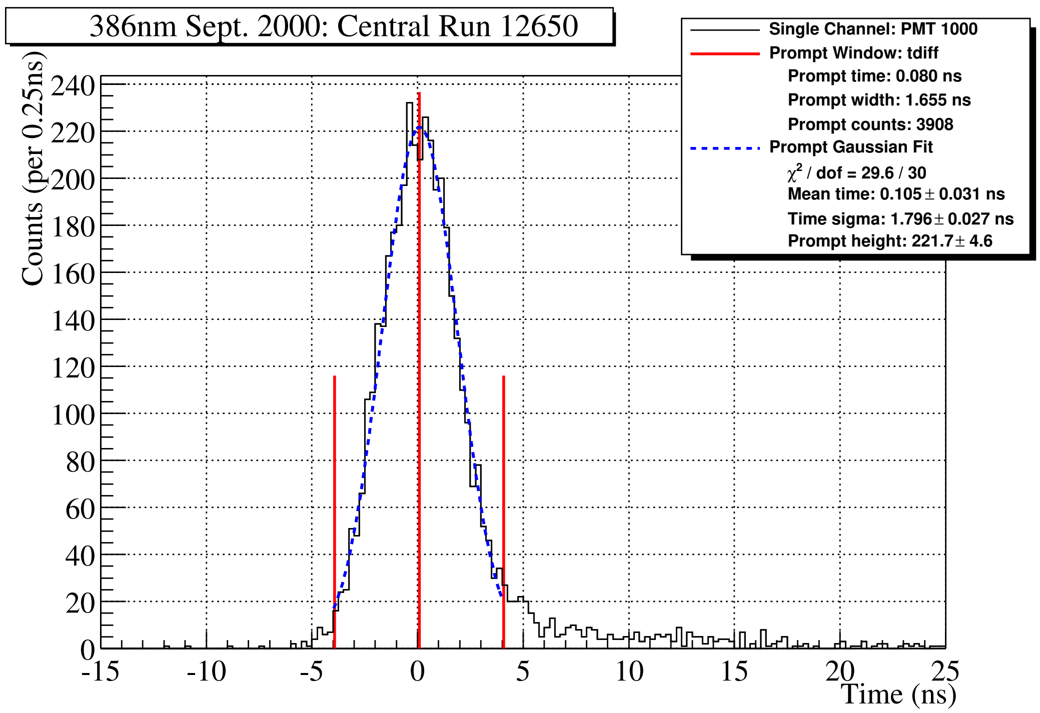

Figure 6.4: *Single channel time spectrum for 386nm data from September 2000.*

and computing the occupancy ratio between a run and an associated central run.

QPath relies on the QOptics class to provide all the path calculations. Light paths passing near AV support ropes, through the thicker, bevelled AV belly plates, near the D_2O recirculation pipes or through the AV neck ring are individually flagged to indicate suspect optical paths. QOptics also stores PMT normal vectors and a list of nearest neighbours. A nearest neighbour is defined to be any PMT within 6° as seen from the centre of the detector.

6.2.5 Queen's Optical Fit

The QOCAFit class was developed to allow extensive control over the fitting of optical parameters at a given wavelength using a QOCATree as input. At the heart of the QOCAFit class are the optical model for the occupancy ratio and the χ^2 minimization routines. The optical model allows the optical model parameters to be applied to the data points (QOCAPmt's) for specific run positions and orientations (QOCARun's). The χ^2 minimization in QOCAFit is based on the Numerical Recipes routine `mrqmin` [72]. This routine implements the Levenberg-Marquardt algorithm for finding a set of parameters which minimize the χ^2 for a non-linear model. Convergence is obtained when the change $\delta\chi^2 < 1$, and the output includes the best-fit parameter values and the covariance matrix. The parameters and the covariance matrix resulting from a QOCAFit can be stored and retrieved from the same ROOT files used to store all other types of ROOT objects.

6.3 Detector Coordinates

Several coordinate systems are important in analyzing optical data. Taking the global coordinate system to be tied to the rock cavity surrounding the detector, one can identify four other coordinate systems:

Acrylic Vessel coordinates The coordinates are referenced to the centre of the acrylic vessel. This system impacts the optics through the calculated path lengths in each medium.

PMT Support structure coordinates Particularly relevant to precise timing calibration, this coordinate system is centred on the PSUP. The PMT's are located at precisely known positions in this frame. Reconstruction of the laserball position relies on the accuracy of the PMT positions.

Manipulator coordinates The manipulator system uses ropes and pulleys to locate the laserball with good repeatability and accuracy. The rope lengths are used to calculate the position of the source. Hysteresis in the lengths, induced by alternating high and low rope tensions, degrades the accuracy over time. Periodically, the system is reset by applying very high tensions on the side ropes with no source attached. The procedure for doing this was continuously improved over the period 1998–2001, and has an impact on the comparison between central positions in the February and September 2000 optical data runs.

Phototube Calibration coordinates The PCA uses a central run at 500 nm to derive timing offsets for all channels. A small correction is applied for the source–PMT time of flight differences based on the manipulator coordinates for the central run. The PCA applies this correction assuming the manipulator and the PSUP coordinate systems were concentric.

In the ideal case, all of the coordinate systems would be perfectly concentric. In practice, shifts of up to several centimeters are plausible. Based on surveys of the detector taken before construction was completed, the relative orientation of the detector coordinate systems can reasonably be assumed to be the same.

6.3.1 Coordinate Checks

To date, two checks have been proposed to confirm the relative positions of the detector coordinate systems:

1. touching the bottom of the AV with the laserball, and
2. PSUP reflection timing.

In the first test, the laserball was lowered until the ball touched the bottom of the AV. The tension on the central rope decreased when contact was made, allowing a measurement to be made of the profile of the bottom of the AV. Agreement to better than 0.5 cm between the expected and measured AV bottom surface has been obtained by this method [74]. The manipulator and AV coordinate systems are therefore expected to be concentric to within this tolerance.

In the second test, a run with the laserball near the manipulator centre was analyzed to determine the time difference between the prompt and the PSUP 180°-reflected light. The geometry under consideration for this analysis is shown in Figure 6.5 for the Z-axis offset.

For prompt light, the light travels a distance d from the source to the PMT:

$$d^2 = z^2 + R^2 - 2zR\cos\theta \tag{6.4}$$

where z is the source offset from the true centre, $R = R_{\mathrm{PSUP}}$ is the average radius of the PSUP and $\theta = \theta_{\mathrm{PMT}}$ is the polar angular coordinate of the PMT (in the global frame). Making use of the knowledge that $z/R \lesssim 0.01 \ll 1$ for $z \lesssim 10\,\mathrm{cm}$ and $\cos\theta = Z_{\mathrm{PMT}}/R$ one can obtain an approximation for d which is linear in Z_{PMT}:

$$\begin{aligned} d &= R\sqrt{1 + \frac{z^2}{R^2} - \frac{2zZ_{\mathrm{PMT}}}{R^2}} && (6.5) \\ &\simeq R\left(1 - \frac{z}{R^2}Z_{\mathrm{PMT}}\right) && (6.6) \end{aligned}$$

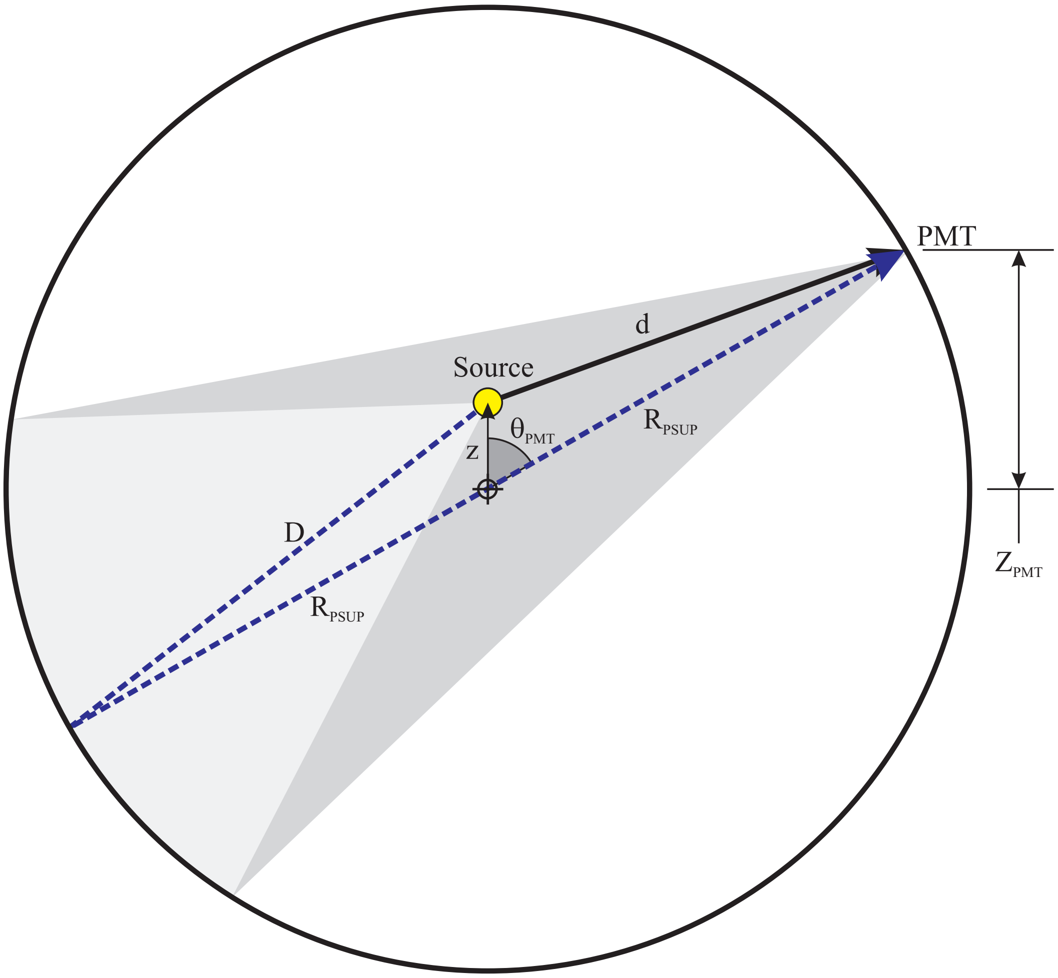

Figure 6.5: *Geometry for the PSUP reflection time difference calculation. See text for details.*

The reflected light came from a small fraction of the total solid angle on the opposite side of the detector from the PMT. Because this reflection was spread out in space, an approximate ray path is sufficiently accurate for calculating the reflected light travel time (see Figure 6.5). The distance D between the source and the reflection point in this model is given by:

$$D^2 = z^2 + R^2 + 2zR\cos\theta \tag{6.7}$$

The same approximation used above can be applied here to obtain:

$$D \simeq R\left(1 + \frac{z}{R^2} Z_{\mathrm{PMT}}\right) \tag{6.8}$$

The reflected light comes a time Δt_R after the prompt light:

$$\Delta t_R = t_{\mathrm{Reflection}} - t_{\mathrm{Prompt}} = \frac{D + 2R}{V_g} - \frac{d}{V_g} \tag{6.9}$$

where V_g is the group velocity of light (distance-weighted average of the group velocity for each medium between source and PMT). Substituting d and D one obtains a linear equation for the time difference:

$$\Delta t_R = \frac{2R}{V_g} + \frac{2z}{V_g R} Z_{\mathrm{PMT}} \tag{6.10}$$

The slope of the time difference Δt_{R} as a function of PMT coordinate Z_{PMT} was then used to determine the offset z of the source from the centre of the PSUP. This procedure was repeated for the offset along the other Cartesian axes.

The offset vectors obtained can be converted from time of flight differences to distances by using the knowledge of the dimensions of the PSUP. However, the average reflection point from the PSUP will be somewhat closer than $2R_{\mathrm{PSUP}}$. The offset vector obtained using this method is therefore a slight overestimate (see Monte Carlo results below).

To test the method, four Monte Carlo runs with positions 10 cm offset from the centre were processed. The PSUP reflection peak contained between 1% and 3% of the prompt light intensity, depending on the wavelength (see Figure 6.10). For a prompt intensity per channel of 3000 counts, the reflection peak contained 45–90 counts spread over nearly 10 ns. These hits are just sufficiently above background noise to determine the timing of the reflected light for each channel. The reflection time is assigned to be the maximum bin in the RCH histogram between 70 and 80 ns after the prompt peak (see Figure 4.3).

Four 386 nm Monte Carlo runs at the centre of the vessel were used to verify the reflection method for determining positioning at the centre of the PSUP. These runs are listed in Table 6.1 along with their nominal source positions: 10 cm off-centre in each coordinate separately and a run at (10,10,10) cm. The reconstructed position is close to the simulated position in all four runs, though there is a systematic shift of $\sim$ 1 cm outwards in each of the single-coordinate shifted runs (−2001, −2002, −2003). The distributions of prompt-reflected time differences as a function of PMT coordinate ($X_{\rm PMT}, Y_{\rm PMT}, Z_{\rm PMT}$) are shown for Monte Carlo Run −2004 in Figure 6.6. For $Z_{\rm PMT}$, points below −600 cm are not included in the fit because of the distortion in the timing spectrum produced by the AV neck. Because of symmetry, the AV neck distortion does not similarly affect the average reflection timing with respect to $X_{\rm PMT}$ or $Y_{\rm PMT}$.

The reflection timing differences as a function of PMT coordinate are shown for a typical data run in Figure 6.7. The reflection time versus cartesian PMT coordinate histograms are qualitatively similar to those obtained using Monte Carlo data, though the laserball offsets are much smaller.

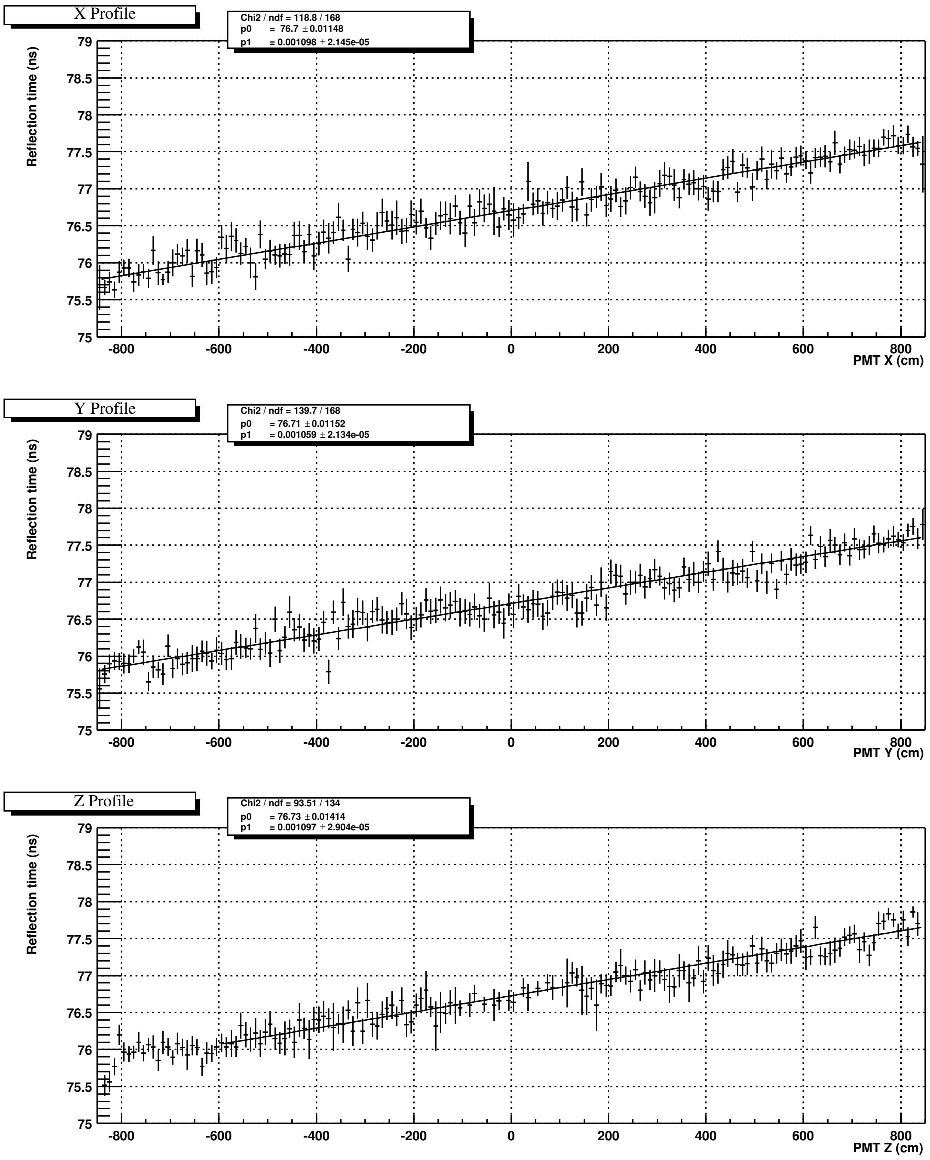

Figure 6.6: *Small central source offsets from reflection timing in Monte Carlo run* -2004 *at* $(10, 10, 10)$ *cm (see also Table 6.1).*

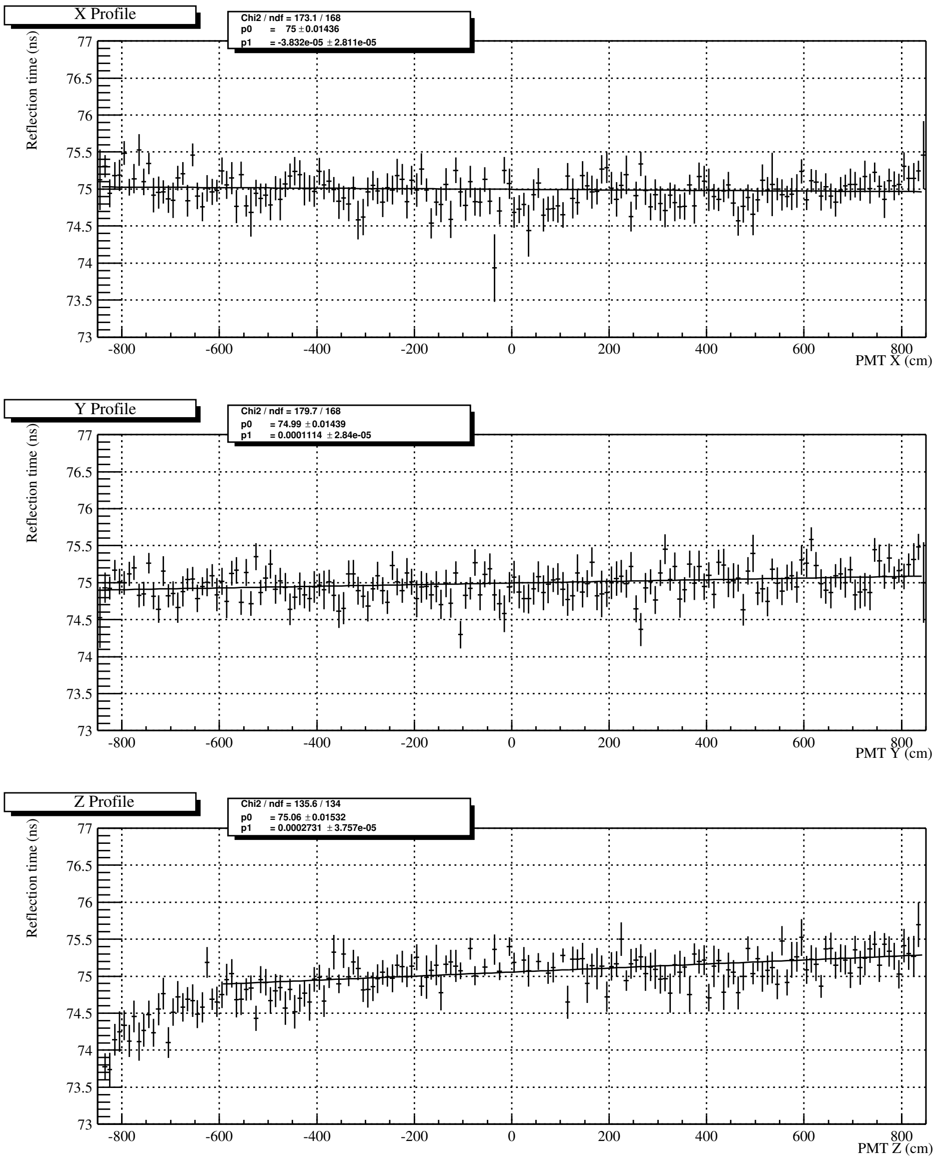

Figure 6.7: *Small central source offsets from reflection timing in data. September 2000, run 12646 at 500 nm.*

Run #	x	y	z	x_{fit}	y_{fit}	z_{fit}
−2001	10	0	0	10.7	−0.1	0.1
−2002	0	10	0	0.0	11.0	−0.1
−2003	0	0	10	−0.5	−0.1	11.6
−2004	10	10	10	10.2	9.8	10.1

Table 6.1: *Results of the Monte Carlo test of the reflection timing method. The error on each coordinate is* ± 0.4 *cm.*

Figures 6.8 and 6.9 show a summary of the reflection timing offsets as a function of run number for the February and September 2000 data sets. There were systematic offsets of order 2 cm in the February 2000 data in the Y and Z coordinates, though the manipulator was able to consistently locate the laserball at the same single-coordinate position to within $\sim$ 2 cm. In the February 2000 data, the average radial deviation of all central runs was 4.2 ± 2.2 cm.

The offsets in Y and Z were corrected in the September 2000 data by careful calibration of the manipulator system. A residual drift in Z position of 2 cm with increasing run number can probably be explained by a drift in the rope length calibrations with time. The manipulator was able to position the laserball within a radial shift of 3.4 ± 1.1 cm of the detector centre, similar to the precision obtained in February 2000.

6.4 Interface between the Optics and the Monte Carlo

The SNOMAN Monte Carlo program is useful in studying the performance of the optical fit procedure on an idealized data set: the laserball is replaced by an isotropic point source, the detector geometry is perfect, and all the PMT's have an identical response to light. Inside the AV, a point source is a reasonable substitute

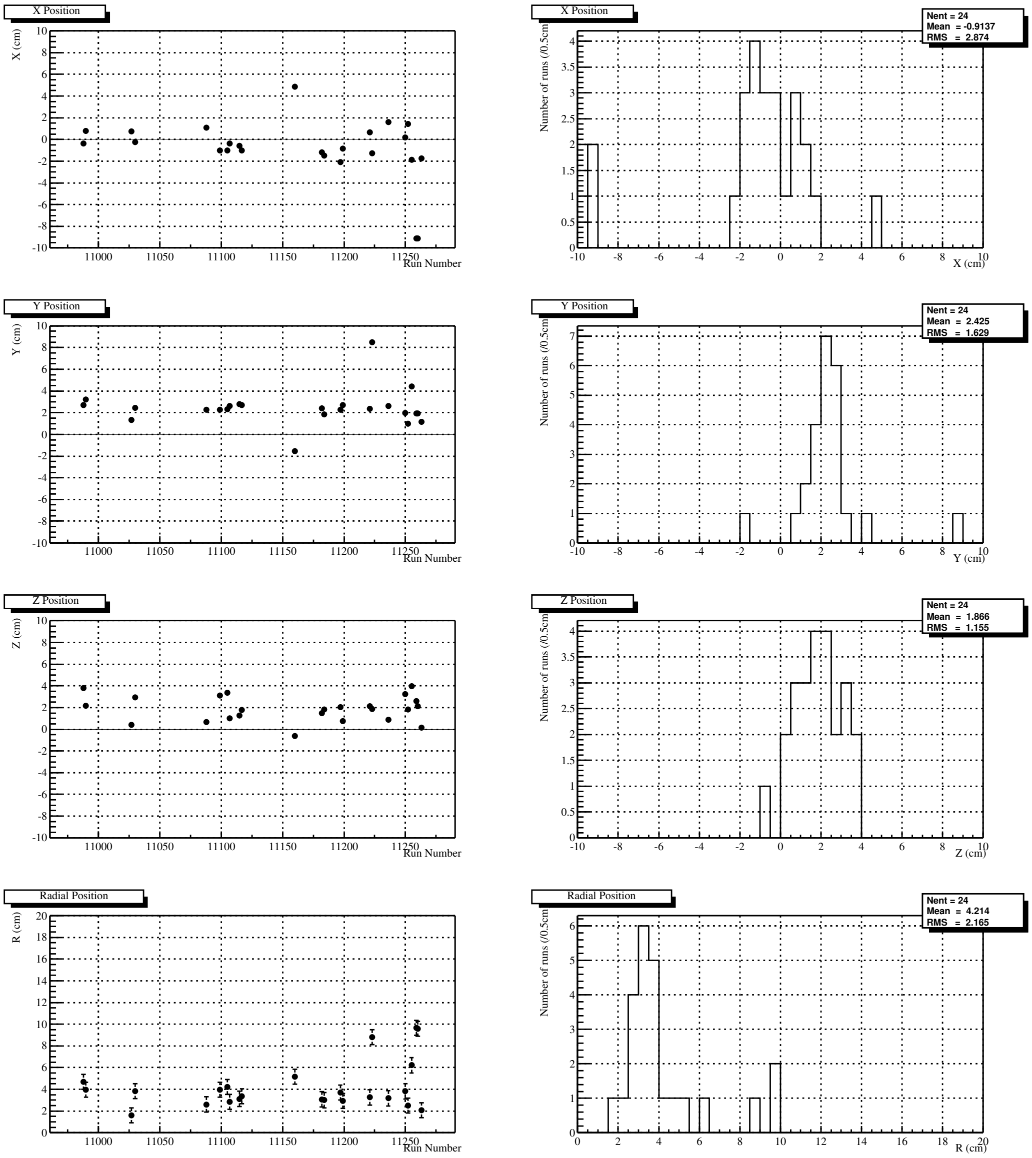

Figure 6.8: *Reflection timing for central runs in February 2000 data.*

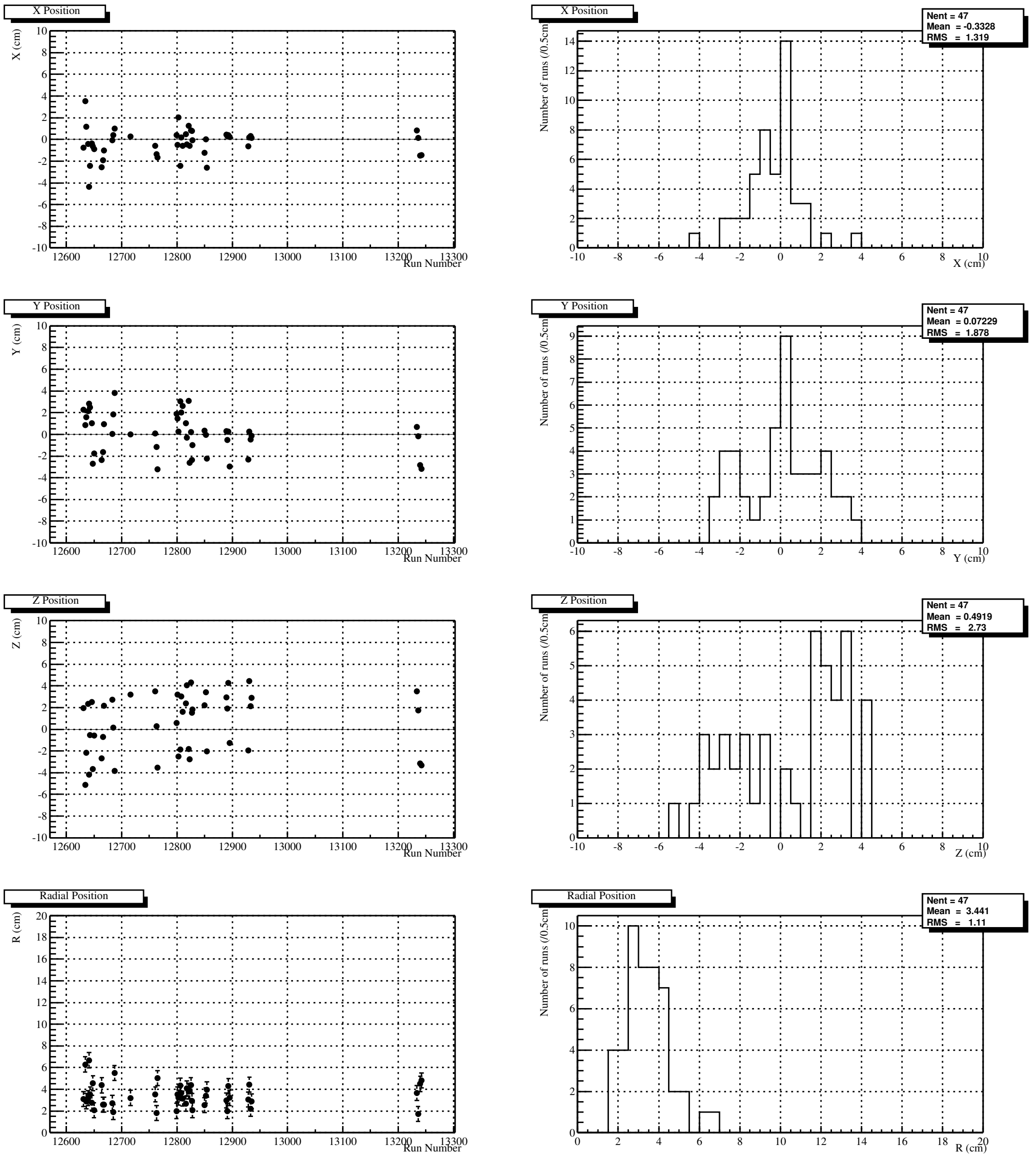

Figure 6.9: *Reflection timing for central runs in September 2000 data.*

for the laserball because source and PMT size effects have negligible impacts on the solid angles used to predict or correct the observed light intensities. The laserball is nearly isotropic in its emission (as will be discussed in Section 7.1.3), and the series of run positions and orientations of source permit the distribution to be accurately measured.

The time distribution of the simulated light source was in good agreement with laserball data. In the simulations, the point source emitted light over an interval $[-1.5 : 10.0]$ ns with a Gaussian distribution centred at 0 ns and of width $\sigma_\ell = 0.7$ ns. The time interval was chosen to avoid non-physical early light (occurring before the laser fired), and the width was chosen to be consistent with the laserball net width from Table 5.2. The PMT timing spread in the Monte Carlo was 1.4 ns, and resulted in an average PMT timing spectrum with a width $\sigma_{\mathrm{MC}} \sim 1.9$ ns, which was only slightly larger than the width observed for the laserball in the data: $\sigma_{\mathrm{data}} \sim 1.85$ ns.

In the Monte Carlo, the absorption and level of Rayleigh scattering must be separately specified. The QOCAFit routines produce measurements of the prompt attenuation, which is a combination of absorption and scattering. The issue of separating the attenuation into the two components will be further addressed in the discussion of results in Chapter 8.

6.4.1 Testing the Optical Calibration with Monte Carlo

A Monte Carlo simulation of an isotropic point source at 386 nm was used to estimate the errors and test the convergence of the global optical fit to synthetic data. The simulation used a detector model which was nearly identical to the optical model. The main differences were in the treatment of the acrylic neck boss ring, the tapered belly plates, the acrylic vessel suspension ropes, and the water pipes. For the global fit, light paths were simply discarded from the data sample if they went through or near these elements. While the Monte Carlo simulated the light trajectories in detail for many detector elements, it did not include the heavy water recirculation pipes. These pipes were made out of acrylic and were clearly identifiable in the detector data. Light paths passing near these pipes were cut in the global fit for both Monte Carlo and detector data sets even though for the analysis of the synthetic data this cut was not necessary.

The optical parameters and PMT model used in the optical Monte Carlo runs are listed in Table 6.2. Position scans were simulated at 386nm, for which the nominal simulated Rayleigh scattering coefficients for each medium are given in Table 6.3. The two PMT models available are a three-dimensional model of the PMT and reflector, and a grey disk model. The grey disk model replaces the front opening of the PMT's with a flat disk. This disk has a photon detection probability which depends on the incident angle of the light. The normal-incidence detection probabilities as a function of wavelength are the same for both the 3D and grey disk PMT models.

6.4.2 Timing Spectra

With the source at the centre of the detector, the light path to all PMT's was nearly the same. In this case, an average time spectrum can be used to elucidate features of the time spectrum. Of particular interest was the contribution of Rayleigh scattering to the prompt peak. If the geometric optics of the Monte Carlo detector model is to be considered adequate for tracking photons, the reflected light time spectrum of the laserball data must be reproduced in the simulations.

Figure 6.10 shows the timing spectra for all data wavelengths. The increased Rayleigh scattering at the shorter wavelengths fills in the valleys between 10 and 30 ns after the prompt peak. Separation by light path history is shown in Figure 6.11. Direct light is light that is neither Rayleigh scattered nor reflected.

The Rayleigh scattered light contributed about 2% of the intensity in the prompt peak at 386 nm. Hits from Rayleigh scattering occurred starting somewhat after

Run series	PMT Model	Optical parameters
200	Grey disk (March 2000)	$\alpha_h = \alpha_d = 1.25 \times 10^{-4}$ cm^{-1} $\alpha_a = 1.25 \times 10^{-2}$ cm^{-1} Nominal Rayleigh scattering.
300	Grey disk (March 2000)	$\alpha_h = \alpha_d = 1.25 \times 10^{-4}$ cm^{-1} $\alpha_a = 1.25 \times 10^{-2}$ cm^{-1} Rayleigh scattering turned off.
400	3D PMT	$\alpha_h = \alpha_d = 1.25 \times 10^{-4}$ cm^{-1} $\alpha_a = 1.25 \times 10^{-2}$ cm^{-1} Rayleigh scattering turned off.
500	3D PMT	$\alpha_h = \alpha_d = 1.25 \times 10^{-4}$ cm^{-1} $\alpha_a = 1.25 \times 10^{-2}$ cm^{-1} Nominal Rayleigh scattering.
600	3D PMT	$\alpha_h = \alpha_d = 4 \times 10^{-5}$ cm^{-1} $\alpha_a = 1 \times 10^{-2}$ cm^{-1} Nominal Rayleigh scattering.
700	3D PMT	$\alpha_h = \alpha_d = 4 \times 10^{-5}$ cm^{-1} $\alpha_a = 1 \times 10^{-2}$ cm^{-1} Four times Rayleigh scattering ($\alpha'_{\mathrm{Ray}} = 4\alpha_{\mathrm{Ray}}$).
800	3D PMT	No absorption ($\alpha_h = \alpha_d = \alpha_a = 1 \times 10^{-10}$ cm^{-1}). Two times Rayleigh scattering ($\alpha''_{\mathrm{Ray}} = 2\alpha_{\mathrm{Ray}}$).

Table 6.2: *Description of optical Monte Carlo run series at 386 nm.*

	α_{Ray} (10^{-5} cm^{-1})	$1/\alpha_{\mathrm{Ray}}$ (m)
D_2O	7.26	137.7
H_2O	7.43	134.6
Acrylic	17.4	57.6

Table 6.3: *Rayleigh scattering coefficients in SNOMAN at 386 nm.*

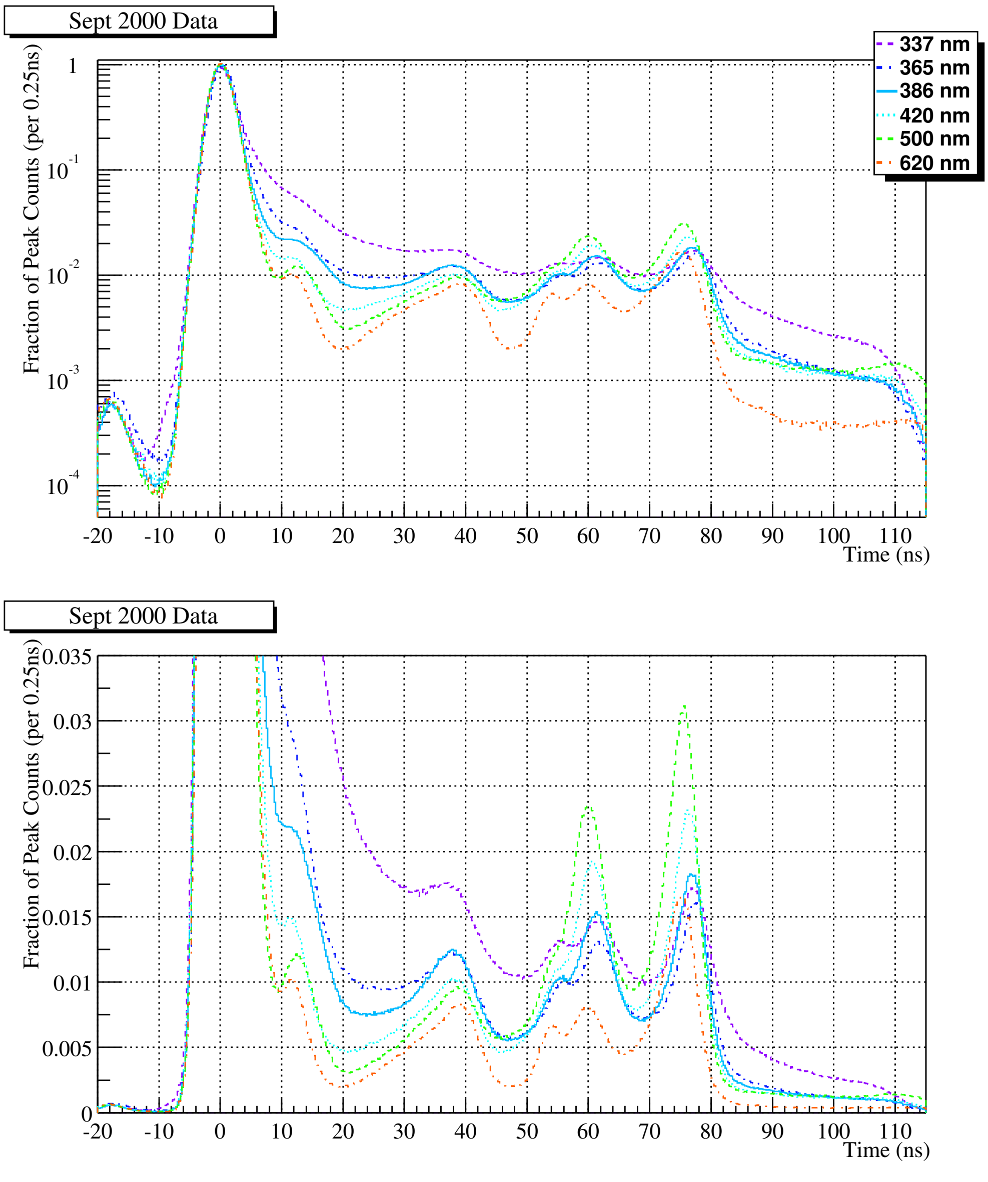

Figure 6.10: *Timing spectrum for central runs from September 2000 data, all wavelengths. The prompt peak of the 386 nm data is scaled to 1.0, and the time integral over the interval* $[-4:4]$ *ns is used to scale the other wavelengths.*

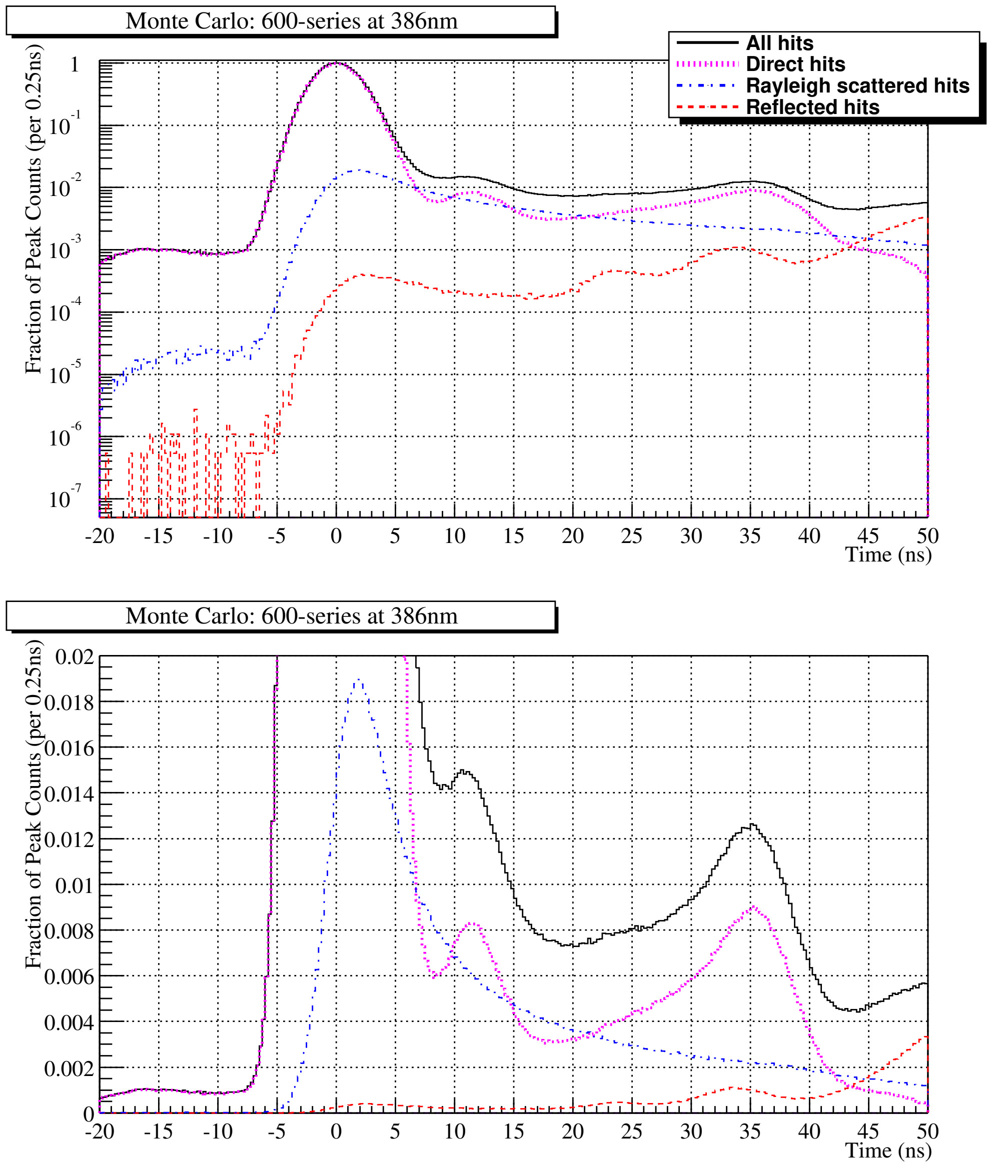

Figure 6.11: *Timing spectrum for the central 600-series Monte Carlo run. All curves are scaled so the prompt peak height is scaled to 1.0.*

the prompt time because the scattering increased their path length. The intensity contribution from Rayleigh scattering dropped rapidly with increasing time.

The structures due to reflected light in the first 50 ns came from double reflections inside the AV (just after 0 ns), double reflections in the H_2O layer (source–PSUP–AV–PMT, starting at 22 ns) and 35° reflections from the PMT reflector (source–PMT(35°)–AV–PMT, starting at 31 ns). These 35° reflections traversed the AV obliquely and produced an intensity peak near 60 ns (as seen in Figure 6.10).

Pre- and late-pulsing in the PMT's was simulated by sampling from a timing spectrum obtained during tube tests in a dark room at Queen's university. In this dark room, the magnetic field of the earth was compensated in both the horizontal and vertical directions by an oriented pair of large Helmholtz coils. The data obtained in the detector did not agree with the Monte Carlo for the late-pulsing peaks: both the early (near 12 ns) and late (near 35-40 ns) pulses were significantly later in the data. This discrepancy is likely caused by an electronic effect in the collection of photoelectrons by the PMT's in the detector. An unmodeled optical effect is unlikely because the detector geometry is well known and carefully modeled in detail inside SNOMAN.

6.4.3 Position Reconstruction

The light travel time depends on the group velocities of the media along the path from source to PMT. In general event reconstruction algorithms for SNO, an average group velocity has to be assumed because the light is distributed in wavelength and the photon statistics are relatively low ($\lesssim$ 200 hits). The situation is considerably different for optical data: the laserball is monochromatic, and each PMT contributes precise timing information based on the centroid of the prompt light peak. The group velocities along the optical path from source to PMT are calculated in the optical model, and are then used in a more elaborate fitting procedure to define the source location. For the 600-series Monte Carlo simulations, where the source positions are known, Figure 6.12 shows the position fit discrepancies using a fixed group velocity (average v_g at the centre), and a group velocity which is recalculated for each source-PMT path.

For Monte Carlo simulations, the laserball was simulated as a point source of light. In reality, the extent of the laserball source was determined by the ball's diameter (10.4 cm) and internal scattering length ($\sim$ 1 cm). The effective size of the source was approximately 4 cm in diameter, as derived from ray-tracing simulations of the light scattering inside the ball. It is reasonable to assume that the timing-centre of the laserball is located within the central region. The light emission centroid can likely be reconstructed with an accuracy comparable to the extent of the central scattering region. Therefore, a position uncertainty of 2 cm was assigned for the reconstruction fit of the laserball position.

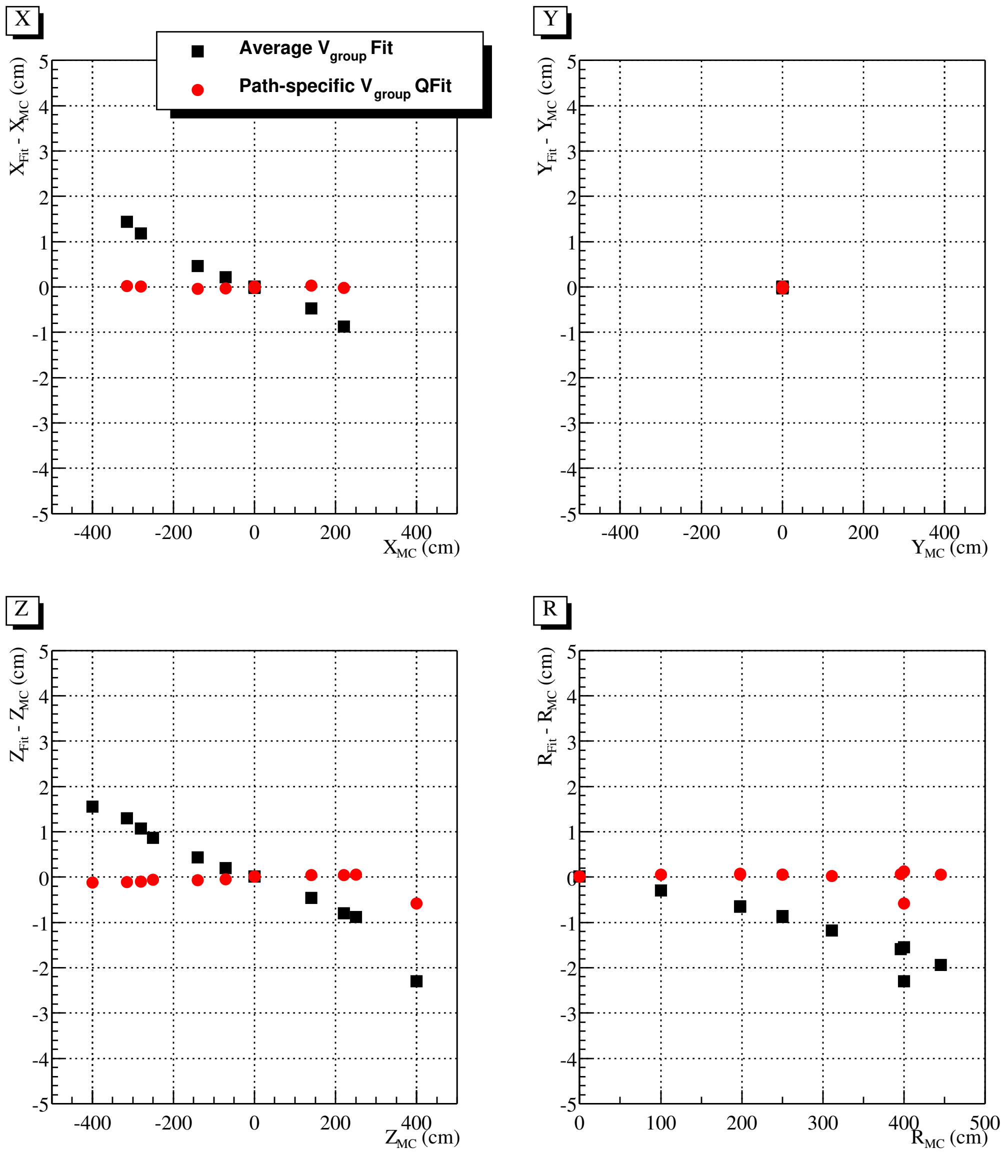

Figure 6.12: *Position fit discrepancies for the 600-series Monte Carlo.*

7 Optical Calibration: Analysis

The analysis of optical data taken with the laserball during production running is used to derive the physical optical model parameters needed to calculate the detector's response to Cherenkov light. Synthetic data sets produced by Monte Carlo simulations where the optical properties are known test the convergence of the fitting procedure and provide guidance in separating the contributions of scattering and absorption to the measured prompt attenuation.

7.1 Results from the Optical Calibration

The primary results of the optical fitting procedure are the determination of:

- heavy water attenuation,
- light water attenuation,
- PMT/reflector assembly angular response.

The separate contributions of absorption and scattering to the prompt attenuation is found from Monte Carlo studies of input and output parameters. In addition to the primary detector optical characteristics, the fit produces a set of parameters describing the laserball light distribution.

λ (nm)	α_d	$\Delta\alpha_d$ (Stat)		α_h	$\Delta\alpha_h$ (Stat)		χ^2/dof	
September data								
337	7.60	0.13	1.7%	56.1	4.9	8.7%	1.09650	147575 / 134587
372	10.17	0.11	1.1%	16.6	4.1	24.7%	1.05335	141629 / 134456
386	9.53	0.11	1.2%	16.8	3.9	22.9%	1.03096	141963 / 137700
420	7.29	0.10	1.3%	20.3	3.5	17.3%	1.09426	161783 / 147847
506	4.91	0.10	2.1%	50.6	3.4	6.8%	0.96757	127520 / 131794
620	4.44	0.10	2.2%	259.9	3.8	1.5%	1.02102	137539 / 134707
February data								
372	5.79	0.06	1.1%	11.5	2.7	23.7%	1.06571	288824 / 271015
506	1.82	0.06	3.2%	56.3	2.5	4.5%	1.02304	308367 / 301422

Table 7.1: *Attenuation results for H_2O and D_2O from the optical fit, in units of 10^{-5} cm^{-1}. The statistical uncertainties are derived from the diagonal elements of the parameter covariance matrix.*

The attenuation coefficients extracted from the fit for D_2O ($\alpha_d(\lambda)$ and for H_2O ($\alpha_h(\lambda)$) are given in Table 7.1, where only statistical errors are reported. These errors are calculated from the diagonal elements of the fit covariance matrix. The attenuation measurements are also shown in Figures 8.1 and 8.2, along with a comparison to the literature. The small increase in attenuation between February and September 2000 is further discussed in Section 8.1.3.

The values of α_a as a function of wavelength were taken from prior measurements of light transmission through the acrylic panels that make up the AV, and the value of α_a was fixed in the optical fit. The measurements of $\alpha_a(\lambda)$ shown in Figure 7.1 and listed in Table 7.1 are averages over all SNO panels and the error bars correspond to the RMS deviation of the individual panel values. The data for SNO production acrylic panels was obtained from Earle [65] for the wavelength range 300–450 nm, while the measurement method is described by Zwinkels et al. [66].

To interpolate between the measured wavelengths, a smooth function was fit to the data:

$$\alpha_a(\lambda) \approx \begin{cases} \alpha_{a0} + m_1\lambda & : \quad \lambda < 310\,\mathrm{nm} \\ \alpha_{a1} + m_2\lambda + \exp(a + b\lambda) & : \quad 310 < \lambda < 450\,\mathrm{nm} \\ \alpha_{a2} & : \quad \lambda > 450\,\mathrm{nm} \end{cases} \tag{7.1}$$

where α_{a0}, α_{a1}, m_1, m_2, a and b are parameters of the model and are fit to the data, while $\alpha_{a2} = 7.09 \times 10^{-3}\,\mathrm{cm}^{-1}$ is fixed. Discontinuities of the function at the two wavelength boundaries (310 nm and 450 nm) are smoothed by averaging the values from each functional form near the boundaries. This function reproduces the data well over the measured wavelength range. The absorption coefficient is assumed to be constant beyond 450 nm, which is reasonable for the acrylic path lengths in the optical model (~5.5–10 cm).

7.1.1 PMT Response

The PMT response obtained from QOCAFit is very robust to systematic changes in the optical model inputs. To illustrate the sensitivity to different PMT responses, Figure 7.2 gives the QOCAFit results for the grey disk model simulation (200- and 300-series optical Monte Carlo) and for the 3D PMT simulation (600-series). In this plot, the points show the QOCAFit results and the lines show the expected response curves for the two different PMT response models in SNOMAN. The differences between the QOCAFit results and the expected values are less than 0.5% over the entire 35° range of incidence angles.

Changing the prompt time window affects the PMT response determined by the QOCAFit, as shown in Figure 7.3 for the 386 nm September 2000 data and in Figure 7.4 for the 600-series Monte Carlo. The effect of various prompt time window widths on the PMT response is less than 0.2% for time window half-widths near the

λ (nm)	α_a(Earle) ($10^{-3}\,\mathrm{cm}^{-1}$)				α_a(Fit) ($10^{-3}\,\mathrm{cm}^{-1}$)
300	435.	$\pm$	38.	(9%)	395.
310	143.	$\pm$	27.	(19%)	156.
320	100.	$\pm$	20.	(20%)	104.
330	71.4	$\pm$	15.3	(21%)	70.6
337					56.4
340	50.0	$\pm$	7.5	(15%)	48.3
350	37.0	$\pm$	5.5	(15%)	33.8
360	26.3	$\pm$	4.2	(16%)	24.2
365					23.0
380	13.3	$\pm$	1.8	(14%)	13.9
386					12.2
400	8.85	$\pm$	1.02	(12%)	9.53
420					7.70
450	7.09	$\pm$	0.86	(12%)	7.14
500					7.09
620					7.09

Table 7.2: *Attenuation measurements for acrylic from Earle [65]. The measurement values are quoted as the mean and RMS width averaged over all acrylic panels. The fit function values (α_a(Fit)) are obtained from a smoothed function (Equation 7.1), and are in good agreement with the measurements.*

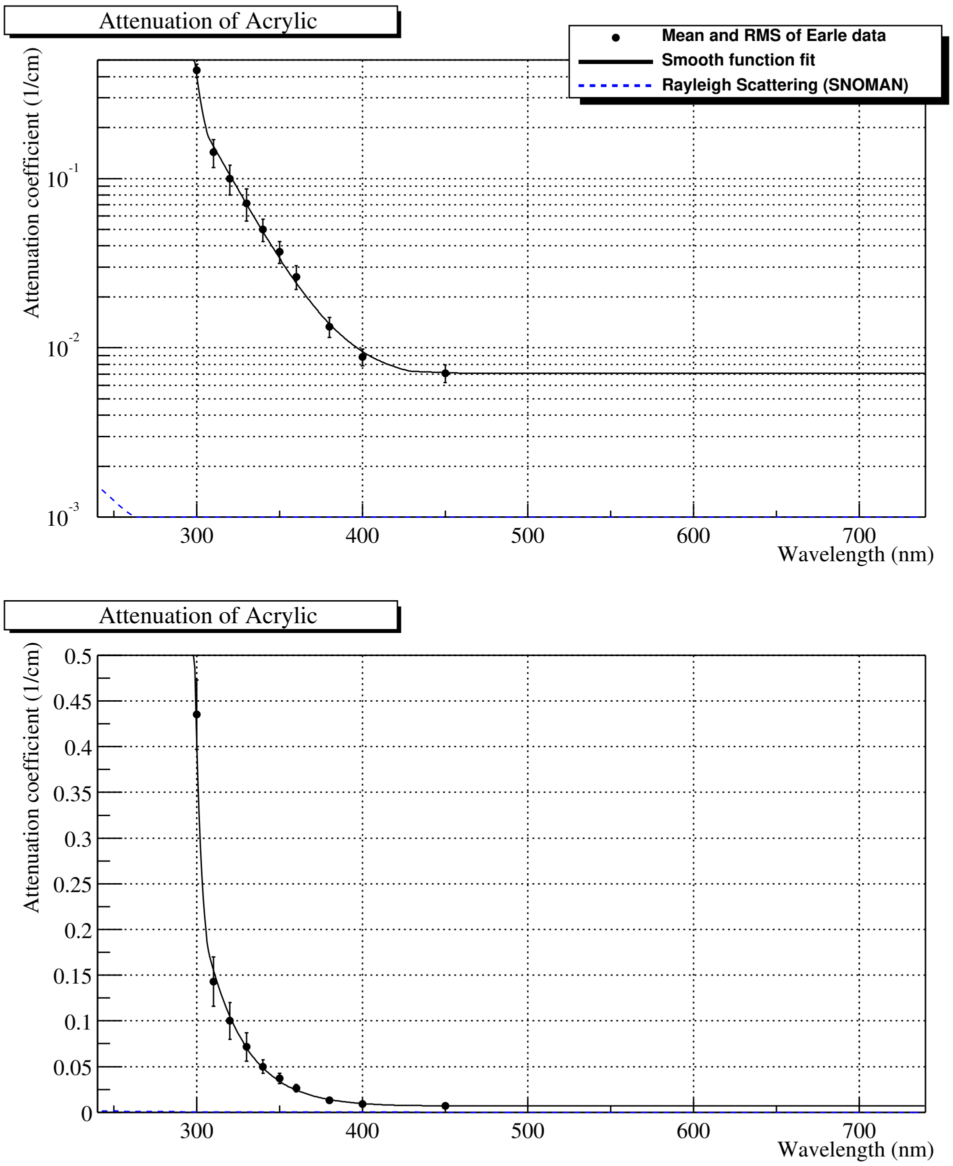

Figure 7.1: *Attenuation coefficient measurements for acrylic. Mean and RMS width for measurements of α_a for the 122 acrylic vessel panels used in SNO [65].*

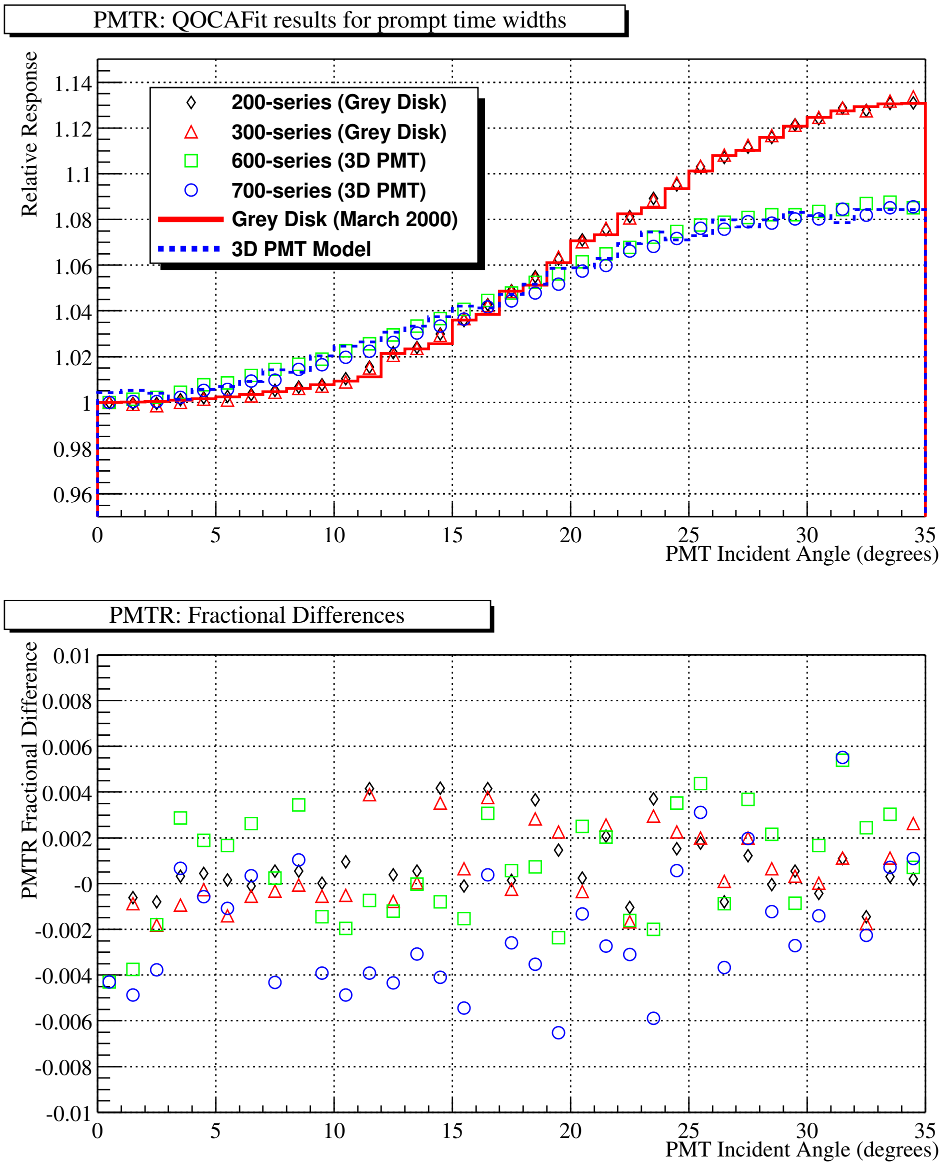

Figure 7.2: *PMT response comparison between Monte Carlo and QOCAFit results. The grey disk expected and all QOCAFit result curves are normalized to unit response at 0°. The expected 3D PMT response is scaled to the QOCAFit result over the range 7–15° where the statistical sampling in the 3D PMT table from SNOMAN shows less variability.*

nominal value of 4 ns. It is interesting to note that the sign of the PMT response change is opposite for the data and the Monte Carlo.

A comparison to *ex situ* measurements of the PMT response is shown in Figure 7.5. The dashed histogram shows the SNOMAN 3D-PMT model Monte Carlo prediction derived by Lay [2]. This model was shown to agree in detail with measurements made with pre-production PMT's and reflectors in an underwater setup at Oxford University. A clear enhancement of the PMT response is observed in the production PMT's used in the detector. An explanation for the discrepancy with the previous measurements is not yet agreed upon, although the explanation may rest with the use of pre-production PMT's and reflectors for the measurements described by Lay [2].

To extrapolate the PMT response from the measured range of incidence angles ($\lesssim 40°$) to higher angles, the average SNOMAN PMT response was scaled to agree with the mean QOCAFit PMT response over the last 4°. The response for the 3D PMT model was used to obtain the average SNOMAN PMT response $\overline{R_{\mathrm{SNOMAN}}}$ by averaging over wavelengths:

$$\overline{R_{\mathrm{SNOMAN}}} = \frac{1}{200\,\mathrm{nm}} \int_{350}^{550} R_{\mathrm{SNOMAN}}(\lambda, \theta_{\mathrm{PMT}})\,\mathrm{d}\lambda. \tag{7.2}$$

The scaling of $\overline{R_{\mathrm{SNOMAN}}}$ to the QOCAFit result is necessary to allow the PMT response to be continued past the end of the optical data at $\sim 36°$.

Figure 7.6 displays a comparison between the various PMT response functions used for Monte Carlo and analysis and the QOCAFit results from the optical calibration. The March 2000 Grey Disk response was used in the 200- and 300-series simulations, and represents the result of early fits to the February 2000 data. The SNOMAN 3D PMT response is taken from the SNOMAN parameter database (from file `pmt_response.dat`). In this file, the PMT response was generated by simulating

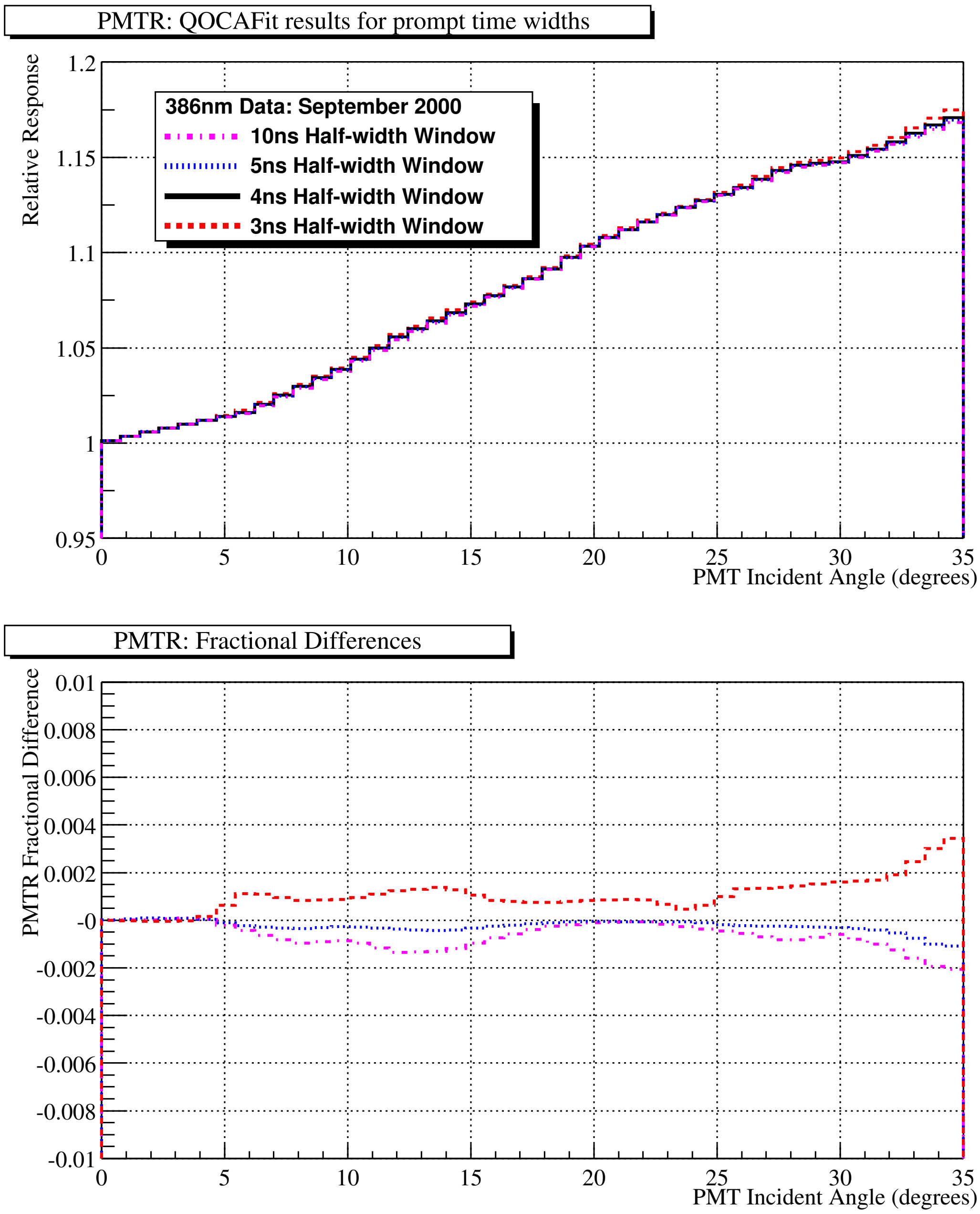

Figure 7.3: *PMT response for 386nm data as a function of prompt time window. The nominal time window has a half-width of 4 ns.*

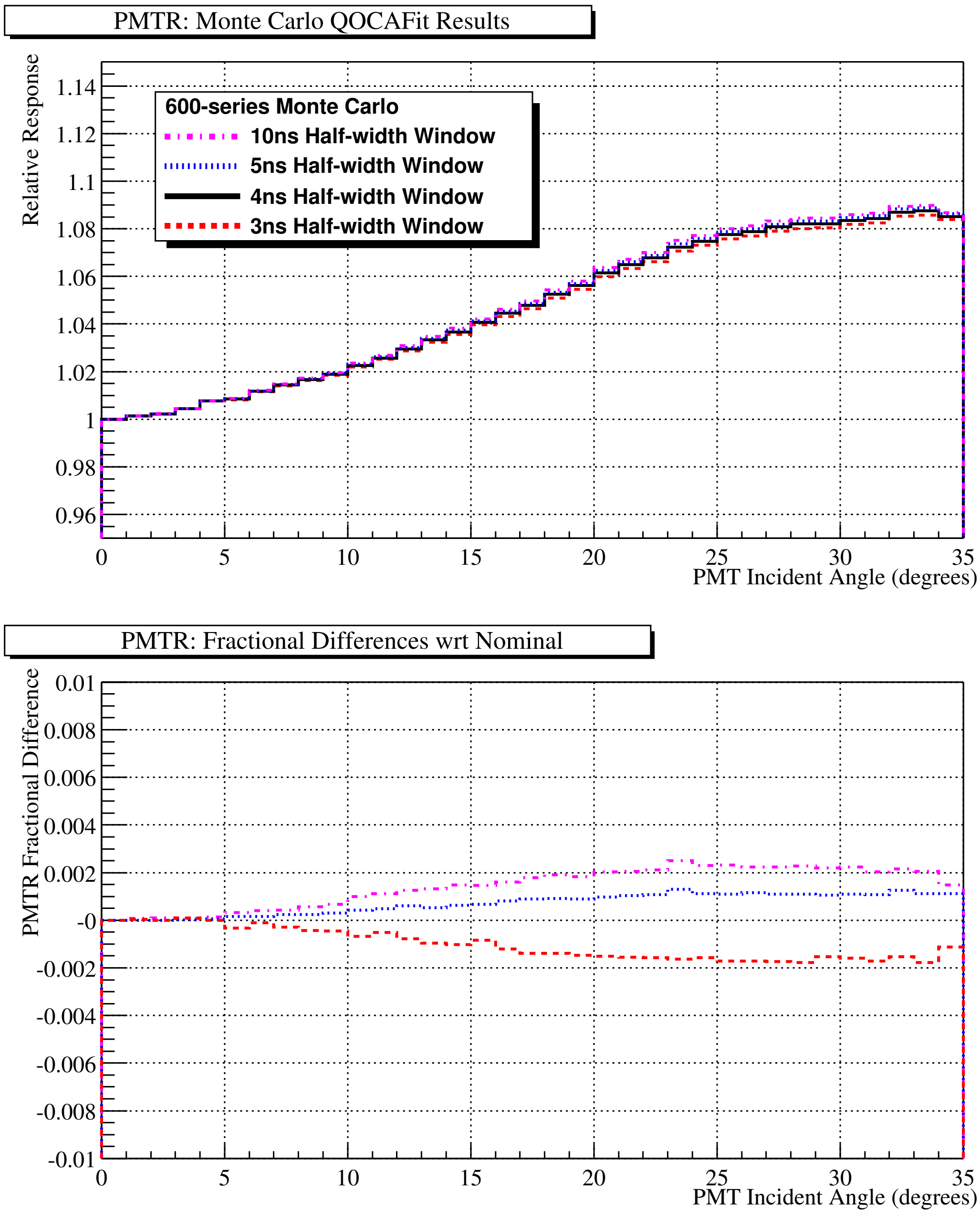

Figure 7.4: *PMT response for Monte Carlo as a function of prompt time window. The nominal time window has a half-width of 4 ns.*

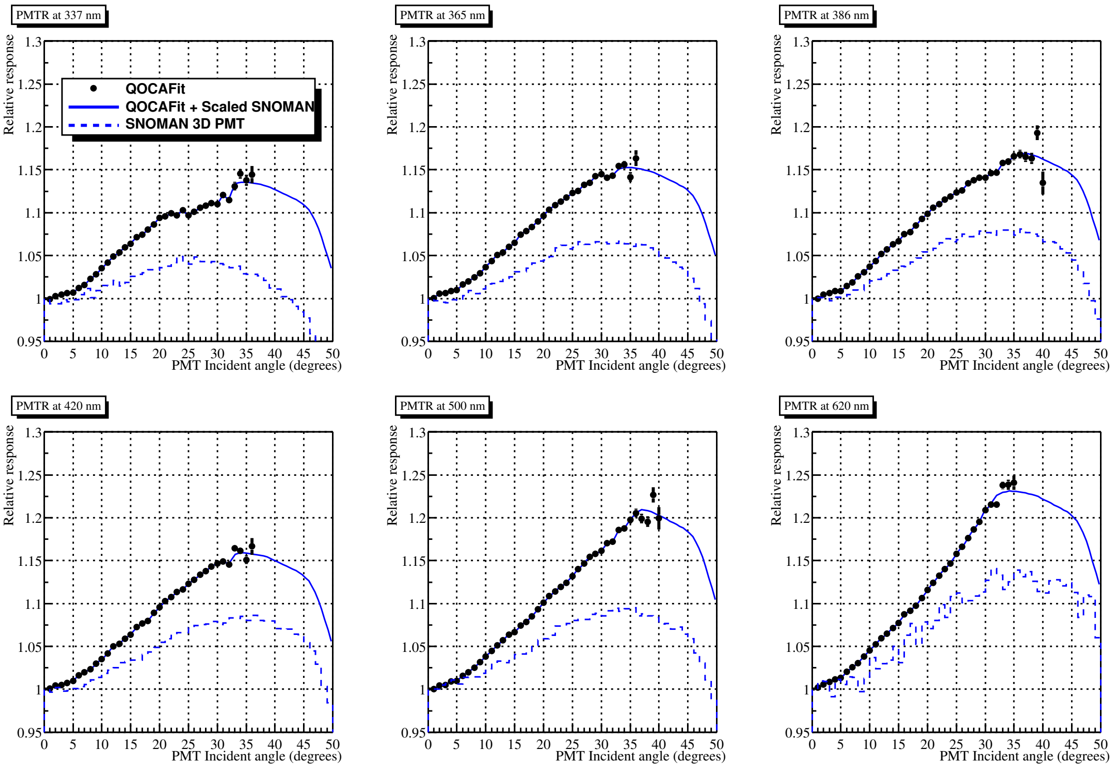

Figure 7.5: *PMT response from QOCAFit for September data compared with* ex situ *measurements. The six wavelengths used in the September dataset are 337 nm (top left) through 620 nm (bottom right). The extrapolation beyond the range of the QOCAFit results was done by scaling the average SNOMAN 3D PMT response to match the mean QOCAFit response over the last 4° of the fit range.*

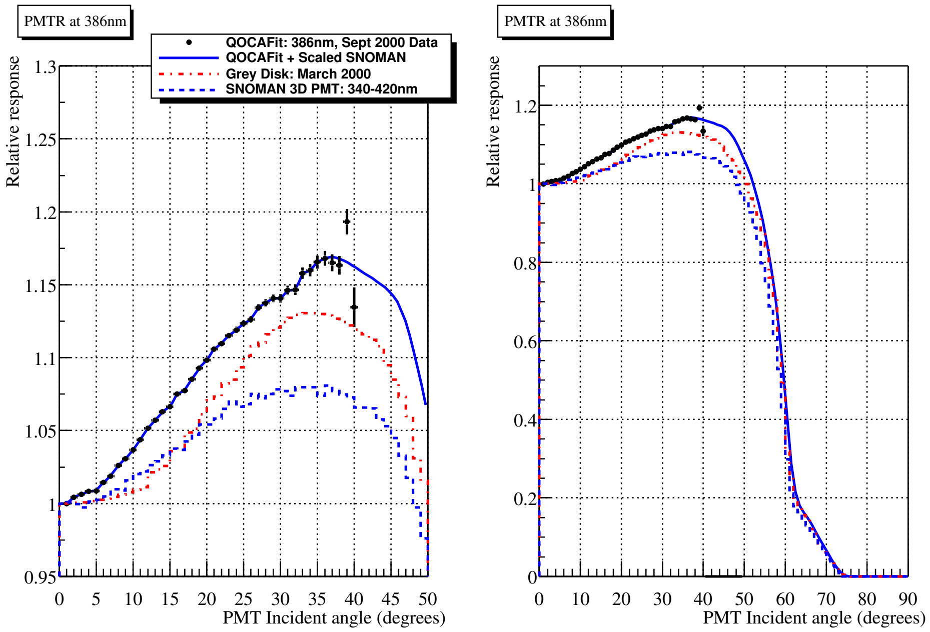

Figure 7.6: *PMT response comparison at 386 nm between QOCAFit on September 2000 data, an early optical fit (March 2000) used in the grey disk Monte Carlo simulations, and the SNOMAN 3D PMT average response over 340–420 nm. The extrapolation of the response past 40° was done by scaling the SNOMAN average response to match the mean QOCAFit result over the range 36–40°.*

Cherenkov events distributed uniformly throughout the detector and recording the PMT hit statistics as a function of the wavelength and the incident angle of the light with respect to the front face of the PMT reflectors. The response is averaged over the wavelength range 340–420 nm to reduce the statistical fluctuations present in the data file for the individual 10 nm wide wavelength bins.

The PMT's and reflectors are subject to degradation caused by sitting in the ultra-pure H_2O saturated with N_2 gas. Accelerated tests at 90°C to 10 years equivalent immersion in pure water have shown that the reflectivity degrades with exposure to water, and that the effect is wavelength dependent [76]. The two wavelengths (365

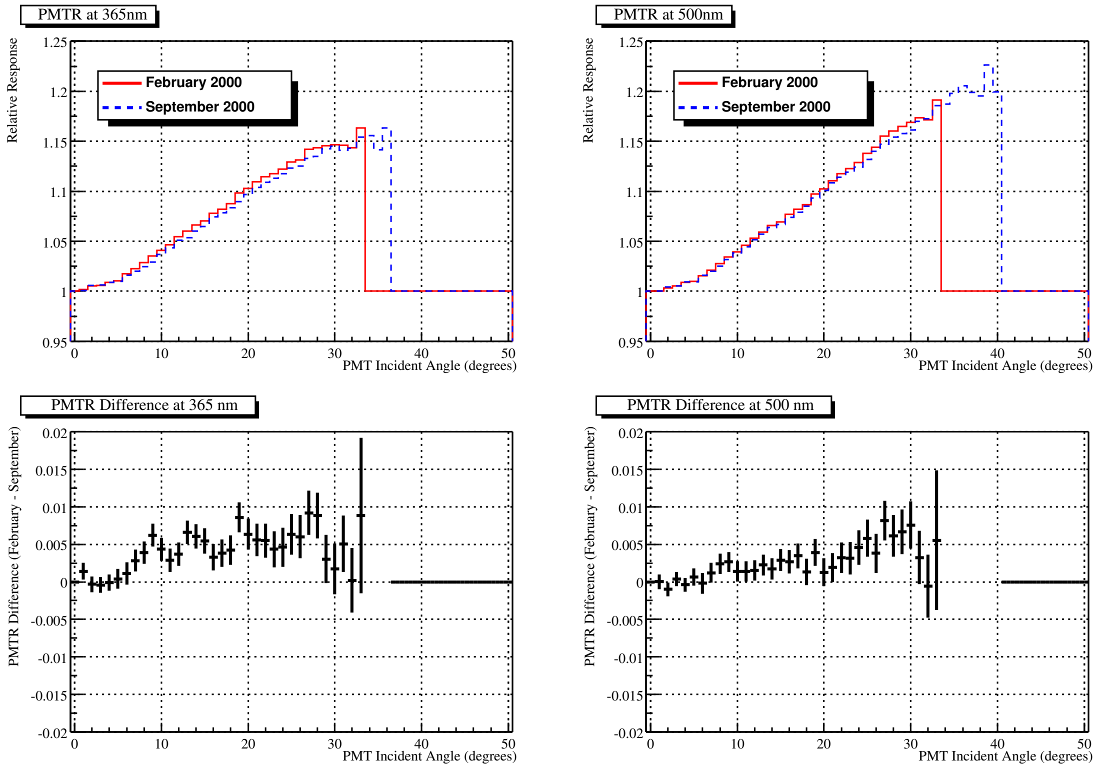

Figure 7.7: *PMT response comparison for February and September 2000 data at the two common wavelengths: 365 nm and 500 nm. Statistical parameter errors from the diagonal elements of the fit covariance matrix are used in the difference histograms.*

and 500 nm) available for comparison show a slight decrease in response at the higher angles over the seven month interval between data sets, as shown in Figure 7.7. However, this result is far from conclusive because the change in response is comparable in magnitude to the errors.

7.1.2 PMT-PMT Variability

The width of the occupancy ratio distribution is not purely statistical, but increases slowly with incident angle. The effect was first observed by comparing the

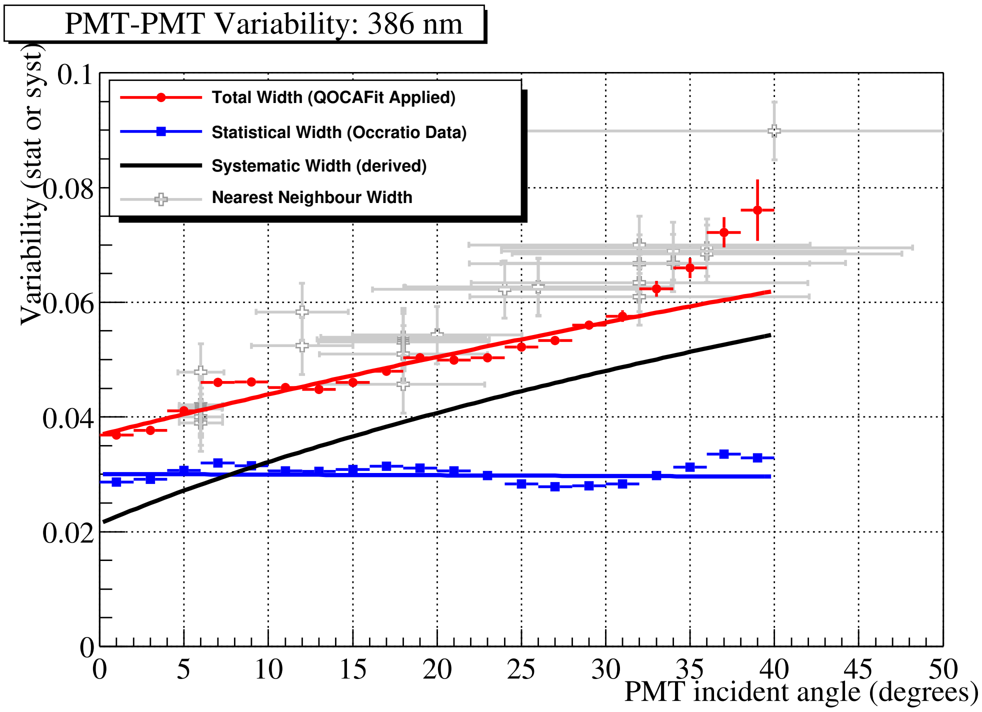

Figure 7.8: *PMT-PMT variability increases with incident angle at 386 nm. All other wavelengths show similar behaviour.*

occupancy ratios of neighbouring PMT's, which are illuminated under nearly identical conditions in both the centre and off-centre runs. The average statistical uncertainty on the occupancy ratio remains relatively constant as a function of incident angle. Figure 7.8 illustrates the increase in PMT variability beyond hit counting statistics, as measured by both the nearest neighbour method and the width of the occupancy ratio distribution obtained as output from the QOCAFit procedure.

The nearest neighbour method computes the difference in occupancy (Equation 4.12) for neighbouring channels in unique pairings. The width of a Gaussian fit to the nearest neighbour occupancy difference distribution characterizes the variability as a function of laserball radius. As shown in Figure 4.13, the laserball radius and the mean PMT incident angle are highly correlated. The nearest neighbour width is therefore plotted as a function of the maximum incident angle for each run position in Figure 7.8. The RMS width of the PMT incident angle distribution at each position is used to set the horizontal error bar for these points. The nearest neighbour width and the QOCAFit occupancy ratio distribution width are computed independently, and they both show a similar increase in PMT-PMT variability. In subsequent analysis, the QOCAFit width was used to determine the PMT-PMT variability because of the direct connection between this width and the PMT incident angle.

The increased variability is fed back in to the QOCAFit procedure as an additional contribution σ_{PMT} added in quadrature to the statistical uncertainty in the denominator of the χ^2 (Equation 4.17). The QOCAFit is first run without any PMT-PMT variations beyond statistics, resulting in a reduced χ^2 which is in the range 1.2 to 1.8. This is unreasonably large for the number of data points in the fit ($\sim 140\,000$). The uncertainty in the denominator of the χ^2 is adjusted for the additional PMT-PMT variability seen in the data. An additional systematic uncertainty σ_{PMT} is added in quadrature to the statistical uncertainty σ_{stat} already computed for the occupancy ratio based on hit counting statistics. The total width σ_{total} of the occupancy ratio distribution as a function of PMT incident angle is used to derive σ_{PMT} from the data. Linear and second-order polynomial fits to the statistical and PMT variability widths are shown in Figure 7.8. The PMT-PMT variability is calculated from these fits as:

$$\sigma^2_{\mathrm{PMT}} = \sigma^2_{\mathrm{total}} - \sigma^2_{\mathrm{stat}}. \tag{7.3}$$

Including σ_{PMT}, the QOCAFit obtains a reduced χ^2 which is much closer to 1.

The uncertainty of this procedure for inserting the additional variability into the optical model is likely to be significant. For this reason, the reduced χ^2 should not be expected to converge to exactly 1 even for the large number of degrees of freedom in the model. The additional contribution to the uncertainty has a significant effect on the value of the χ^2 at the minimum, but only a small effect on the derived physical parameters, as will be shown in the systematics studies in Section 7.4. For typical values of $\sigma_{\rm PMT}$ and $\sigma_{\rm stat}$, an error as small as 5% on the PMT-PMT variability has an 8% effect on the χ^2 value. The scatter of the statistical and total widths about the polynomial fits in Figure 7.8 of about 10% indicates that the error in determining $\sigma_{\rm PMT}$ is likely to be less than about 20%.

7.1.3 Laserball Light Distribution

The light distribution must remain constant from run to run for it to be accurately measured by the occupancy ratio method. The rotated laserball runs taken at the centre of the AV (described in Section 6.1) were used as a direct measure of the laserball anisotropy. This determination using only the rotated central runs is largely independent of the global QOCAFit procedure, which uses all the runs at a given wavelength to determine the detector and laserball optical parameters simultaneously.

The laserball light distributions obtained from the QOCAFit results for February data are displayed in Figures 7.9 and 7.10 along with a fit to spherical harmonics using the four rotated central runs (manipulator slot facing south, east, north and west). The QOCAFit results (bottom) are obtained with $36 \times 12 = 432$ bins, each of which corresponds to a free parameter in the fit.

The top plots are the results of the fit to arbitrarily oriented spherical harmonic functions:

$$L(\theta,\phi) = \sum_{l=0,m=0}^{l=2,m\leq l} a_{lm} Y_{lm}(\theta+\theta_{lm},\phi+\phi_{lm}) \tag{7.4}$$

where $Y_{lm}(\theta,\phi)$ are spherical harmonic functions of order lm and the first six real terms are included in $L(\theta,\phi)$. The magnitudes a_{lm} and orientations for each order (θ_{lm},ϕ_{lm}) are included in the fit as free parameters. These fits were performed by F. Duncan at Queen's University using his own library of computer routines (SNOFD).

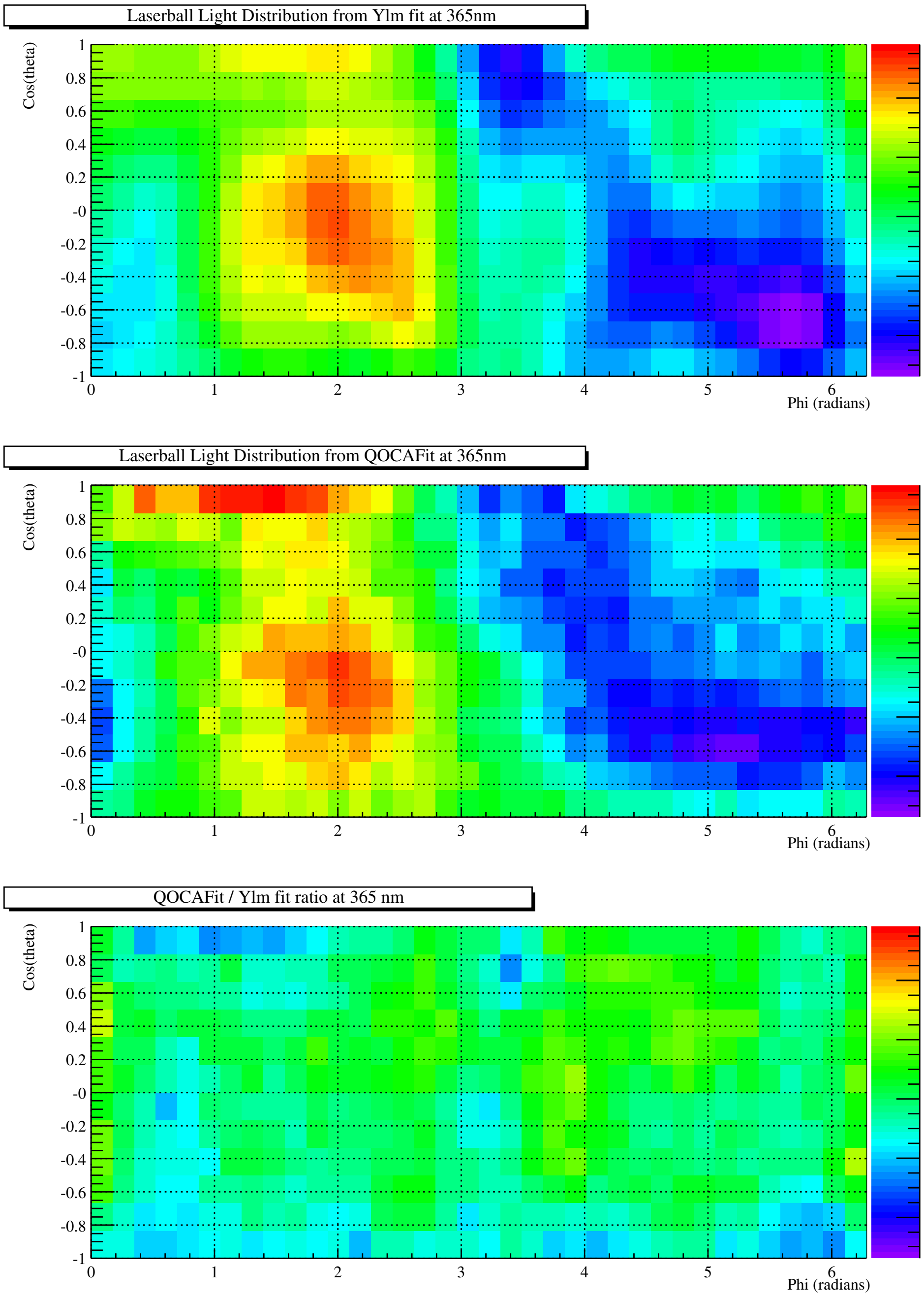

Figure 7.9: *Laserball light distribution for February 2000 data at 365 nm.*

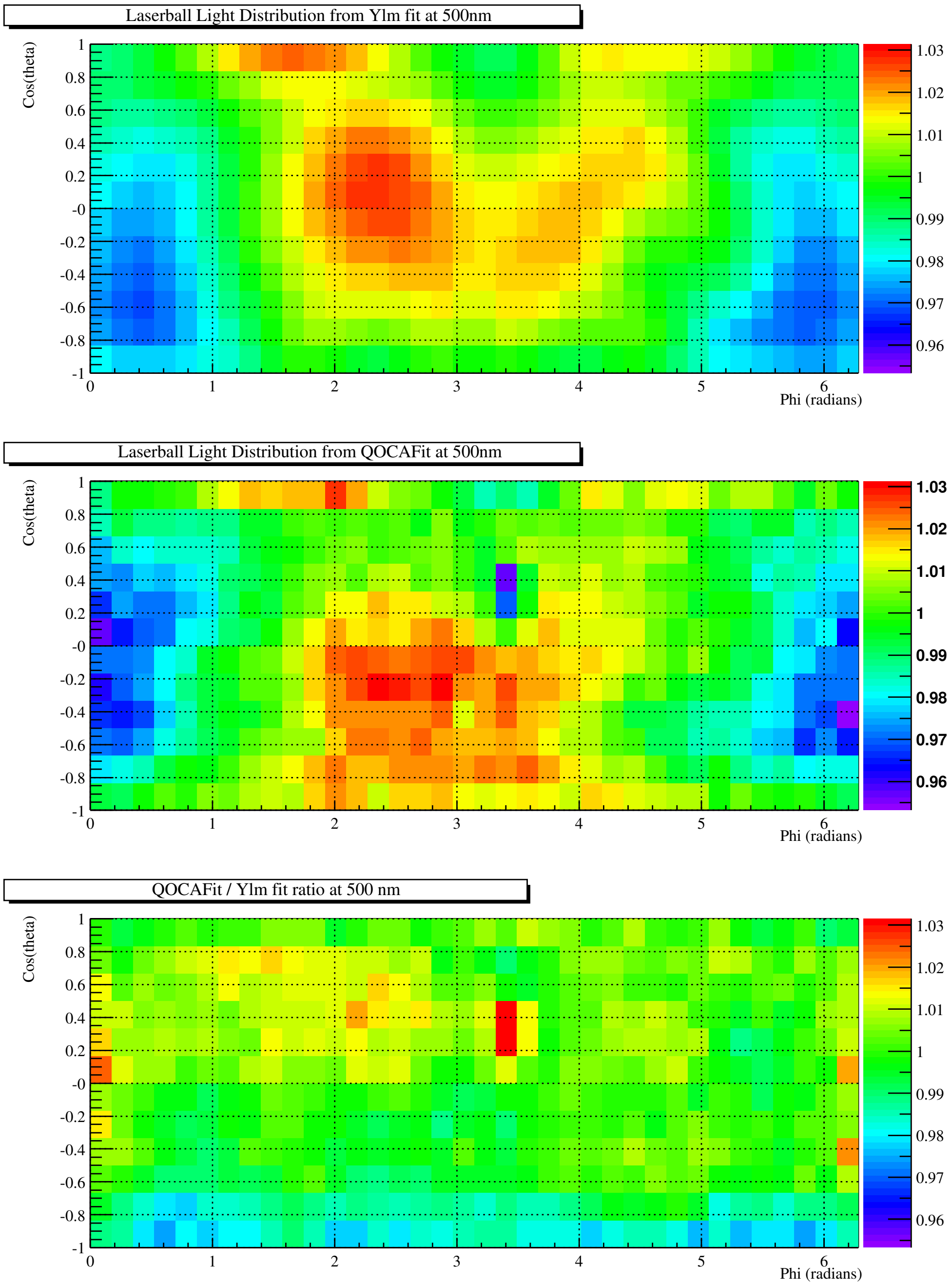

Figure 7.10: *Laserball light distribution for February 2000 data at 500 nm.*

During the optical runs, the laserball was placed at the centre in four discrete orientations. The orientation was fixed by the planes of the East-West and North-South side ropes. The laserball was rotated through 90° steps, with the slot on the manipulator connection to the ropes facing south, north, east and west. By taking the ratio of occupancies for each tube in the runs 180° apart, a direct comparison can be made with the results from the Y_{lm} fits or from the QOCAFit. This comparison is shown in Figures 7.11 and 7.12 as a function of ϕ for 6 slices in $\cos\theta$. The difference between the ratio of the data and the ratio of the QOCAFit results is less than approximately 3% everywhere. Because only six terms were included, the Y_{lm} fit does somewhat worse and includes several bumps and cusp-like features which are clearly not present in the ratio of the flipped data.

Figure 7.13 shows the result obtained from the QOCAFit's for each wavelength in the September data. The laserball anisotropy has increased compared to the February data, particularly at the shorter wavelengths. In April 2000 the ball was accidentally filled with heavy water and had to be disassembled for cleaning. It was then re-assembled correctly, but the geometry of the fibre guide tube could not be adjusted to the required precision to obtain a nearly isotropic light distribution. The resulting laserball light distribution is dominated by a dipole distribution, which can be caused by the fibre tip being displaced only millimeters from the centre of the ball [9].

The agreement in the ratio N/S or E/W to better than about 3% indicates that the anisotropy is known to better than 1.5% when the laserball is at the centre of the detector. The fibres are securely fastened in the laserball, and it is unlikely that moving the source could change the light pattern emitted from the laserball in a significant way. To be conservative, a larger uncertainty of 5% in the laserball distribution is assigned to allow for additional uncertainty due to:

- intensity variations when the source is manipulated away from the centre, and
- the laserball mask function, which is not tested by the N/S or E/W ratios.

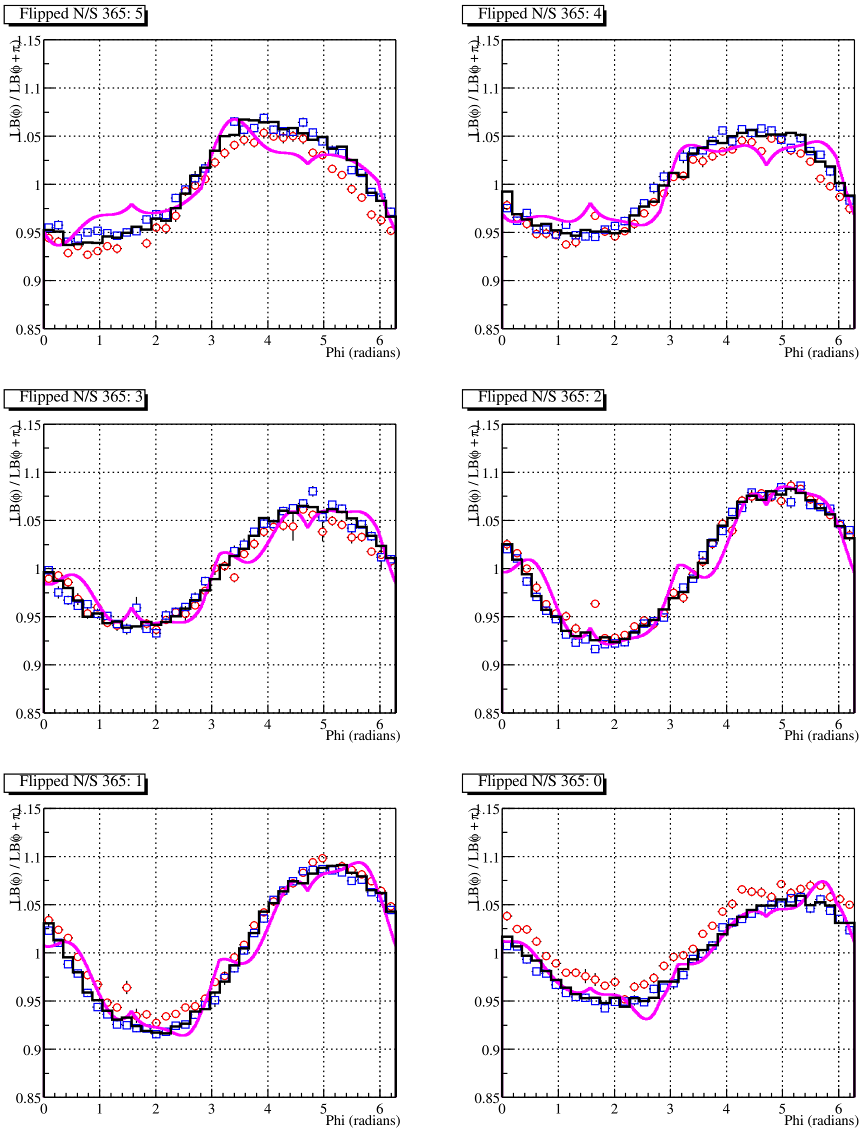

Figure 7.11: *Ratio of the laserball light distribution for rotated runs taken in February 2000 at 365 nm. The solid histogram (black) shows the ratio of the QOCAFit results for a 180° rotation of the laserball distribution. The circles show the N/S data, while the squares show the E/W data with a further rotation of $-\pi/2$ to align the distributions. The smooth solid curve (magenta) shows the result of the Y_{lm} fit. All distributions are given in six equal slices of $\cos\theta$: the top left plot is for the top of the detector, at bottom right is the bottom of the detector.*

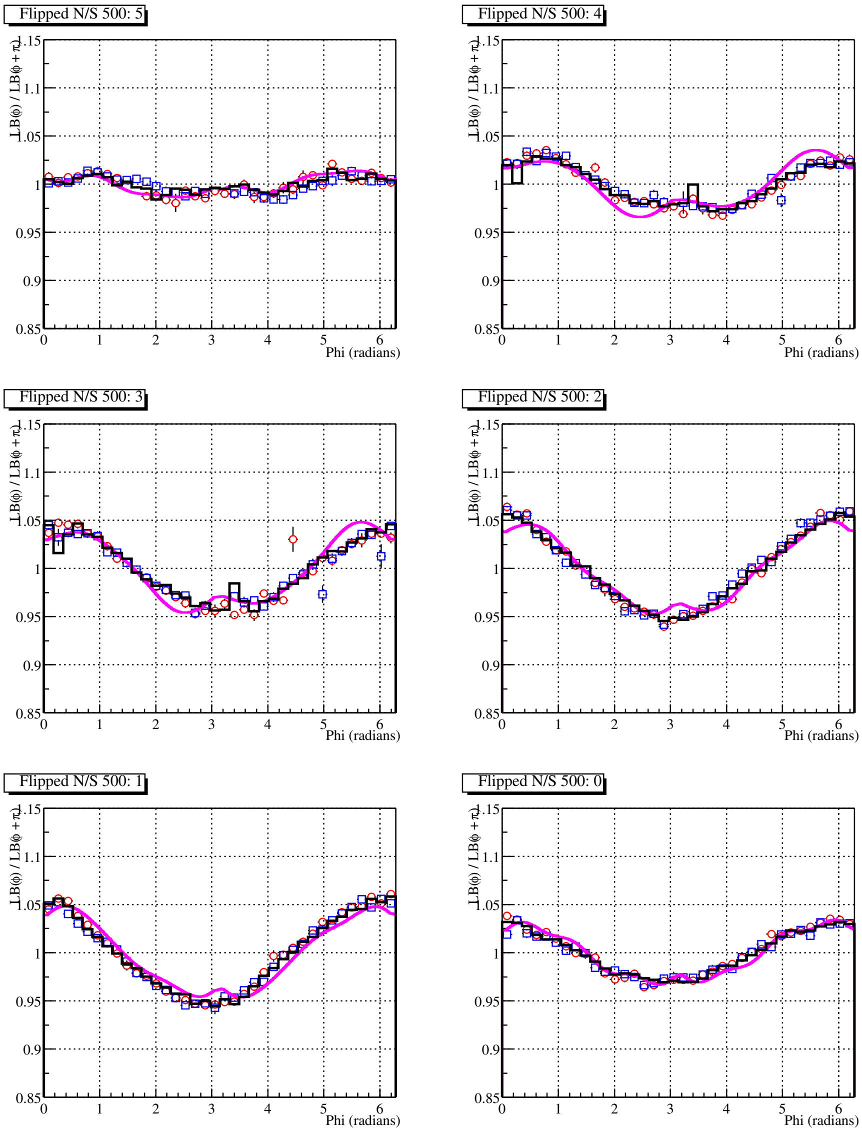

Figure 7.12: *Ratio of the laserball light distribution for rotated runs taken in February 2000 at 500 nm. The histogram, function curves and data points follow the same description as in Figure 7.11.*

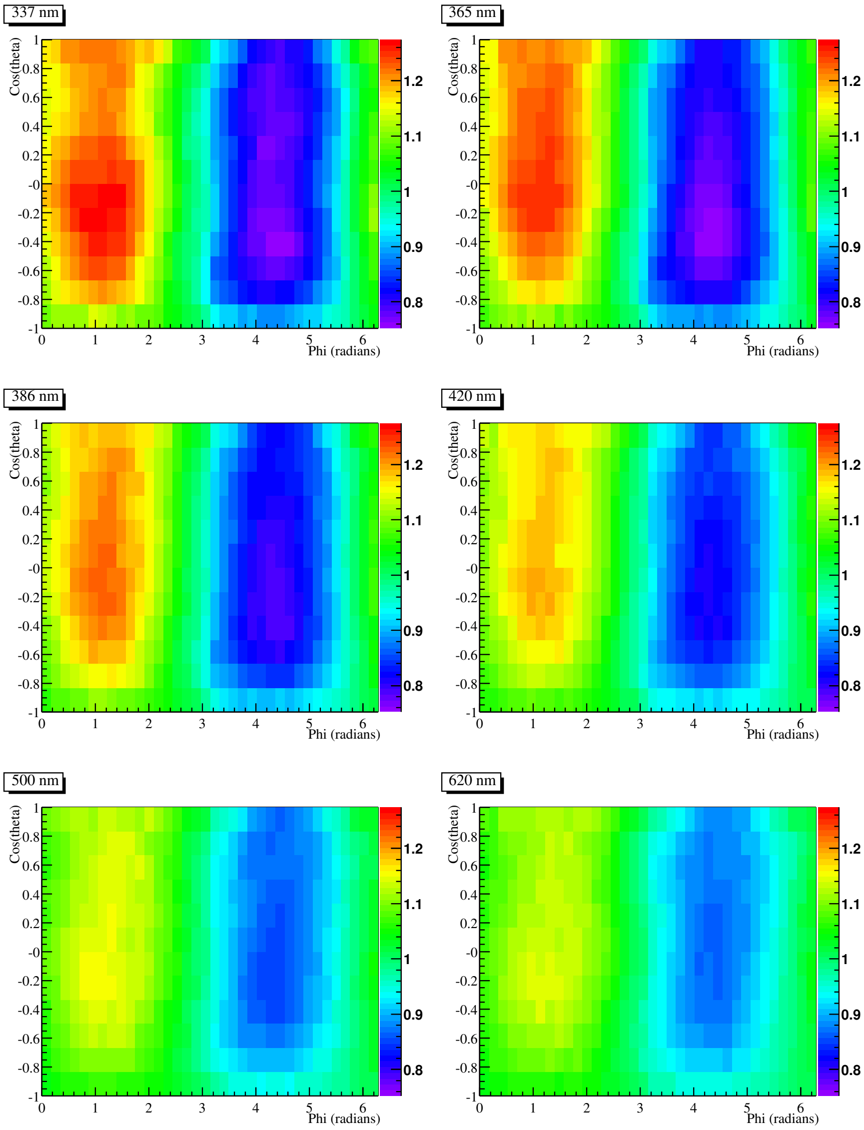

Figure 7.13: *Laserball light distribution for September 2000 data. The data for all wavelengths are displayed with the range of the 337nm data.*

7.2 Covariance Matrix

The fit covariance matrix obtained from the optical fits can be displayed most easily using percent covariances. Percent covariances have been obtained from the covariance matrix by dividing the covariance matrix element Cov_{ij} by the corresponding parameter values a_i and a_j:

$$C_{ij} = \sqrt{\frac{|\mathrm{Cov}_{ij}|}{a_i a_j}}. \tag{7.5}$$

In this section, the C_{ij} matrix elements are plotted as proxies for the covariance matrix elements themselves.

The diagonal elements of C_{ij} are estimators for the percentage standard errors on the parameters. The off-diagonal elements are normalized by the parameter values such that the covariance matrix can be displayed for parameters of widely varying magnitudes.

For the 386 nm data from September 2000, the covariance matrix C_{ij} is displayed for the detector parameters in Figure 7.14. To illustrate the large (negative) covariance between the acrylic and H_2O attenuations, Figure 7.15 shows the same parameter range for a fit where both α_a and α_h were left free to vary. The matrix elements are correspondingly smaller at wavelengths where either α_a (337 nm) or α_h (620 nm) is large.

The covariance matrix was examined in detail for other significant covariances between the model parameters. No significant covariances with the physical parameters (attenuations and PMTR) of the optical model were found at any wavelength.

Another way to examine the covariance matrix output from the QOCAFit is to

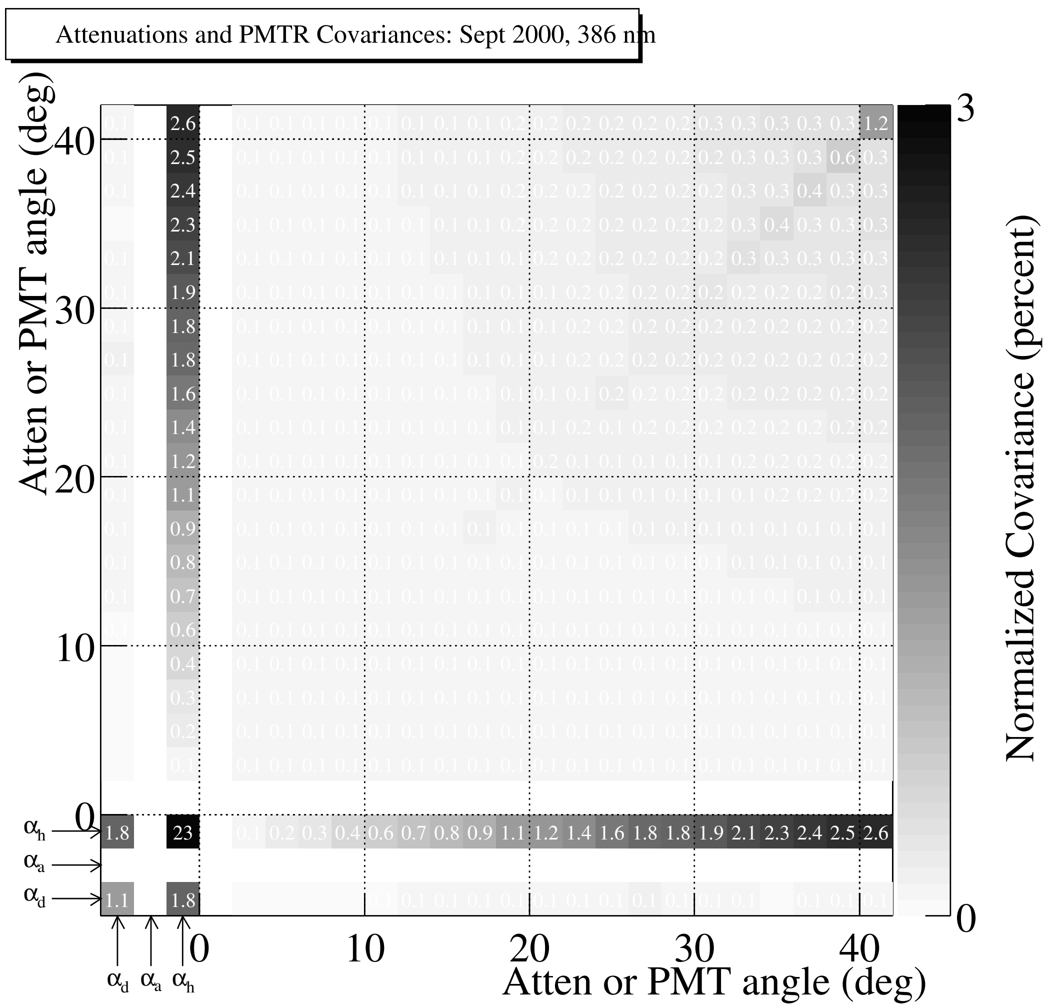

Figure 7.14: *Covariance matrix for the attenuations and PMT response: September 2000 data at 386 nm. Fit under nominal fit conditions with α_a a fixed parameter. The quantity C_{ij} (Equation 7.5) is shown with a vertical scale of $0-3\%$; only the element corresponding to α_h is off the scale at 23%. To improve the clarity of the figure, the PMT response parameter covariances are shown in 2° steps (at 0, 2, 4, ..., 40°) rather than in the 1° steps used in the QOCAFit.*

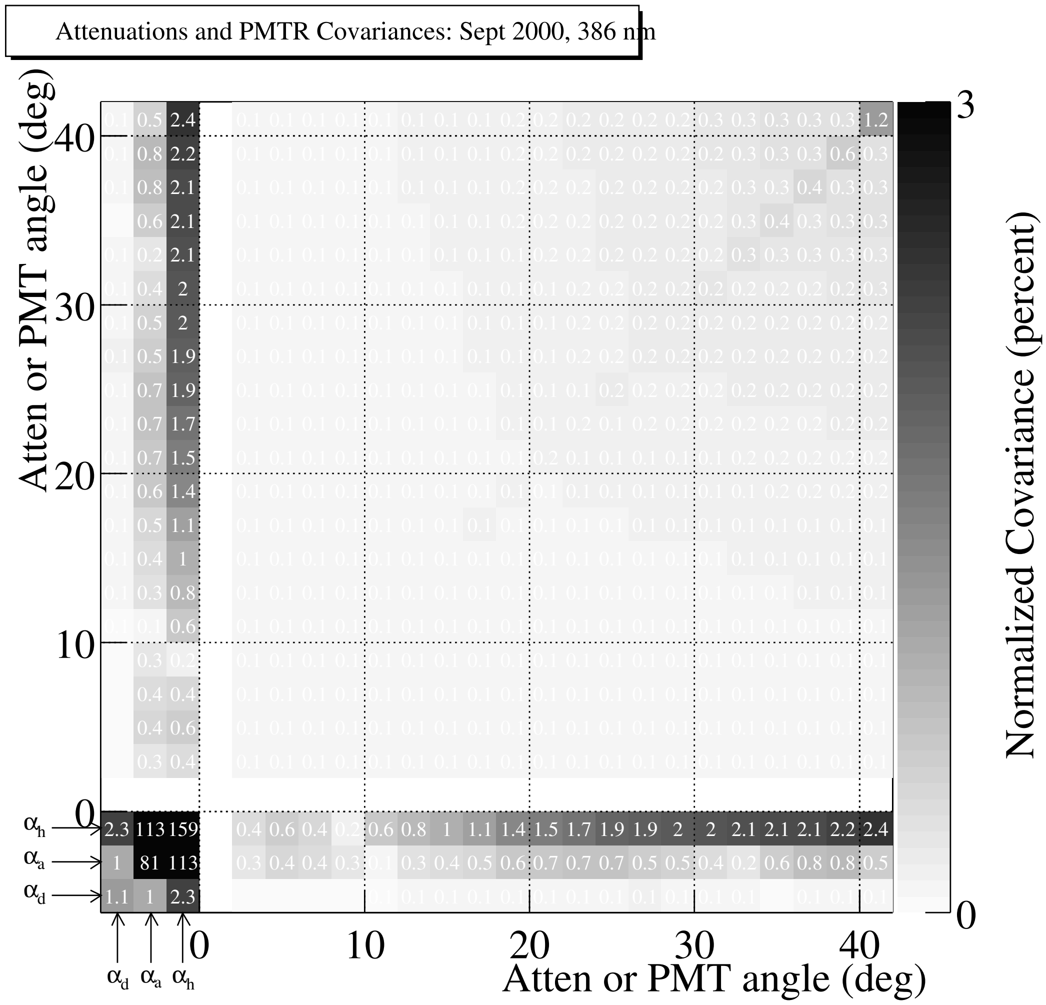

Figure 7.15: *Covariance matrix for the attenuations and PMT response: September 2000 data at 386 nm. Both α_a and α_h free in fit, and the large covariance is evident in the bottom left corner of the figure. Otherwise, this figure and Figure 7.14 show very similar behaviour in the covariance matrix. The quantity C_{ij} (Equation 7.5) is shown with a vertical scale of $0-3\%$. To improve the clarity of the figure, the PMT response parameter covariances are shown in 2° steps (at 0, 2, 4, ..., 40°) rather than in the 1° steps used in the QOCAFit.*

compute the correlation matrix:

$$\mathrm{Corr}_{ij} = \frac{\mathrm{Cov}_{ij}}{\sqrt{\mathrm{Cov}_{ii}\mathrm{Cov}_{jj}}}. \tag{7.6}$$

The correlation matrix elements are normalized over the range $[-1:1]$ and indicate the correlation between the errors on the parameters a_i and a_j. The correlation matrix for the nominal fit with α_a fixed is displayed in Figure 7.16. Longer acrylic and H_2O path lengths are associated with higher PMT incident angles, which produces the correlation between the errors on α_h and on the PMT response seen in Figure 7.16.

The correlation matrix Corr_{ij} for the fit with both α_a and α_h free to vary is shown in Figure 7.17. The errors in α_h and α_a are nearly perfectly anti-correlated, as expected for these two paramters given the linear relationship between d_h and d_a (see Figure 4.6).

7.3 Optical Fit Residuals and χ^2 Projections

The fit residual distributions for the 600-series Monte Carlo and for the 386 nm data from September 2000 are illustrative of the behaviour for the other Monte Carlo's and for the other data runs. The global behaviour of the residuals is shown in Figures 7.18 and 7.19, where the progression of cuts is shown. Without any cuts, the residuals still remain reasonably gaussian in shape, but the tails of the distribution indicate that the optical model is not complete. By cutting PMT's with dubious optical paths or anomalous occupancies, the wings of the residual distribution are much reduced. Light paths from the source to a PMT are dubious if they pass through a belly plate or the AV neck, near a rope or a water recirculation pipe. Tube occupancies are considered anomalous if the statistical error on the occupancy is greater than 25%, which occurs for low-occupancy channels; the typical values are 2% error for a

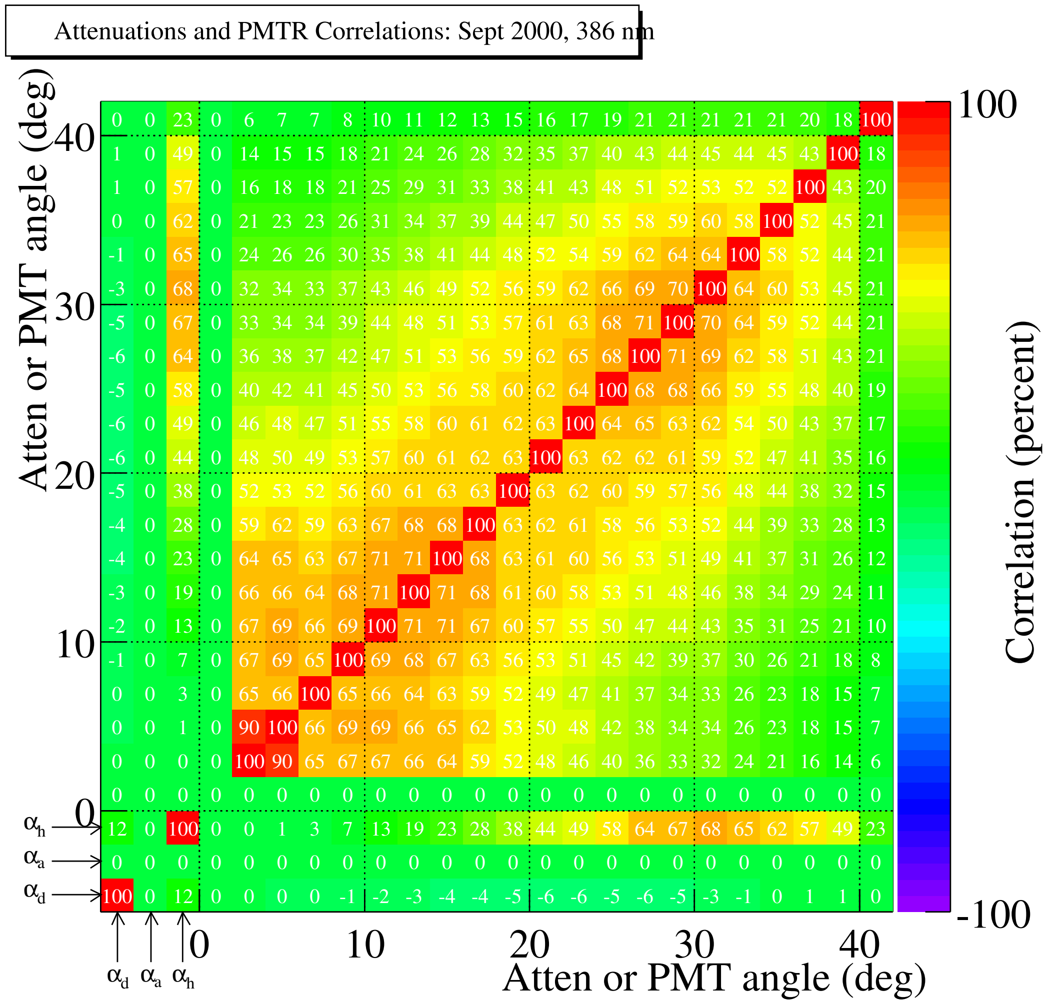

Figure 7.16: *Correlation matrix for the attenuations and PMT response: September 2000 data at 386 nm. Fit under nominal fit conditions with α_a a fixed parameter. The correlation coefficient $Corr_{ij}$ (Equation 7.6) is shown with a vertical scale of $[-100 : 100]$%. The diagonal elements have perfectly correlated errors because they are for the same parameter. To improve the clarity of the figure, the PMT response parameter covariances are shown in 2° steps (at 0, 2, 4, . . . , 40°) rather than in the 1° steps used in the QOCAFit.*

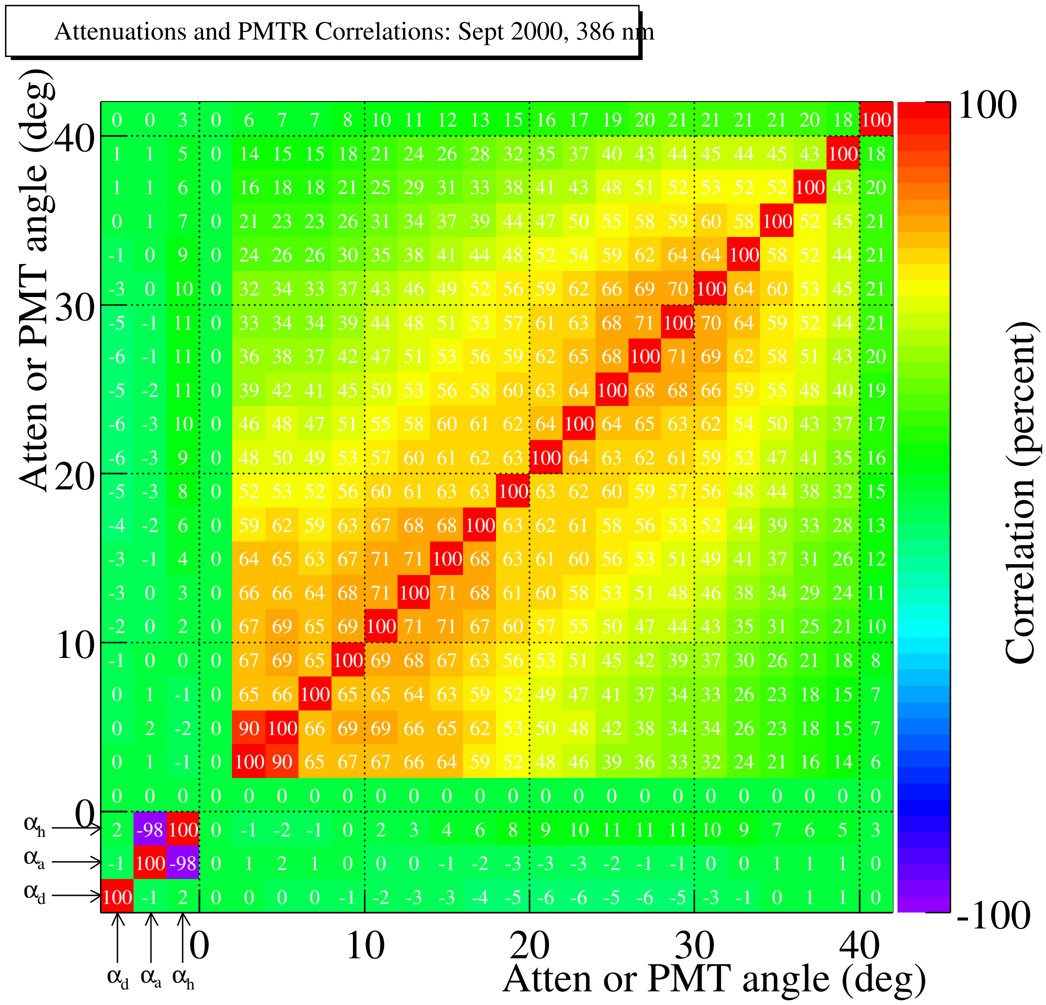

Figure 7.17: *Correlation matrix for the attenuations and PMT response: September 2000 data at 386 nm. Both α_a and α_h free in fit, and the large negative correlation between these parameters is evident in the bottom left corner of the figure. The correlation coefficient $Corr_{ij}$ (Equation 7.6) is shown with a vertical scale of $[-100 : 100]$%. The diagonal elements have perfectly correlated errors because they are for the same parameter. To improve the clarity of the figure, the PMT response parameter covariances are shown in 2° steps (at 0, 2, 4, ..., 40°) rather than in the 1° steps used in the QOCAFit.*

prompt tube occupancy of about 2500 hits.

Geometrical variables can indicate areas where the optical model fits poorly, and which parts of the model should be carefully examined to discover ways of improving the model. The optical model is calculated from the position and orientation of the laserball with respect to the PMT's. The geometrical variables which enter the calculation are: D_2O Distance (cm), Acrylic Distance (cm), H_2O Distance (cm), PMT incident angle (θ_{PMT}), AV incident angle (θ_{AV}), Total Distance (cm), Laserball-PMT Direction (θ_{LB}, ϕ_{LB}), Run Number, PMT coordinates (X,Y,Z). The residuals are found to be completely independent of any of the geometrical variables, as illustrated in Figure 7.20 for the 600-series Monte Carlo and in Figure 7.21 for 386 nm data. The vertical scale on these figures corresponds to ± 5 standard deviations.

The χ^2 surface has been found to be smooth and well-behaved over the parameter space. To illustrate the smooth quality of the χ^2 surface, three surface plots in 2-dimensions are shown in Figure 7.22. The large number of degrees of freedom in the fit ensures that the χ^2 surface has a smooth gradient which can easily be followed to minimize χ^2.

Varying a single parameter produces a smooth χ^2 curve, which is well approximated by a parabolic form near the minimum. For the small covariances between parameters (see Section 7.2), the parabolic approximations used to derive the covariance matrix elements in the Numerical Recipes routine `mrqmin` [72] are likely to be reasonable estimators for the single-parameter uncertainties. Because they are based on a χ^2, these estimates represent statistical uncertainties. The full parameter uncertainties are dominated by systematic errors, as will be shown in Section 7.4.

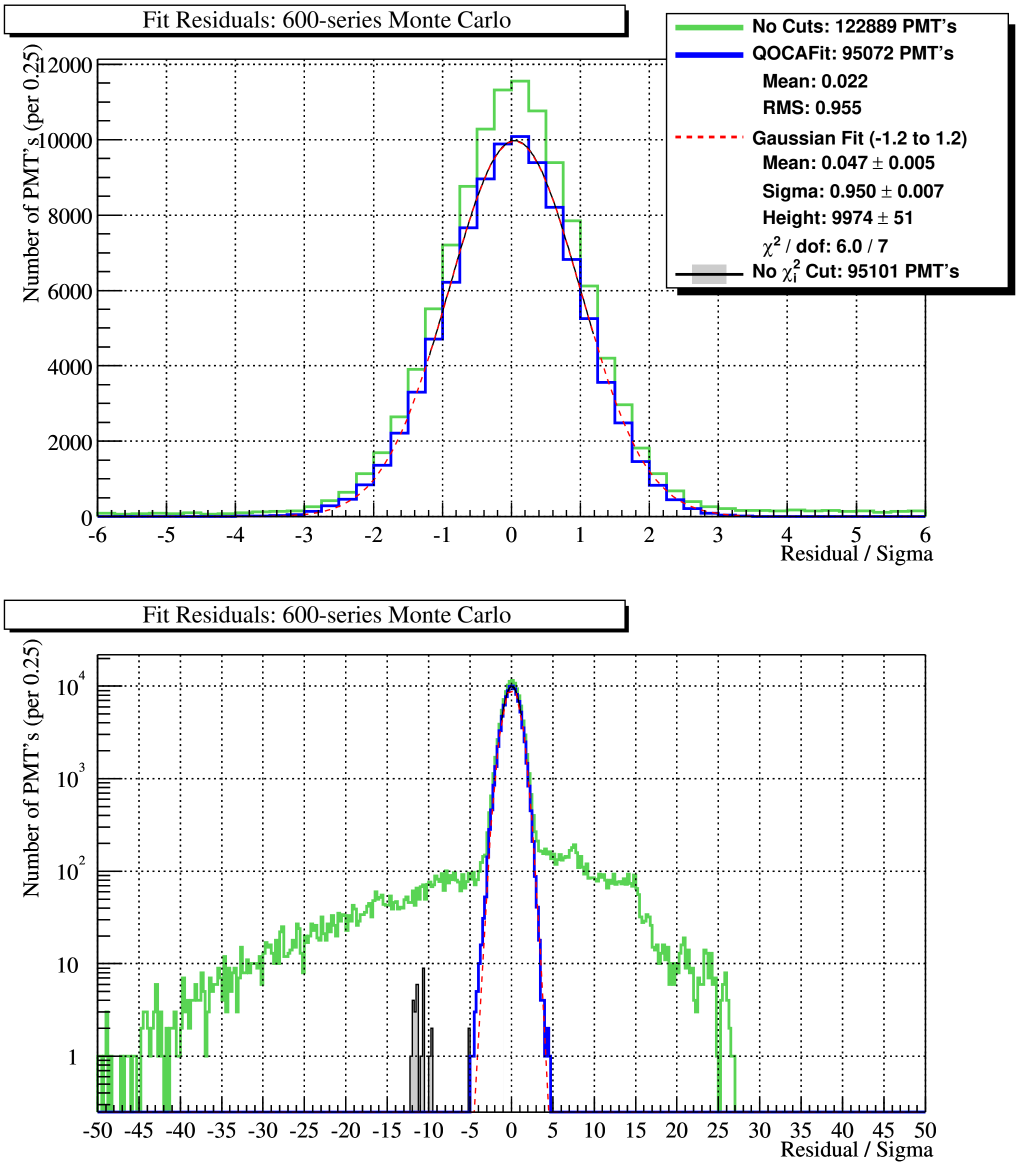

Figure 7.18: *Global fit residuals for the 600-series Monte Carlo.*

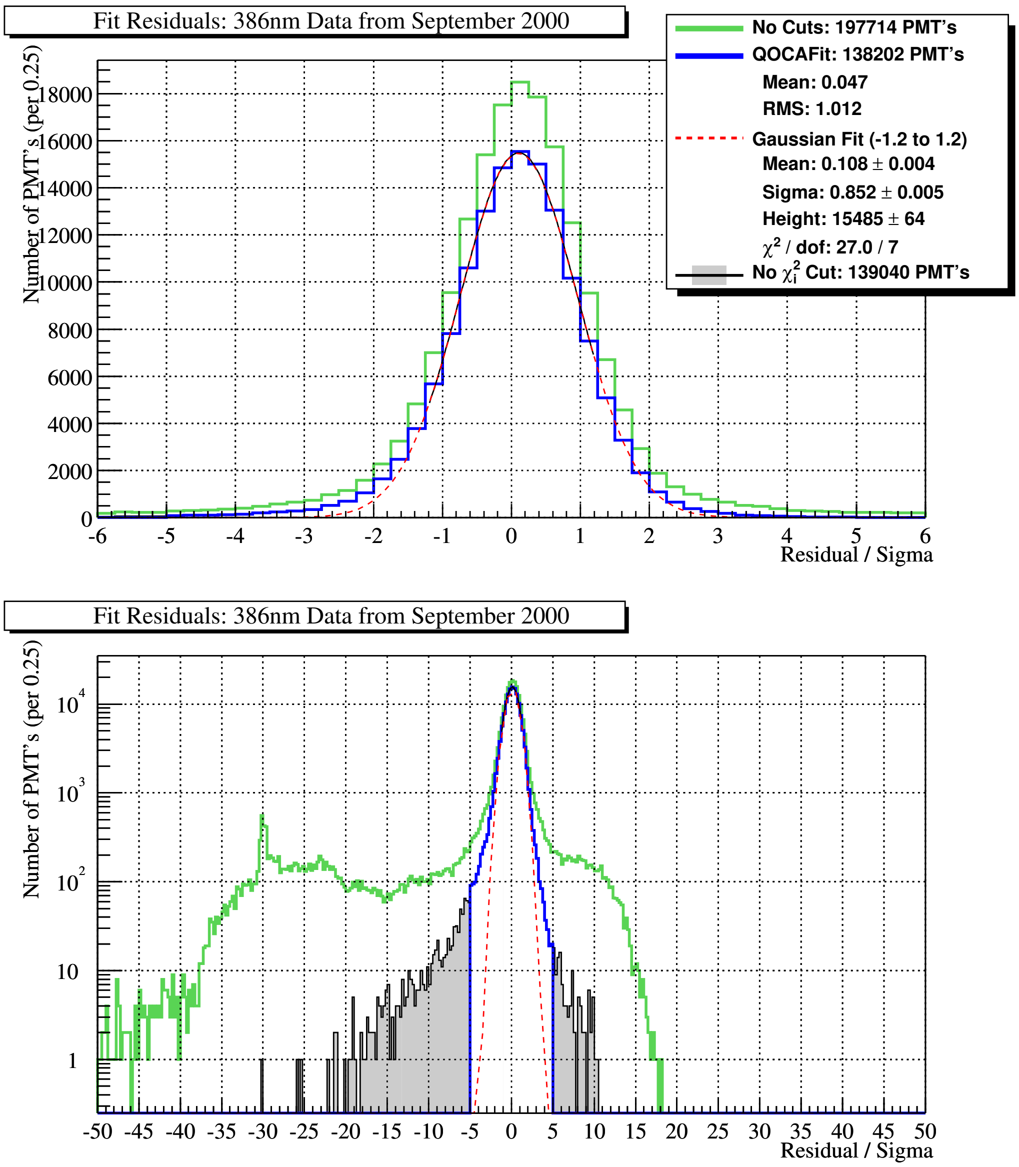

Figure 7.19: *Global fit residuals for the 386 nm data from September 2000.*

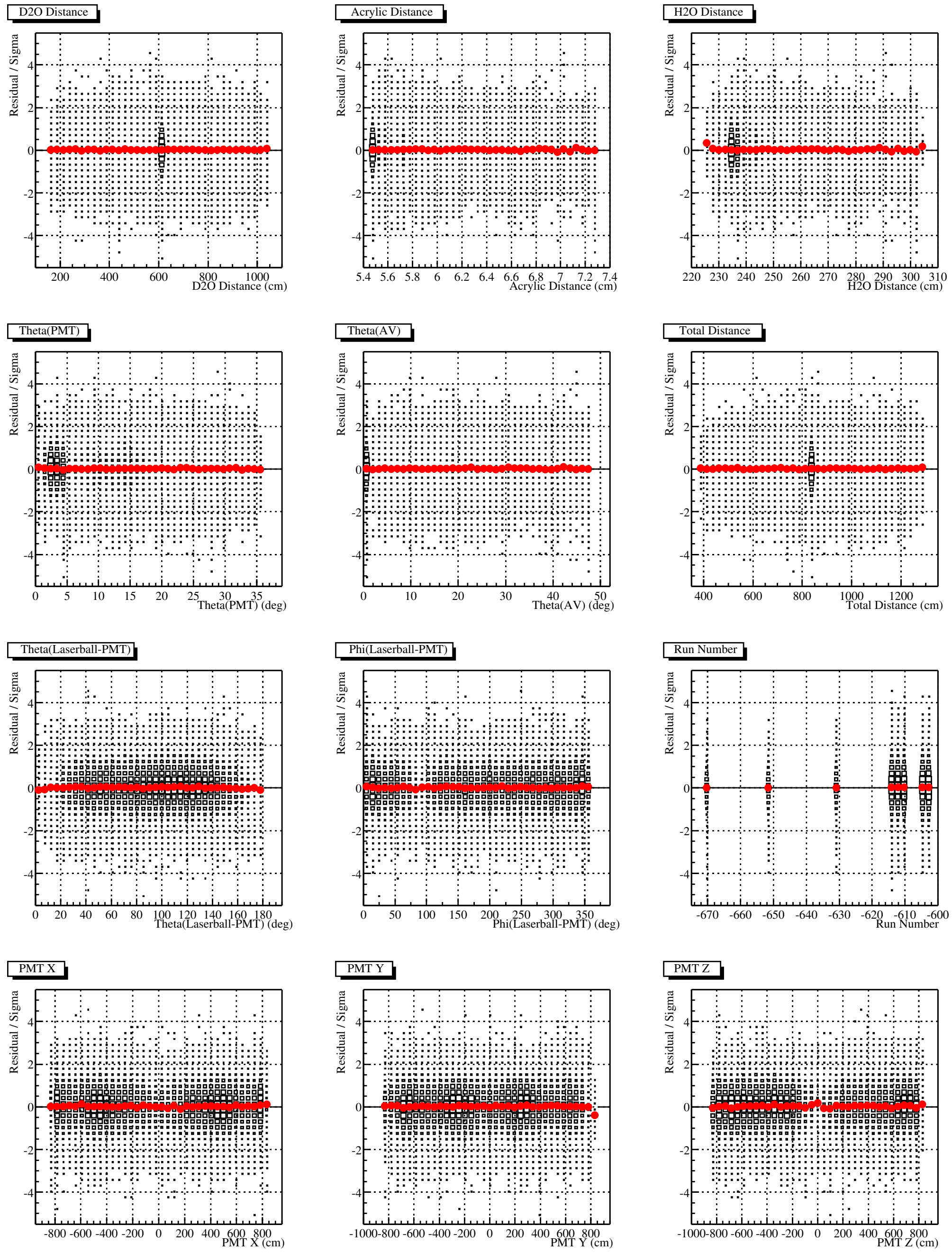

Figure 7.20: *Fit residuals for the 600-series Monte Carlo as a function of geometric variables.*

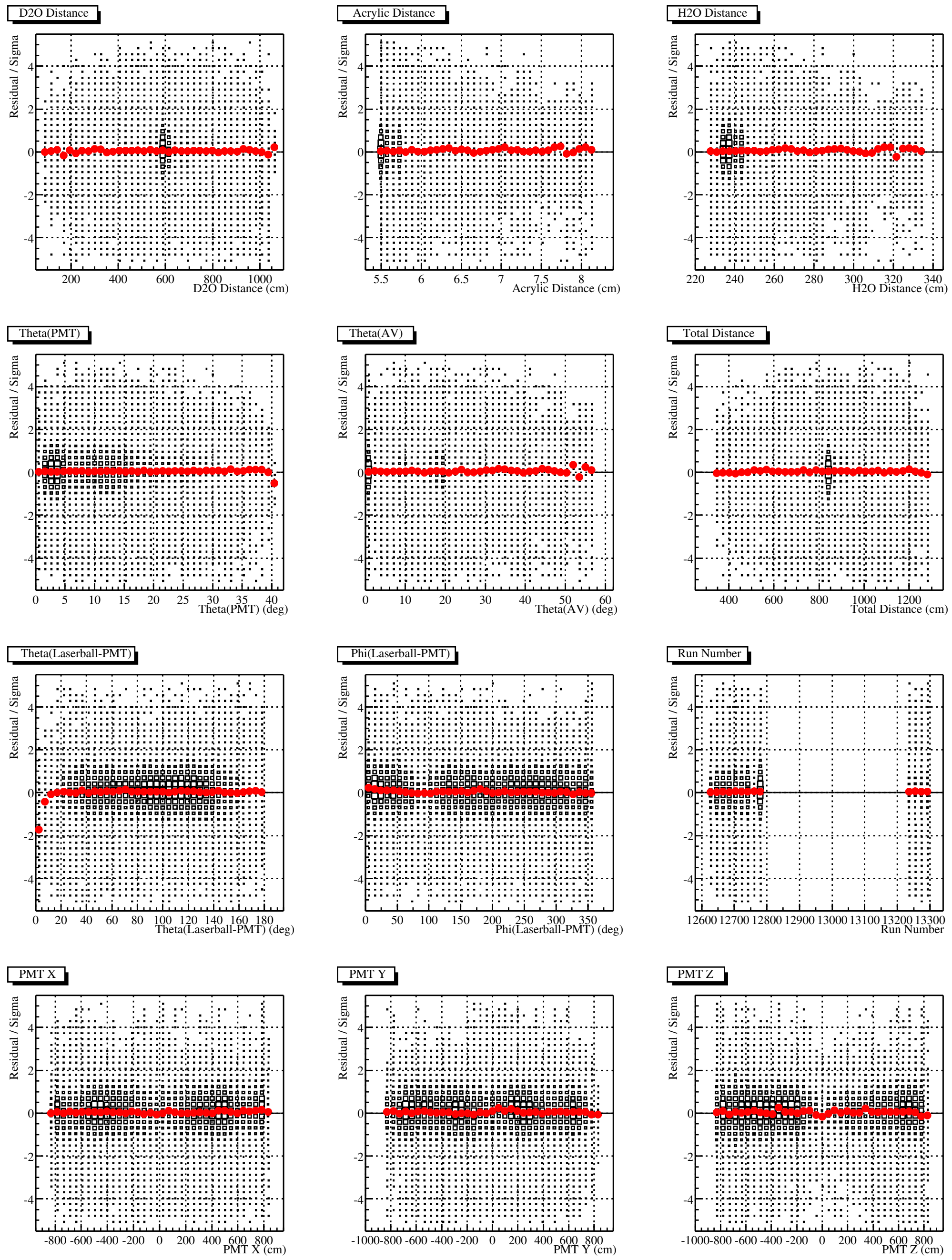

Figure 7.21: *Fit residuals for 386 nm data from September 2000 as a function of geometric variables.*

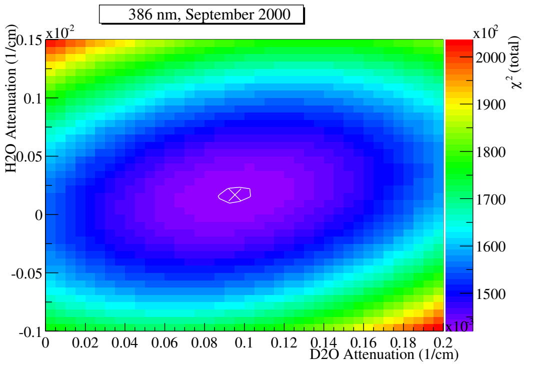

(a) *H_2O (α_h) versus D_2O (α_d) attenuation coefficients. The scale for α_d should be multiplied by 10^{-3}.*

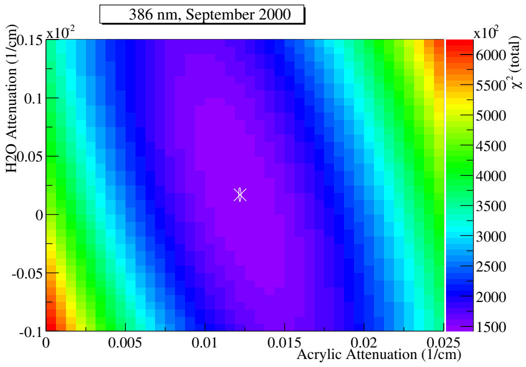

(b) *H_2O (α_h) versus acrylic (α_a) attenuation coefficients.*

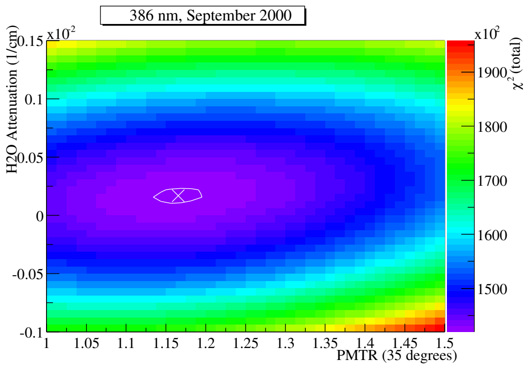

(c) *H_2O (α_h) attenuation coefficient versus PMTR at 35°.*

Figure 7.22: *χ^2 projections for the QOCAFit to September 2000 data at 386 nm. The white crosses mark the nominal fit results, and the white contour lines demarcate an increased value $\chi^2 = \chi^2_{min} + 100$. The χ^2 surfaces are smooth and the minimum is well defined for each parameter.*

7.4 Systematic Errors on Optical Parameters

To determine the uncertainty on the physical parameters of the optical model, systematic errors in the laserball positions relative to the PMT's and changes to the way the fit is executed have been investigated. The systematics investigated are:

1. **Radial scale shift** All run positions were moved radially outward by $R' = 1.01R$. This is approximately equivalent to rescaling the size of the detector in time units, which can be caused by changes to the PMT calibration time slopes used to convert ADC counts to nanoseconds, or by a change in group velocity at the effective laserball wavelength.

2. **Z position shift** All runs were displaced vertically by $Z' = Z + 5\,\text{cm}$.

3. **X position shift** All runs were displaced horizontally by $X' = X + 5\,\text{cm}$.

4. **Radial position shift** All runs were displaced radially by $R' = R + 5\,\text{cm}$.

5. **Radial position smear** All runs were displaced radially by a random amount sampled from a Gaussian with $\sigma = 5\,\text{cm}$: $R' = R + \text{Gaus}(\mu = 0; \sigma = 5\,\text{cm})$.

6. **Laserball-PMT distance shift** The distance from the laserball to the PMT was decreased by $D'_{\text{PMT}} = D_{\text{PMT}} - 3\,\text{cm}$. Because of the finite size of the laserball, the light is actually emitted several centimeters closer to the PMT's on average.

7. **& 8. Laserball distribution variations** The laserball distribution was forced to be flat $H(\cos\theta, \phi) = 1.0$, and then forced to be the square of the previous fit results $H = H^2_{\text{free}}$, where H_{free} is the distribution obtained for the systematics-free fit. Although H is normally an output of the fit and not an input to the model, these variations were used to quantify the effects of H on the determination of the other output parameters of the optical model. The laserball masking function $P_m(\cos\theta)$ was included with freely varying parameters in all fits.

9. PMT-PMT variability The variability is ignored by setting $\sigma_{\mathrm{PMT}} = 0$ in the χ^2 used in the optical fit (Equation 4.17).

10. & 11. Restricted Chi-squared for PMT selection Starting from the nominal fit results (with $\chi^2 < 25$), three successive iterations were performed with only PMT's with $\chi^2 < 16$ or $\chi^2 < 9$ remaining in the QOCAFit.

12. Time window width The optical fit is repeated for time windows of 2–20 ns full width in 2 ns steps. The centre of the time windows is the mean time for the prompt light peak, which is always found using the nominal 8 ns full width window.

The systematic model variations are larger than expected for actual conditions in the detector in order to exaggerate the effect on the attenuation and the PMT response. Estimates of the fraction of the systematic which actually applies to the data are summarized in Table 7.3. The justifications for these multiplicative factors (f_i) are as follows:

- Position changes come from comparisons between the manipulator coordinates and the optical position fit coordinates. The mean position shift is $\sim 1 \pm 1.5$ cm in any single coordinate, and 0.4 ± 1.9 radially [77].

- The laserball distribution is tested against the ratio of occupancies in central runs with flipped orientations (Section 7.1.3). A conservative 5% uncertainty in the laserball distribution appears reasonable.

- The PMT-PMT variability is determined with an uncertainty of at most 20% from the widths of the PMT occupancy ratio distributions (Section 7.1.2).

- The individual χ^2 values for each PMT to be included in the QOCAFit are used to select the data to be included in the fit. The cut is assigned at $\chi^2 < 25$ for

Syst	Factor (f_i)	Description
1	0.20	Radial scale shift (0.2%)
2	0.40	Z shift (2 cm)
3	0.40	X shift (2 cm)
4	0.20	Radial shift (1 cm)
5	0.20	Radial smear (1 cm)
6	0.50	Laserball-PMT position shift (1.5 cm)
7	0.05	Laserball distribution squared
8	0.05	Laserball distribution flat
9	0.20	PMT-PMT variability turned off
10	1.00	χ^2 cut at 16 for PMT selection
11	1.00	χ^2 cut at 9 for PMT selection

Table 7.3: *Systematics multipliers (f_i).*

the nominal fits to include most PMT's, based on the fit residual distribution obtained for the Monte Carlo runs (see Figure 7.18). For a Gaussian residual distribution, other reasonable values for this cut are at 3σ ($\chi^2 < 9$) and 4σ ($\chi^2 < 16$).

The resulting changes in extracted media attenuations for the first eleven of these systematic model or QOCAFit data selection variations are summarized in Tables 7.4 through 7.11. In these tables, the attenuations for both light and heavy water are given in units of $10^{-5}\,\mathrm{cm}^{-1}$, along with the net percentage change including the systematic reduction factor.

The main systematic effects in the attenuation lengths arise from radial positioning errors (systematics 1 and 4). The main correction to the observed light intensity is the solid angle correction, which is inversely proportional to the source-PMT distance squared. A radial scale factor of 1.01 changes the solid angle correction by 2%. To produce a compensating change of -2% demands a much larger fractional change in the attenuation coefficient. For example, with $\alpha \sim 1 \times 10^{-4}\,\mathrm{cm}^{-1}$ an intensity high

Syst	α_d	$f_i \times \Delta\alpha_d/\alpha_d$	α_h	$f_i \times \Delta\alpha_h/\alpha_h$	χ^2/dof	
0	5.79	0.0%	11.49	0.0%	1.06571	288824 / 271015
1	2.99	-9.7%	-9.73	-36.9%	1.06295	287943 / 270890
2	6.12	2.3%	13.05	5.4%	1.06890	289529 / 270866
3	5.57	-1.5%	10.00	-5.2%	1.07868	292024 / 270724
4	1.06	-16.3%	-24.78	-63.1%	1.07390	290759 / 270750
5	6.56	2.7%	16.17	8.1%	1.10086	298318 / 270987
6	4.76	-8.9%	6.72	-20.8%	1.06620	288960 / 271018
7	5.91	0.1%	25.11	5.9%	1.93994	519203 / 267639
8	5.67	-0.1%	-4.37	-6.9%	1.92713	515774 / 267639
9	5.73	-0.2%	0.87	-18.5%	2.40154	640149 / 266558
10	5.80	0.2%	9.10	-20.8%	0.98576	266017 / 269859
11	5.76	-0.4%	3.11	-72.9%	0.87422	233515 / 267111
Net		21.3%		109.9%	(summed in quadrature)	

Table 7.4: *Table of systematics for 365 nm data from February 2000. Both* α_d *and* α_h *are in units of* 10^{-5} *cm*$^{-1}$.

by +2% can be compensated by a change in attenuation coefficient of approximately -33% to $\alpha = 6.7 \times 10^{-5}$.

Figure 7.23 shows the fractional changes to the PMT response for the first eleven systematics in the September 386 data, and is illustrative of the small changes observed in the PMT angular response for any of the other wavelengths.

The derived PMT response depends on the calculated incidence angles for the various source positions. Small systematic errors in the laserball position have only a tiny effect on the calculated incidence angles. This is the primary reason why position shifts have very little effect on the derived PMT response. The PMT response is robustly determined to better than 0.5% differences by the fitting procedure.

For the 600-series Monte Carlo (parameters in Table 6.2), Table 7.12 gives the systematic variations for similar variations to the optical model, while Figure 7.24 shows the variation in PMT response. Since the expected laserball distribution is perfectly flat (*i.e.* isotropic) for the Monte Carlo, two other distributions were used:

Syst	α_d	$f_i \times \Delta\alpha_d/\alpha_d$	α_h	$f_i \times \Delta\alpha_h/\alpha_h$	χ^2/dof	
0	1.81	0.0%	56.27	0.0%	1.02304	308367 / 301422
1	-0.94	-30.4%	34.74	-7.7%	1.01858	306888 / 301291
2	2.09	6.1%	58.14	1.3%	1.05605	318076 / 301194
3	1.67	-3.3%	55.21	-0.8%	1.04167	313677 / 301130
4	-2.91	-52.1%	19.61	-13.0%	1.02940	309937 / 301084
5	2.89	11.8%	63.68	2.6%	1.05608	318279 / 301377
6	0.80	-28.0%	51.64	-4.1%	1.02302	308361 / 301421
7	1.29	-1.4%	58.36	0.2%	1.09046	324832 / 297885
8	2.24	1.2%	45.08	-1.0%	1.08538	323319 / 297885
9	1.78	-0.3%	50.25	-2.1%	2.09178	622435 / 297562
10	1.80	-0.8%	53.27	-5.3%	0.94032	282204 / 300115
11	1.79	-1.4%	50.64	-10.0%	0.83912	249511 / 297350
Net		67.9%		19.7%	(summed in quadrature)	

Table 7.5: *Table of systematics for 500 nm data from February 2000. Both α_d and α_h are in units of 10^{-5} cm^{-1}.*

Syst	α_d	$f_i \times \Delta\alpha_d/\alpha_d$	α_h	$f_i \times \Delta\alpha_h/\alpha_h$	χ^2/dof	
0	7.60	0.0%	56.06	0.0%	1.09650	147575 / 134587
1	4.33	-8.6%	41.79	-5.1%	1.08427	142235 / 131180
2	9.03	7.5%	58.03	1.4%	1.13181	155920 / 137762
3	7.87	1.4%	60.82	3.4%	1.10374	148399 / 134451
4	2.27	-14.0%	30.19	-9.2%	1.07468	140868 / 131078
5	8.80	3.2%	57.54	0.5%	1.10869	149175 / 134551
6	6.87	-4.8%	36.71	-17.3%	1.10057	150606 / 136844
7	8.82	0.8%	60.72	0.4%	5.62646	748403 / 133015
8	7.13	-0.3%	40.62	-1.4%	5.79300	770556 / 133015
9	8.19	1.5%	4.77	-18.3%	2.97764	389984 / 130971
10	8.06	6.1%	57.56	2.7%	1.00577	134717 / 133944
11	8.41	10.7%	54.93	-2.0%	0.88069	116621 / 132420
Net		22.7%		27.8%	(summed in quadrature)	

Table 7.6: *Table of systematics for 337 nm data from September 2000. Both α_d and α_h are in units of 10^{-5} cm^{-1}.*

Syst	α_d	$f_i \times \Delta\alpha_d/\alpha_d$	α_h	$f_i \times \Delta\alpha_h/\alpha_h$	χ^2/dof	
0	10.17	0.0%	16.60	0.0%	1.05335	141629 / 134456
1	7.14	-6.0%	-8.77	-30.6%	1.03571	132350 / 127787
2	11.55	5.4%	27.07	25.2%	1.07360	144341 / 134446
3	9.88	-1.2%	13.78	-6.8%	1.06683	139869 / 131107
4	5.35	-9.5%	-17.89	-41.6%	1.03613	132324 / 127710
5	11.11	1.8%	16.69	0.1%	1.05956	138974 / 131162
6	9.12	-5.2%	11.62	-15.0%	1.05401	141720 / 134458
7	10.18	0.0%	4.62	-3.6%	5.90519	786040 / 133110
8	9.10	-0.5%	8.99	-2.3%	6.09851	811772 / 133110
9	9.86	-0.6%	7.18	-11.4%	2.30910	306769 / 132852
10	9.99	-1.7%	13.62	-17.9%	0.97497	130550 / 133901
11	9.81	-3.6%	8.97	-46.0%	0.86880	115206 / 132604
Net		14.2%		78.4%	(summed in quadrature)	

Table 7.7: *Table of systematics for 365 nm data from September 2000. Both α_d and α_h are in units of 10^{-5} cm^{-1}.*

Syst	α_d	$f_i \times \Delta\alpha_d/\alpha_d$	α_h	$f_i \times \Delta\alpha_h/\alpha_h$	χ^2/dof	
0	9.53	0.0%	16.80	0.0%	1.03096	141963 / 137700
1	6.73	-5.9%	-9.42	-31.2%	1.02415	137563 / 134320
2	10.57	4.4%	28.07	26.8%	1.05989	149360 / 140920
3	9.61	0.3%	18.00	2.8%	1.04145	143321 / 137616
4	4.71	-10.1%	-16.61	-39.8%	1.02094	137025 / 134215
5	11.13	3.4%	24.46	9.1%	1.04000	143164 / 137658
6	8.49	-5.4%	13.10	-11.0%	1.03478	144834 / 139967
7	9.17	-0.2%	7.07	-2.9%	4.93298	672430 / 136313
8	9.07	-0.2%	0.01	-5.0%	5.05623	689230 / 136313
9	9.24	-0.6%	8.26	-10.2%	2.26561	308075 / 135979
10	9.37	-1.6%	13.14	-21.8%	0.95613	131142 / 137159
11	9.22	-3.3%	6.97	-58.5%	0.84949	115384 / 135827
Net		14.5%		86.7%	(summed in quadrature)	

Table 7.8: *Table of systematics for 386 nm data from September 2000. Both α_d and α_h are in units of 10^{-5} cm^{-1}.*

Syst	α_d	$f_i \times \Delta\alpha_d/\alpha_d$	α_h	$f_i \times \Delta\alpha_h/\alpha_h$	χ^2/dof	
0	7.28	0.0%	20.32	0.0%	1.09426	161783 / 147847
1	4.32	-8.1%	-1.15	-21.1%	1.08248	156380 / 144464
2	8.34	5.8%	28.36	15.8%	1.12541	166303 / 147771
3	7.07	-1.2%	19.83	-1.0%	1.11519	161123 / 144480
4	2.52	-13.1%	-13.08	-32.9%	1.08562	156743 / 144382
5	8.58	3.5%	29.89	9.4%	1.10578	163476 / 147837
6	6.23	-7.2%	15.57	-11.7%	1.09434	161794 / 147847
7	7.09	-0.1%	8.17	-3.0%	4.85989	710452 / 146187
8	6.75	-0.4%	21.83	0.4%	4.98113	728177 / 146187
9	7.12	-0.5%	17.78	-2.5%	2.16267	316361 / 146283
10	7.17	-1.6%	20.28	-0.2%	1.01410	149299 / 147223
11	7.03	-3.6%	17.26	-15.1%	0.90133	131323 / 145700
Net		18.8%		47.4%	(summed in quadrature)	

Table 7.9: *Table of systematics for 420 nm data from September 2000. Both* α_d *and* α_h *are in units of* 10^{-5} *cm*$^{-1}$.

Syst	α_d	$f_i \times \Delta\alpha_d/\alpha_d$	α_h	$f_i \times \Delta\alpha_h/\alpha_h$	χ^2/dof	
0	4.91	0.0%	50.61	0.0%	0.96757	127520 / 131794
1	2.05	-11.7%	25.30	-10.0%	0.95738	122942 / 128415
2	6.13	10.0%	63.37	10.1%	1.00429	135610 / 135031
3	4.75	-1.2%	48.90	-1.4%	0.98935	130302 / 131705
4	0.27	-18.9%	20.94	-11.7%	0.95730	122844 / 128324
5	6.45	6.3%	57.43	2.7%	0.98227	129456 / 131792
6	3.97	-9.6%	46.14	-4.4%	0.97423	130591 / 134046
7	4.68	-0.2%	43.88	-0.7%	2.51722	328568 / 130528
8	4.61	-0.3%	40.22	-1.0%	2.55406	333376 / 130528
9	4.66	-1.0%	40.72	-3.9%	2.26447	293717 / 129707
10	4.80	-2.2%	47.76	-5.6%	0.89057	116895 / 131259
11	4.64	-5.4%	42.28	-16.5%	0.78555	102129 / 130010
Net		27.6%		26.2%	(summed in quadrature)	

Table 7.10: *Table of systematics for 500 nm data from September 2000. Both* α_d *and* α_h *are in units of* 10^{-5} *cm*$^{-1}$.

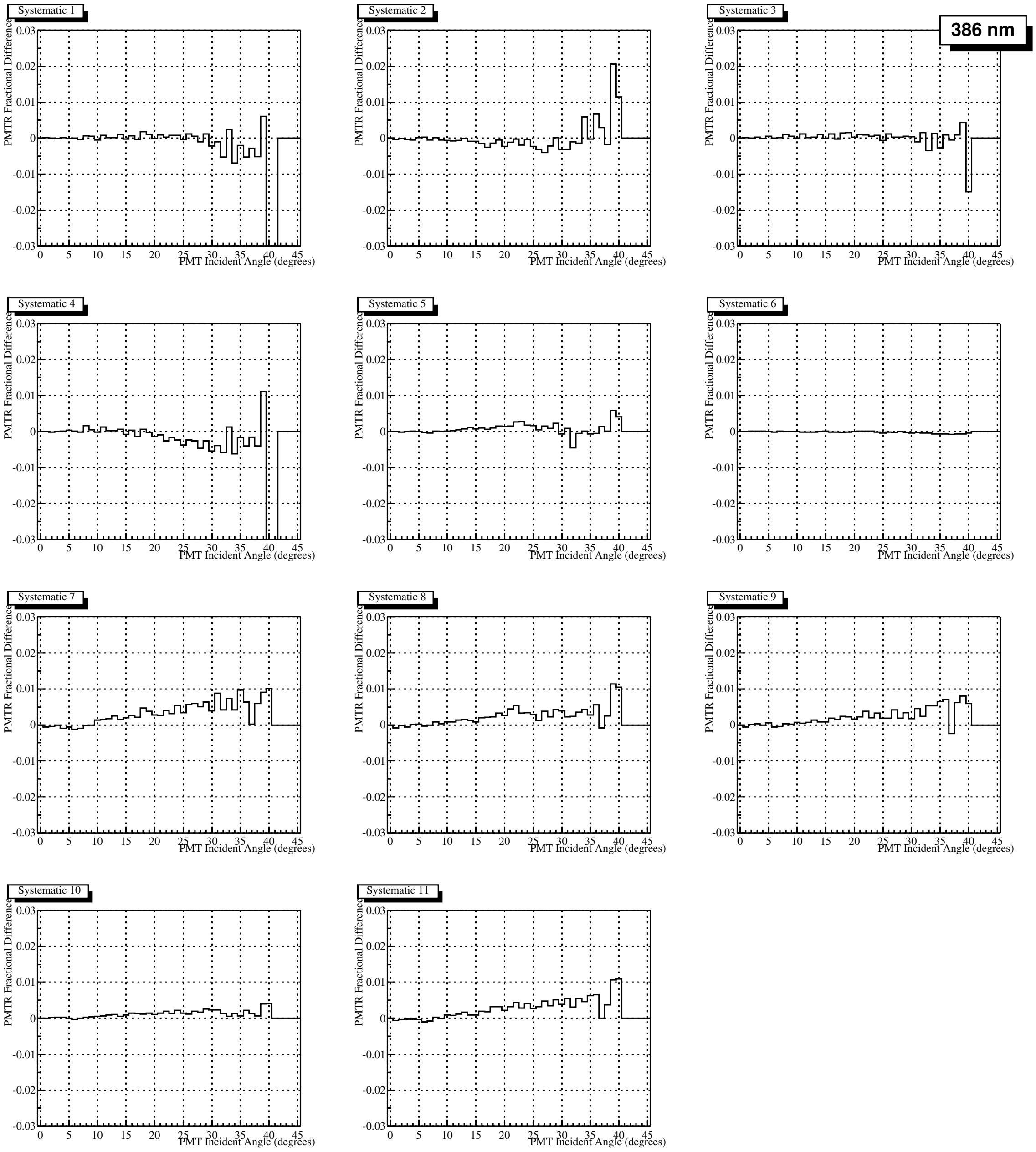

Figure 7.23: *Effect of systematic model variations on PMT angular response for 386 nm data from September 2000.*

Syst	α_d	$f_i \times \Delta\alpha_d/\alpha_d$	α_h	$f_i \times \Delta\alpha_h/\alpha_h$	χ^2/dof	
0	4.44	0.0%	259.87	0.0%	1.02102	137539 / 134707
1	1.67	-12.5%	233.98	-2.0%	1.01738	137006 / 134666
2	5.17	6.6%	267.89	1.2%	1.06452	143347 / 134659
3	4.79	3.1%	268.62	1.3%	1.05574	142189 / 134682
4	-0.29	-21.3%	217.53	-3.3%	1.02002	137267 / 134573
5	5.23	3.5%	266.50	0.5%	1.04291	140490 / 134710
6	3.42	-11.5%	254.94	-0.9%	1.02116	137559 / 134708
7	4.12	-0.4%	267.82	0.2%	3.19691	426363 / 133367
8	4.09	-0.4%	245.18	-0.3%	3.25618	434267 / 133367
9	4.18	-1.2%	253.46	-0.5%	2.34810	311752 / 132768
10	4.24	-4.6%	258.09	-0.7%	0.94074	126190 / 134138
11	4.11	-7.5%	257.75	-0.8%	0.83916	111518 / 132893
Net		29.8%		4.5%	(summed in quadrature)	

Table 7.11: *Table of systematics for 620 nm data from September 2000. Both α_d and α_h are in units of 10^{-5} cm^{-1}.*

systematic 7 correponds to a laserball distribution $1 + 0.1\sin(\phi)$, and systematic 8 is $1 + 0.1\cos\theta$. Again, only the radial shifts in position show a large systematic effect, but these should be multiplied by the expected uncertainty in position, which is very small for the Monte Carlo. In Table 7.12, the same multipliers as for the data have been used (see Table 7.3).

In Figure 7.25 the effect of varying the prompt time window is shown. A 6 ns increase in time window half-width, from the nominal 4 ns to 10 ns, results in a decrease of $1 \times 10^{-5}\,\mathrm{cm}^{-1}$ or 10% in α_d. For α_h, there is almost no sensitivity to changes in time window width.

All wavelengths except 337 nm look similar in shape to the curves shown in Figure 7.25 for 386 nm. The September 337 nm departs from the norm by having a positive slope for the variation in α_d, as shown in Figure 7.26. Because the 337 nm data likely includes up to 10% fluroescence to another longer wavelength band, the attenuation behaviour with time window width is no longer dominated by Rayleigh

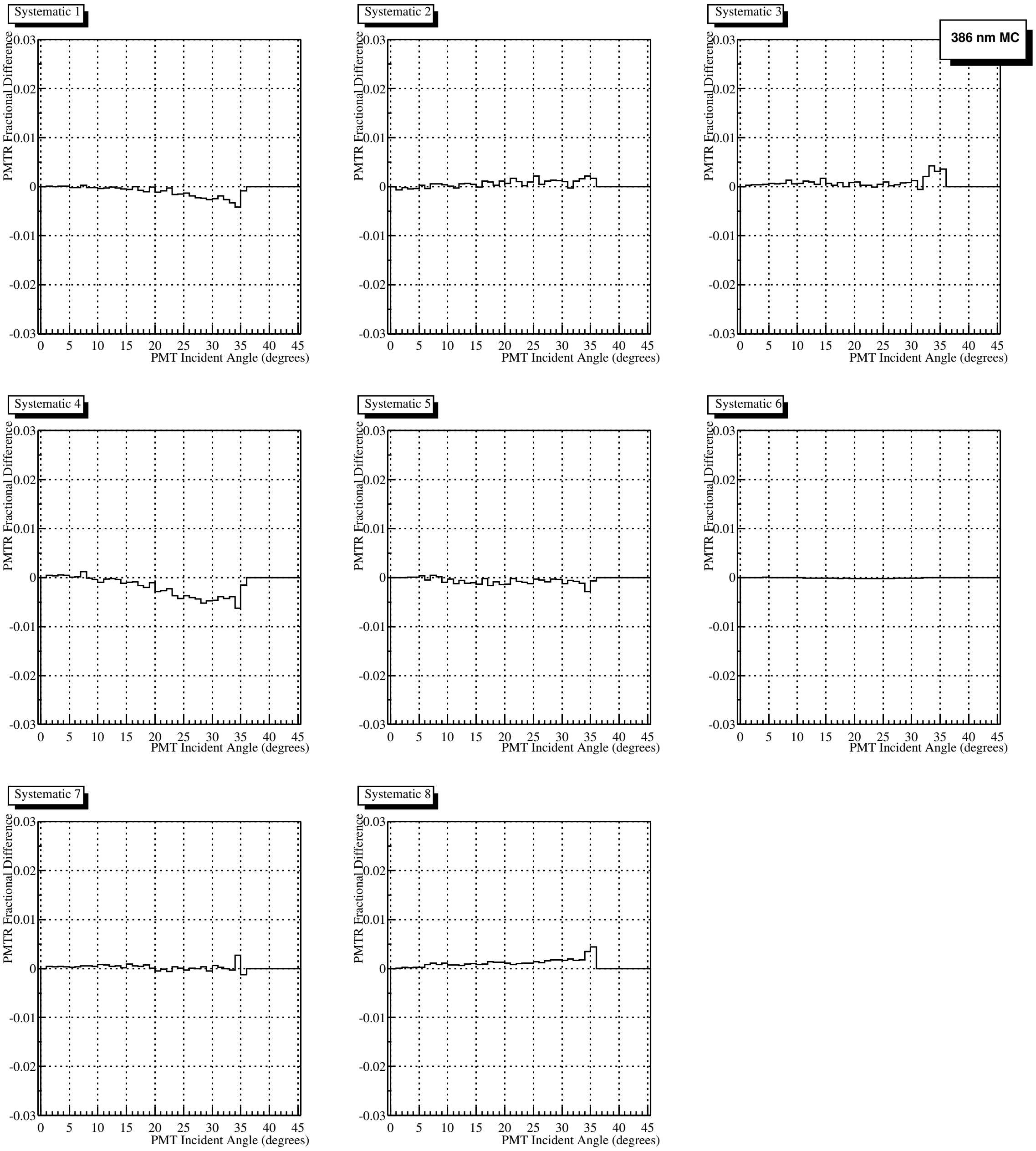

Figure 7.24: *Effect of systematic model variations on PMT angular response for the 600-series Monte Carlo.*

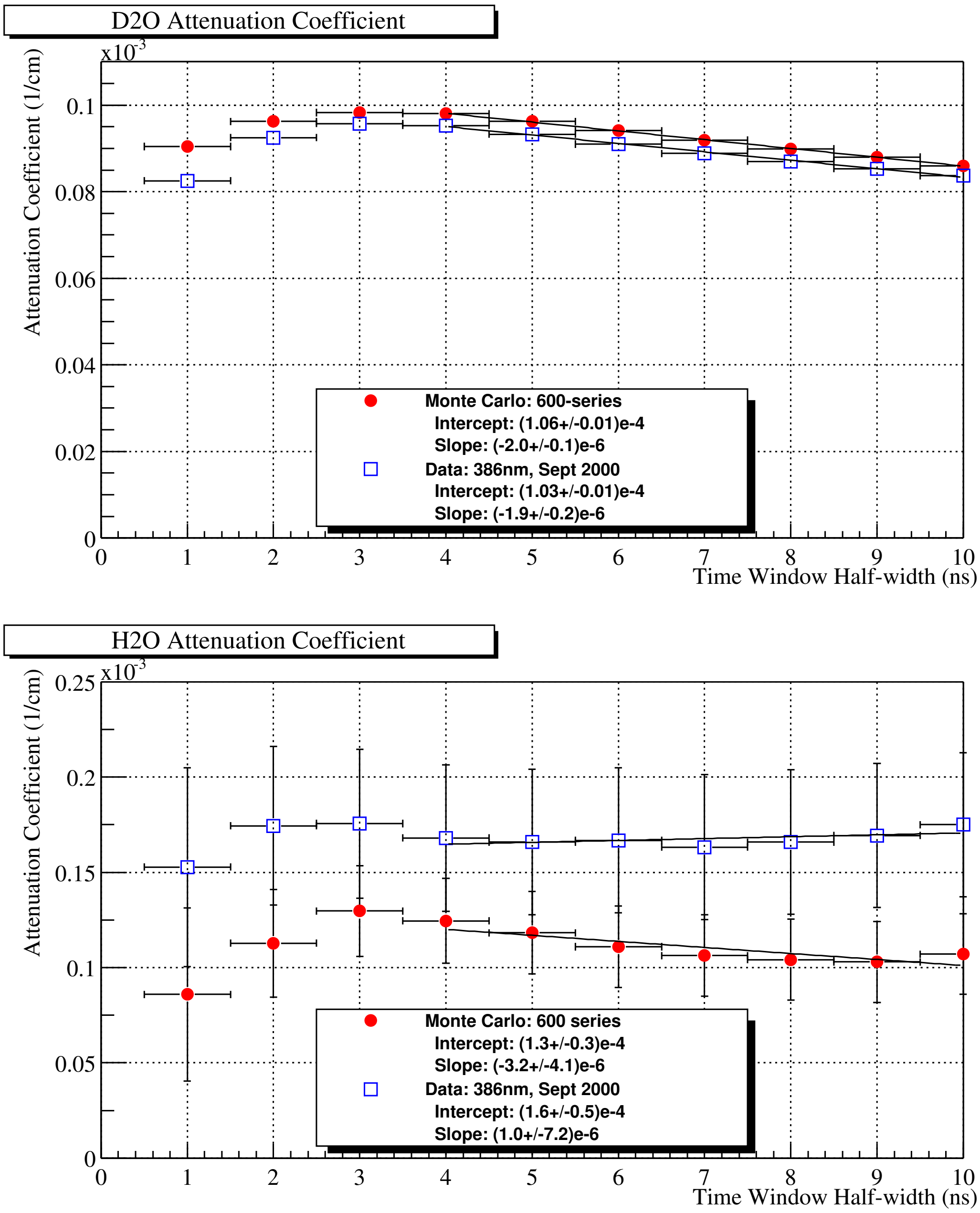

Figure 7.25: *Attenuation parameters for 386 nm data and 600-series Monte Carlo as a function of prompt time window width. The error bars shown are the single-parameter errors from the diagonal elements of the QOCAFit covariance matrix.*

Syst	α_d (10^{-5}cm^{-1})	$\Delta\alpha_d/\alpha_d$ (Net)	α_h (10^{-5}cm^{-1})	$\Delta\alpha_h/\alpha_h$ (Net)	χ^2/dof	
0	9.80	0.0%	12.46	0.0%	0.91764	86800 / 94590
1	6.93	-5.9%	-8.89	-34.3%	0.91760	86729 / 94518
2	10.69	3.6%	21.97	30.5%	1.00524	95013 / 94518
3	10.63	3.4%	22.30	31.6%	1.00312	94761 / 94466
4	5.22	-9.3%	-15.88	-45.5%	0.93905	85282 / 90818
5	9.27	-1.1%	9.41	-4.9%	0.94933	89743 / 94533
6	8.74	-5.4%	7.49	-19.9%	0.91766	86802 / 94590
7	10.20	0.2%	14.98	1.0%	6.55720	623039 / 95016
8	9.77	-0.0%	10.00	-1.0%	0.98683	93764 / 95016

Table 7.12: *Table of systematics for 600-series Monte Carlo.*

scattering but is also affected by the fluorescence light time distribution. Short of measuring the fluorescence directly, there is very little that can be done about its contamination of the 337 nm fit result. Further discussion of fluorescence in the 337 nm data is in Section 8.1.4.

The slopes and intercepts for the attenuation coefficient as a function of time window width for all data runs are listed in Table 7.13. For D_2O the general trend is for the slope to get steeper for the shorter wavelengths, while for H_2O there is no significant trend as a function of wavelength.

The optical Monte Carlo series include a number of variations on the amount of Rayleigh scattering (0, 1, 2 and 4 times nominal) and the levels of absorption. Rayleigh scattered light which is included in the prompt time window affects the derived attenuation coefficients, as shown in Figure 7.27. Rayleigh scattering produces late PMT hits with respect to the prompt time. In principle, therefore, a narrow prompt integration window is immune to the effects of Rayleigh scattering. The finite time resolution of the PMT's (~ 1.5 ns) and the pulse width of the laser (~ 1 ns) set a lower bound on the usable minimum window width of about 2-3 ns. For wide windows, the net attenuation decreases because the Rayleigh scattered light remains

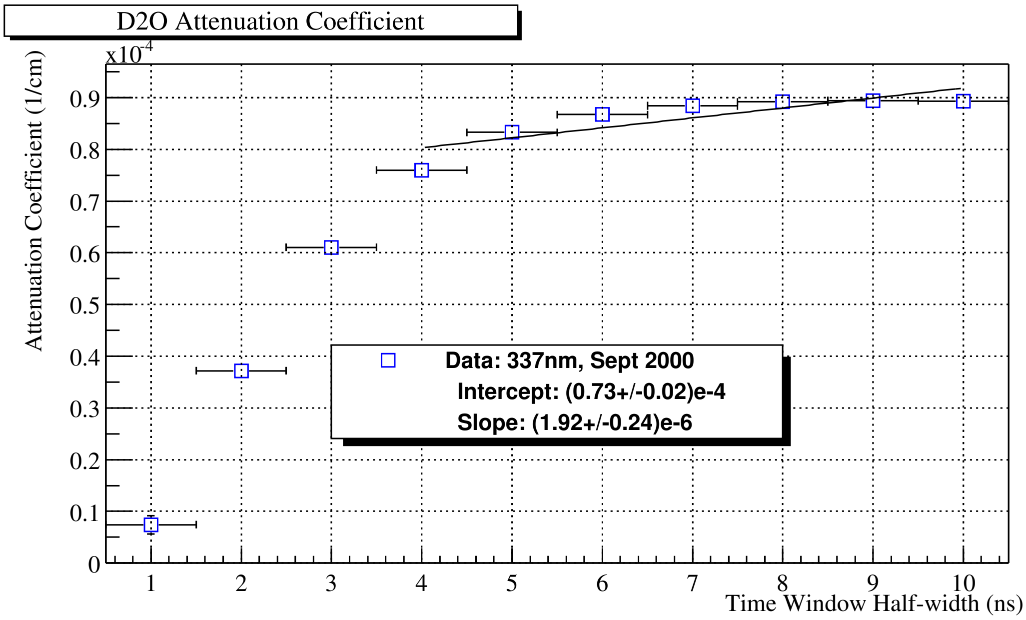

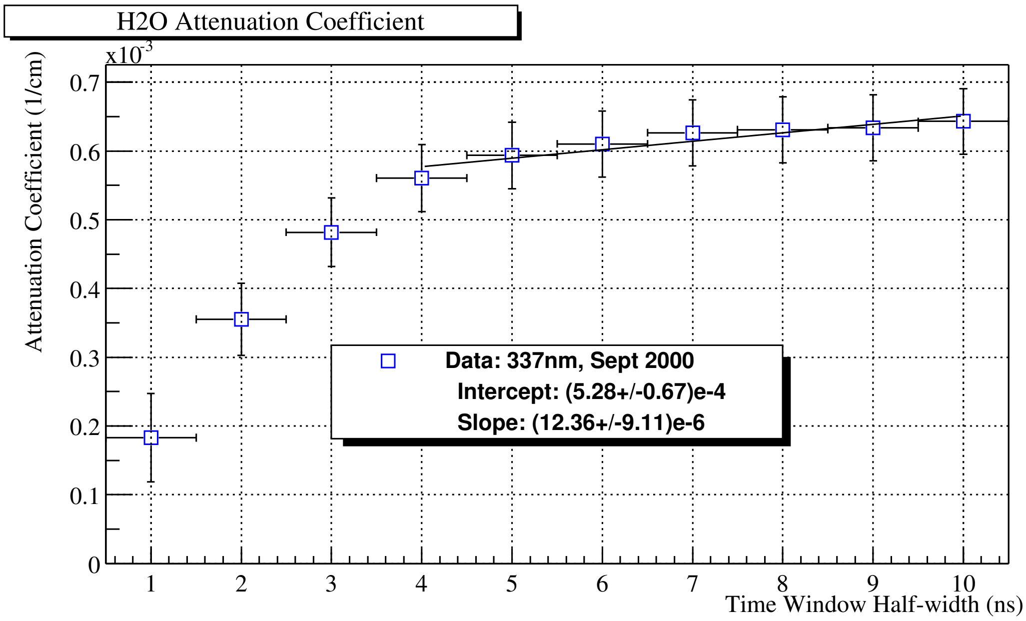

Figure 7.26: *Attenuation parameters for 337nm data as a function of prompt time window width. The error bars shown are the single-parameter errors from the diagonal elements of the QOCAFit covariance matrix.*

Data	D_2O		H_2O	
	Slope ($10^{-6}\,\mathrm{cm}^{-1}/\mathrm{ns}$)	Intercept ($10^{-4}\,\mathrm{cm}^{-1}$)	Slope ($10^{-6}\,\mathrm{cm}^{-1}/\mathrm{ns}$)	Intercept ($10^{-4}\,\mathrm{cm}^{-1}$)
Sept 337 nm	$+1.92 \pm 0.24$	0.73 ± 0.02	12.4 ± 9.1	5.3 ± 0.7
Sept 365 nm	-1.15 ± 0.21	1.07 ± 0.02	4.7 ± 7.7	1.4 ± 0.6
Sept 386 nm	-1.95 ± 0.20	1.03 ± 0.01	1.0 ± 7.2	1.6 ± 0.5
Sept 420 nm	-1.79 ± 0.17	0.80 ± 0.01	-3.1 ± 6.6	2.0 ± 0.5
Sept 500 nm	-1.24 ± 0.19	0.54 ± 0.01	-2.5 ± 6.5	5.2 ± 0.5
Sept 620 nm	-0.51 ± 0.19	0.46 ± 0.01	0.1 ± 7.1	25.9 ± 0.5
Feb 365 nm	-1.47 ± 0.12	0.64 ± 0.01	-3.9 ± 5.1	1.2 ± 0.4
Feb 500 nm	-0.74 ± 0.11	0.21 ± 0.01	-5.7 ± 4.7	5.7 ± 0.4

Table 7.13: *Slope and intercept values for the attenuation results as a function of time window for the September and February 2000 data.*

in the window. The slope of the attenuation coefficient as a function of time window width serves as a diagnostic for the level of Rayleigh scattering present in the data. The absolute values depend on the absorption and on the scattering and provide important information about the total attenuation as a function of prompt window width.

In Figure 7.27, the 300-series Monte Carlo has no Rayleigh scattering and the change in α between 4 and 10 ns is nearly zero for both H_2O and D_2O. (The parameters for the Monte Carlo run series are listed in Table 6.2). For the 600-series Monte Carlo the D_2O attenuation changes by 10% between 4 and 10 ns, while the H_2O attenuation only changes by 5%. The 700-series Monte Carlo includes 4 times the nominal amount of Rayleigh scattering in all media, and the changes in attenuation with time window width are commensurately larger. With no absorption and twice the nominal amount of Rayleigh scattering, the 800-series simulation results in 20% change in α_d and 10% change in α_h, corresponding to double the variation seen in the 600-series result. Unlike the general trends in the data, the slopes for the Monte Carlo results are well-correlated, for both D_2O and H_2O, with the amount of

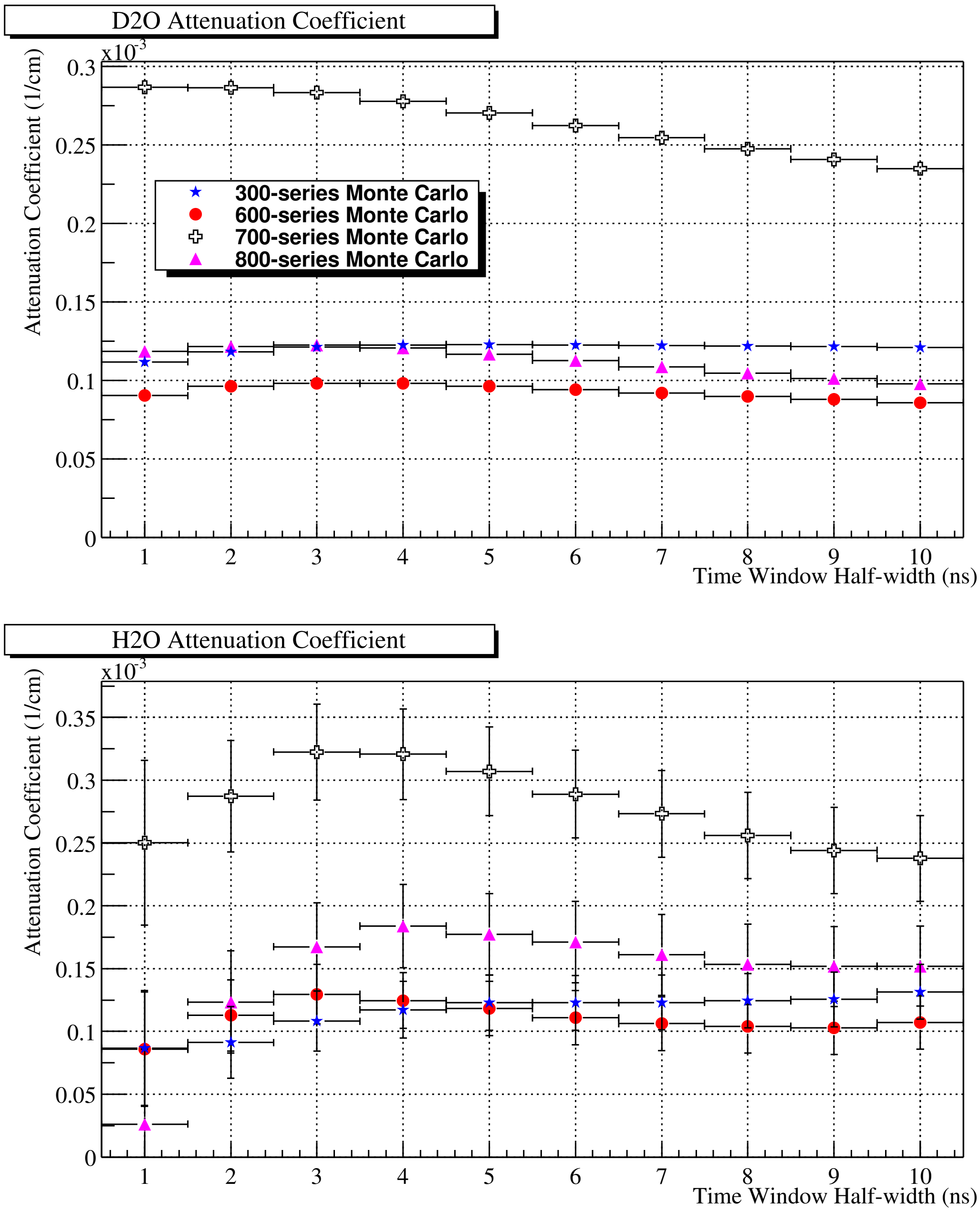

Figure 7.27: *Attenuation parameters for the 300-, 600-, 700-, and 800-series Monte Carlo simulations (see Table 6.2) as a function of prompt time window width. The error bars shown are the single-parameter errors from the diagonal elements of the QOCAFit covariance matrix.*

Series	D_2O Slope ($10^{-6}\,\mathrm{cm}^{-1}/\mathrm{ns}$)	D_2O Intercept ($10^{-4}\,\mathrm{cm}^{-1}$)	H_2O Slope ($10^{-6}\,\mathrm{cm}^{-1}/\mathrm{ns}$)	H_2O Intercept ($10^{-4}\,\mathrm{cm}^{-1}$)
300	-0.29 ± 0.12	1.242 ± 0.009	1.7 ± 4.2	1.1 ± 0.3
600	-2.03 ± 0.12	1.063 ± 0.009	-3.2 ± 4.1	1.3 ± 0.3
700	-7.23 ± 0.19	3.060 ± 0.014	-14.5 ± 6.6	3.8 ± 0.5
800	-3.84 ± 0.18	1.358 ± 0.013	-5.8 ± 6.1	2.0 ± 0.4

Table 7.14: *Slope and intercept values for the Monte Carlo attenuation results as a function of time window.*

Rayleigh scattering in each simulation.

8 Optical Calibration: Discussion

The QOCAFit results indicate significantly less attenuation in D_2O than previously measured. The H_2O measurements are comparable to the literature values for water.

In order to make full use of the attenuation measurements, they must be separated into absorption and scattering contributions. Scattered light is not removed from the signal, but only shifted to later times because of the increased path length the scattering photons have to travel. Increasing the width of the prompt time window will include more of the scattered light, thereby reducing the effective attenuation.

The PMT response curve is needed for calculations of the detector response. The phenomenological grey disk PMT model accurately accounts for the prompt light detection efficiency variation with incident angle. However, the grey disk model cannot realistically simulate reflections from the PMT's. The reflected light pattern produced by the real PMT and reflector assemblies is better simulated using the SNOMAN 3D-PMT model, but this model does not agree with the *in situ* measurements of PMT response. Modifications to the 3D-PMT model which reproduce both the PMT response curves and the late light distributions are highly desirable, and are being pursued by the SNO collaboration.

λ (nm)	α_d ($10^{-5}\,cm^{-1}$)	σ_{syst}	σ_{total}	α_h ($10^{-5}\,cm^{-1}$)	σ_{syst}	σ_{total}
September data						
337	7.60 ± 1.73	22.7%	22.8%	$56. \pm 16.$	28.%	29.%
372	10.17 ± 1.45	14.2%	14.2%	$17. \pm 14.$	78.%	82.%
386	9.53 ± 1.39	14.5%	14.6%	$17. \pm 15.$	87.%	90.%
420	7.28 ± 1.37	18.8%	18.8%	$20. \pm 10.$	47.%	50.%
506	4.91 ± 1.36	27.6%	27.7%	$51. \pm 14.$	26.%	27.%
620	4.44 ± 1.33	29.8%	29.9%	$260. \pm 12.$	4.5%	4.7%
February data						
372	5.79 ± 1.23	21.3%	21.3%	11.5 ± 12.9	110.%	112.%
506	1.81 ± 1.23	67.9%	68.0%	56.3 ± 11.4	19.7%	20.2%

Table 8.1: *Attenuation results from the optical fit in units of $10^{-5}\,cm^{-1}$. The systematic uncertainties (σ_{syst}) come from Tables 7.4 through 7.11, and are added in quadrature to the statistical errors to obtain the total uncertainty (σ_{total}).*

8.1 Attenuation Uncertainties

The results from the QOCAFit procedure with total errors are shown in Table 8.1. The total errors are obtained by adding in quadrature the statistical and systematic errors reported in Sections 7.1 and 7.4, respectively. The systematic uncertainties dominate the total error assigned to the measurements of both α_d and α_h. The means of the broad emission spectra of the 365 and 500 nm dyes (Figure 5.2) are used in reporting the attenuation results in this chapter; the means are 372 and 506 nm, respectively.

The D_2O attenuation coefficients are shown in Figure 8.1. For clarity, only the total errors are shown in the figure. The measurements of Boivin et al. [1] are taken at seven wavelengths: 254, 313, 366, 406, 436, 546 and 578 nm.

The H_2O attenuation coefficients are shown in Figure 8.2. For the H_2O four data sets are shown in order to cover the wavelength range of interest:

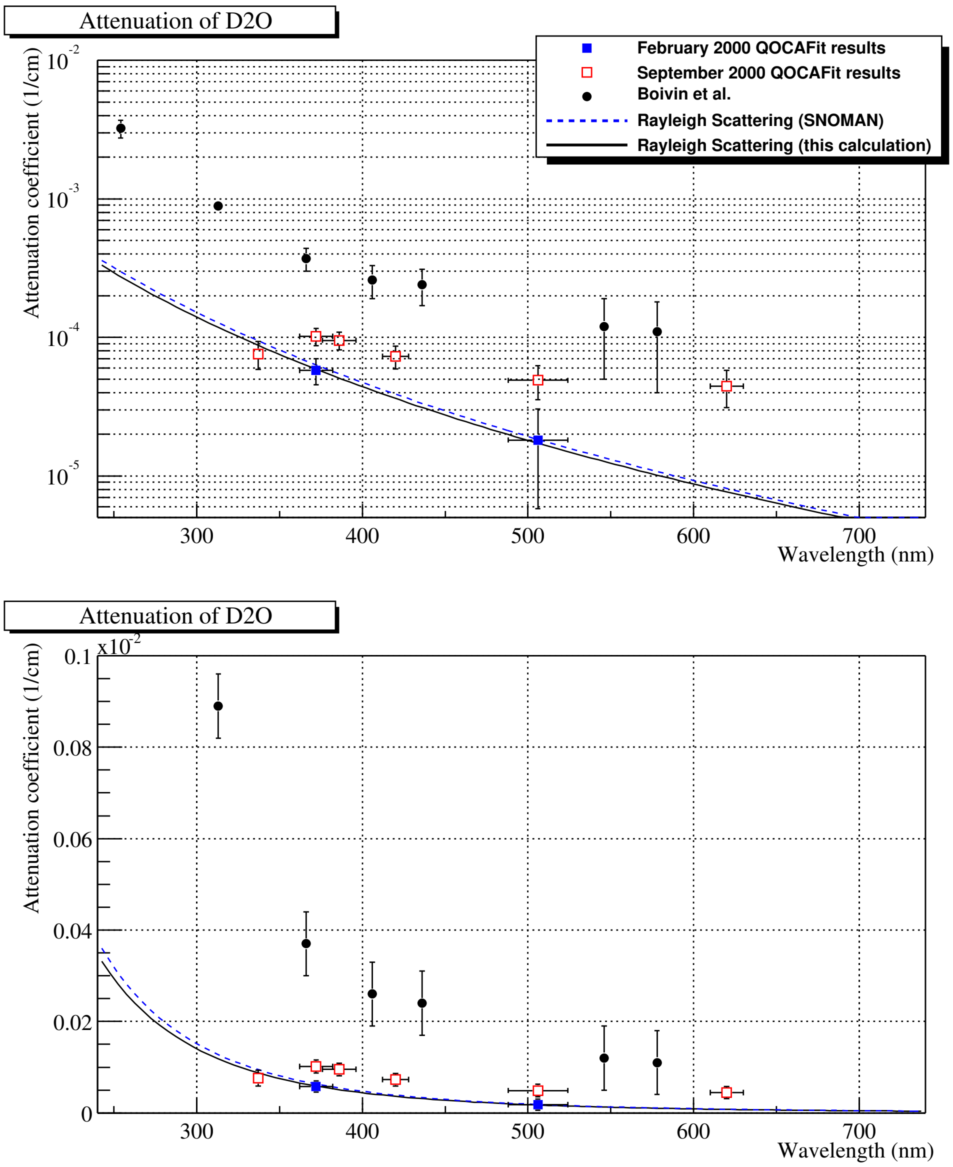

Figure 8.1: *Attenuation length measurements for D_2O.*

$\lambda \leq 320\,\text{nm}$	Quickenden and Irvin [68]
$\lambda \geq 380\,\text{nm}$	Pope and Fry [71]
$200 \leq \lambda \leq 800\,\text{nm}$	Smith and Baker [78]
$\lambda = 254, 313, 366, 406, 436, 546, 578\,\text{nm}$	Boivin et al. [1]

For the H_2O, the Rayleigh scattering calculation of Buiteveld et al. [64] compares very well to the table given in Smith and Baker [78] over their common range ($350 \leq \lambda \leq 800\,\text{nm}$). The SNOMAN Rayleigh scattering function is taken from the program's code for H_2O and for D_2O. The third scattering calculation is based on an extensive literature search conducted by Pickel [79] and is executed for a temperature of 8°C. This temperature is only slightly below the nominal detector conditions of 11 ± 2°C [80]. The uncertainty in this calculation is estimated to be 5% for H_2O, and 9% for D_2O [79]. If the temperature is changed from 8°C to 25°C for all parameters in the calculation of the Rayleigh scattering coefficient (see Equation 8.3), the calculations of Pickel [79] reproduce the SNOMAN calculations. The change in temperature is equivalent to scaling the SNOMAN Rayleigh scattering coefficients by 0.94 for D_2O, 0.95 for acrylic, and 0.87 for H_2O.

8.1.1 Heavy Water Attenuation

The measurements of Boivin et al. [1] represent the state of the art in D_2O measurements. Up until now, that group had the cleanest and largest sample of D_2O available for analysis (10 kg). Earlier papers (cited in Boivin et al.) obtained significantly higher attenuation coefficients, often by several orders of magnitude. These measurements were part of the motivation for the work by Boivin et al. because they were seeking to prove the viability of D_2O as an optical medium for SNO.

The small attenuation coefficients measured in the heavy water are essential to understanding the radial dependence of the energy scale. For example, in earlier work by Ford [11] the larger attenuation coefficients of Boivin et al. and the *ex situ* PMT re-

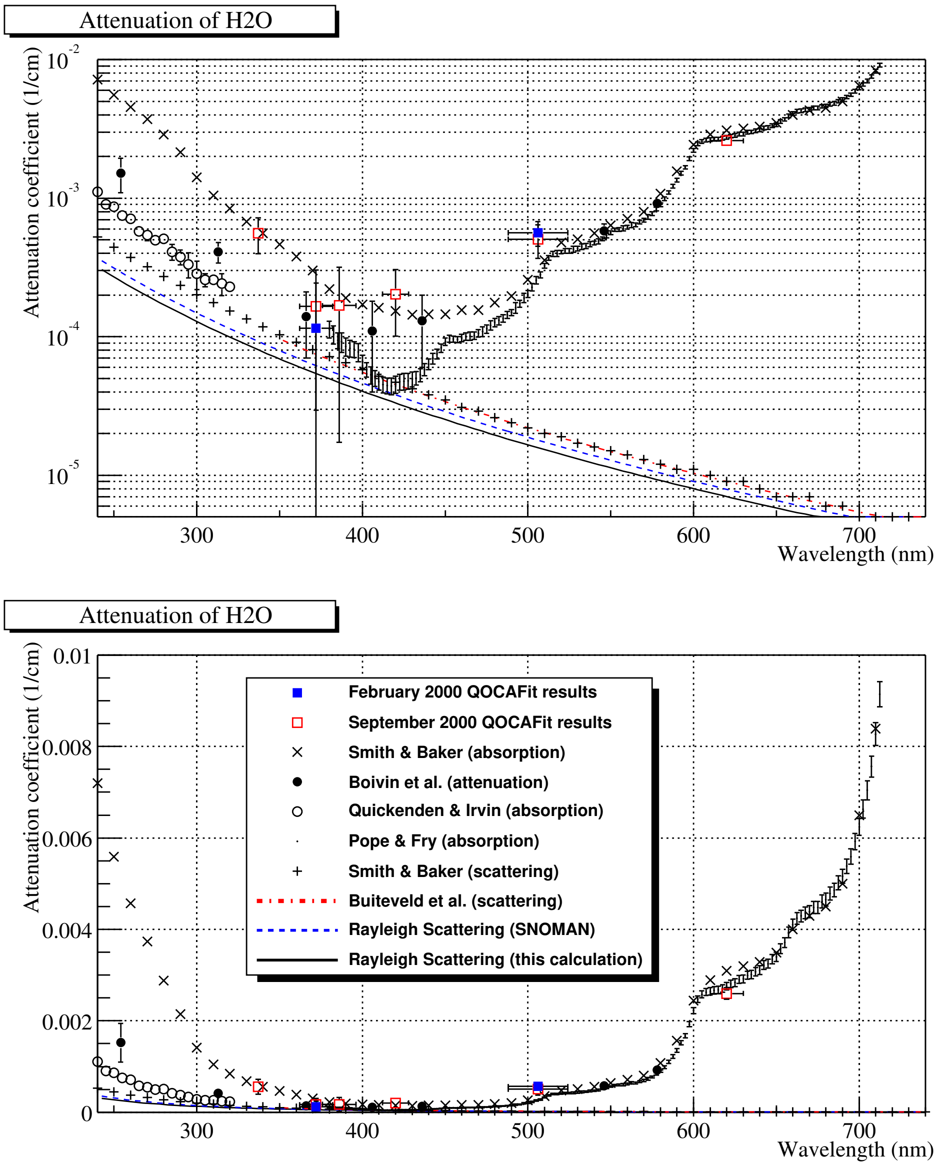

Figure 8.2: *Attenuation length measurements for H_2O. The data of Pope and Fry [71] are given every 2.5 nm over the range 380 − 727.5 nm and are displayed with small (black) error bars.*

sponse measurements of Lay [2] result in a calculated detector response with a similar radial dependence to that observed with the ^{16}N source measurements [56]. However, the angular $\vec{u} \cdot \vec{r}$ dependence is severely affected by the larger D_2O attenuation, in disagreement with the distributions measured with the ^{16}N source. By measuring both the D_2O attenuation and the PMT response in the detector, a self-consistent set of parameters is obtained by the QOCAFit procedure. Using these parameters in the optical model of the detector implemented in the RSP response function results in agreement for both the radial (R) and the angular ($\vec{u} \cdot \vec{r}$) dependences of the ^{16}N source measurements.

8.1.2 Light Water Attenuation

The results for α_h obtained in this work are compatible with the literature values. However, the uncertainty on the value of the attenuation coefficient means the result is not competitive with the best determinations in the literature. In particular, the results of Pope and Fry [71, P&F] are considered to represent the state of the art in the marine optics community (Højerslev [81]; see also Fry [82]).

The success of P&F at measuring extremely low absorption coefficients and their sensitivity to several higher-order OH-resonances can be attributed to their extreme care in preparing their water samples and to the development of a new measurement apparatus. Their apparatus consists of a special quartz flask in an integrating cavity and allows very long path lengths to be sampled. This technique is nearly immune to the effects of scattering on the measurements – a distinct advantage when attempting to determine water absorption with precision. The samples of pure water were used within approximately 30 minutes of being prepared to avoid possible contamination due to leaching from the quartz containment vessel. The authors found that the attenuation in the blue ($\sim 420\,\mathrm{nm}$) was already degraded after only 4 h sitting in a quartz flask. The same laboratory obtained substantial agreement for water absorption using a different measurement technique (photothermal probe beam deflection) and the same water source [69], lending further support to the validity of their results.

The results of Quickenden and Irvin [68] represent the most reliable determination of the attenuation of water in the UV (220–320 nm) because of the great care they took in preparing their water samples. The extrapolation of this measurement past 320 nm meets the values of P&F at 380 nm, and has a slope similar to that of Smith and Baker [78, S&B]. This extrapolation procedure is endorsed by one of the authors (Fry [82]).

The tabulated work of S&B is primarily a literature review and synthesis of available data for absorption in pure fresh and salt water, including their own measurements over the range 300–400 nm. These authors also present a tabulation of the calculated Rayleigh scattering coefficient, presumably made for typical laboratory temperatures of 20–25°C. Their absorption results agree well with the results obtained in P&F for pure water which has been stored in Pyrex for several days. Given the relatively dirty environment for the H_2O in SNO, which includes PSUP steel and several types of plastic, it is reasonable that the measurements of α_h are in better agreement with the S&B determination than the P&F measurements.

8.1.3 Changes between February and September, 2000

The difference between February and September D_2O attenuations are likely a real change in the water clarity. At 372 nm the change is $(4.4 \pm 1.9) \times 10^{-5}\text{cm}^{-1}$ (2.3σ), and at 506 nm the change is $(3.1 \pm 1.8) \times 10^{-5}\text{cm}^{-1}$ (1.7σ).

This change in α_d is consistent with the differences found using the same fit procedure for the recirculation tests done in January 2001 [8]. In these tests, a short optical scan was performed before and after one week of D_2O recirculation (long enough to completely turn over the water volume, assuming no mixing on the return). The D_2O attenuation did not change between September 2000 and the first optical scan before recirculation. After recirculation, the D_2O had a lower attenuation coefficient. It was also found that manganese levels decreased from 2 ppb to 1 ppb as a result of recirculation [83]. The most likely source of manganese is the D_2O radioactive assay process, which was carried out regularly since the detector was filled with water.

The optical analysis is based on occupancy ratios, where the PMT efficiencies drop out entirely from the analysis. There is no mechanism to couple an overall shift in detector gain to the attenuation coefficient measurements.

The change between February and September attenuations is unable to produce a large overall detector gain shift, when averaged over the Cherenkov spectrum. This is difficult to demonstrate conclusively, because we only have the full wavelength spectrum of data in September 2000. The change at 372 nm is consistent with a reduction of about 2% in observed light intensity at that wavelength. The change at 506 nm produces a completely negligible response change.

8.1.4 Attenuation at 337 nm

Fluorescence in the quartz fibres at 337 nm produces delayed light at longer wavelengths at the laserball [11]. Communications with the fibre manufacturer confirm that ultra-violet excitation in their fibres produces fluorescence, and that this is largely dependent on the levels of impurities in the quartz. Ongoing improvements to the manufacturing methods of high-purity quartz used to produce the fibre optics are expected to lower the fluorescence in the future.

For the fibre optic used in February 2000, the fluorescence was found to contribute $(13 \pm 4)\%$ to the output of the laserball [11]. A time constant of $9.1 \pm 0.8\,\mathrm{ns}^{-1}$ is obtained by comparing the time spectrum of the laserball at 337 nm to the time spectrum at 500 nm taken with the unfilled detector. This is consistent with fluorescent lifetimes for atomic transitions [84].

The exponential increase in absorption with decreasing wavelength below 350 nm is the same for H_2O and D_2O in the literature (see Figures 8.2 and 8.2). Extrapolating from the measured values for α_d at 365 and 386 nm using the slope derived from the combined literature values gives a value for the attenuation of $\alpha_d(337\,\mathrm{nm}) = 2.2\times10^{-4}\,\mathrm{cm}^{-1}$. This value is recommended for use in simulations and data processing for SNO because it is a more realistic estimate of the attenuation, and is free from the influence of fluorescence in the fibre optic.

The fit value for $\alpha_h(337\,\mathrm{nm})$ is not similarly adjusted. The effects of a small change in attenuation at this wavelength is expected to have only a tiny impact on the overall detector response to Cherenkov light, which is essentially determined by the acrylic attenuation below 350 nm.

8.2 PMT Response

The PMT response curves are consistent up to 32° between February and September 2000. There is less than about 0.5% decrease in response over the 7 month interval. Combining statistical and systematic uncertainties, which are both about 0.5% on an absolute scale, the change is less than a 1-sigma effect.

The differences observed with respect to the *ex situ* measurements reported in Lay [2] and modeled in SNOMAN are significant. Because only four PMT's with reflectors were measured in the earlier work by Lay, the most likely source of the discrepancy is a systematic difference between those PMT's and the average response behaviour of the much larger sample of $\sim$ 9400 PMT's available for the *in situ* measurements using QOCAFit. A reasonable phenomenological change to the distribution of photocathode material thickness on the inner surface of the phototube glass appears to resolve the discrepancy [85]. This change in the SNOMAN PMT model reproduces the QOCAFit PMT response measurements with differences of $\lesssim 2\%$.

8.3 Covariances and Parameter Errors

In showing only the normalized covariances C_{ij}, the signs of the covariance matrix elements have been lost. However, of all the covariances examined, only the (negative) covariance between α_h and α_a is found to be significant. For these two parameters, increasing one results in the decrease of the other to obtain the same predicted PMT intensities. By fixing α_a to the *ex situ* measured values, all of the uncertainty in the combined attenuation due to the acrylic and H_2O layers has been assigned to α_h. The uncertainty in α_a of 10–20% (Table 7.1) implies that the reported uncertainty in α_h is slightly overestimated.

Because of the functional dependence of the PMT intensities on the attenuations and on the PMT response, the covariance is mostly positive between these two quantities. An increase in attenuation reduces the predicted intensity, and is compensated for by an increase in PMT response.

None of the fits showed any evidence of significant covariance between the detector and laserball parameters. Small negative covariances are found in the the polynomial coefficients of the laserball mask and the histogrammed laserball distribution. The covariances of the detector parameters with the laserball mask function (P_6) were $\lesssim 0.1\%$, and with the laserball distribution histogram ($H(\cos\theta_{LB}, \phi_{LB})$) they were $\lesssim 0.5\%$.

8.4 Rayleigh Scattering

The SNO detector has been shown to be very transparent using prompt light from the laserball. Rayleigh scattering is a major effect causing extinction of prompt light signals in the detector. In all measurements of water attenuation, the absorption and scattering components need to be separately accounted for. Finding the absorption by subtracting the scattering from the measured attenuation is a general technique used in measurements of the optical properties of pure water, as discussed in Morel [86].

The dominant scattering mechanism in ultra-pure water is dipolar Rayleigh scattering from local stochastic changes in the index of refraction caused by density fluctuations in the liquid. The theory of density fluctuations is used to estimate the turbidity α of the water as a function of wavelength, temperature and pressure. The turbidity is the inverse Rayleigh scattering length. The statistical-thermodynamical approach to Rayleigh scattering in liquids originated with Einstein and Smoluchowski [87, 88, in German].

The probability of being scattered at an angle θ with respect to the original direction is:

$$P(\theta) \sim (1 + \cos^2 \theta). \tag{8.1}$$

The probability of undergoing Rayleigh scattering per unit path length is a strong function of wavelength:

$$\alpha \sim \frac{1}{\lambda^{4.3}} \tag{8.2}$$

where the 4.3 in the exponent comes from a combination of the Rayleigh scattering dependence on wavelength and on dispersion of the index of refraction, which increases at short wavelengths in both H_2O and D_2O. A 300 nm photon is almost 20 times more likely to scatter than a 600 nm photon.

Thermal motion of the molecules in the liquid cause local density variations. The pressure dependence of the index of refraction (as a proxy for the polarizability of the liquid) results in a locally different dielectric constant. Propagating light which encounters such a density fluctuation will experience a deviation in its trajectory.

The turbidity or Rayleigh scattering coefficient is given by:

$$\alpha_R = \left(\frac{32\pi^3 kT}{3\lambda^4 \beta_T}\right) n^2 \left(\frac{\partial n}{\partial p}\right)_T^2 C_\tau, \tag{8.3}$$

where λ is the wavelength, k the Boltzmann constant, T the temperature, and β_T is the isothermal compressibility of the fluid, and C_τ is the Cabannes factor which accounts for the effects of molecular anisotropy (for a derivation see Kerker [89]). The power dependence of the turbidity on wavelength in Equation 8.2 is slightly higher than the explicit power dependence included in Equation 8.3 because of the wavelength dependence of the index of refraction n and of the isothermal piezo-optic coefficient $(\partial n/\partial p)_T$.

The turbidity α is defined as the inverse of the length where the intensity of the incident beam is reduced by a factor $1/e$. The extinction of the intensity follows $I(x) = I_0 \exp(-\alpha x)$, where I is the intensity at a distance x from the source of intensity I_0. The nearly 4π solid angle geometry of the detector allows scattered light to be detected by another PMT at a later time. Small-angle forward-scatters are not separated well in space or in time from the unscattered light. A very small fraction of the prompt light intensity is due to Rayleigh scattered light: about 0.7% at 506 nm, 2% at 386 nm and 3.5% at 337 nm. Of the detected scattered photons, most are outside the prompt time window. Separating the Rayleigh scattered light from the direct light is a problem which can best be addressed by the Monte Carlo, where the history of all photons is known.

8.4.1 Scattering Contribution to Prompt Light Attenuation

The net prompt attenuation depends on the intensity losses to absorption and scattering between the source and the PMT's. This was discussed briefly in Section 4.4.5. What follows are the derivation and approximations used in obtaining Equation 4.21.

For attenuation in the heavy water over the wavelength range 300–700 nm, one is always in the regime where $\alpha_R \sim \alpha_{\text{abs}}$ (see Figure 8.1). Each of these contributions to α_{net} also satisfies $\alpha d \ll 1$ such that the total amount of attenuation is small.

In the case of light water attenuation (see Figure 8.2), there are two cases of interest:

- for the longer wavelengths ($\lambda \gtrsim 500\,\mathrm{nm}$) $\alpha_R \ll \alpha_{\mathrm{abs}}$ and $\alpha_{\mathrm{net}} \sim \alpha_{\mathrm{abs}}$,
- for the shorter wavelengths $\alpha_R \sim \alpha_{\mathrm{abs}}$, but the product αd is small for both Rayleigh scattering and absorption. This case is the same as that for D_2O.

At a single wavelength, the Rayleigh timing spectral shape depends only on the form of the scattering distribution (Equation 8.1). This assumption is correct provided the chance for double scatters is small, a condition which is approximately realized at all wavelengths in the optical data (337–620 nm).

Rayleigh scattering contributes to the net prompt attenuation by removing light from the prompt time window. However, some forward-scattered light remains in the time window, which reduces the contribution of the Rayleigh scattering coefficient to the net attenuation. In contrast, the absorption of light, which removes light completely from the time window, is independent of the geometry of the light ray.

The light intensity in a beam propagating from the laserball to a particular PMT changes as a function of distance following Lambert's law:

$$\frac{\mathrm{d}I}{\mathrm{d}x} = -\alpha_{\mathrm{net}} I \tag{8.4}$$

where I is the intensity at a distance x along the line between the source and the PMT, and α_{net} is the net attenuation coefficient. The main contributions to α_{net} are absorption and scattering out of the direct light path:

$$\frac{\mathrm{d}I}{\mathrm{d}x} = -I\left(\alpha_{\mathrm{abs}} + \alpha_R\left[\int_{t_+}^{\infty} P_{\mathrm{scat}}(t; x, \vec{s}, \vec{p})\,\mathrm{d}t + \ldots\right]\right) \tag{8.5}$$

where $P_{\mathrm{scat}}(t; x, \vec{s}, \vec{p})$ is the probability of hitting the PMT at $\vec{p}$ and time t for the laserball at $\vec{s}$, and $t_+ = 4\,\mathrm{ns}$ is the nominal late edge of the prompt time window.

The time integral between t_+ and ∞ is done to obtain the integrated probability of Rayleigh scattered light leaving the prompt window at a position x. The ellipsis indicates higher order terms due to multiple scattering and scattering into the prompt time window. These terms are expected to be small because of the low levels of scattering in pure water.

The probability of scattering is small, and the integral in Equation 8.5 could be directly evaluated in the simple case of a point source and a small light detector of known size at a distance d. In the case of the SNO PMT's, the integral is complicated by the changing PMT angular response, particularly as the beam reaches the source. The integral in Equation 8.5 is replaced by:

$$k = \left[\int_{t_+}^{\infty} P_{\mathrm{scat}}(t; x, \vec{s}, \vec{p})\, \mathrm{d}t + \ldots \right]. \tag{8.6}$$

In principle, k is a function of x, $\vec{s}$, $\vec{p}$. However, Monte Carlo studies show that these dependencies are small for optical data inside the AV, and that it is adequate to write Equation 8.5 in terms of a position-independent average $\overline{k}$.

Figure 7.21 shows that the data fit an exponential model of attenuation in the D_2O. Significant position dependence in the Rayleigh scattering contribution would lead to a systematic shift in the residual curve as a function of D_2O distance.

From Equation 8.5 one obtains:

$$I = I_0 \exp\left[-d\left(\alpha_{\mathrm{abs}} + \overline{k}\alpha_R\right)\right] \tag{8.7}$$

which implies $\alpha_{\mathrm{net}} = \alpha_{\mathrm{abs}} + \overline{k}\alpha_R$, as given in Equation 4.21.

The higher order terms in Equation 8.6 are included in the Monte Carlo calculation. The analyses of simulated optical data in Section 8.4.2 indicate that the values of $\overline{k}$ for H_2O and D_2O are independent of the magnitude of the scattering coefficient.

	QOCAFit α_d $(10^{-5}\,\mathrm{cm}^{-1})$	Monte Carlo parameters α_{abs} $(10^{-5}\,\mathrm{cm}^{-1})$	α_{scat} $(10^{-5}\,\mathrm{cm}^{-1})$	Rayleigh k_d
300-series	12.26 ± 0.07	12.50	0.00	
600-series	9.80 ± 0.06	4.00	7.26	0.799 ± 0.009
700-series	27.78 ± 0.10	4.00	29.00	0.820 ± 0.004
800-series	12.06 ± 0.10	0.00	14.50	0.832 ± 0.007
Mean				0.820 ± 0.003

Table 8.2: *D_2O prompt attenuation separation from Monte Carlo.*

8.4.2 Prompt Rayleigh Scattering Contribution from Monte Carlo

Four Monte Carlo simulations with varying optical parameters were generated and fit using the same procedure as for the data optical fits. A description of the input parameters for these simulations is given in Table 6.2. The simulations included 0, 1, 2 and 4 times the normal Rayleigh scattering at 386 nm. A comparison between the QOCAFit results and the Monte Carlo input parameters was used to determine the Rayleigh contribution to prompt attenuation. For D_2O the contribution is $k_d = 0.82 \pm 0.003$ while for H_2O the contribution is $k_h = 1.03 \pm 0.10$. In calculating these uncertainties, only the statistical error on the attenuation coefficients was used. Given the 2% discrepancy between the QOCAFit attenuation and the simulated absorption in the 300-series Monte Carlo (no Rayleigh scattering), and the spread in the values for k_d, an uncertainty of ± 0.02 is more reasonable.

These coefficients are used to extract estimates for α_{abs} for use in the Monte Carlo and in the energy response function described in Chapter 9.

	QOCAFit	Monte Carlo parameters		Rayleigh
	α_h $(10^{-5}\,\mathrm{cm}^{-1})$	α_{abs} $(10^{-5}\,\mathrm{cm}^{-1})$	α_{scat} $(10^{-5}\,\mathrm{cm}^{-1})$	k_h
300-series	11.7 ± 2.2	12.50	0.00	
600-series	12.5 ± 2.2	4.00	7.43	1.14 ± 0.30
700-series	32.1 ± 3.6	4.00	29.70	0.95 ± 0.12
800-series	18.4 ± 3.3	0.00	14.90	1.23 ± 0.22
Mean				1.03 ± 0.10

Table 8.3: *H_2O prompt attenuation separation from Monte Carlo.*

9 Energy Calibration

In this chapter, the detector response to Cherenkov light is calculated using the simplified detector model in the RSP response processor in SNOMAN. The uncertainties in RSP due to optics are evaluated, and the calculated response is compared to the response measurement using the ^{16}N source. A comparison to energy calibration methodology used in Super-Kamiokande is included at the end.

Motivation for the optical calibration comes from a desire to build an accurate model of the detector response to electrons. This model is a simplified version of the full geometry available in SNOMAN. Because the simplified model has a small number of physical input parameters, variations in the response can be easily tested without requiring extensive simulations. As well, the implementation of the response model (see Boulay [5]) is simple and fast to calculate. It is used by the SNO collaboration to calibrate the energy of each event registered in the detector, thereby completing the reconstruction of neutrino events from detector measurables (total number, spatial and timing distributions of phototubes registering light signals) to physical quantities (electron energy).

The energy estimator in SNO is based on the number of hit PMT's. Cherenkov light from events in the detector is at a very low intensity level, and most PMT hits will be at the single photoelectron level. Because the integrated charge for a channel triggered at the single photoelectron level displays large statistical and systematic fluctuations, the total charge in an event is a poor estimator of the Cherenkov light intensity. Therefore, each triggered channel is counted as a single photon hit, and the number of hit channels within a ± 10 ns window is used to reconstruct the event energy.

Energy calibration at the centre of the detector is straightforward because the response in all directions is essentially the same. Therefore, the most reliable overall energy normalization is provided by a monoenergetic source of electrons or gamma-rays located at the centre of the AV. This data provides the baseline for the energy calibration of the detector by providing the conversion factor between mean number of hit PMT's and initial particle energy. Details of the SNO calibration device based on ^{16}N are discussed in Hamer [56].

The energy calibration is based on gamma-rays, and the difference between gamma-rays and electrons is established through the SNOMAN Monte Carlo. Gamma-rays of energies relevant to SNO predominantly undergo Compton scattering rather than pair production, and produce a multiplicity of electrons. When each of these electrons falls below the Cherenkov velocity threshold ($\beta \sim 0.748$ in D_2O), the remaining energy is lost. The corresponding electron kinetic energy at the Cherenkov threshold is 259 keV. For 6.1 MeV gamma rays, the mean number of Compton scattering interactions above this threshold is 2.46, as evaluated by Hamer [56]. Multiplying the mean number of Compton electrons by the Cherenkov energy threshold, the visible energy for gamma-rays is expected to correspond to an electron of 637 keV lower energy. The contribution of pair production to the mean value of $N_{\rm hit}$ is only 2% [56].

An analytic response function is constructed based on the average angular distribution of Cherenkov light for single events. The optical calibration provides the key physical parameters which allow accurate calculations of the effects of attenuation and PMT angular response on the observed light signals. In SNOMAN, the average response is calculated by the RSP processor developed by Boulay [5], following the earlier work of Ford [11].

9.1 Energy Response

The SNO detector response to Cherenkov light is defined by the number and distribution of hit PMT's in an event. Event reconstruction includes the event location, and the direction and energy of the initiating particle. Over the energy range of interest to solar neutrinos in SNO (4–20 MeV), the initiating particle is either a gamma-ray or an electron, both of which generate similar Cherenkov light distributions. The electron equivalent energy is determined by the energy response algorithm, and the difference between gamma-ray and electron energy is calculated from simulations using EGS4 [58] as incorporated into SNOMAN [6, 7].

The relative timing and distribution of PMT's hit in an event allow reconstruction of the position and direction of the initial particle. Position reconstruction is based on minimizing the time residuals for all PMT's hit by light from an event at position $\vec{r}$ and time t_0:

$$\Delta t_i = t_i - \frac{|\vec{p} - \vec{r}|}{\overline{V_g}} - t_0 \tag{9.1}$$

where Δt_i is the time residual in nanoseconds, t_i is the PMT time in nanoseconds, $\vec{p}$ is the position of the PMT, $\overline{V_g}$ is the average group velocity for light.

The event direction $\vec{u}$ is reconstructed based on the spatial distribution of PMT hits relative to the event location. The direction reconstruction assumes that the event is due to a single particle, and is based on a PMT hit probability distribution function obtained from Monte Carlo simulations.

Once the event location and direction are reconstructed, the energy can be calculated from the number of hit PMT's. Approximately 80% of the light from an event is detected by the PMT's within a prompt time residual window of ± 10 ns. A prompt light energy calibration avoids uncertainties in the calibration of late light, which accounts for only 20% of the PMT hits. Because the late light is made up of reflected and scattered light spread over several detector transit times ($t_{\mathrm{transit}} \sim 75\,\mathrm{ns}$), it is difficult to unambiguously identify the optical path followed from the source to a particular PMT. The relatively large increase in systematic uncertainty associated with the reflected light offsets the small gain in statistical precision obtained from the reflected light hits.

For individual events, the statistical uncertainty in the energy is of order 8–18% for $N_{\mathrm{hit}} = 30-150$. By taking an average over many events at the same position in the detector, the centroid of the energy distribution is much better determined. However, attenuation in the D_2O, acrylic and H_2O PMT response, and the multiple photon effect engender systematic differences in the reconstructed energy as a function of position and direction. These systematic variations can be corrected for by applying an energy calibration function.

9.1.1 Response Function

The source light distribution can be corrected for transmission through the heavy and light waters and the AV, and for PMT response as a function of incident angle. This is what is meant by the "optical response" of SNO. The inverse problem is to derive the event energy from the observed intensity. This is of particular interest because it allows the neutrino data to be analyzed in terms of energy (MeV), which uses the same scale for all events, rather than in terms of N_{hit}, which does not.

In the energy calibration function, only prompt hits with time residuals in a 10 ns window are included (N_{win}). The effective number of hits (N_{eff}) is calculated from N_{win} by subtracting the small contribution of noise hits (N_{dark}) to the prompt window:

$$N_{\mathrm{eff}} = N_{\mathrm{win}} - N_{\mathrm{dark}} \tag{9.2}$$

The PMT dark rate is calculated from the $N_{\rm hit}$ distribution of pulsed random sampling of the detector electronics. This is known as the "Pulsed Global Trigger" (PGT): 400 ns long events are recorded at a rate of 5 Hz regardless of the input channel signals. This PGT data is taken continuously during all types of detector run conditions. The mean of the PGT $N_{\rm hit}$ spectrum is $N_{\rm PGT} \sim 2$ hits, as analyzed by Dragowsky [90].[1] The hits are uniformly distributed throughout the 400 ns event. Consequently, the contribution of background dark hits to the 20 ns prompt window used for energy calibration is:

$$N_{\rm dark} \sim N_{\rm PGT} \frac{20\,{\rm ns}}{400\,{\rm ns}} = 0.1\,{\rm hit} \tag{9.3}$$

For events with $N_{\rm win} \gtrsim 30$ this represents less than a 0.3% change in $N_{\rm eff}$, and the energy calibration based on $N_{\rm eff}$ is insensitive to small uncertainties in $N_{\rm dark}$.

The response processor (RSP) calculates the optical response corrections ($R_{\rm opt}$) to $N_{\rm eff}$ such that each event can be assigned a corrected number of prompt hits ($N_{\rm corr}$). The correction is unity for events at the centre of the detector. Events further out are corrected so that $N_{\rm corr}$ is the equivalent number of hits at the detector centre. Additional corrections are also applied by RSP to account for the number of active PMT's in the detector ($R_{\rm hardware}$), and for potential overall detector gain shifts with time ($G(t)$). The corrections are multiplicative factors applied to $N_{\rm eff}$:

$$N_{\rm corr} = \frac{N_{\rm eff}}{R_{\rm opt} R_{\rm hardware} G(t)} \tag{9.4}$$

where the terms in the denominator are described further in what follows.

The optical response correction $R_{\rm opt}(\vec{r}, \vec{u})$ is calculated as a function of event position ($\vec{r}$) and direction ($\vec{u}$) through the use of a Riemann sum over solid angle and

[1] The PGT mean $N_{\rm hit}$ trend is a slow decrease from ~ 2.1 to ~ 1.8 between runs 10000 – 14000 over 1.5 years from November 1999 through April 2001.

wavelength [5, 11]. The unnormalized optical response function is:

$$R'_{\mathrm{opt}}(\vec{r},\vec{u}) = \sum_{\cos\theta'}\sum_{\phi'}\sum_{\lambda} \epsilon \frac{C(\cos\theta')}{\lambda^2} \exp(-\alpha_d d_d - \alpha_a d_a - \alpha_h d_h) R_{\mathrm{PMT}}(\psi) M \qquad (9.5)$$

where the angular variables (θ', ϕ') are defined relative to the event direction $\vec{u}$. The other terms are defined as follows:

$\boldsymbol{\epsilon}$ PMT effective quantum efficiency as a function of wavelength.

$\boldsymbol{C(\cos\theta')/\lambda^2}$ Normalized Cherenkov light distribution as a function of solid angle and weighted by wavelength (see Ford [11]).

$\boldsymbol{d_d}$, $\boldsymbol{d_a}$, $\boldsymbol{d_h}$ Distances for light paths through heavy water, acrylic and light water, respectively.

$\boldsymbol{\alpha_d}$, $\boldsymbol{\alpha_a}$, $\boldsymbol{\alpha_h}$ The attenuation coefficients of the heavy water, acrylic and light water, respectively. The effective attenuation is made up of absorption and scattering contributions for the 20 ns prompt window.

$\boldsymbol{R_{\mathrm{PMT}}(\psi)}$ PMT response as a function of incident angle on the PSUP (ψ).

$\boldsymbol{M}$ MPE correction for the absolute light intensity level at the PMT's.

The normalized optical response is calculated by dividing out the sum obtained at the centre of the detector:

$$R_{\mathrm{opt}} = \frac{R'_{\mathrm{opt}}(\vec{r},\vec{u})}{R'_{\mathrm{opt}}(\vec{0},\vec{0})} \qquad (9.6)$$

such that $R_{\mathrm{opt}}(\vec{0},\vec{0}) = 1$.

The hardware response correction is included to account for the number of active channels participating in a given event. A channel is considered active if the PMT is under high voltage and can be read out by the electronics, and if the channel has valid electronics and timing calibration constants. The hardware response correction is:

$$R_{\text{hardware}} = \frac{\text{Number of active channels}}{\text{Nominal number of channels}} \tag{9.7}$$

where the nominal number of channels (9453) is taken from the SNOMAN Monte Carlo to permit consistent scaling between detector data and simulated data. This correction assumes that the non-active channels are uniformly distributed such that the average coverage is independent of position on the PSUP.

The function $G(t)$ can be determined by the drift in ^{16}N source response at the centre of the detector. Over the ten-month period from November 1999 through August 2000, Boulay [5] has shown that $\mathrm{d}G/\mathrm{d}t \sim -0.4\%$ per month, though the uncertainty in $G(t)$ is large because of the lack of ^{16}N measurements between December 1999 and April 2000. Other instrumental effects, such as timing issues with the triggering of the ^{16}N source, may conspire with other small effects to affect the apparent detector gain over time. The detector operational characteristics (deck temperature and humidity, number of electronics channels on-line with valid calibrations) changed slightly over this period, so a careful accounting of active channels may reduce the difference between the measured detector response in December 1999 and April 2000.

9.1.2 Response Uncertainties due to Optics

The calculated response for the nominal optical parameters was compared to the response for the three largest systematics in the optical analysis (listed in Section 7.4): 4 (radial shift of 5 cm), 9 (no PMT-PMT variability) and 11 (restricted PMT selection to $\chi^2_{ij} < \chi^2_{\text{lim}} = 9$). These three systematic changes to the optical model inputs contribute approximately 75% of the total systematic uncertainty on the water attenuations (Tables 7.4 through 7.11), and a similar amount to the PMT response uncertainty (Figure 7.23).

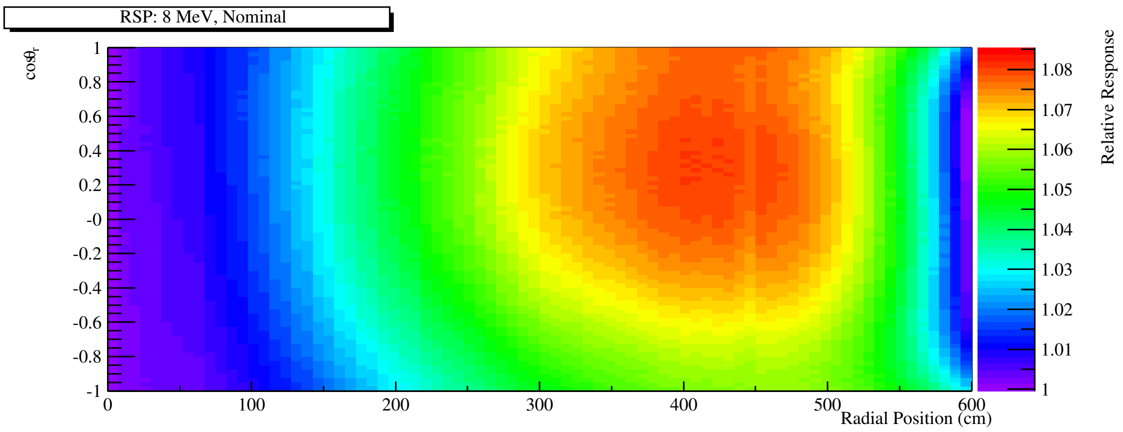

Figure 9.1: *Detector response* $(r, \cos\theta_r)$ *map for nominal optical parameters.*

The RSP processor in SNOMAN was used to obtain the optical response as a function of event position ($\vec{r}$) and event radial direction (θ_r). The angle between the reconstructed event direction ($\vec{u}$) and position relative to the detector centre ($\vec{r}$) determines the event radial direction via:

$$\cos\theta_r = \vec{u} \cdot \vec{r} \tag{9.8}$$

The detector optical response map $R_{\text{opt}}(r, \cos\theta_r)$ is shown in Figure 9.1 for an electron of 8 MeV. This map shows a gradual increase in response with radius up to ~ 400 cm, a plateau from 400 to 500 cm, and a relatively rapid decrease from 500 to 600 cm. The directional dependence is asymmetric: the response to inward-going events ($\cos\theta_r \lesssim 0$) is up to 3% lower than outward-going events ($\cos\theta_r \gtrsim 0$).

The optical response maps calculated by RSP for the three systematics are shown in Figure 9.2. In generating these maps, the full systematic changes in the optical parameters were used, not the changes multiplied by systematics multipliers (f_i) of Table 7.3.

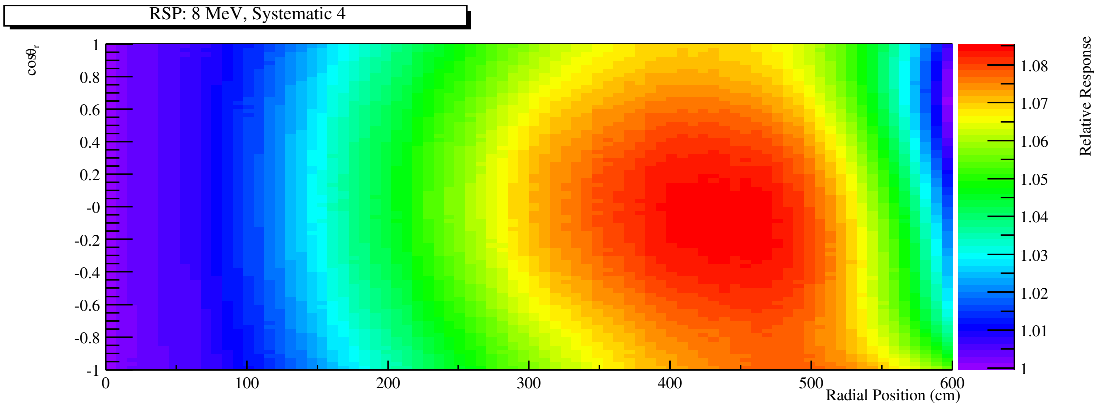

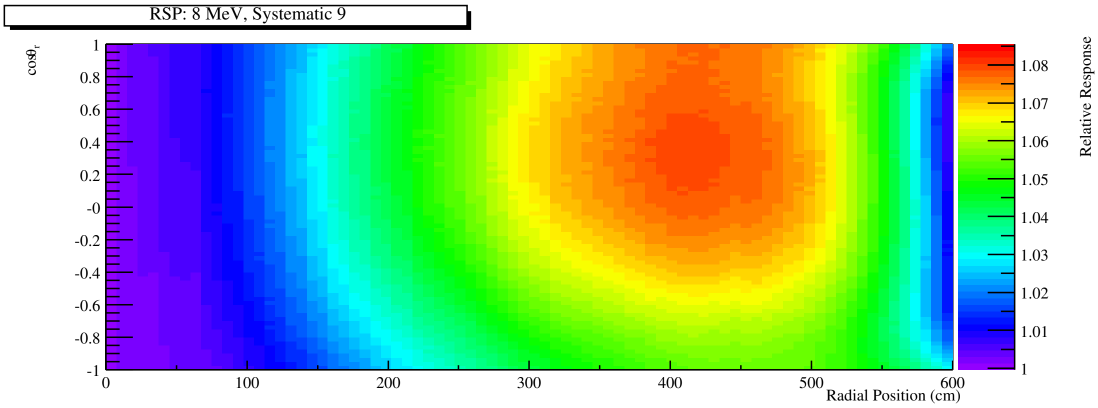

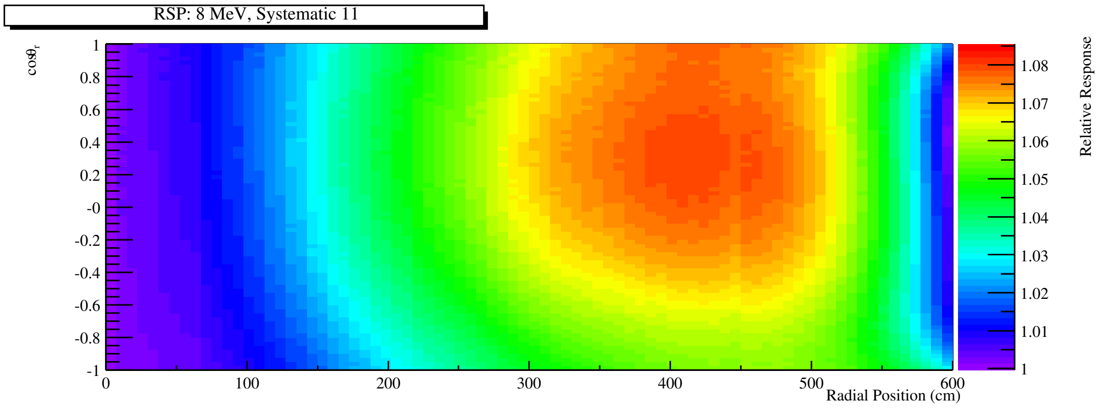

Figure 9.2: *Detector response* $(r, \cos\theta_r)$ *map for optical parameters from systematics 4 (radial shift), 9 (no PMT-PMT variability) and 11 (restrictive* $\chi^2_{lim} = 9$*).*

	Mean response ratio R'/R		Response uncertainty $f_i \times (R'/R - 1)/0.75$	
Syst	$r < 550\,\mathrm{cm}$	$r < 600\,\mathrm{cm}$	$r < 550\,\mathrm{cm}$	$r < 600\,\mathrm{cm}$
4	1.00465	1.00587	0.12%	0.16%
9	0.99886	1.00000	-0.03%	0.00%
11	0.99973	1.00023	-0.03%	0.02%
Net			0.13%	0.16%

Table 9.1: *Mean detector response ratio ($\overline{R'/R}$) and net response uncertainty ($f_i \times (R'/R - 1)/0.75$) for optical systematics, weighted by volume. The systematics multipliers (f_i) are listed in Table 7.3, while the additional factor of* $1/0.75$ *takes into account the contribution of these three systematics to the total systematic uncertainties in the optical parameters.*

The ratio, R'/R, between the systematic and the nominal response maps is shown in Figure 9.3. The large decreases in α_d and α_h for systematic 4 contribute to a directional systematic in the response, while the other two optical systematics produce much smaller changes to the detector response. The mean response ratio, weighted by the detector volume in each spherical shell of the D_2O fiducial volume, is given in Table 9.1.

The mean response ratio ($\overline{R'/R}$) is calculated for two choices of fiducial volume in Table 9.1: $r < 550\,\mathrm{cm}$ and $r < 600\,\mathrm{cm}$. The 550 cm fiducial volume selects events which reconstruct comfortably away from the AV to avoid signal contamination from radioactive backgrounds in the acrylic. However, this fiducial volume only contains 77% of the D_2O and it is desirable to eventually include the full fiducial volume out to 600 cm.

The scaling factors of Table 7.3 were used to obtain estimates of the uncertainty in detector response due to errors in the optical calibration constants with the result that changes in energy response due to systematic effects in the optical calibration are limited to 0.13%, when averaged over the 550 cm detector fiducial volume, and to

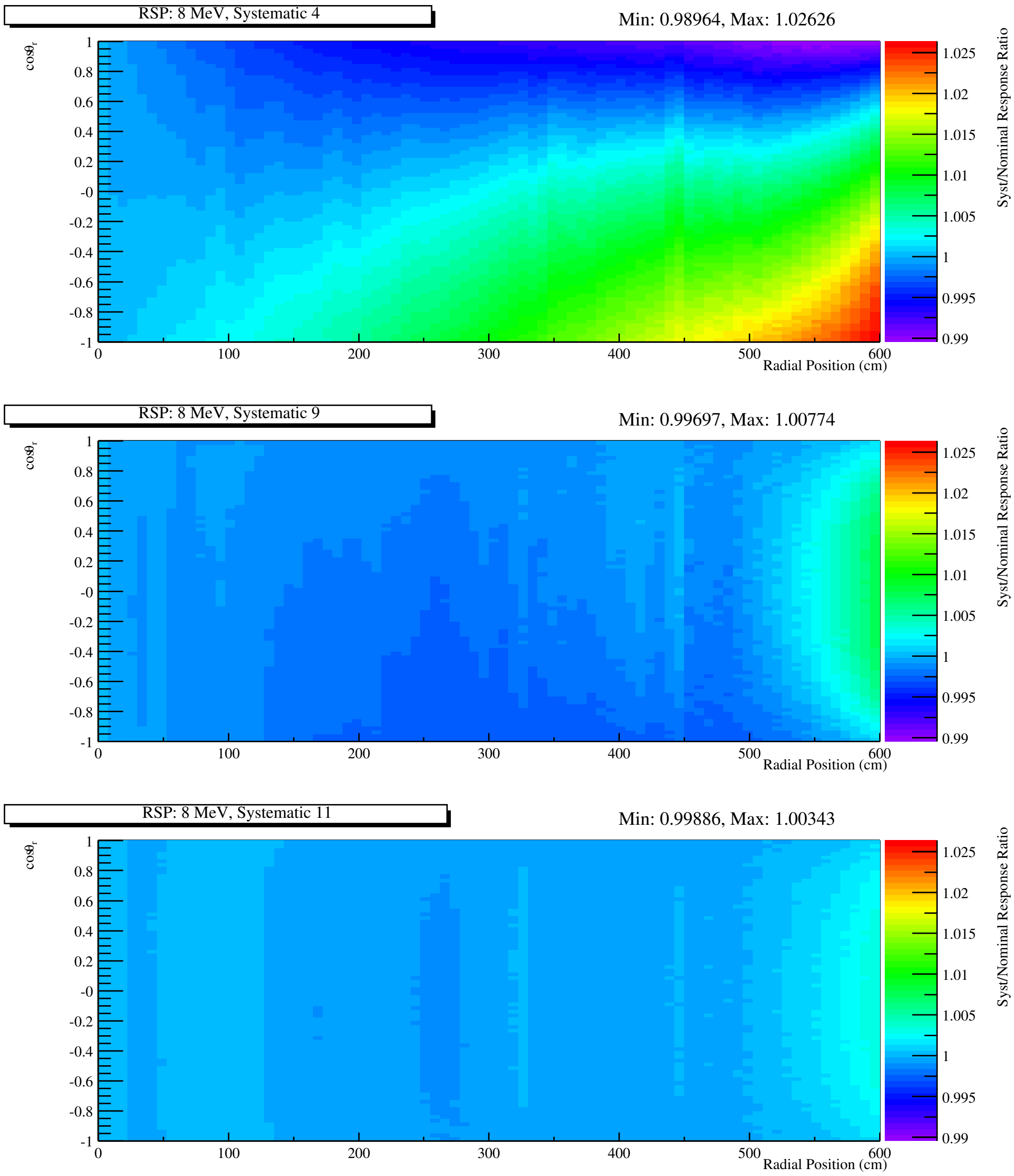

Figure 9.3: *Detector response $R_{opt}(r, \cos\theta_r)$ map ratio between systematics 4, 9 and 11 and the nominal optical parameters.*

0.16% when the full 600 cm D_2O volume is used. These uncertainties are characteristic of the extraction of the optical parameters.

The PMT angular response was measured in the range of approximately 0–40°, corresponding to the inner 500 cm of the detector (see Figure 4.13). Outside 500 cm it is necessary to extrapolate PMTR into a region for which optical constants have not been fit.

The extrapolation of PMTR beyond the measured values is shown in Figures 7.5 and 7.6. The extrapolation of PMTR over the range 40–45° largely determines the energy response over the volume between 500 cm and 550 cm (25% of the fiducial volume inside 550 cm). The range 45–50° in PMTR extends the reach of the calculated detector response to the last part of the D_2O volume to the AV, representing 23% of the total volume inside the vessel.

The PMT response in [2] is the SNOMAN PMT response that was scaled to the QOCAFit results to allow the extrapolation past the angular range of the optical data in Section 7.1.1. The difference of 5% between the measurements and the calculations given in Lay [2] over the range 40–50° is taken as an estimate of the uncertainty in the shape of the PMT response for these angles. This uncertainty remains when scaled to the QOCAFit data.

The uncertain PMT response at the outer limits of the fiducial volume leads to a volume-weighted uncertainty in the energy scale of:

$$\begin{aligned}\Delta\mathrm{RSP}(R_{\mathrm{fid}}) \;\sim\; & \Delta\mathrm{RSP}(\text{known optics}, r < 500\,\mathrm{cm}) + \\ & \Delta\mathrm{RSP}(\text{uncertain PMTR}, r > 500\,\mathrm{cm}) \times \left(\frac{R_{\mathrm{fid}}^3 - 500^3}{R_{\mathrm{fid}}^3}\right) \end{aligned} \quad (9.9)$$

where ΔRSP(known optics, $r < 500$ cm)$=$ 0.1%, ΔRSP(uncertain PMTR, $r > 500$ cm)$=$ 5% from the uncertainty in the PMTR extrapolation, and $R_{\mathrm{fid}} = 550$ cm or 600 cm is the fiducial volume boundary. The values for the two fiducial volumes in Table 9.1 are ΔRSP(550 cm) = 1.25% and ΔRSP(600 cm) = 2.11%. These uncertainties are the estimated total uncertainties on energy scale due to the optical parameters.

The ^{16}N source can be used to constrain the response in regions of the detector for which the dominant angles for the PMT response have not yet been measured. However, it is highly desirable to measure the PMT response using an optical source to provide a separate and independent calibration of the detector response.

9.1.3 Average Radial Response

The average radial response of SNO to electrons is verified by comparing a Monte Carlo simulation to the calculated corrections of the RSP processor. Figure 9.4 shows the various contributions to the response, as a function of event radius. The mean correction due to the attenuation, PMTR and MPE contributions to RSP indicate that the PMTR is the largest effect.

9.2 Energy Scale using the ^{16}N-Source

The ^{16}N source emits γ-rays, primarily of $E_\gamma = 6.1$ MeV, and is fully described by Hamer [56]. The mean detector response to the gamma rays shifts by up to 7% as a function of the radial position of the source. However, the original parameters for the PMT response and the attenuations as a function of wavelength in the SNOMAN Monte Carlo predicted a change of approximately half that amount and resulted in an energy scale uncertainty of 6.1% within a 550 cm radius fiducial volume [56, page 169]. Measured detector optical parameters were needed to reduce the uncertainty in extrapolating the energy scale from the ^{16}N data to points throughout the detector volume.

The detector response was calculated using the RSP processor using the attenua-

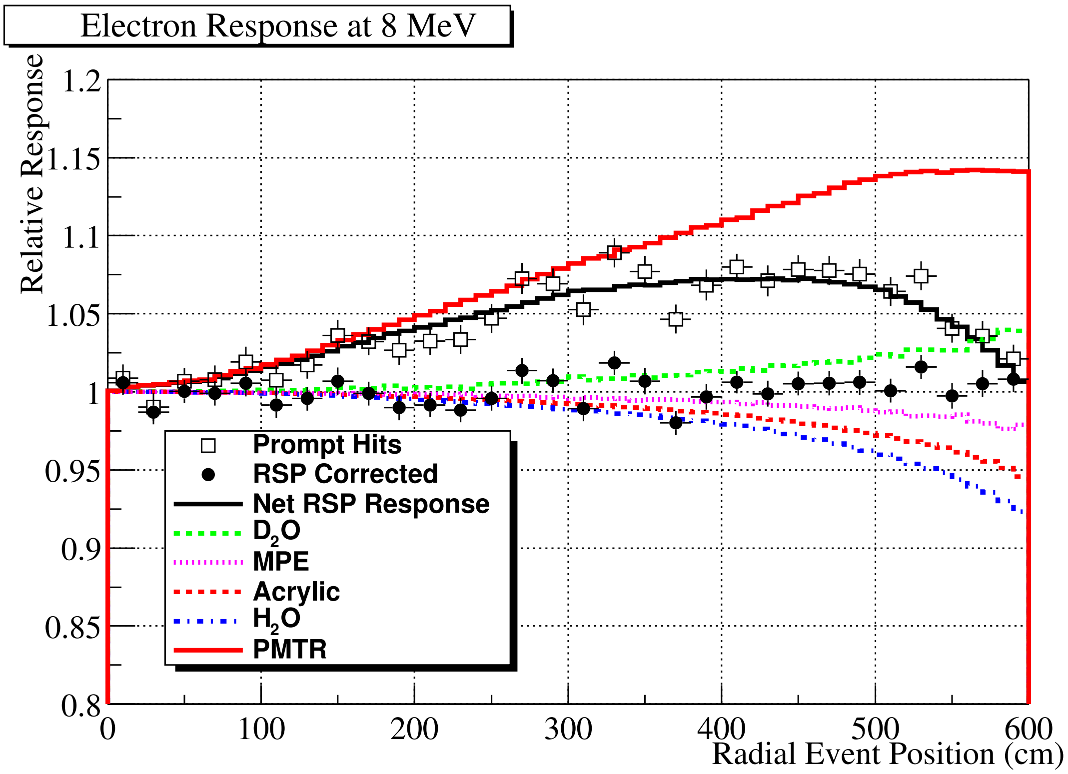

Figure 9.4: *Average radial detector response for electrons at 8 MeV There is good agreement between the number of prompt hits from simulated electron events and the RSP calculated response as a function of the radial position of the events. The separate mean contributions to the RSP function are shown.*

tion and PMT response parameters derived from the optical calibration in this thesis. Figure 9.5 shows the agreement in the mean visible energy obtained from RSP for the ^{16}N data. This plot shows the ratio of the mean N_{hit} for various radial source positions to the mean N_{hit} for runs with the source at the centre of the D_2O. The spread of the corrected response points is 0.7% [5]. The mean corrected response is essentially independent of the systematic shifts caused by attenuation and PMT response as a function of radius.

9.3 Comparison to Super-Kamiokande

In contrast to the SNO energy calibration philosophy, the Super-Kamiokande (SK) collaboration has published results where a tuned Monte Carlo is used to evaluate the energy calibration. The average optical attenuation of the water and an overall PMT collection efficiency are the two principal tuned quantities.

An overview of some of the SK calibration devices and procedures is given in Ishino [91]. The energy scale and resolution are measured as a function of position within the fiducial volume using a number of calibration devices, principal among which is a linear electron accelerator (LINAC; described in Nakahata et al. [92]). The LINAC injects electrons going downwards into the detector, at precisely known energies and positions. Monte Carlo simulations of the LINAC data are used to tune the input parameters to the Monte Carlo. The absolute energy scale derived from the LINAC data are checked against ^{16}N decays in the water, and agreement in the energy scale is found to be better than 1% [93].

The Monte Carlo is tuned by adjusting the water absorption and scattering coefficients of Morel and Prieur [94][2] and an overall light collection factor to produce agreement with the data taken with the LINAC. The attenuation of the H_2O in SK

[2] The evaluation of Smith and Baker [78] uses the earlier work of Morel and Prieur [94] over a significant portion of the wavelength range (380 – 700 nm).

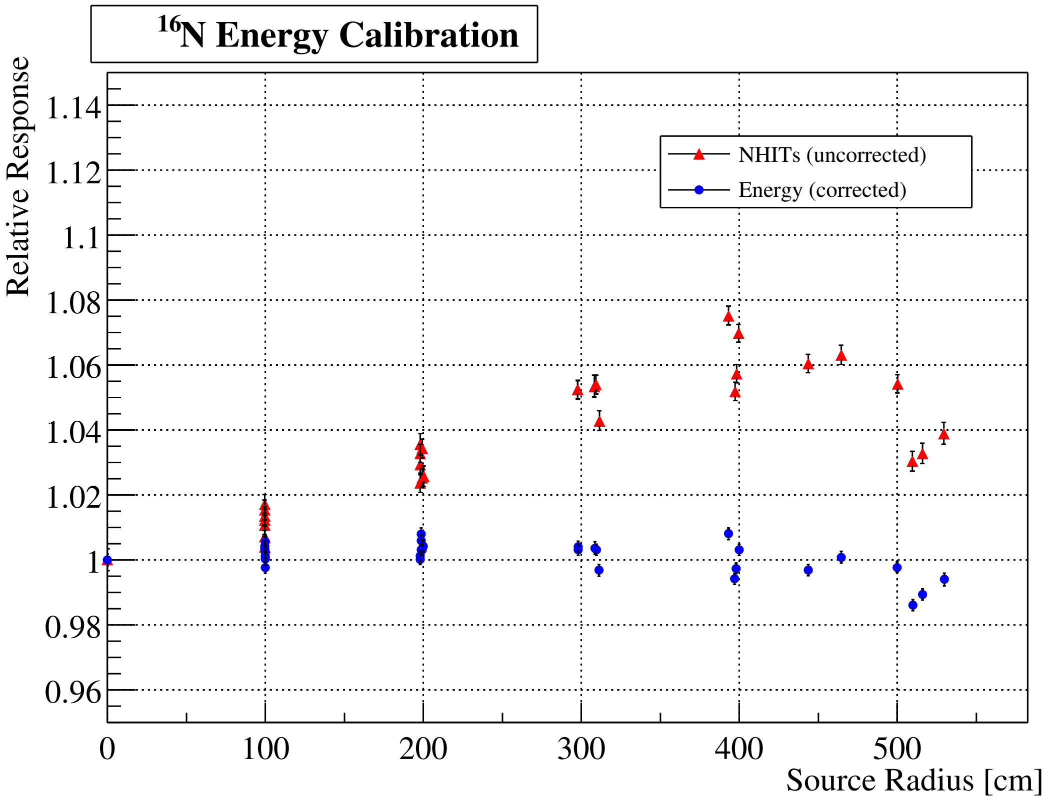

Figure 9.5: *Optical calibration applied to ^{16}N calibration source events [5]. The values in the figure are NHITs = $N_{eff}(r)/N_{eff}(0)$ and Energy = $N_{corr}(r)/N_{corr}(0)$, where r is the source radius. The mean value of N_{eff} for triggered events at each source position is divided by the mean value at the centre of the detector to give the relative response. Applying the RSP processor to individual events produces an energy spectrum at each source radius which is essentially free of residual optical effects on the detector response.*

is measured using a nitrogen/dye laser and diffusing ball system, similar to the one used in SNO. In this system, the light intensity emitted over a range of wavelengths is measured by an electronic camera placed above the detector volume, and not by the PMT's themselves. The measured water attenuation coefficients display good agreement with the tuned Monte Carlo parameters.

Corrections to the energy of each event are applied in a similar way to those in the SNO energy response function [91]. However, the SK PMT response as a function of incident angle is calculated from prior measurements and the detector geometry, and is not measured *in situ*.

10 Conclusions

The attenuation coefficients for D_2O are the lowest yet achieved (see Chapter 8), and are measured on a sample of unprecedented size and with very low impurity levels. The measured H_2O attenuations in SNO are in reasonable agreement with literature values, though they are higher than measurements made on H_2O samples of the highest purity [71]. The PMT angular response is measured over the range 0–40° and with an uncertainty rising to $\sim 1\%$ at 40°. The response is significantly higher than previous measurements and calculations [2, 3], and this change is a very important contribution to the understanding of the variation in energy response as a function of position.

All SNO event analyses rely on the optical parameters measured for this thesis. The calibration of neutrino events in the heavy water fiducial volume of the SNO detector ($r \leq 550$ cm) is accomplished with the parameters obtained with the optical model used in this thesis.

The optical response of SNO is dominated by the PMT response, followed closely by the attenuations of the light water and acrylic. The precise extrapolation of the PMT angular response to higher incident angles is highly desirable. The PMT angular response will be constrained by further analysis of calibration data from both the laserball and from the ^{16}N source. However, the higher PMT incident angles are only accessible to sources placed near the AV or in the H_2O region where the effects of reflections from the AV and of the finite source and PMT sizes on the solid angle will have to be taken into account.

Additional work on the optical calibration will be required to extend the measured range of the PMT angular response to the H_2O volume of the detector. The influence of reflections of light from the AV on the measured prompt occupancies must be taken into account in order to measure the PMT response beyond $40°$. The extrapolation of the PMT response to higher incident angles presented in this thesis is likely adequate for the entire volume of D_2O. However, the fall-off in response beyond $45°$ (equivalent to $R = 550\,\mathrm{cm}$) results in increased uncertainty in the energy scale for analyses of events in the H_2O.

SNO is on the threshold of publishing its first results (Summer 2001). To make a strong statement about solar neutrino oscillations, the level of precision required for the SNO results are very high. The uncertainty in energy scale due to the optical calibration has been reduced to $\sim 1.25\%$. It is hoped that the other systematic uncertainties in the data analysis, such as the detector livetime and the D_2O fiducial volume, can be accurately determined and that a significant solar neutrino result will be forthcoming. This is an exciting time to be involved in neutrino research!

Bibliography

[1] L.P. Boivin, W.F. Davidson, R.S. Storey, D. Sinclair, and E.D. Earle. Determination of the attenuation coefficients of visible and ultraviolet radiation in heavy water. *Applied Optics*, 25(6):877–882, March 1986.

[2] M.D. Lay. *Creation and Detection of Čerenkov Light in the Sudbury Neutrino Observatory*. PhD thesis, Oxford University, April 1994.

[3] M.J. Lyon. *Neutron Transport in the Sudbury Neutrino Detector*. PhD thesis, Oxford, November 1996. Also circulated as SNO-STR-96-071.

[4] R. Brun and F. Rademakers. ROOT - An object oriented data analysis framework. *Nuclear Instruments and Methods*, A389:81–86, April 1997. URL `http://root.cern.ch/`.

[5] M.G. Boulay. *Direct Evidence for Weak Flavour Mixing with the Sudbury Neutrino Observatory*. PhD thesis, Queen's University, Kingston, Ontario, Canada, April 2001.

[6] SNO Collaboration. *The SNOMAN Programmer's Manual*, 4.01 edition, April 2000. SNO Collaboration internal reference manual. Released periodically with updates.

[7] SNO Collaboration. *The SNOMAN User's Manual*, 4.01 edition, November 2000. SNO Collaboration internal reference manual. Released periodically with updates.

[8] D. Grant and A.L. Hallin. Results from the January laserball miniscan. Internal report, March 2001. Preliminary optical measurements done before and after the first D_2O recirculation exercise in January 2001.

[9] R.J. Ford. Nitrogen/dye laser system for the optical calibration of SNO. Master's thesis, Queen's University, Kingston, Ontario, Canada, October 1993.

[10] R.J. Ford. *SNO N_2/Dye Laser and Fibre Optic Diffuser Ball System Manual.* Queen's University, 1997. SNO-STR-96-056.

[11] R.J. Ford. *Calibration of SNO for the Detection of ^8B Neutrinos.* PhD thesis, Queen's University, Kingston, Ontario, Canada, December 1998.

[12] Eli Waxman and John N. Bahcall. Neutrino afterglow from gamma-ray bursts: $\sim 10^{18}$ eV. *The Astrophysical Journal*, 541:707–711, October 2000.

[13] Particle Data Group. Review of particle properties. *The European Physical Journal*, C15, 2000.

[14] K. Kodama et al. Observation of tau neutrino interactions. *Physics Letters B*, 504:218–224, April 2001.

[15] J. N. Bahcall. *Neutrino Astrophysics.* Cambridge University Press, Cambridge, UK, 1989.

[16] M. Butler, J.-W. Chen, and X. Kong. Neutrino-deuteron scattering in effective field theory at next-to-next-to-leading order. *Physical Review C*, 63:035501–1–035501–17, February 2001.

[17] F.H. Shu. *The Physical Universe: An Introduction to Astronomy.* University Science Books, Mill Valley, California, 1982.

[18] B. T. Cleveland et al. Measurement of the solar electron neutrino flux with the Homestake chlorine detector. *The Astrophysical Journal*, 496:505–526, March 1998. Results from all extractions since 1970.

[19] Y. Fukuda et al. Solar neutrino data covering solar cycle 22. *Physical Review Letters*, 77(9):1683–1686, August 1996. Results from Kamiokande II and III.

[20] Y. Fukuda et al. Measurement of the solar neutrino energy spectrum using neutrino-electron scattering. *Physical Review Letters*, 82(12):2430–2434, March 1999.

[21] Y. Suzuki. Solar neutrino results from Super-Kamiokande. *Nuclear Physics B (Proceedings Supplement)*, 91(1-3):29–35, January 2001. Neutrino 2000 Conference Proceedings.

[22] J. N. Abdurashitov et al. Measurement of the solar neutrino capture rate with gallium metal. *Physical Review C*, 60(055801):1–32, 1999. SAGE Collaboration.

[23] V.N. Gavrin. Solar neutrino results from SAGE. *Nuclear Physics B (Proceedings Supplement)*, 91(1-3):36–43, January 2001. Neutrino 2000 Conference Proceedings.

[24] W. Hampel et al. GALLEX solar neutrino observations: results for GALLEX IV. *Physics Letters B*, 447:127–133, February 1999.

[25] M. Altmann et al. GNO solar neutrino observations: Results for GNO I. *arXiv:hep-ex/0006034*, June 2000. Submitted to Physics Letters B.

[26] J.N. Bahcall. How the sun shines, June 2000. Published at site of Nobel e-Museum (`http://www.nobel.se/physics/articles`). Also available as `astro-ph/0009259` on `http://arXiv.org`.

[27] N. Hata and P. Langacker. Solutions to the solar neutrino anomaly. *Physical Review D*, 56(10):6107–6116, November 1997.

[28] G.T. Ewan et al. Sudbury Neutrino Observatory Proposal. Technical report, Queen's University, October 1987. SNO-87-12.

[29] G.T. Ewan et al. Scientific and Technical Description of the Mark II SNO Detector. Technical report, Queen's University, 1989. SNO-89-15.

[30] J.N. Bahcall, M. Kamionkowski, and A. Sirlin. Solar neutrinos: Radiative corrections in neutrino-electron scattering experiments. *Physical Review D*, 51(11): 6146–6158, June 1995.

[31] J.N. Bahcall, M.H. Pinsonneault, and S. Basu. Solar Models: current epoch and time dependences, neutrinos, and helioseismological properties. *Preprint: astro-ph/0010346 on http://arXiv.org*, March 2001. Accepted for publication in The Astrophysical Journal.

[32] C. E. Rolfs and W. S. Rodney. *Cauldrons in the Cosmos: Nuclear Astrophysics*. The University of Chicago Press, Chicago, 1988.

[33] J. N. Bahcall and A. Ulmer. Temperature dependence of solar neutrino fluxes. *Physical Review D*, 53(8):4202–4210, April 1996.

[34] B. E. J. Pagel. *Nucleosynthesis and Chemical Evolution of Galaxies*. Cambridge University Press, Cambridge, U.K., 1997.

[35] J.N. Bahcall and M.H. Pinsonneault. Solar models with helium and heavy-element diffusion. *Reviews of Modern Physics*, 67(4):781–808, October 1995. With an Appendix on the Age of the Sun by G.J. Wasserburg.

[36] J. N. Bahcall et al. Standard neutrino spectrum from ^{8}B decay. *Physical Review C*, 54(1):411–422, July 1996.

[37] E. K. Warburton. R-matrix analysis of the $\beta^{m}p$-delayed alpha spectra from the decay of ^{8}Li and ^{8}B. *Physical Review C*, 33(1):303–313, January 1986.

[38] C.E. Ortiz, A. García, R.A. Waltz, M. Bhattacharya, and A.K. Komives. Shape of the ^{8}B alpha and neutrino spectra. *Physical Review Letters*, 85(14):2909–2912, October 2000.

[39] M.C. Gonzalez-Garcia, M. Maltoni, C. Peña-Garay, and J.W.F. Valle. Global three-neutrino oscillation analysis of neutrino data. *Physical Review D*, 63: 033005–1–033005–21, January 2001.

[40] L. Wolfenstein. Neutrino oscillations in matter. *Physical Review D*, 17(9):2369–2374, May 1978.

[41] S.P. Mikheev and A.Yu. Smirnov. Neutrino oscillations in a variable-density medium and ν-bursts due to the gravitational collapse of stars. *Soviet Physics JETP [translation of Zh. Eksp. Theor. Fiz.]*, 64(1):4–7, July 1986.

[42] H. A. Bethe. Possible explanation of the solar-neutrino puzzle. *Physical Review Letters*, 56(12):1305–1308, March 1986.

[43] E. Kh. Akhmedov. Neutrino physics. arXiv:hep-ph/0001264, January 2000. Lectures given at the Trieste Summer School in Particle Physics, June 7 – July 9, 1999.

[44] J.N. Bahcall, P.I. Krastev, and A. Yu. Smirnov. Solar neutrinos: global analysis and implications for SNO. *Preprint:* `hep-ph/0103179` *on* `http://arXiv.org`, March 2001.

[45] J.N. Bahcall, P.I. Krastev, and A.Yu. Smirnov. SNO: Predictions for ten measurable quantities. *Physical Review D*, 62:093004–1–093004–27, November 2000.

[46] F.J. Kelly and H. Überall. Absorption of solar neutrinos in deuterium. *Physical Review Letters*, 16:145–147, 1966.

[47] S.D. Ellis and J.N. Bahcall. Neutrino absorption by deuterium. *Nuclear Physics A*, 114:636–640, 1968.

[48] S. Nakamura, T. Sato, V. Gudkov, and K. Kubodera. Neutrino reactions on the deuteron. *Physical Review C*, 63:034617–1–034617–18, March 2001.

[49] J. D. Jackson. *Classical Electrodynamics.* John Wiley & Sons, Inc., New York, 2^{nd} edition, 1975.

[50] J.V. Jelley. *Čerenkov Radiation and its applications.* Pergamon Press, New York, 1958.

[51] C.J. Jillings. *The Electron-Scattering Reaction in the Sudbury Neutrino Observatory.* PhD thesis, Queen's University, Kingston, Ontario, Canada, July 1999.

[52] J. Boger et al. The Sudbury Neutrino Observatory. *Nuclear Instruments and Methods*, A449:172–207, July 2000.

[53] N. Tagg. *The ^{8}Li Calibration Source and Through-going Muon Analysis in the Sudbury Neutrino Observatory.* PhD thesis, The University of Guelph, January 2001.

[54] C. Athanassopoulos et al. The liquid scintillator neutrino detector and LAMPF neutrino source. *Nuclear Instruments and Methods*, A388:149–172, 1997.

[55] G. Doucas et al. Light concentrators for the Sudbury Neutrino Observatory. *Nuclear Instruments and Methods*, A370:579–596, 1996.

[56] A.S. Hamer. *Energy Calibration of SNO for measurement of the Charged-Current Neutrino Reaction.* PhD thesis, Queen's University, Kingston, Ontario, Canada, October 1999.

[57] CERN. *ZEBRA*. CERN Program Library Long Writeup Q100/101. CERN, Geneva, Switzerland, 1993.

[58] W. R. Nelson, H. Hirayama, and D. W. O. Rogers. The egs4 code system. Technical Report SLAC-Report #265, Stanford University, December 1985.

[59] LANL. MCNP4A, a monte carlo n-particle transport code system. Technical report, Radiation Shielding Information Center, Los Alamos National Laboratory, November 1993.

[60] CERN. *GEANT - Detector Description and Simulation Tool.* CERN, Geneva, Switzerland, 1993.

[61] P. Schiebener, J. Straub, J.M.H. Levelt Sengers, and J.S. Gallagher. Refractive index of water and steam as a function of wavelength, temperature and density. *Journal of Physical and Chemical Reference Data*, 19(3):677–717, 1990. Table 7, page 704 is for wavelength 0.22650 μm by comparison with the wavelengths listed in Table 8, page 711.

[62] A.M. Hellwege. Brechzahl reiner anorganischer flüssigkeiten. In K.-H. Hellwege and A.M. Hellwege, editors, *Eigenschaften der Materie in Ihren Aggregatzuständen. 8. Teil: Optische Konstanten*, Zahlenwerte und Funktionen aus

Physik, Chemie, Astronomie, Geophysik und Technik (Landolt-Börnstein), pages 5–561–5–571. Springer-Verlag, Berlin, 1962. II. Band, 8. Teil, Sechste Auflage.

[63] R.J. Boardman. *The detection of Cerenkov radiation from neutrino interactions.* PhD thesis, Oxford University, 1992. Index of refraction reference for SNOMAN: H_2O, D_2O and acrylic.

[64] H. Buiteveld, J. H. M. Hakvoort, and M. Donze. The optical properties of pure water. In J. S. Jaffe, editor, *Ocean Optics XII*, volume 2258, pages 174–183. Society of Photo-Optical Instrumentation Engineers, 1994.

[65] E.D. Earle. Private communication, 2000.

[66] J.C. Zwinkels, W.F. Davidson, and C.X. Dodd. Optical properties of UV transmitting acrylics for use in a heavy water Cerenkov [*sic*] detector. *Applied Optics*, 29(22):3240–3248, August 1990.

[67] E.D. Earle. Summary report on acrylic vessel. Technical report, SNO, Sudbury, Canada, 1998. Internal report: SNO-STR-98-005.

[68] T. I. Quickenden and J. A. Irvin. The ultraviolet absorption spectrum of liquid water. *Journal of Chemical Physics*, 72(8):4416–4428, April 1980.

[69] F. M. Sogandares and E. S. Fry. Absorption spectrum (340–640 nm) of pure water. I. Photothermal measurements. *Applied Optics*, 36(33):8699–8709, November 1997.

[70] A.C. Tam and C.K.N. Patel. Optical absorptions of light and heavy water by laser optoacoustic spectroscopy. *Applied Optics*, 18(19):3348–3358, October 1979.

[71] R. M. Pope and E. S. Fry. Absorption spectrum (380–700 nm) of pure water. II. Integrating cavity measurements. *Applied Optics*, 36(33):8710–8723, November 1997.

[72] W.H. Press, S.A. Teukolsky, W.T. Vetterling, and B.P. Flannery. *Numerical Recipes in C: The Art of Scientific Computing.* Cambridge University Press, Cambridge, United Kingdom, 2 edition, 1992.

[73] Molectron Corporation. Molectron nitrogen lasers, 1975. Obtained in May, 2000 from Exciton Corporation.

[74] F. Duncan. Calibration source positioning. Technical report, Queen's University, March 2000. Internal report.

[75] C.J. Jillings. Multiple photo-electron effects in optical calibration. Technical report, Queen's University, November 1999. Internal report.

[76] C. Waltham. DCA aging tests. Technical report, University of British Columbia, Vancouver, Canada, 1994. SNO-STR-94-017.

[77] B. Fulsom. Private communication, January 2001.

[78] R. C. Smith and K. S. Baker. Optical properties of the clearest natural waters (200–800 nm). *Applied Optics*, 20(2):177–184, January 1981.

[79] M. Pickel. Rayleigh scattering in heavy and light water. Technical report, Queen's University, May 2000. Internal report.

[80] T. Noble, 2000. Private communication from the Director of the SNO Water Group.

[81] N.K. Højerslev. Private communication, December 2000.

[82] E. S. Fry. Visible and near-ultraviolet absorption spectrum of liquid water: comment. *Applied Optics*, 39(16):2743–2744, June 2000.

[83] D. Grant. Private communication, May 2001.

[84] P. W. Milonni and J. H. Eberly. *Lasers.* John Wiley & Sons, New York, 1988.

[85] S. D. Biller, M. G. Boulay, J. Dunmore, K. C. Frame, A. L. Hallin, A. S. Hamer, J. R. Klein, B. A. Moffat, M. S. Neubauer, and D. L. Wark. Optics 6b. Technical report, Oxford University, Los Alamos National Laboratory, Queen's University and the University of Pennsylvania, April 2001. Internal report.

[86] A. Morel. Optical properties of pure water and pure sea water. In N. G. Jerlov and E. S. Nielsen, editors, *Optical Aspects of Oceanography*, pages 1–24. Academic Press, London, New York, 1974.

[87] A. Einstein. Theorie der opaleszenz von homogenen flüssigkeiten und flüssigkeitsgemischen in der nähe des kritischen zustandes. *Annalen der Physik*, 33:1275–1298, 1910.

[88] M. v. Smoluchowski. Molekular-kinetische theorie der opaleszenz von gasen im kritischen zustande, sowie einiger verwandter erscheinungen. *Annalen der Physik*, 25:205–226, 1908.

[89] M. Kerker. *The Scattering of Light and Other Electromagnetic Radiation.* Academic Press, New York, 1969. Chapter 3 gives general information about dipole scattering and a historical overview of the subject. See Chapter 9 for a derivation of the equation for turbidity following Einstein-Smoluchowski theory of density fluctuations.

[90] M. Dragowsky. PGT mean N_{hit}. Internal reports, 1999-2001. Reports at regular intervals cover all runs during production data taking.

[91] H. Ishino. *Measurement of the solar neutrino energy spectrum at Super-Kamiokande.* PhD thesis, University of Tokyo, Tokyo, Japan, January 1999.

[92] M. Nakahata et al. Calibration of Super-Kamiokande using an electron LINAC. *Nuclear Instruments and Methods*, A421:113–129, 1999.

[93] E. Blaufuss et al. ^{16}N as a calibration source for Super-Kamiokande. *arXiv:hep-ex/0005014*, January 2001. Submitted to Nuclear Instruments and Methods.

[94] A. Morel and L. Prieur. Analysis of variations in ocean color. *Limnology and Oceanography*, 22(4):709–722, July 1977.

[95] E.A. Avallone and T. Baumeister, editors. *Mark's Standard Handbook for Mechanical Engineers.* McGraw-Hill Book Company, New York, 9$^{\text{th}}$ edition, 1987.

[96] B.S. Massey. *Mechanics of Fluids.* Van Nostrand Reinhold Company, New York, 2 edition, 1970.

[97] GE Silicones, 2000. URL `http://www.gesilicones.com`. Extensive technical reference data from the manufacturer is available on their web site.

A Umbilicals

This appendix describes the details of the fabrication of the SNO calibration umbilicals for all sources.

A.1 Materials and Components Selection

The components selected for the umbilical have to be as small as possible to fit within size constraints imposed by the manipulator pulley system. To reduce wire radius for a given current-carrying capacity, Teflon insulated wires are used. Thin-walled Teflon tubes in a concentric arrangement provide gas flow and return lines for the ^{16}N and ^{8}Li sources. The gas flows down the thin-walled tube to the source, where it has a residency time of many seconds before returning in the space between the Teflon and the polyflow tubes. The central polyflow tubing or coaxial cable provides radial support (against crushing), as well as longitudinal support together with the helically wrapped wires.

Silicone Compounds

Both the hard silicone rubber compound used in umbilicals and the softer gel used in the PMT bases and in the laserball have excellent physical, electrical and optical properties. The main characteristics of the compounds are given in Table A.1. The

Silicone Rubber (umbilicals)	RTV 615 from GE (General Electric) Silicones. Similar product: Rhodorsil RTV 141 from Rhône-Poulenc. Clear, colourless, easily pourable. A+B fluids in 10:1 mixture. Viscosity: 4000 centipoise (4 Pa·s). Work time at 25°C: 4 hours. Hardness: 44 Shore A Durometer. Refractive index: 1.406. Dielectric strength: 19.7 kV/mm. Specific gravity: 1.02.
Silicone Gel (laserball)	RTV 6196 from GE Silicones. Clear, colourless. A+B compounds in 1:1 mixture. Viscosity: 750 centipoise (0.75 Pa·s). Work time at 25°C: 15 minutes. Refractive index: 1.41. Dielectric Strength: 19.7 kV/mm. Specific gravity: 0.98.

Table A.1: *Silicone compounds used for SNO.*

Canadian supplier for the silicone compounds is Silchem Inc. Naptha (camping fuel) is a useful, cheap solvent for cleaning surfaces that come in contact with the uncured silicones. Neither compound can be completely removed from clothing. Spills of the mixed compounds are best left to cure completely, after which they can be simply removed as one big piece. Mixing guns and cartridges (1:1 or 10:1) are purchased from Cammda Corp. to ensure rapid and accurate mixing. The use of 30-component static mixing nozzles ensures complete mixing of the A+B silicone liquids as they are pushed out of the guns.

Tubing used for Umbilicals

The outer silicone rubber jacket for all umbilicals is highly impermeable and also very resistant to abrasion. They can be handled very roughly without damage. Standard sizes of polyflow and capillary tubing are used for the gas flow sources. The gas flows down the teflon capillaries to the source, and returns in the space between

Silicone tube A (all but ^{8}Li)	Silicone rubber tubing. Translucent, medium hard: 50 Durometer (Shore A). ID: 3/8" (9.53 mm), OD: 1/2" (12.7 mm).
Silicone tube B (^{8}Li)	Silicone rubber tubing. Translucent, medium hard: 50 Durometer (Shore A). ID: 1/2" (12.7 mm), OD: 5/8" (15.9 mm).
Polyflow A (laserball, ^{16}N)	Low-density Polyethylene tubing. Flame-retardant: Black (max 100 psi (0.69 MPa)). FDA: Translucent white (max 120 psi (0.83 MPa)). ID: 0.170" (4.32 mm), OD: 1/4" (6.35 mm).
Polyflow B (^{8}Li)	Low-density Polyethylene tubing. Metric size: ID: 8 mm, OD: 10 mm. Transparent white. Maximum 90 psi (0.62 MPa).
Capillary A (laserball, ^{16}N)	Teflon TFE Spaghetti tubing. 11 AWG TW (thin wall: 0.012" (0.30 mm)), natural white. ID: 0.106" (2.69 mm), OD: 0.130" (3.30 mm). Maximum 100 psi (0.69 MPa).
Capillary B (^{8}Li)	Teflon TFE Spaghetti tubing. 8 AWG TW (thin wall: 0.015" (0.38 mm)), natural white. ID: 0.133" (3.38 mm), OD: 0.163" (4.14 mm).

Table A.2: *Tubing used for umbilicals.*

the polyflow and the capillary to be exhausted. The 22 fibres used in the laserball umbilical are protected by inserting them into a teflon capillary tube. At the centre of a polyflow tube, this capillary follows the neutral bending axis of the umbilical and further isolates the fibres from mechanical stresses. The "A" tubing in Table A.2 is used for all umbilicals but the ^{8}Li, which uses the "B" tubing. All tubing was acquired from McMaster Carr Supply Company.

Umbilical Electrical Wires

Teflon insulated hook-up wire is much smalled in diameter than wires insulated with most other plastics. Stranded wires are used whenever possible because they are much more flexible than solid-core wires. The thinnest available hook-up wire and thin coaxial cable from Belden Inc. were chosen for the umbilicals. The PC-source requires a fast coaxial wire for both bias (3kV) and signal. The signal is subjected to pulse-shape discrimination before generating a global trigger for SNO, which involves very tight timing constraints for tagging the desired Th-decays in the chamber. The pt-source accelerator requires the highest voltages of any calibration source: 30kV for the proton accelerator and 3kV for the focusing grid. These two wires are chosen to be as small as possible to fit inside a standard umbilical. The wires used in making all umbilicals are listed in Table A.3. Wire stranding is listed as A (N$\times$B) where A gives the cross-sectional area of the wire in American Wire Gauge (AWG) units, and N is the number of strands of gauge B (also in AWG units).

The fibre chosen for the laserball umbilical has low absorption and low dispersion over the wavelength range of interest (approximately 300 to 700 nm). The main properties given by the manufacturer, Fiberguide Industries, are listed in Table A.4.

Umbilical Connections

The fibre connections to the laser box are made with stainless steel SMA 906 connectors. These connectors have a hole big enough to fit a single 140 μm fibre. To fit all 22 fibres in the bundle used in the umbilical, the connector is drilled out and the fibres are fixed in place with fast-curing epoxy glue. The fibre ends are trimmed and polished using very fine grit polishing paper: first wet carbide papers of 240 and 600 grit, then 5 μm and 1 μm wet lapping film. The polishing procedure is much more successful if the acrylate jacket is not removed from the fibre ends – it normally would be stripped away for use in single-fibre connectors.

Wire connections are made with miniature plugs, and gas connections with standard 1/4” (6.35 mm) Swagelok fittings. The electrical connectors are all able to fit through a 0.5” (12.7 mm) hole, where the umbilical is sealed as it enters each source. Unfortunately, the nuts on the Swagelok connectors are too large to fit through such

Thin Wires (all)	Belden 83003. Hook-up Wire: 600V, 200°C 24 (19×36) AWG, silver-coated copper. Insulation: Extruded TFE Teflon, thickness 0.25 mm Nominal OD: 0.044" (1.12 mm)
Thin Coax (all)	Belden 83265. Plenum coaxial cable. MIL-C-17F, M17/169-00001, RG-178B/U. 30 (7×38) AWG, 0.012" silver coated copper covered steel. Resistivity: 820.2 Ω/km. Core insulation: TFE Teflon 0.84 mm. Shielding: silver coated copper, 47.9 Ω/km, 96% coverage. White FEP (Teflon) jacket, nominal OD: 1.80 mm (0.071"). Stripped of jacket: approximate OD 1.27 mm (0.050"). Impedance: 50 Ω. Capacitance: 95.10 pF/m. Velocity of propagation 69.5% *c*.
Fast Coax (PC-source)	LMR-200, high performance communications coaxial cable. From Times Microwave Systems. Solid bare copper conductor, diameter 0.044" (1.12 mm). Core insulation: polyethylene, thickness 0.072" (1.83 mm). Shielding: Al-polyester tape, tinned copper braid (90% cov.) Black polyethylene jacket, nominal OD: 0.195" (4.95 mm). Impedance: 50 Ω. Capacitance: 80.4 pF/m. Velocity of propagation 83% *c*.
High Voltage (pt-source)	Belden 8866. 18 (16×30) AWG, tinned copper. Conductive polyethylene layer: uniform HV stresses. Insulation: polyethylene, thickness 1.45 mm. Red PVC outer jacket: thickness 0.38 mm. Nominal OD: 0.208" (5.28 mm). Breakdown voltage 80kV, suggested working voltage 40kV.
Medium Voltage (pt-source)	Belden 8890. Miniature test prod wire. 24 (45×40) AWG, tinned coper. Insulation: rubber, thickness 0.48 mm. Nominal OD: 0.066" (1.68 mm). Breakdown voltage 10kV, suggested working voltage 1kV.

Table A.3: *Wires used for umbilicals.*

Optical Fibre (laserball)	Superguide G Fiber from Fiberguide Industries. Geometry: 100/140/250 μm (core/cladding/jacket). Core is high-OH (hydroxyl) fibre. Acrylate jacket. Attenuation: 6.0 dB/km at 820 nm. Fibre ID: BA-0031-1 (August 2000 umbilical). Prooftest: 64 kpsi (440 MPa). Part #: SFS 100/140Y

Table A.4: *Optical fibre used for the laserball umbilical.*

a small hole which means the gas sources can only be completely disassembled by cutting a small section (several cm) from the end of the umbilical.

A.2 Potting Procedure

To obtain solid cables, the space between the internal wires and outer silicone tube is potted with a silicone rubber compound. After mixing its two component liquids, this compound remains fluid for several hours. However, it is a challenge to get it to flow 30 m through the restricted annular volume between the wires and the silicone jacket of the umbilical. In outline, the procedures and equipment for accomplishing this are:

- Helically wrap the polyflow with thin wires. During this step, the polyflow is supported by a rope through its length. The rope allows the tube to be freely rotated and the wires are wrapped by paying them out onto the rotating tube. For solid central members such as coaxial or high-voltage wire the cable ends are held in a rotating support.

- The silicone tubing is inserted into eight 3.65 m sections of copper pipe. The pipe acts as a restraining surface, both against lengthwise slipping when the wires are drawn into the tube and against radial expansion during the high-pressure injection. The pipes mate mechanically through a pipe joint which is soldered to one end of each of the eight 3.65 m sections of pipe. A vacuum seal is made by clamping a short section of rubber vacuum pump hose over the joint. The side with the pipe joint seals well enough without a clamp, which make assembly and disassembly somewhat easier. Figure A.1 shows a cross-section of the joint between the pipe sections.

- The silicone tube is wrapped around ends of pipe to form seal and is "inflated" by pulling a vacuum in the volume between the copper pipes and the outside of the silicone tubing. This will anchor the tubing to the pipe by friction and allows the helically-wrapped central wires to be drawn through the silicone tube.
- At the injection end of the umbilical, a special "T"-fitting is used to ensure the potting compound is forced through the annular region between the central wires and the silicone tube. As illustrated in Figure A.2, the terminal section is back-filled to anchor the central wires and to force the silicone compound down the umbilical to be potted.
- The assembly is connected at one end to an injection piston (see Figure A.3), and at the other to an evacuated drum (see Figure A.4). The piston will force liquid silicone into the volume between the helically-wrapped wires and the inside of the silicone tubing. Eliminating trapped air between cables or at the front edge of the flow of the liquid silicone is the primary reason for the vacuum drum at the other end of the umbilical.

The potting piston is designed to fulfull two goals: degassing the silicone compound at moderate vacuum pressure ($\lesssim$ 3.3 kPa), and injecting the silicone compound into the umbilical at relatively high pressure ($\sim$ 2.1 MPa). Because the silicone liquid begins curing as soon as it is mixed, the degassing step must be accomplished in as short a time as possible. It is therefore desirable to maximize the surface area of

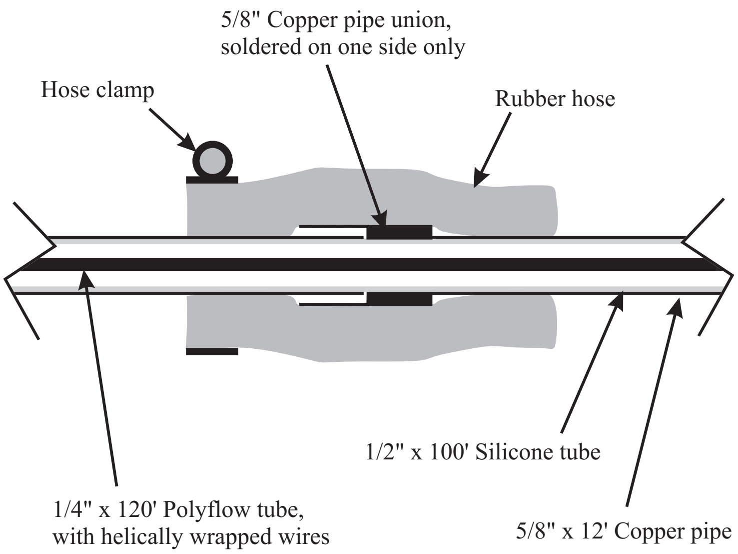

Figure A.1: *Potting pipe joint.*

liquid which is exposed to the vacuum. To be able to monitor the degassing, the piston is made entirely out of clear acrylic.

Effective injection requires pressures of order 2 MPa, which imposes a constraint on the allowable diameter and wall thickness of the piston. Standard acrylic tubing is desirable because it can be bought relatively cheaply and is readily available. The tensile strength of the acrylic used in the construction of the AV is 79 MPa [52]. This is somewhat higher than the typical numbers 48–75 MPa given for acrylic in Avallone and Baumeister [95]. The maximum ratio of the average tube diameter D to the wall thickness w can be specified from this information as follows:

$$\frac{D}{w} = \frac{P_{\max}}{P} \sim \frac{48-79}{2} = 24-39 \tag{A.1}$$

A tube 6' long (=183 cm) with an outer diameter of 3" (=7.62 cm) and wall thickness of 1/4" (=6.35 mm) was selected to meet all these criteria. With $D/w = 11$, the safety factor is at least 2.2 and the piston is thus deemed safe for careful use in a laboratory

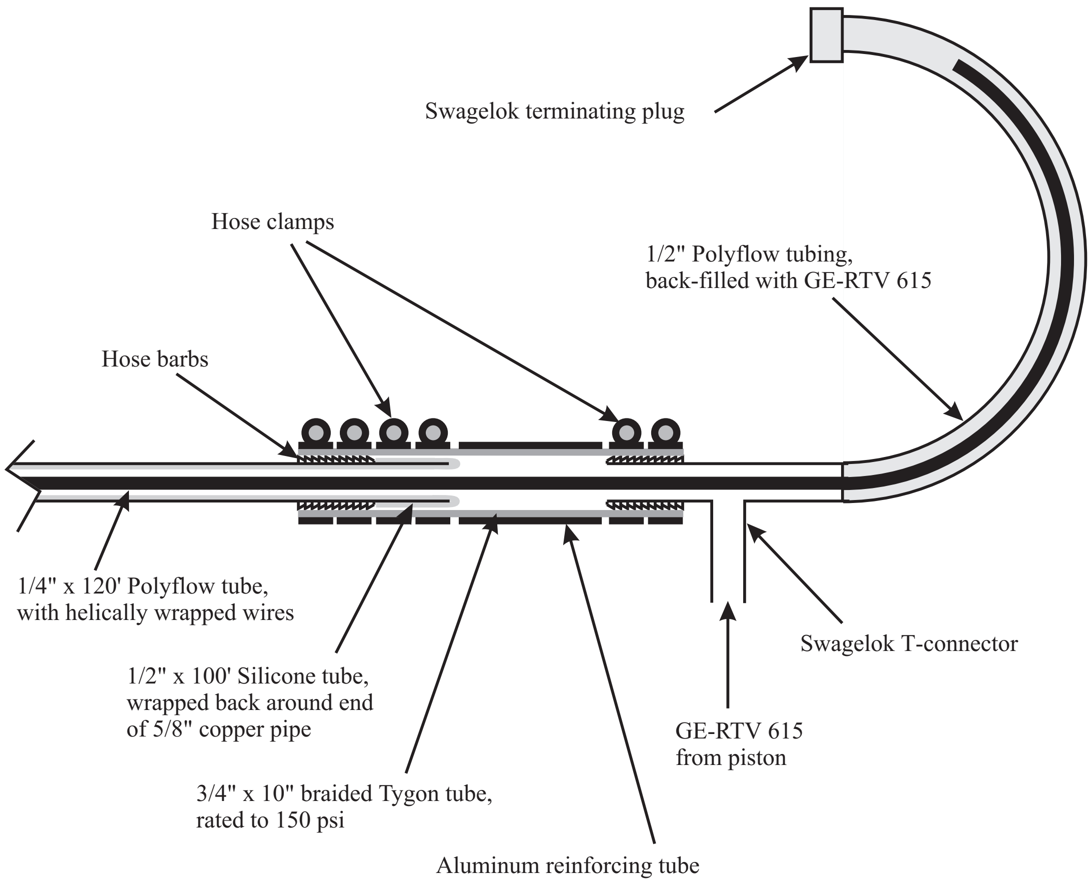

Figure A.2: *Potting injection hardware.*

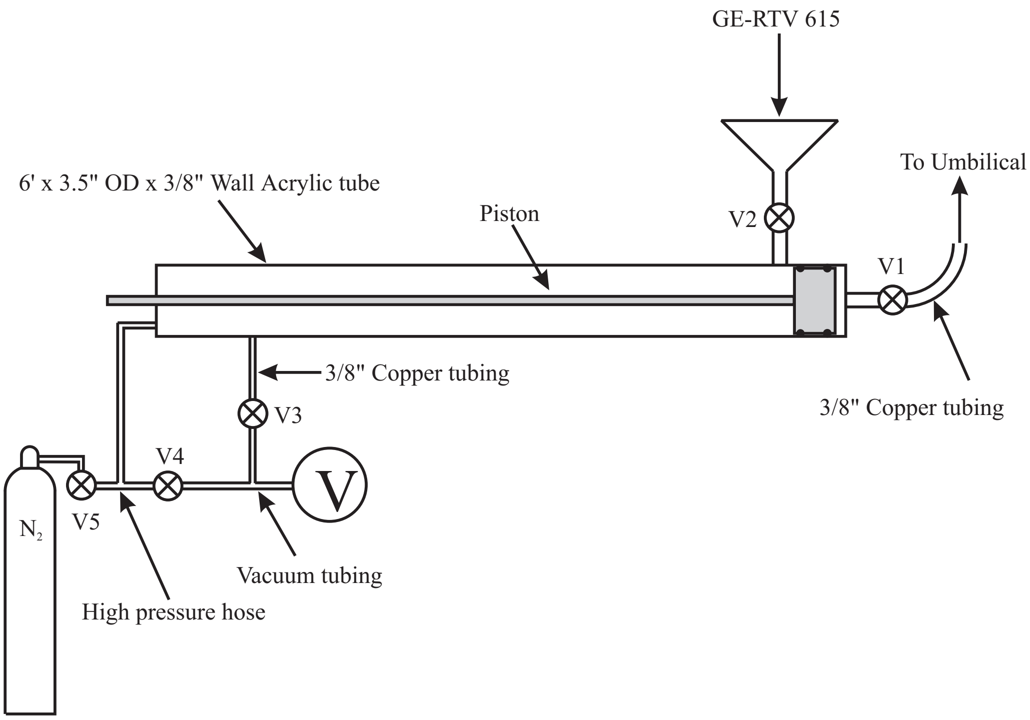

Figure A.3: *Potting piston.*

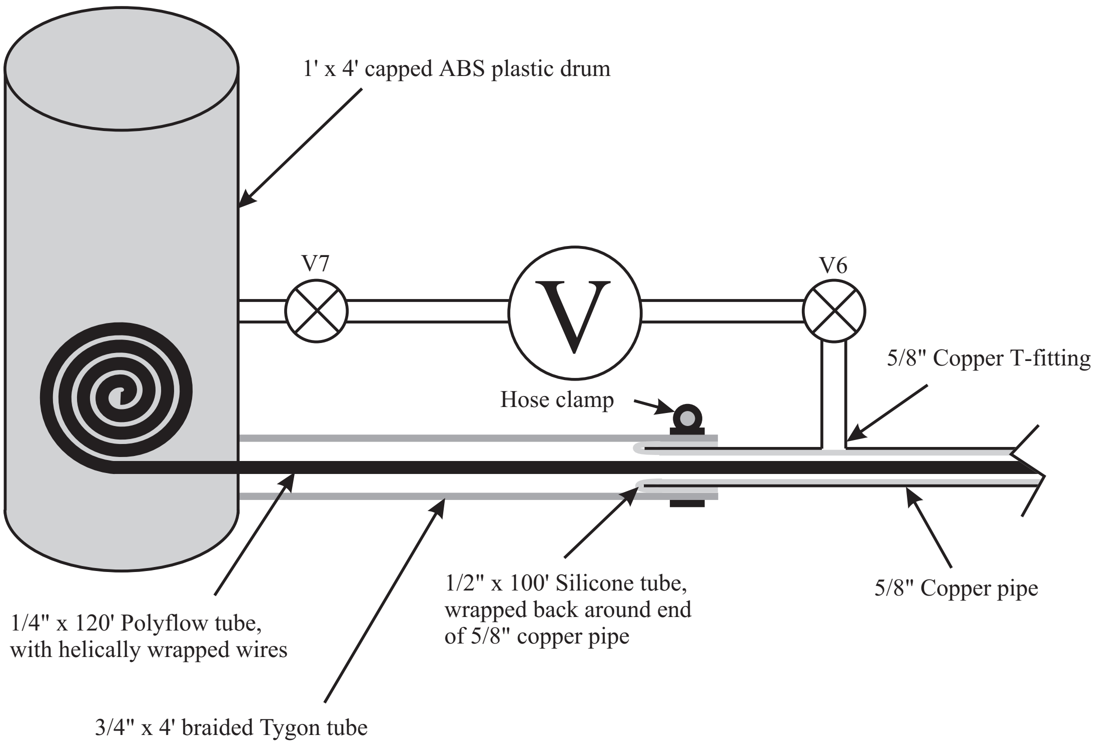

Figure A.4: *Potting drum and vacuum connections.*

environment.

A.3 Potting Method: Viscous Flow Calculations

Assuming Poiseuille flow conditions for an incompressible fluid gives a velocity profile for a round pipe of [96]:

$$u_z(r) = \frac{1}{16\eta}\left(\frac{dp}{dz}\right)\left(D^2 - 4r^2\right) \tag{A.2}$$

where $u_z(r)$ is the velocity at radius r and position z along the length of the pipe, η is the viscosity of the fluid, $\mathrm{d}p/\mathrm{d}z = P/l$ is the pressure gradient along the length of the pipe (P is the pressure difference between injection end and the leading edge of the flow at l; the leading edge is kept at a fraction of an atmosphere's pressure), and D is the inner diameter of the pipe. The flow rate is calculated from this velocity profile as

$$dQ = u_z(r)\,2\pi r\,\mathrm{d}r \tag{A.3}$$

$$Q = \frac{\pi P}{8\eta l}\left(D^2 - 4r^2\right) r\,\mathrm{d}r \Big/_{0}^{D/2} = \frac{\pi P}{128\eta l} D^4 \tag{A.4}$$

where $Q = (\pi D^2/4)(\mathrm{d}l/\mathrm{d}t)$ is the linear flow rate down the pipe. Integration yields the time to fill a given length L of pipe with fluid:

$$t = \frac{16\eta L^2}{PD^2} \tag{A.5}$$

Fluid flow between two concentric pipes predicts a modified time to fill a given length, starting with the rate of linear flow between the inner (R_1) and outer (R_2)

radii of the pipe:

$$Q = \frac{\pi P}{8\eta l}\left(R_2^2 - R_1^2\right)\left(R_2^2 + R_1^2 - \left[\frac{R_2^2 - R_1^2}{\ln(R_2/R_1)}\right]\right) \tag{A.6}$$

This flow rate can again be integrated as above to give a prediction for the time needed to fill a length L of pipe:

$$t = \frac{4\eta L^2}{P\left(R_2^2 + R_1^2 - \left[\frac{R_2^2 - R_1^2}{\ln(R_2/R_1)}\right]\right)} \tag{A.7}$$

In our case, however, the viscosity increases as the silicone compound sets. The increase in viscosity has been found to match the following functional form:

$$\eta = A + B\mathrm{e}^{Ct} \tag{A.8}$$

where A, B and C are to be determined experimentally. Although viscosity versus time data were not available for the GE RTV-615 silicone used in the umbilicals, the data sheets for the Rhône-Poulenc RTV-141 silicone indicate identical properties and include viscosity versus time information. This information is adopted for use in the flow calculations for GE RTV-615, and are shown in Figure A.7.

Equation A.8 can easily be integrated and used to calculate the pottable length L as a function of time t in combination with the flow rate Q from Equation A.6.

$$\int_0^L l\,\mathrm{d}l = \int_{t_0}^{t} \frac{Q}{\pi(R_2^2 - R_1^2)}\,\mathrm{d}t \tag{A.9}$$

$$\frac{L^2}{2} = \frac{P}{8}\left(R_2^2 + R_1^2 - \left[\frac{R_2^2 - R_1^2}{\ln(R_2/R_1)}\right]\right)\int_{t_0}^{t}\frac{dt}{\eta(t)} \tag{A.10}$$

$$L^2 = \frac{P}{4}\left(R_2^2 + R_1^2 - \left[\frac{R_2^2 - R_1^2}{\ln(R_2/R_1)}\right]\right)\left(\frac{t - t_0}{A} - \frac{1}{AC}\ln\left[\frac{A + B\mathrm{e}^{Ct}}{A + B\mathrm{e}^{Ct_0}}\right]\right) \tag{A.11}$$

where t_0 is the time delay between mixing (at time $t = 0$ when η starts to increase)

	$R_{1,\text{eff}}$ (mm)	R_2 (mm)
Nominal 1/4" OD polyflow	3.1750	6.7352
^{16}N / Laserball umbilical	3.7338	6.7352
pt-source umbilical	3.4798	6.7352
PC-source umbilical	3.0353	6.7352
Nominal 10 mm OD polyflow	5.0000	7.3180
^{8}Li umbilical	5.5588	7.3180

Table A.5: *Umbilical injection model parameters.*

and the start of injection (when the flow down the pipe starts).

The results of this calculation of $L(t)$ for several umbilical geometries and injection pressures appears in Figure A.5. The two manual guns used to mix the silicone can produce 1 ℓ each in about 15 minutes, and the degassing time is typically 20 minutes before injection resulting in a time offset $t_o \sim 0.6$ h.

The helically wrapped wires are a perturbation on the concentric flow model, and are included in the calculation by using an effective inner radius $R_{1,\text{eff}} = R_1 + r_{wire}/2$ where r_{wire} is a typical radius for one of the helically wrapped wires. Given the uncertainty on the time evolution of the viscosity, this somwhat arbitrary increase in R_1 has a negligible impact on the calculated injected length L. The radial parameters $R_{1,\text{eff}}$ and R_2 used to make these plots are listed in Table A.5.

A pressure of 2.1 Mpa (300 psi) was selected for injection of the umbilicals. Although it is possible to inject the silicone at lower pressures and obtain the desired length of umbilical, the time under pressure is too long. The silicone cures with the umbilical expanded against the constraining pipes, which prevents the finished cable from being removed. By trial and error it was found that stopping the injection about 1 h after mixing the A+B compounds of the silicone allows the silicone jacket to relax to its nominal diameter, with the excess uncured silicone oozing back out the ends of the umbilical.

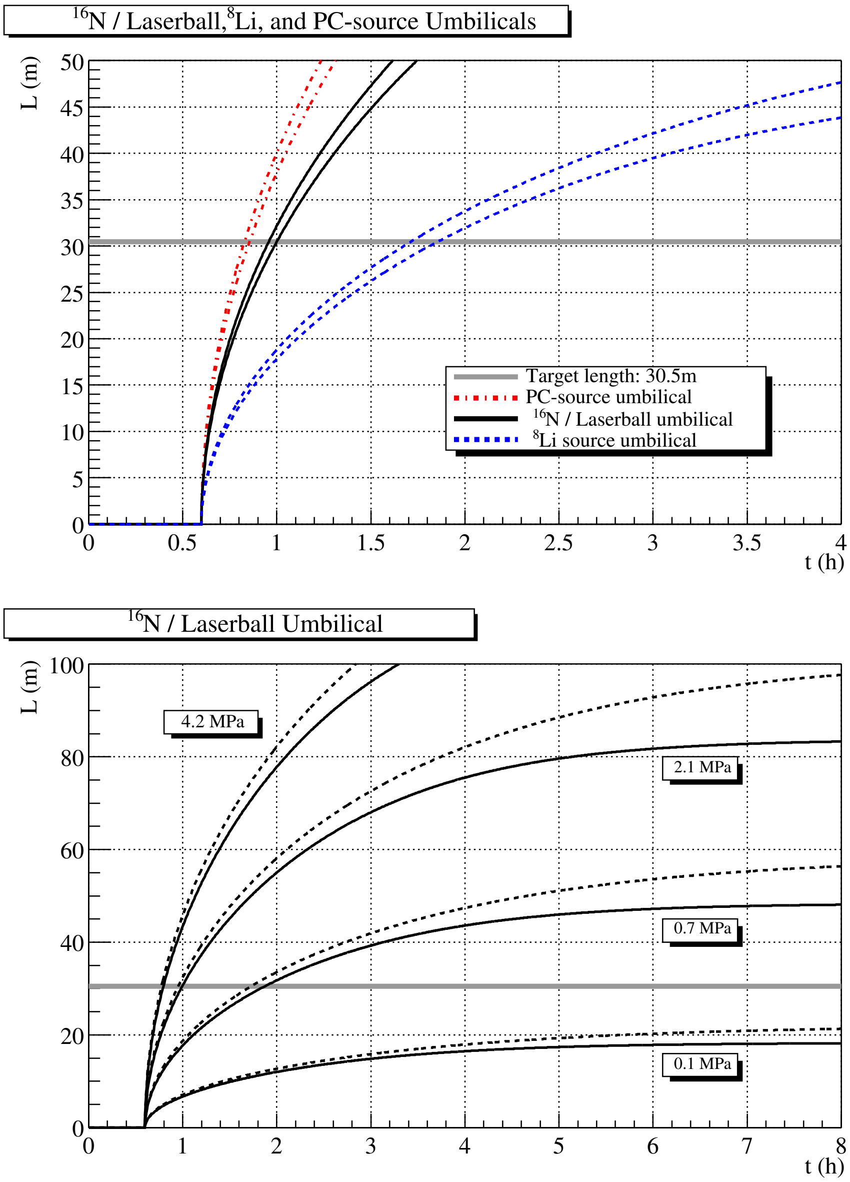

Figure A.5: *Umbilical injected length as a function of time, injection pressure and umbilical geometry. The top plot shows the predicted injection times with $P \sim 2.1$ MPa. The bottom plot shows the effect of varying the pressure differential from atmospheric (0.1 MPa) to twice the nominal operating pressure (4.2 MPa).*

The injection of silicone at about 20 times atmospheric pressure leads to an adjustment to R_2 which takes into account the stretching of the silicone tubing as it is forced up against the metal pipe constraining the flow. The volume of the tubing material itself is assumed not to decrease significantly under pressure, which results in an increased R_2 compared to the nominal value. The nominal wall thickness of the silicone tubing is 1/16" (= 1.5875 mm).

The effect of temperature on the rate of curing of the silicone compound is significant, as shown for data from the GE RTV 615 silicone in Figure A.6. The fit shown is $t = A\exp(E_A/kT) = 1.573 \times 10^{-6}\exp(0.438(eV)/kT)$ where t is in hours, T is in Kelvin, E_A is an activation energy, and k = 8.617342 eV/K is the Boltzmann constant. Potting in the air-conditioned building in the summer worked, while potting in the heated building in December resulted in umbilicals 20 feet shorter. Storing the RTV-615 compound in the fridge at $T \sim 4°$C slowed the rate of curing enough to permit successful injection of the compound into the umbilical, regardless of the building temperature. Correlated with the slower rate of curing is a longer rise time for the viscosity, which had the beneficial consequence that more fluid was able to ooze out of the umbilical after injection. This allowed the umbilical to be easily removed from the slightly oversize piping used to constrain it during the injection.

The viscosity of the mixed silicone compound increases with time, as expected for a two-component silicone as it polymerizes and cures. Cross-linking of silicone polymer chains is controlled by the chemistry of the additives included in the mix [97]. The pot-life of the mixed compound is given by the manufacturer as 4 hours at room temperature ($T \sim 25°$C). Starting with the components in the fridge at $T \sim 4°$C extends the pot-life dramatically. The silicone reaches room temperature within a few hours of being taken out of the fridge and injected into the umbilical, and proceeds to cure at the usual room temperature rate. It was found that during the summer months the air conditioning brought the building temperature down to

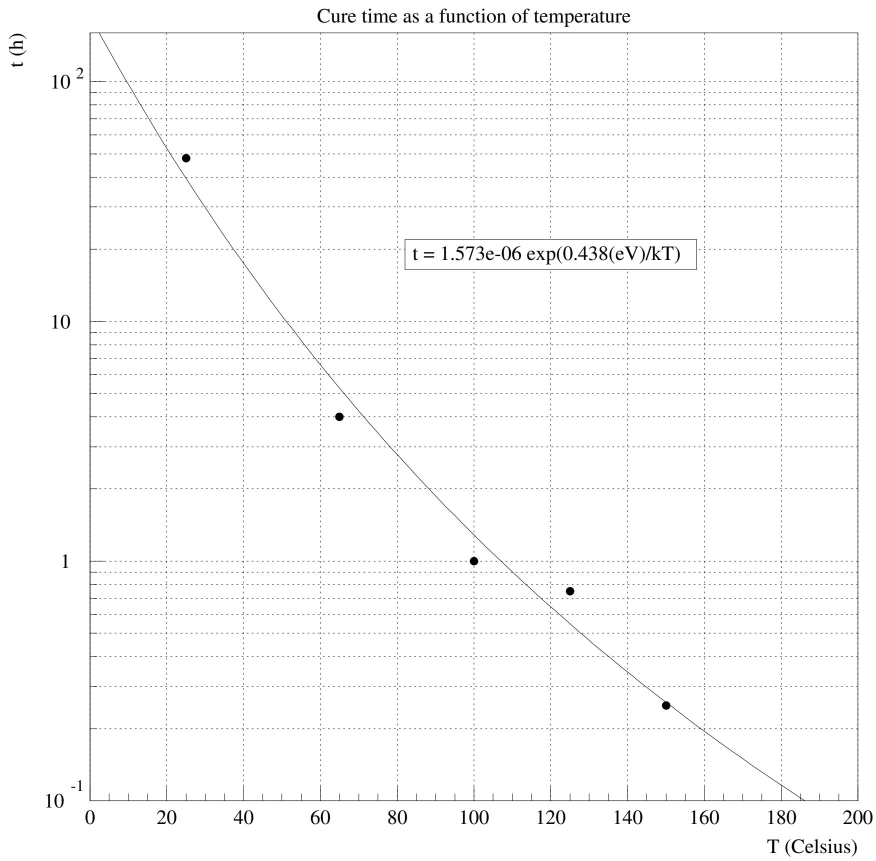

Figure A.6: *The cure time for GE RTV 615 silicone after mixing the two components, as a function of temperature. Data points are from the literature provided by General Electric.*

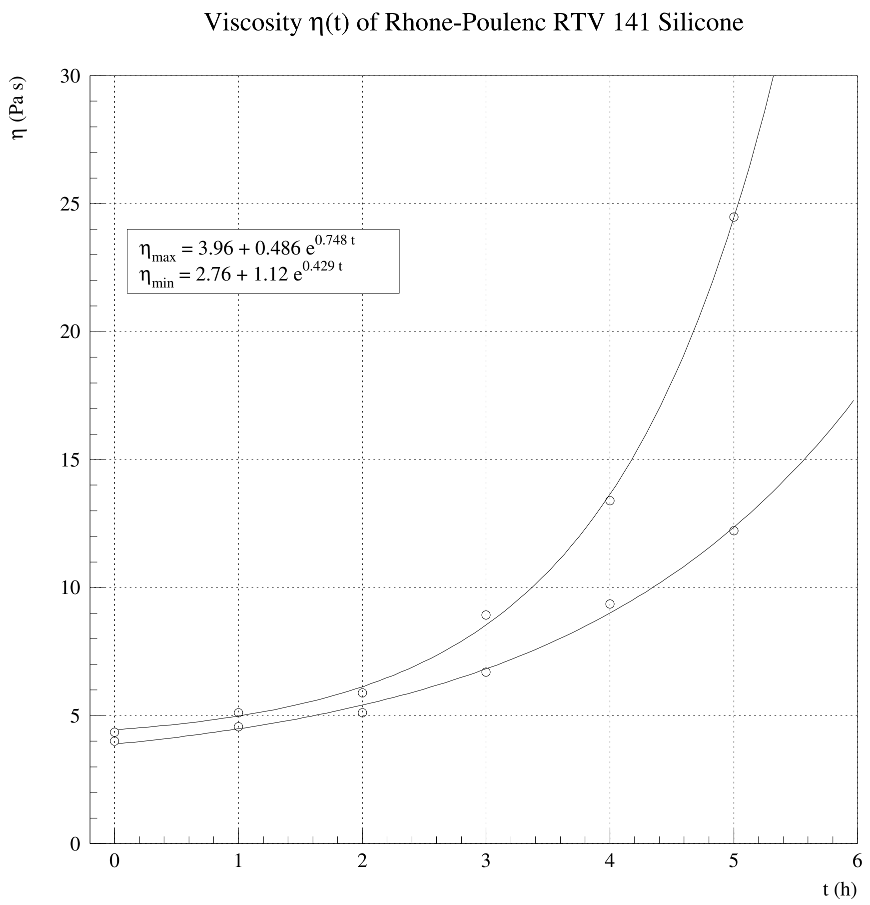

Figure A.7: *Viscosity of Rhône-poulenc RTV 141 silicone potting compound at room temperature ($T \sim 25°C$). The exponential fits shown are to the maximal batch viscosity (upper curve) and minimum batch viscosity (lower curve) reported in the literature data sheets from Rhône-Poulenc.*

18–20°C and we obtained relatively long pot life compared to the fall/winter when the buildings were heated to 23–25°C. Storing the unmixed silicone compounds in the fridge ensures that the injection and initial relaxation of the umbilical can be done consistently and essentially independently of the temperature of the building.

B Reflections from the SNO PMT's

Photographs of the reflected light pattern for a PMT under normal incidence illumination in air are shown. These photos were taken to illustrate the complex pattern of reflected light which the SNOMAN Monte Carlo seeks to model [2]. The complicated pattern of the reflected light suggests that a completely realistic model of the PMT and reflector assembly will remain elusive. Work by the Oxford group responsible for the PMT model in SNOMAN is ongoing in an effort to improve the model. The goals of this effort are to obtain agreement with the *in situ* measurements of PMT response presented in this thesis, and to obtain satisfactory late time distributions compatible with calibration source measurements in the detector.

Figure B.1 gives an overview of the setup used to take these photographs. The PMT is oriented so that light from the projector illuminates the entire PMT at normal incidence. The HeNe (633 nm) laser beam is expanded to a spot size of nearly 1 cm and is directed towards the PMT so that only a single petal is illuminated.

Figures B.2 and B.3 show the reflection patterns observed in air for the red laser and white projector illumination, respectively For Figures B.3(a) and B.4(a), the camera was placed on a tripod several meters away from the PMT and at an angle of 35° with respect to the light source-PMT axis. In Figures B.3(b) and B.4(b), a white screen was placed directly next to the PMT and reflector, and the camera was

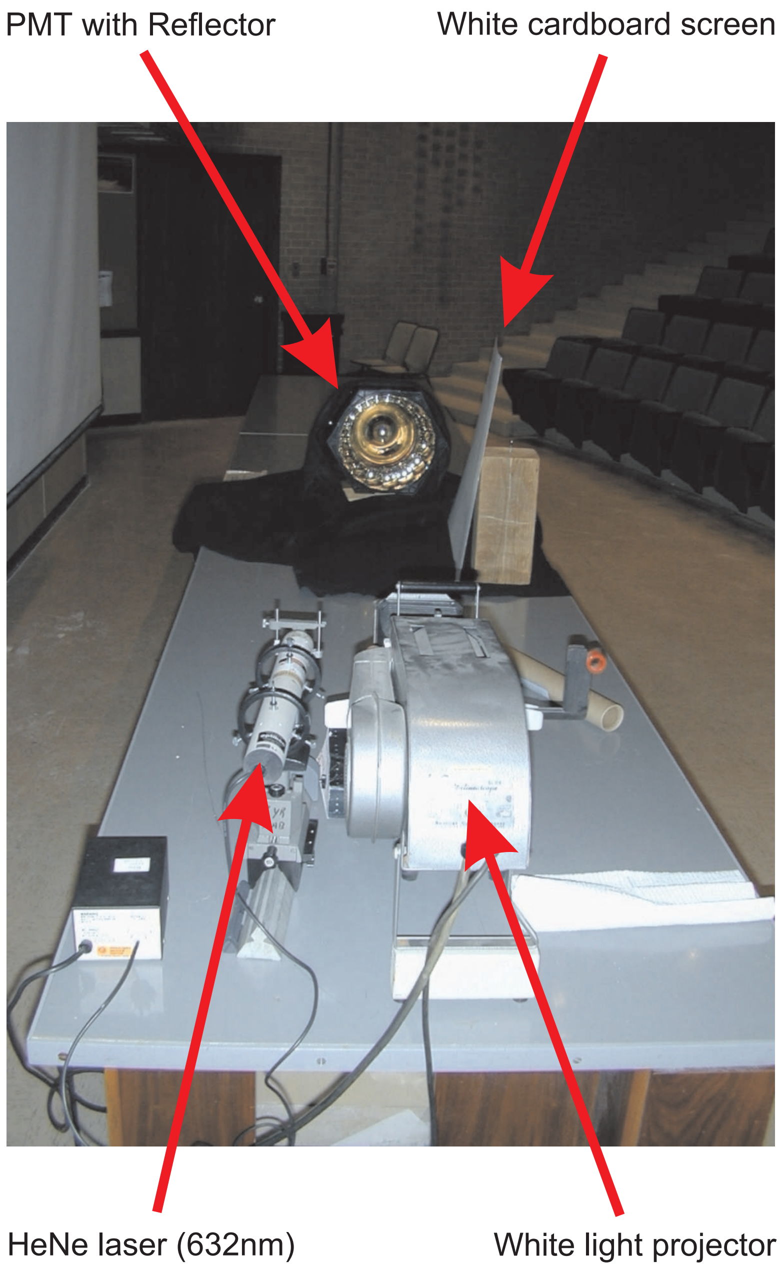

Figure B.1: *Setup used for taking photographs of the SNO PMT and its reflector.*

placed on a tripod directly facing this screen.

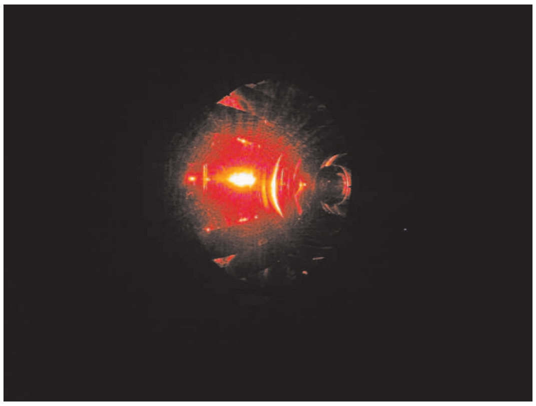

(a) Camera at 35° angle with respect to PMT axis.

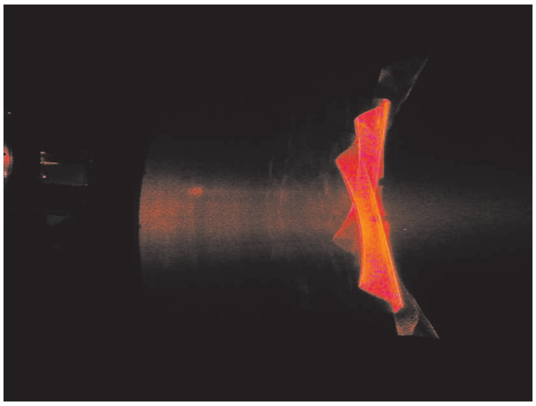

(b) Image of reflection on white screen next to PMT.

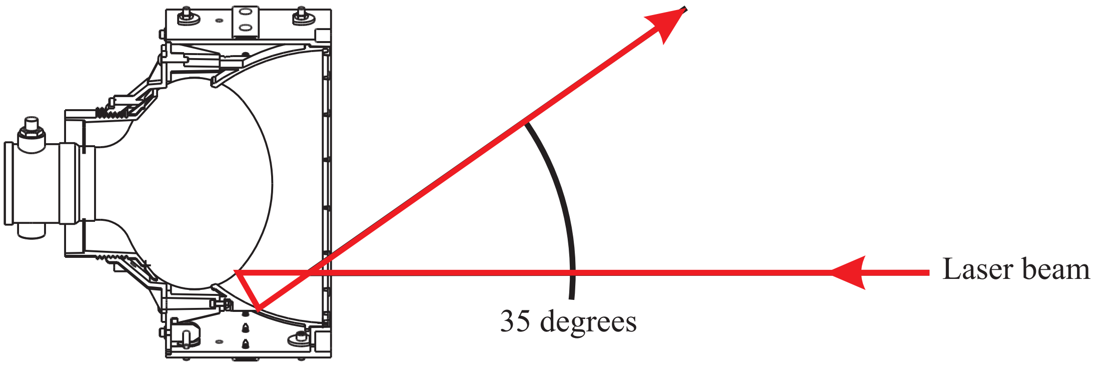

(c) Light paths.

Figure B.2: *Reflections from the SNO PMT and its reflector under laser illumination.*

(a) Camera at 35° angle with respect to PMT axis.

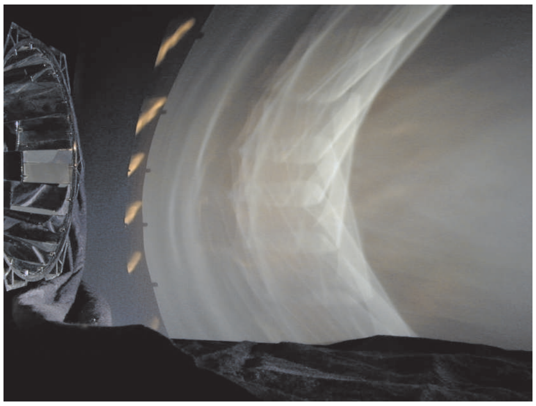

(b) Image of reflection on white screen next to PMT.

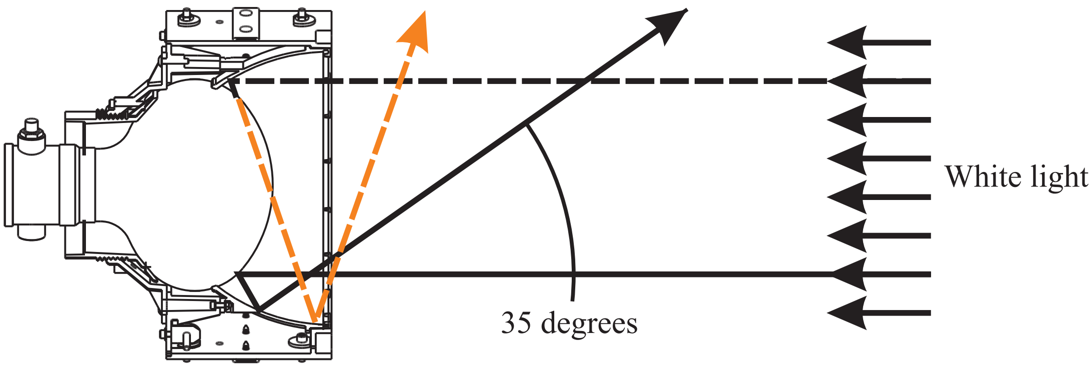

(c) Light paths.

Figure B.3: *Reflections from the SNO PMT and its reflector under white light.*

Vita

Bryce Anton Moffat.

Born in Bochum, Germany on June 2nd, 1972.

Education

B.Eng. (Engineering Physics) from the École Polytechnique de Montréal (1994).

M.Sc. (Physics) from the Université de Montréal (1996). Thesis directors: Prof. P. Depommier and Prof. G. Azuelos. Thesis title: *Les π^0 produits dans les détecteurs Cherenkov du projet d'oscillations de neutrinos E889 à BNL.*

Ph.D. (Physics) from Queen's University at Kingston (2001). Thesis director: Prof. A.L. Hallin. Thesis title: *The Optical Calibration of the Sudbury Neutrino Observatory.*

Awards

Thesis completion bursary from Queen's University, 2000.

Fonds pour les Chercheurs et l'Aide à la Recherche (FCAR) bursary for Ph.D. studies, 1996–1999.

National Science and Research Council of Canada (NSERC) bursary (PGS-B) for Ph.D. studies, 1996–1998.

Fonds pour les Chercheurs et l'Aide à la Recherche (FCAR) bursary for M.Sc. studies, 1994–1995.

Publications

J. Boger, ..., B.A. Moffat, ... (200 authors, alphabetical order, The Extended SNO Collaboration), The Sudbury Neutrino Observatory, Nuclear Instruments and Methods A449, 172–207 (2000).

Q.R. Ahmad, ..., B.A. Moffat, ... (178 authors, alphabetical order, The SNO Collaboration). Measurement of charged current interactions produced by ^{8}B solar neutrinos at the Sudbury Neutrino Observatory. *Physical Review Letters, 87(7):071301–1–071301-6, July 2001.*

Q.R. Ahmad, ..., B.A. Moffat, ... (178 authors, alphabetical order, The SNO Collaboration), Calibration Devices for the Sudbury Neutrino Observatory, in preparation. To be submitted to Nuclear Instuments and Methods in 2001.

Experience

Research Assistant with SNO, Queen's University, Kingston, Canada (05/1996–07/2001).

Teaching Assistant at Queen's University, Kingston, Canada (1996–1999).

Teaching Assistant at the Université de Montréal, Montreal, Canada (1994–1995).

Volunteer Work: SNO mini-course lectures for high-school students, Science Fair Judge, and organizer of the Particle Physics Journal Club (1995–2000).